2016

Sinkhole Monitoring Using Groundwater Table Data

Ton Tu
University of Central Florida

SINKHOLE MONITORING USING GROUNDWATER TABLE DATA

by
TON NHU TU
B.S. University of Central Florida, 2014

A thesis submitted in partial fulfillment of the requirements
for the degree of Master of Science
in the Department of Civil, Environmental and Construction Engineering
in the College of Engineering and Computer Science
at the University of Central Florida
Orlando, Florida

Fall Term
2016

Major Professor: Hae-Bum Yun

ABSTRACT

Florida might be one of the most sinkhole-active areas on the earth. Due to its unpredictability and significance of occurrence, the development of sinkhole monitoring techniques is imperative to minimize sinkhole-induced hazards. Several methods have been used to evaluate sinkhole risks, including destructive methods, such as Standard Penetrating Tests (SPT) and Cone Penetrating Tests (CPT), geophysical method, and sensor-based groundwater monitoring method. However, few studies are available for comprehensive understanding of spatiotemporal sinkhole mechanism by combining different exploration methods under realistic experimental conditions.

The objective of this study is to understand spatiotemporal sinkhole mechanism, using SPT, CPT, ground penetrating radar (GPR), and piezo pressure sensors tested at actual sinkhole sites. A small-scale test was conducted prior to the field test to validate data analysis technique using piezo pressure sensors, developed in this study. Eight piezo pressure sensors were used located at different distances from the sinkhole center to measure the ground water levels (GWLs) during artificially made sinkhole events. A total of 24 scaled tests was conducted with different sinkhole soil thickness and initial GWL. The cone of water depression was observed during the tests, which indicates there are strong relationship between sinkhole and sinkhole occurrence. A novel peak-counting method was developed and validated to estimate spatiotemporal relations of the relations between GWLs and sinkhole collapse patterns.

The field test was conducted at an active sinkhole site in Lake county, Florida to determine locations of points of breach and to monitor fluctuation GWL over time. Twenty piezometer

sensors were installed, and the GWLs were monitored for three months at 30-min sampling rate. The daily moving average of GWL was calculated and visualized in ArcGIS map to understand spatiotemporal behavior of GWL at different locations from sinkhole positions. The monitoring results were compared with CPT, SPT and GPR results that were conducted prior to the piezo sensor installations. Strong correlations were observed between CPT, SPT, GPR and GWL results. From the results, it can be concluded that size and shape of the cone of water depression depend on dimensions of point discharges and properties of surrounding soil.

This work is dedicated to my mother "Thuyen Nguyen", my wife "Thuy Pham", my brother "Trong Tu", and my sister "Daisy Tu"

Without their supports, this work would have not been possible

ACKNOWLEDGMENTS

The writer of this thesis wishes to express his sincerest appreciation and gratitude to his major advisor, Dr. Hae-Bum Yun, for his patient guidance, continuous support, and kindness. The writer also would like to express special thanks to his committee members, Dr. Boo-Hyun Nam and Dr. Ding-Bao Wang for their valuable time to review the writer's paper.

The writer would also expand his special thanks to his research group, especially Mr. Namgyu Kim, Mr. Mingyu Cha, and Mr. Ryan Shamet from Dr. Boo-Hyun Nam's research group for their supports and friendship.

In addition, the writer would like to thank Florida Department of Transportation, State Materials Office and District 5, and Dr. Mohamed Alrowaimi for providing valuable information and data for his research.

Finally, the writer would like to thank the Department of Civil, Environmental and Construction Engineering for providing technical and financial supports for this work.

TABLE OF CONTENTS

LIST OF FIGURES

LIST OF TABLES

CHAPTER 1: INTRODUCTION

1.1 Background of the Study

Sinkholes are geologic feature and naturally occur in karst terrain areas. Sinkholes play an important role to public health and safety because it causes structural damages, property losses, and dramatic impact on people lives. The most destructive developed suddenly on May 8-10, 1981, in Winter Park, and caused over four-million dollars of damages (Jammal amd Associates, 1982). Moreover, according to a book published in 2006, Lerche and Glaesser reported that the economic damage risk to housing are estimated to be five-million dollars per year for the city of Tampa itself and expected to increase in the near future.

Sinkholes also threaten water and environmental resources by creating direct pathways between surface water to underlying aquafers. In the areas of developed pathways, surface contaminants can be transmitted into underlying aquafers causing degrade of ground water resources (Tihansky, 1999). On September 16, 2016, the sinkhole opened up at the plant under a gypsum stack, which was a pile of hazardous waste, as the Tampa Bay Times reported "It drained millions of gallons of acidic water laced with sulfate and sodium from a pool atop a 120-foot gypsum stack. An unknown amount of gypsum, a fertilizer byproduct with low levels of radiation, also fell into the sinkhole, which is believed to be at least 300 feet deep." Aerial view of this giant sinkhole is shown in Figure 1.

Because of negative impacts of sinkholes on public health and safety and environmental resources, sinkhole detection and monitoring are the key factors to predict and reduce its risk levels. Many researches have been conducted to determine sufficient methods to detect and

evaluate sinkholes and its levels of risks. However, a standard method for sinkholes detection have not been selected yet. The writer of this thesis wants to contribute his efforts to find an effective way to monitor sinkhole using groundwater table.

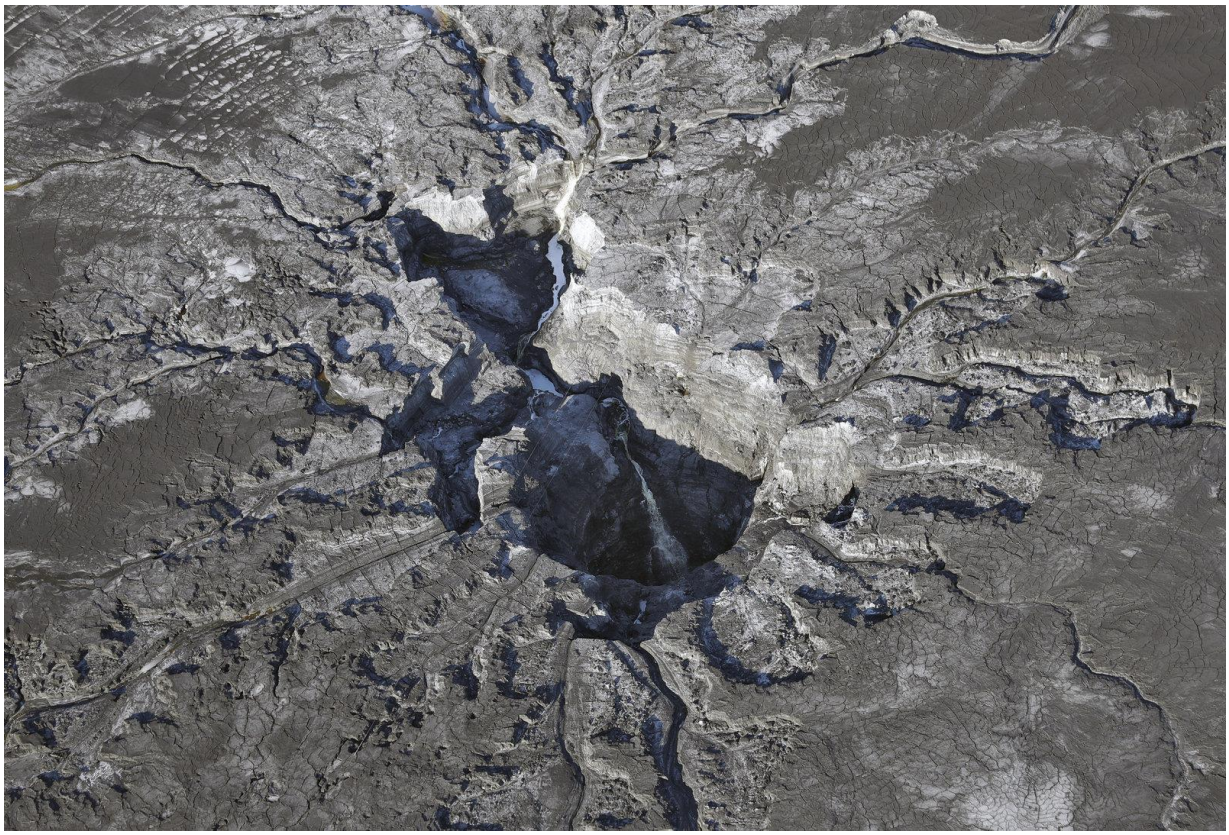

Figure 1: Water continues to flow into a large sinkhole on the Mosaic Co. property in Mulberry, Florida (O'Meara, 2016)

1.2 Statement of Objective

The objective of this study is to understand spatiotemporal sinkhole mechanism, using Standard Penetration Test (SPT), Cone Penetrating Test (CPT), Ground Penetrating Radar (GPR), and piezo pressure sensors tested at actual sinkhole sites. A small-scale test is conducted prior to the field test to validate data analysis technique using piezometer pressure sensors, develop in this

study. The field test is conducted at an active sinkhole site in Lake county, Florida to determine locations of points of breach and to monitor fluctuation GWL over time.

1.3 Outline of Dissertation

Chapter 1 provides background and objectives of this study

Chapter 2 reviews literatures on karst terrain, sinkholes formation, and sinkhole detection and prediction methodologies, which include Cone Penetration Test (CPT), Ground Penetrating Radar (GPR) and piezometer sensor.

Chapter 3 provides detailed development and result of sinkhole detection using scaled model test.

Chapter 4 presents development of ground monitoring system using piezometer sensors as well as analyzed results from piezometers' data.

Chapter 5 summarizes the findings from investigated data. In addition, limitations and future researches are also presented in this chapter.

CHAPTER 2: LITERATURE REVIEW

2.1 Karst Terrain

Karst terrains develop in the areas underlain by carbonate rocks, primary limestone and dolomite, and have drainage in form of sinkholes, springs, caves, disappearing streams, and underground drainages. Karst topography is generally irregular because of acidic water, which dissolve carbonate rock forming cavities and allowing surficial sediments to collapse or subside. Carbonates are large group of minerals when they all have common carbonate ion (CO_3). When combined with other elements, it formed various carbonate minerals. The three most common carbonate mineral are calcite, aragonite ($CaCO_3$) and dolomite ($CaMg(CO_3)_3$). Calcite is by far the most abundant carbonate mineral that dominates other carbonate minerals. In pure limestones calcite contributes up to 98 to 100 percent. Practically, limestones in Florida are either calcite or dolomite with calcite predominant over dolomite (Lane, 1986).

2.2 Florida Geology and Sinkhole

Sinkhole is part of natural process in the karst terrain area where the existing of soluble rock such as limestone, gypsum, dolomite, and other carbonate rocks is present. There are two types of processes that create sinkholes, dissolution and suffusion. Dissolution occurs where soluble rock such as limestone, gypsum, dolomite, and other carbonate rocks dissolve into water. Rainfall (H_2O) percolating through atmosphere and soil reacts with carbon dioxide (CO_2) to form weak carbonate acid (H_2CO_3). When carbonate acid (H_2CO_3) infiltrates over the cover sediment layer, it slowly reacts with limestone ($CaCO_3$) or dolomite [$CaMg(CO_3)_3$]. Cavities and voids develop as limestone and dolomite dissolve into ions, calcium (Ca^{2+}) Magnesium (Mg^{2+}), and bicarbonate (HCO_3^-). When dissolved minerals in the water become supersaturated, further

dissolution is impossible. Carbonate salts of calcium and magnesium may precipitate from the water, often forming interesting shapes such as stalactites (Tihansky, 1999). The detailed process shown in Figure 2. The other type of sinkhole creation process is suffusion. Suffusion occurs when the non-cohesive materials infill the carbonate bedrocks as shown in Figure 3. The erosion begins at the top of the carbonate bedrock, and develop toward the soil surface.

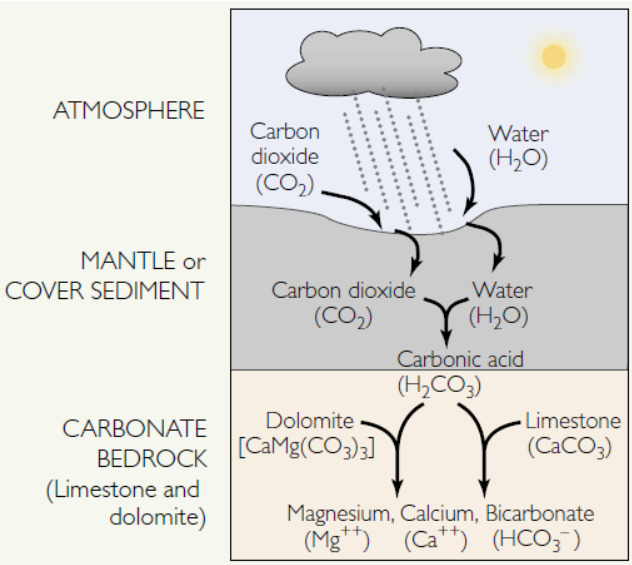

Figure 2: Dissolution process (Tihansky, 1999)

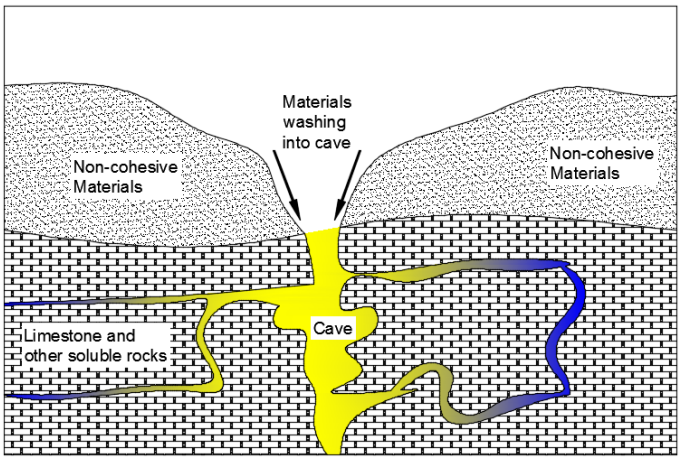

Figure 3: Suffusion process

From two types of process, dissolution and suffusion, create three classes of sinkholes, gradually subsidence, cover-subsidence, and collapsed-subsidence. On outcrop soluble rocks without significant soil cover, rainwater percolates through limestone joints to water table then the soluble rock adjacent to these joints arose faster than elsewhere and small depression gradually form. For the area where soluble rocks expose to atmosphere, aggressive dissolution also occurs where flow is focused in preexisting openings in the rock, such as along joints, fractures, and bedding planes, and in the zone of water-table fluctuation where ground water is in contact with the atmosphere as shown in Figure 4 (Tihansky, 1999).

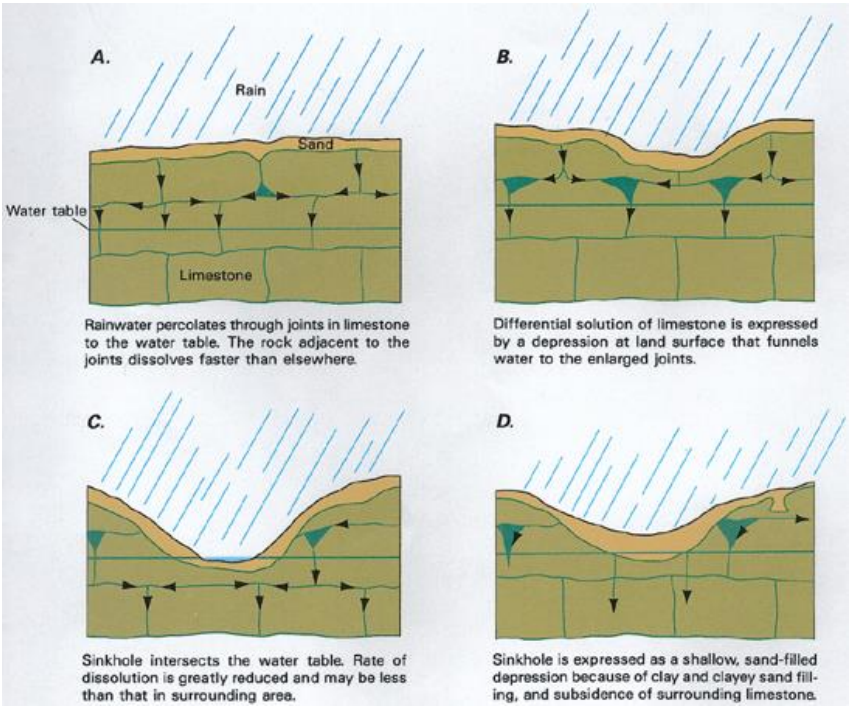

Figure 4: Gradually subsiding of shallow sinkholes at the area overlain by a layer of sand (U.S. Geological Survey, n.d.)

Cover-subsidence sinkhole normal occurs when sandy soil underlain by preexisting cavity. Soil sediments settle into the vacated space until certain point when surface depression can be noticeable. Details of process is in Figure 5. Both gradually subsidence and cover-subsidence are slow process. Thus, any signs of sinkhole formation can be noticeable and evacuateable. On the other hand, collapsed-subsidence occurs without any noticeable signs. Preexisting cavity in soluble rocks covers by a thick and strong clay layers. Sinkhole develops upward to form structural arch. At certain point when clayey soil cannot be able support weights on top of cavity, sudden and dramatic sinkhole form. An example of cover-collapse near Tampa, Florida, where the limestone is covered by 4 feet of clay and 30 feet of sand, is shown in Figure 6. The geology is typical for most of Florida where limestone layer and sand layer are separated by a clay layer. Solution cavity is created by leak of acidic water from upper aquafer. Clay layer may bridge the cavity for considerable time by its cohesive strength, but eventually the clay layer also collapses causing quick abruption of overlaying sand layer (Beck & Sinclair, 1986). Collapsed-subsidence accounts for over 95% of Florida sinkhole (Lerche & Glaesser, 2006).

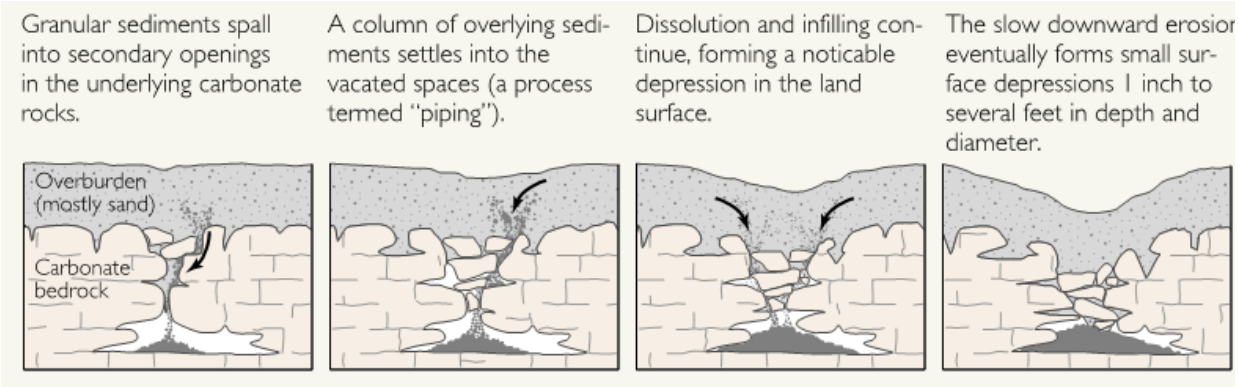

Figure 5: Cover-Subsidence sinkhole (Tihansky, 1999)

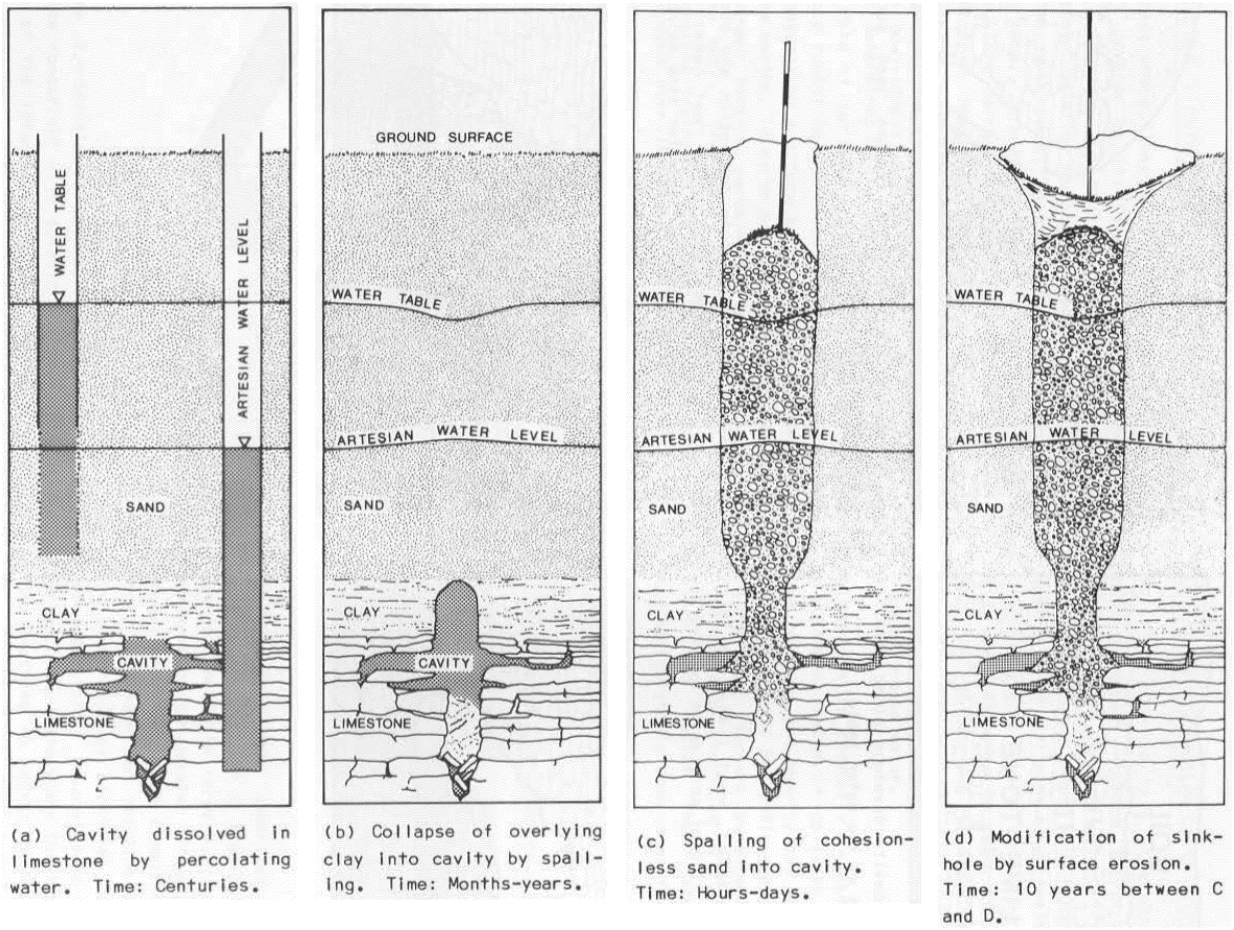

Figure 6: Cover-collapse sinkhole (Beck & Sinclair, 1986)

Based on types and thicknesses of cover materials overlaying limestone, U.S. Geological Survey (USGS) categorized sinkhole in Florida into 4 areas as shown in Figure 7. In Area I, the cover material is very thin and permeable, or limestone outcrops to weathering. Area I is reportedly very few collapse-sinkhole with shallow and develop slowly. Solution sinkholes dominate and decrease with depth. Area II consists of incohesive material and permeable sand. Thickness of cover material from 30 feet to 200 feet. Sinkholes are few with shallow depth and small diameter. Cover-subsidence sinkholes dominate because developing cavity in limestone is quickly filled by incohesive materials. Area III is dominant by cohesive clayey sediments with low permeability. Similar to Area II, cover material for this area is also from 30 feet to 200 feet thick. Sinkholes are

most numerous, varying in diameter, and develop precipitously. Cover-collapse sinkholes dominate. This area and throughout Florida cohesive clayey sediments increase with depth. Clay component provides degree of cohesiveness to overlay material that allows bridge between surficial aquafer and develops sinkhole in carbonate aquafer. Actually, Areas II and III have the same failure mechanism. However, developing cavity in Area II is quickly filled by incohesive materials while developing cavity in Area III is supported by cohesive soil on the top. Failure of the cohesive layer results to cover-collapse sinkhole. Another factor that plays important role as cohesive sediments in cover-collapse failure is groundwater. In a report in 1986, Beck and Sinclair illustrated the abruption of giant cover-collapse sinkhole near Tampa which is similar to those throughout Florida as shown in Figure 6. The difference in water levels between sand aquafer and its underlain carbonate aquafer is many feet. The clay layer between these two aquafers is stressed under hydrostatic force caused by different head of water levels, its own weight, and the weight of cover layers. The fluctuations of the hydrostatic force have weakening effect on top of limestone layer or clay layer spanning over developing cavity in limestone. An increase in difference of water levels between the two aquafers, either because of flooding at land surface or decline water level at carbonate aquafer, stresses the roof is often enough to trigger its collapse. Pumping water from lower aquafer that consequence withdrawn down water level is possibly the most common mechanism that sinkholes are induced by man. Area IV consists of cohesive sediments interlayer with discontinuous carbonate beds, and cover layers are more than 200 feet thick. Sinkhole is rarely occurred in this area, but if it does, it should be large and deep. Cover-collapse sinkholes dominate. Figure 8 illustrates locations of Florida subsidence incidents which reported to Florida Geological Survey from 1954 to 2016. Central and Midwest Florida dominate the quantity of reported subsidence incidents. When overlaying the reported subsidence incidents in Figure 8 over

types of sinkholes map in Figure 7, It is clearly show that reported subsidence incidents in Areas II and III.

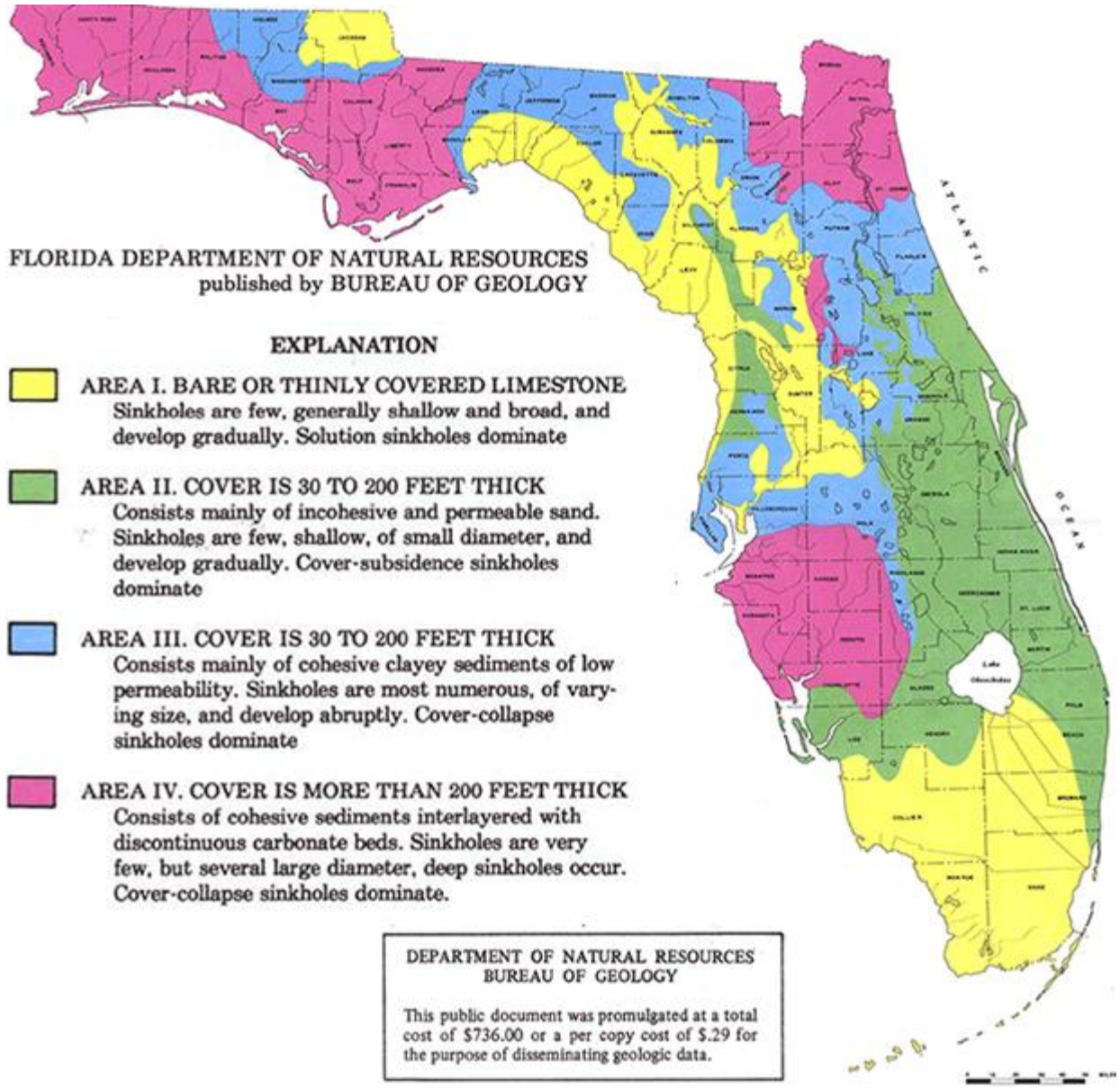

Figure 7: Types of sinkholes in Florida (U.S. Geological Survey, 1985)

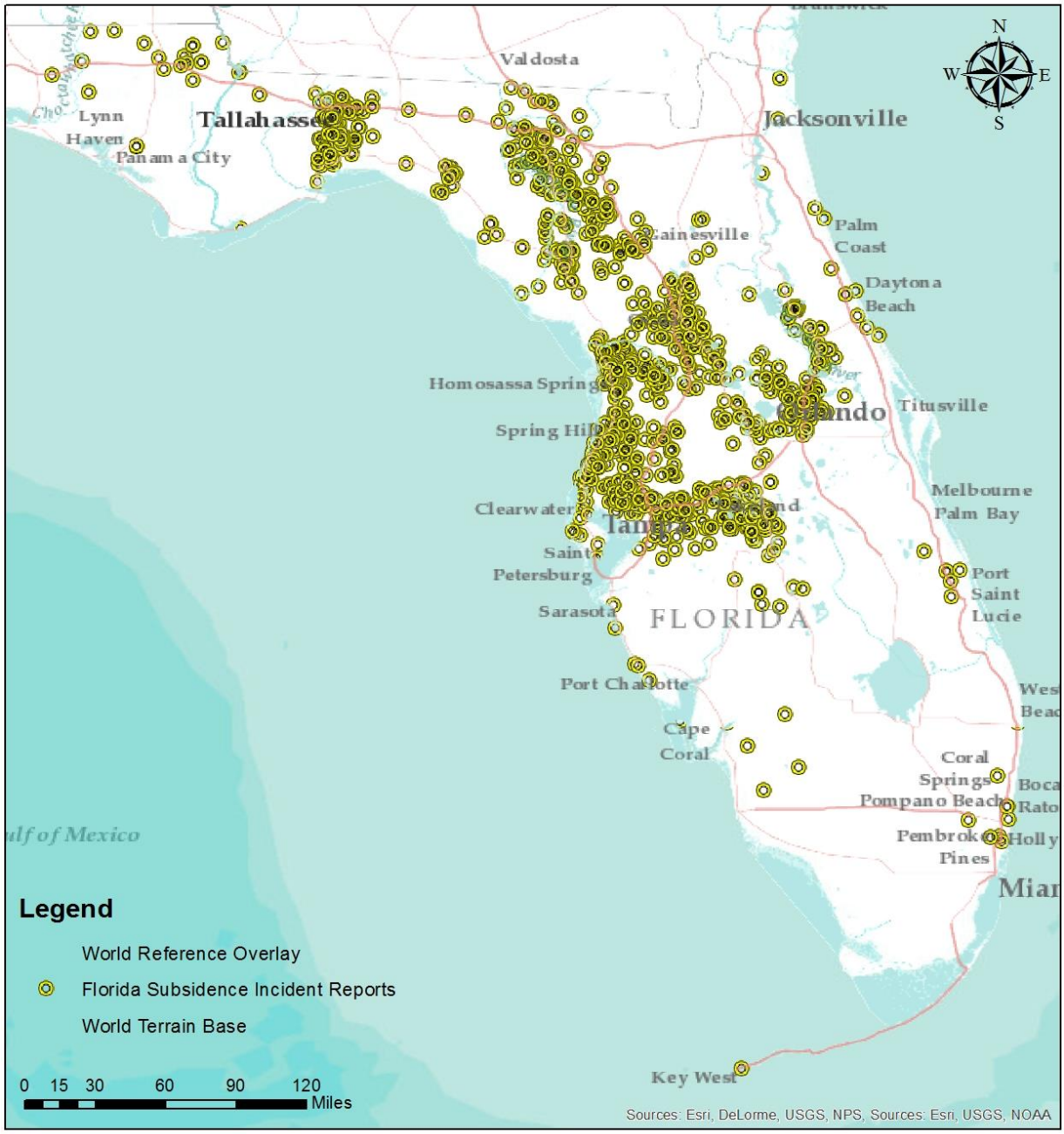

Figure 8: Map of Florida subsidence incident reports (FLorida Geological Survey, 2016) base map from ESRI

2.3 Sinkhole Detection and Prediction Methodologies

2.3.1 Cone Penetration Test (CPT)

Both Standard Penetration Test (SPT) and Electric Cone Penetration Test (CPT) have been used for sinkhole exploration. Even though widely used, SPT data are limited in volume and hard to apply for sinkhole mapping. In the other hand, CPT is sensitive to minor lithologic variability and cost-effective technique for determining geotechnical properties of sinkholes when compare to SPT (Bloomberg, Upchurch, Hayden, & Williams, 1988).

Cone Penetrating Test (CPT) is the method to determine point resistance, frictional resistance, pore water pressure as well as inclination, temperature, electrical conductivity if the cone tip (penetrometer) has these built-in sensors. Technically, CPT test can have both penetrometer types, mechanical and electronic penetrometers as stated in ASTM D3441 and D5778, respectively. However, with the advanced sensor techniques, most CPT cones these days are electronic penetrometer. Thus, information presenting in this paper is accordance with electronic penetrometer. Useful engineering information of soil properties will be interpolated and correlated from the cone data. Cone resistant (q_c), friction sleeve resistant (f_s), fiction ratio (R_f), and hydro static water pressure (u_0) are defined in the following equations (ASTM Standard D5778, 2012):

Cone resistant: $$q_c = {Q_c}/{A_c}$$

Friction sleeve resistant: $$f_s = {Q_s}/{A_s}$$

Friction ratio: $$R_f = \left({f_s}/{q_c}\right) \cdot 100$$

Pore-water pressure: $u_0 = (z - z_w) \cdot \gamma_w$

Where: q_c = cone resistant (MPa)

Q_c = force on cone (kN)

A_c = cone base area = 10cm^2

f_s = friction sleeve resistant (kPa)

Q_s = force on friction sleeve (kN)

A_s = Area of friction sleeve = 150cm^2

R_f = friction ratio (%)

u_0 = hydro static water pressure (kPa)

z = depth of interest (m)

z_w = depth to groundwater table (m)

γ_w = unit weight of water = 9.81 (kN/m^3)

In 1988 Bloomberg, Upchurch, Hayden, and Williams used firction ratio (R_f) as an indicator of soil stragraphy and properties. The row friction ratio was noisy, so it was smoothed according to the following algorithm.

$$R_f(S,Q) = 0.05R_f(Q-3) + 0.075R_f(Q-2) + 0.225R_f(Q-1) + 0.3R_f(Q) + 0.225R_f(Q+1) + 0.075R_f(Q+2) + 0.05R_f(Q+3)$$

Where $R_f(S,Q)$ = the smooth R_f value at positon Q, and $R_f(Q-3)$, $R_f(Q-2)$,… $R_f(Q+2)$, $R_f(Q+3)$ are raw R_f values at positions $Q-3$, $Q-2$, …, $Q+2, Q+3$, respectively. For each stratigraphic unit delineated by smoothed R_f data, average values for thickness, q_c, f_s, and R_f were calculated.

In 1994, Foshee and Bixler introduced a term to define degree of raveling in soils called raveling index (RI). Raveling index was defined by divided the thickness of raveled zone to the depth to top of raveled zone. A reduction factor of 0.75 was applied to the area which was partially raveled. There was twenty CPT soundings, as shown in Figure 9, was performed in the investigated site at the intersection of State Road 434 and Harbour Isle way in Longwood, Florida. Raveling index for those CPT soundings was calculated and contoured as presented in Figure 10.

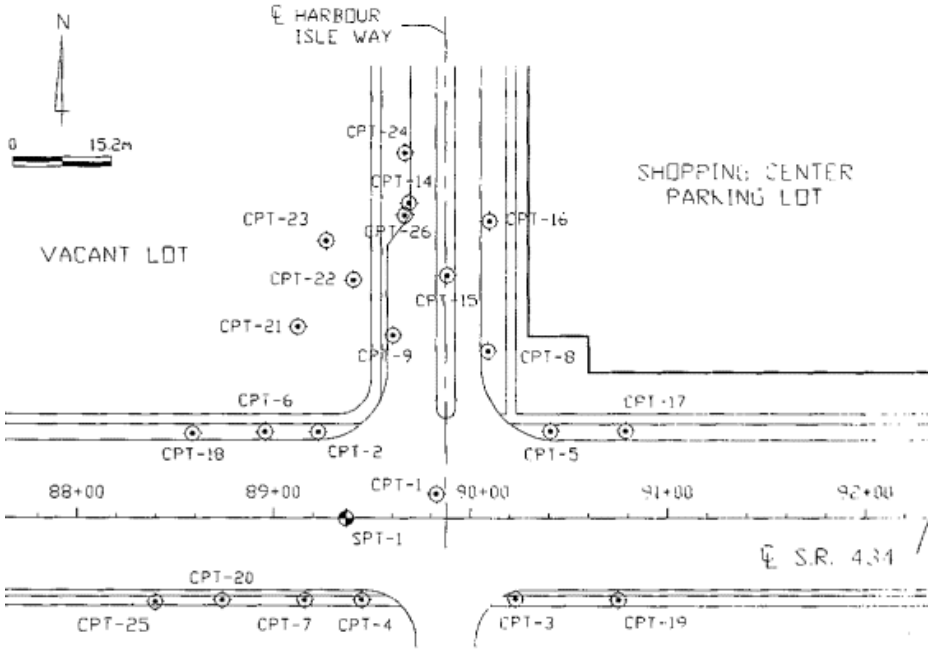

Figure 9: Locations of CPT soundings at intersection between SR434 and Harbour Isle Way (Foshee & Bixler , 1994)

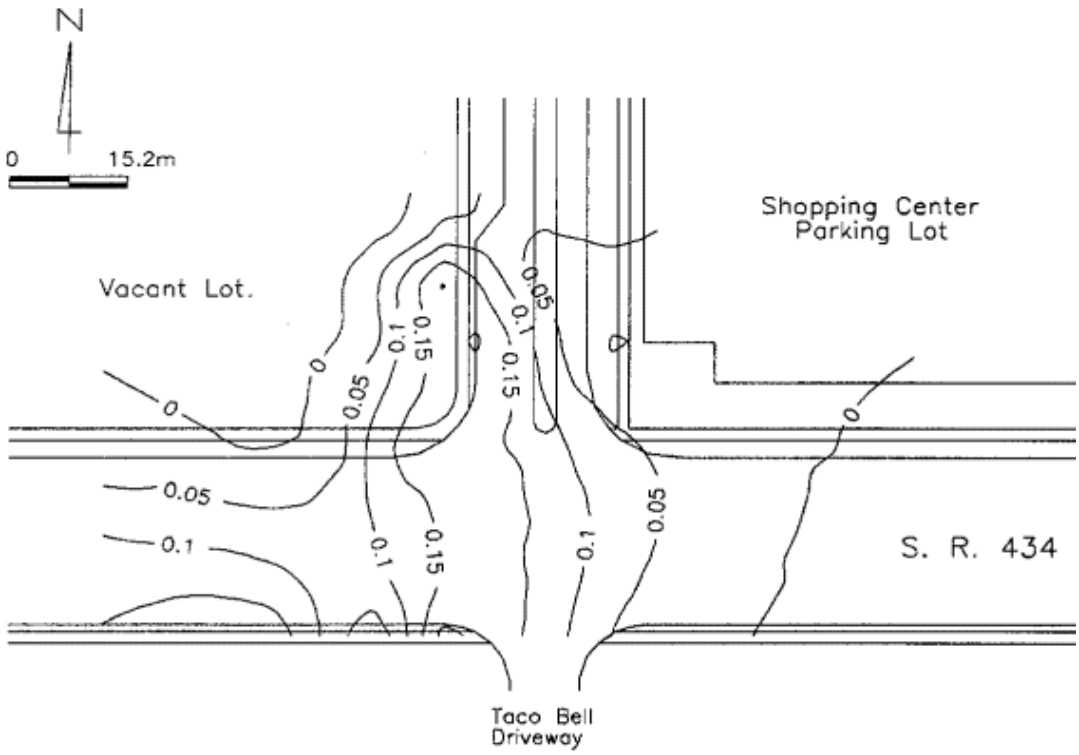

Figure 10: Contours of raveling index (Foshee & Bixler , 1994)

2.3.2 Ground Penetrating Radar (GPR)

Ground Penetrating Radar (GPR) is widely used as a technique that uses high frequency electromagnetic waves (10 to 3000 MHz) to acquire subsurface information. Electromagnetic properties such as dielectric permittivity, conductivity, and magnetic permeability are varied for different types of soils (ASTM Standard D6432, 2011). The frequency of electromagnetic waves is adjustable depend on application. Higher-frequency uses for shallow depth and small targets while lower-frequency uses for deeper depth and large targets. Survey area with high conductivity such as mineralogic clays soil can limit the depth and the effectiveness of GPR by converting electromagnetic energy to thermal energy.

A GPR system generally consists of five components, transmitter antenna, receiver antenna, control unit, data display, and data storage as shown in Figure 11. Transmitted pulse control by control unit will be sent by transmitter antenna and penetrated through subsurface; two-way travel time and amplitude of the signal will be received by receiver antenna. Simultaneously, signal from receiver antenna will be displayed and stored in data display unit and data storage unit for result interpolation and later use if necessary. The velocity of GPR signal is varied among materials. Dielectric permittivity for each material is a unique value; and it represents how fast GPR signal travel in that medium. Air has dielectric permittivity of 1 and fresh water has dielectric permittivity of 81, so GPR signal travels in air faster than water. All other types of materials have dielectric permittivity values between air and water. To convert two-way travel times to depths, it is necessary to determine the transmitted velocity of the electromagnetic pulse. The propagation velocity through the material can be calculated by the following equation (Balanis, 1989).

$$V_m = {}^{c}/_{\sqrt{\varepsilon_r}}$$

Where: c = propagation velocity in air ($c = 3 \cdot 10^8 m/s$)

V_m = propagation velocity through the material

ε_r = dielectric permittivity

If dielectric permittivity is unknown, propagation velocity can be calculated using a reflector of known depth as shown in the following equation (ASTM Standard D6432, 2011).

$$V_m = {}^{(2D)}/_{t}$$

Where: D = measured depth to reflecting interface

t = two-way travel time of an electromagnetic pulse

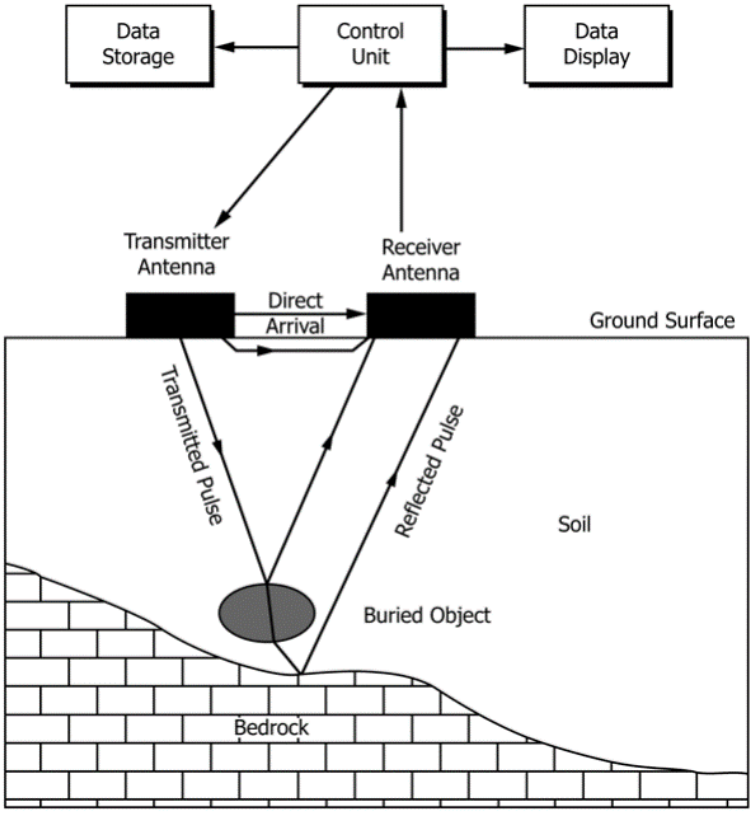

Figure 11: Schematic diagram of GPR system (ASTM Standard D6432, 2011)

2.3.3 Piezometer Sensors

2.3.3.1 Principal of Vibrating Wire Piezometer Sensor

Piezometer sensors measure pressure. They are available in several different types including Casagrande, vibrating wire, strain gauge, hydraulic, and pneumatic. Among those types of piezometers, vibrating wire piezometer is the most common due to its advantages such as easy handling, short lag time, can be automated, can read both positive and negative pressure, and minimal effect of long cable length. The fundamental component of the vibrating wire sensor is a tensioned steel wire that vibrates at a resonant frequency that depends on the strain in the

wire. Because it uses frequency rather than amplitude to convey the signal, vibrating wire sensors are relatively resistant signal degradation from electrical noise, long cable runs, and other changes in cable resistance. This has contributed to their reputation for long term stability and wide usage for monitoring structures such as dams, tunnels, mines, bridges, foundations, piles, unstable slopes, and excavations (National Instruments, 2016).

2.3.3.2 Flow of Ground Water

Because water plays an important role in sinkhole development and formation as well as sinkhole detection and monitoring, this section introduces an overview of underground water flow through soil medium. According soil mechanics, the total head at any point in water under steady flow condition can be expressed by Bernoulli's Equation.

Total head = Pressure head + Velocity head + Elevation head

$$h = \frac{p}{\gamma} + \frac{v^2}{2g} + Z$$

Where: p = pressure head

γ = specific weight of water

v = velocity of the flow

g = acceleration due to gravity

Z = Elevation of a point compare to datum

If the Bernoulli's Equation is applied of water through s porous soil medium, the velocity head term can be negligible since velocity of seepage is slow. Thus, Bernoulli's Equation can be rewritten as

$$p = \frac{p}{\gamma} + Z$$

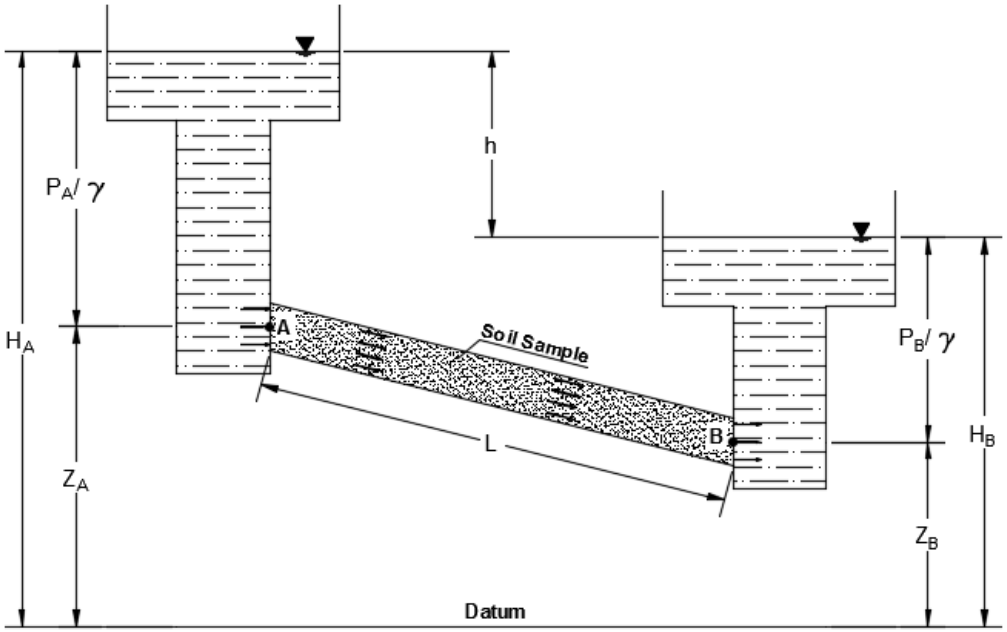

Figure 12: Flow of water through a sample soil

$$\Delta h = H_A - H_B = \left(\frac{p_A}{\gamma} + Z_A\right) - \left(\frac{p_B}{\gamma} + Z_B\right)$$

The head loss, Δh, can be expressed in a nondimensional form as

$$i = \frac{\Delta h}{L}$$

Where i = hydraulic gradient

L = distance between points A and B

For most soils, the flow of water through void spaces can be considered as laminar flow. Thus velocity is proportion to hydraulic gradient (Das & Sobhan, 2014).

The discharge of water through saturated soils can be expressed by Darcy's Equation

$$v = k \cdot i$$

Where $v = discharge\ velocity$, which is the quantity of water flowing in unit of time through a unit gross cross-sectional area of soil at right angle to the direction of flow.

k = hydraulic conductivity or the coefficient of permeability (m/s or ft/s)

The hydraulic conductivity of depends on several factors: fluid viscosity pore-size distribution, grain-size distribution, void ratio, roughness of mineral particles, and degree of soil saturation. The values of hydraulic conductivity (k) vary widely for different soils. Some typical values for saturated soil are given in Table 1.

Table 1: Typical values of Hydraulic Conductivity of Saturated Soil (Das & Sobhan, 2014)

Soil Type	**k**	
	(cm/s)	(ft/min)
Clean gravel	100-1.0	200-2.0
Coarse sand	1.0-0.01	2.0-0.02
Fine sand	0.01-0.001	0.02-0.002
Silty clay	0.001-0.00001	0.002-0.00002
Clay	<0.000001	<0.000002

CHAPTER 3: SINKHOLE DETECTION FROM SCALED MODEL DATA

3.1 Introduction

The objectives of this study are to show that sinkhole can be simulated using small scaled models, and sinkhole events are spatial-temporal dependent. A series of parametric studies were performed to determine proper parameters for the simulation. There were 5 factors to consider: soil depth, ground water table, artificial rainfall intensity, edge effects, and size of the base opening (which represented for crack in limestone bedrock). In order to minimize the edge effects, the mold diameter should be large enough so that the edge did not influence the formation of sinkhole. In this study, a 55-gallon metal mold with diameter of 56 cm was selected. A proper base opening for the selected mold was 5 mm. This study presents results from 24 different tests which are divided into eight cases (three tests per case). The first 12 tests used the soil thickness (h) of 150 mm with four different ground water table (GWT) levels 15 mm, 22.5 mm, 30 mm, and 40mm correspond to 0.1h, 0.15h, 0.2h, and 0.30h, respectively. The next 12 samples used soil thickness (h) of 200 mm with four GWT level cases 20 mm, 30 mm, 40 mm, and 60 mm also correspond to 0.1h, 0.15h, 0.2h, and 0.30h, respectively. The tests were repeated three times for each GWT levels to avoid any bias and abnormal behaviors that can influence the results.

The hypothesis of this study is that sinkhole and fluctuation of ground water table have spatial – temporal relationships. For spatial factor, the closer the sensor to the sinkhole location the more number of drastically change in water level it will have. This rate of change is referred as drops or peaks in water level. Not all drops will be counted as peaks. In this study, when the rate of change in water level has magnitude four times larger than standard deviation of the average drops and the minimum time between these changes is one second, it will be counted as a peak.

For temporal factor, the rate of water fluctuation will be accelerated when time is approaching to the final stage of sinkhole formation.

3.2 Sinkhole Model

3.2.1 Equipment

The eTape is a solid state, continuous sensor for measuring levels in water. The immersed part of sensor experiences hydrostatic pressure on its envelope resulting in a change in resistance which corresponds to the distance from the top of the sensor to the fluid surface. The resolution of the 12 inches eTape sensors that used for these tests was 0.25 mm (0.01 in). It means that the sensor be able to distinguish the change of whenever lager or equal 0.25 mm. Data aquisition system used in these tests including a NI PXIe-1062 computer, a BNC 2120 board, and Labview programing software from National Instruments, and a voltage divider circuit. Water level sensors were hooked up with computer through BNC 2120 board and voltage divider circuit. Then, this system was controlled by coded Labview program with the sensitivity of 0.5 mm and sampling frequecy of 100Hz, which is 100 samples would be stored every second. With that sensitivity and sampling frequency, the system been able to capture a small water level change.

Figure 13: Sensor and DAQ system. Left: 12-in water level sensor. Right: DAQ system

3.2.2 Soil Samples Preparation

Dark brown fine sand (ASSHTO Type A-3) with 1% passing sieve 200, was used for all of the physical models. The sandy soil had optimum moisture content (ω) of 13%, maximum dry unit weight (γ_d) of 16.3 kN/m^3, and specific gravity (G_s) of 2.6. Those properties were determined by means compaction tests. Both Standard (ASTM D698) and Modified (ASTM D1557) Test Methods for Laboratory Compaction Characteristics of Soil were used to compact soil samples during preparation process. In the standard test, hammer weight of 24.5 N (5.5 lbf.) was dropped from the height of 30.48 cm (12 inches) producing a compactive effort of 12,400 ft-lbf/ft^3 (600 kN-m/m^3). While, modified compaction test used a hammer weight of 44.48 N (10.0 lbf.) dropped from height of 45.72 cm (18 inches) producing a compactive effort of 56,000 ft-lbf/ft^3 (2,700 kN-m/m^3). Since the metal mold was not an ASTM standard molds (4 inches or 6 inches in diameter) and the thickness of each soil layer was larger than the ASTM standards, the compaction procedures were modified to achieve maximum dry unit weight. To uniformly distribute the compactive energy, a 120 mm diameter circular plate with 7 mm thickness was used. Total 24 soil samples were prepared in which 12 of those samples had compacted thickness of 150 mm, and the others 12 samples had compacted thickness of 200mm. The first 12 samples with thickness of 150 mm were divided into three layers as shown in Figure 14. The bottom layer, which had average loose soil thickness of 80 mm, were compacted in two stages. 80 blows of low energy standard compaction test were applied two the first stage then follow by 65 blows of high energy modified compaction test. The middle and top layers, both had average lose soil thickness of 50 mm, also compacted in two stages but using less number of blow counts, 65 blows for standard hammer and 50 for modified hammer. The next 12 samples, which had average compacted thickness of 200 mm, were divided into four layers as shown in Figure 15. The first three layers had similar

thickness and compaction efforts as those in the 150 mm soil thickness samples while the top layer had similar thickness and compaction manner to middle and top layers of the first 12 samples. All samples had achieved target dry unit weight of 16.3±0.15 kN/m^3 using optimum moisture content of 13 ±2 %.

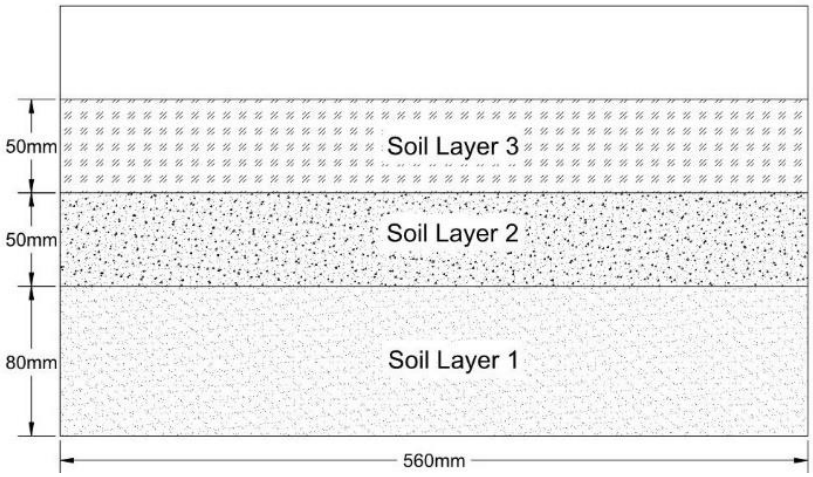

Figure 14: Average soil thickness of three layers' samples

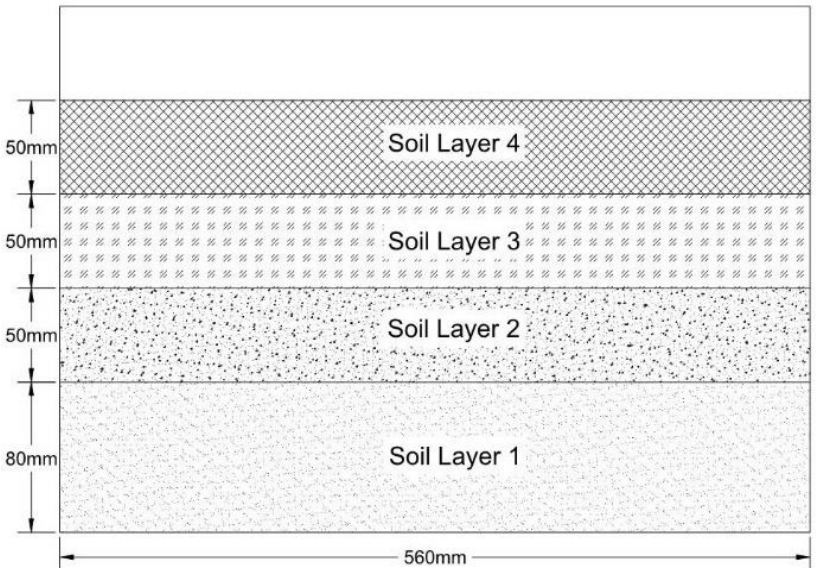

Figure 15: Average soil thickness of four layers' samples

The mold was sealed by placing on top of a thin rubber sheet to check for water leakage before put any soil into it. Then, place PVC pipes, which served as monitoring wells, into its designated positions. The radial distances from the mold's center to the wells can be assigned randomly. However, to avoid the equidistance and sinkhole zone, the ideal distances from the center of the mold were 10 cm, 12cm, 14 cm, 16 cm, 18 cm, 20 cm, 22 cm, and 26 cm as shown in Figure 16. However, because of the difficulty to keep those PVC pipes in a fixed position, the recorded positions of those wells might differ from those in ideal case. The only mandatory need to be met was that the wells need to be out of sinkhole zone, which was about 8 cm from center of the mold.

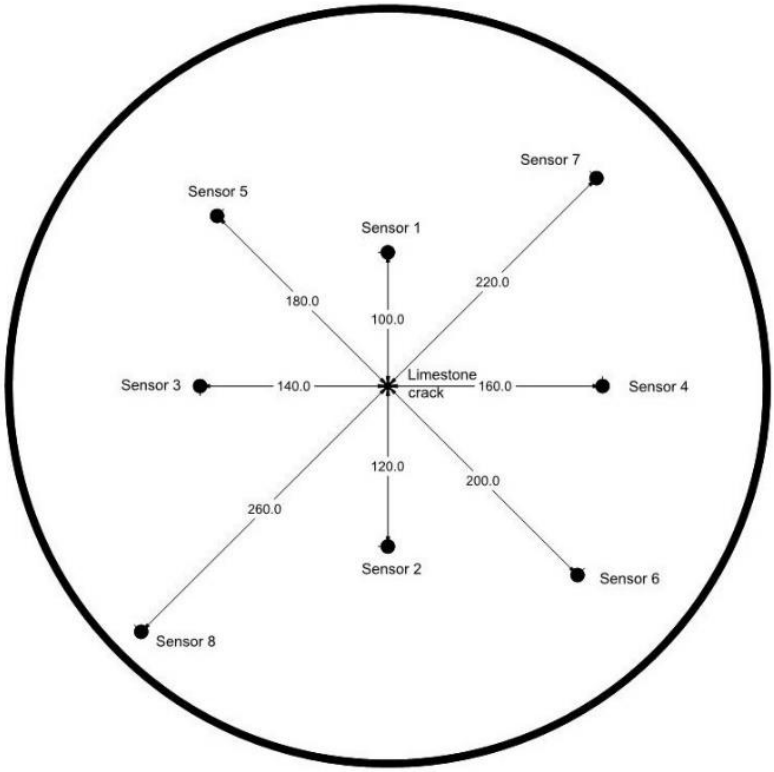

Figure 16: Radial distribution of the 8 sensors

Figure 17: Metal Mold with Soil and Sensors Location

3.3 Result

As mentioned earlier, there were 24 tests divided into 8 cases (three tests per case). The following analysis showing detail graphs for only one case. Graphs of all cases are presented in APPENDIX C. Figure 20 shows ground water table profile decreasing over time when water and soil sediment keep drain out through the hole at bottom of the mold. All results proved that sensors have the same water level before the hole is opened. Then, the ground water table level gradually increases from the opened hole toward the rim of the mold because of a phenomena called cone of water depression. Water levels are getting stiffer over time until the time of sinkhole's formation when measured data from monitoring wells diverges from the origin as shown in the graphs. The graph in Figure 20 is comparison of water level between two wells of sample 1, which have radial distances of 9.4 cm and 20.2 cm from the center of the mold. Vertical distance clearly shows the differences in water heads between the two wells at a time while the horizontal distance shows the

time delay between drops. Results also prove that time delay and different water head are normally inversely proportional to each other because water moves from high elevation to low elevation under gravity force, so the larger the head difference between two points the faster the rate water flow. Signal processing method will be used in the next steps to see whether or not the spatial – temporal relationships exist.

Table 2: Summary of Test Parameters and Time of Sinkhole Formation

Cases	Sample No.	Test Date	Soil Thickness h (mm)	Ground Water Level (%h)	Ground Water Level (mm)	Sinkhole Time (minutes)
1	1	10/13/2014	150	10	15	15.316
	2	10/13/2014				11.833
	3	10/19/2014				12.166
2	1	2/18/2014		15	22.5	19.683
	2	2/24/2014				16.067
	3	3/28/2014				14.083
3	1	9/24/2014		20	30	12.750
	2	10/2/2014				12.150
	3	10/9/2014				14.700
4	1	08/25/201		30	40	13.583
	2	09/01/2014				15.833
	3	09/01/2014				10.167
5	1	10/22/2014	200	10	20	29.833
	2	10/29/2014				20.083
	3	11/5/2014				18.583
6	1	11/12/2014		15	30	20.067
	2	11/13/2014				26.683
	3	11/13/2014				20.533
7	1	11/7/2014		20	40	21.917
	2	11/10/2014				20.467
	3	11/11/2014				22.367
8	1	11/14/2014		30	60	47.150
	2	11/16/2014				52.500
	3	11/16/2014				44.000

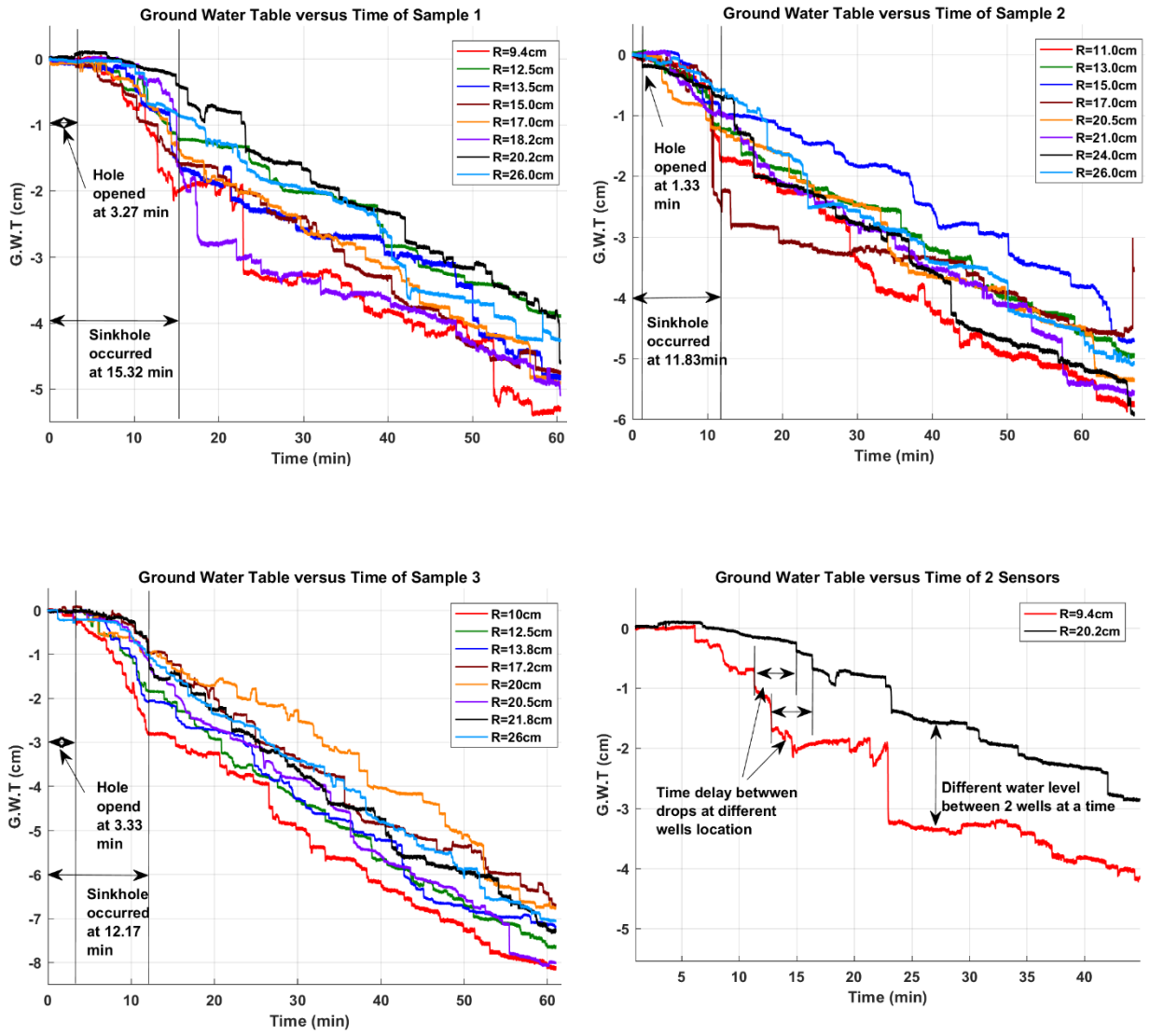

Figure 18: Fluctuation of groundwater table over time of sample 1with soil layer thickness (h) = 150mm and ground water table (GWT) = 0.10h = 15mm. Top left: Sample 1. Top right: Sample 2. Bottom left: Sample 3. Bottom right: Enlarge progressive drop of Sample 1

3.3.1 Peak Count Analysis

The following detailed analysis only shows peak count results from channel 1 and channel 8, which is 9.4 cm and 26 cm from the center of the mold. The full plots for all channels and cases are in Appendix C. The water drop graph of channel 1 (R= 9.4 cm) in Figure 19 is similar to channel one of sample 1 in Figure 18. However, Figure 19 only shows the time domain from

starting of test 1 until sinkhole occurred and initial water level does not set to zero. With the evaluation parameters as shown previously, it is observed that the number of peak count for the closest and farthest wells is 23 and 10, respectively. Details is shown in Figure 20. Temporally, the results clearly show that most of the peak occurred at the last quarter of time before the formation of sinkhole. Spatially, the closer the wells to the sinkhole location the more peak it will have, which is proved by comparing number of peak at the closest wells (R = 9.4 cm) to the farthest wells (R = 26cm) of sample 1. Not only sample one experiences this behavior but also all 24 samples in the test.

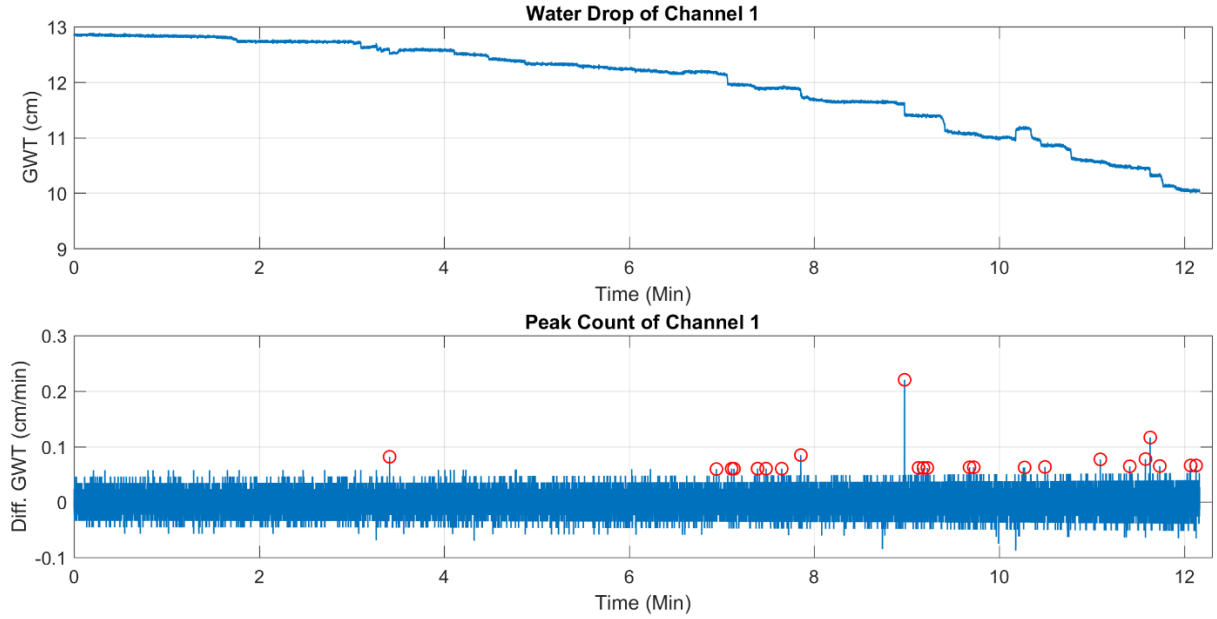

Figure 19: Water drop and peak count of channel 1 (R = 9.4 cm) for soil thickness (h) = 150mm and ground water table (GWT) = 0.10h = 15mm

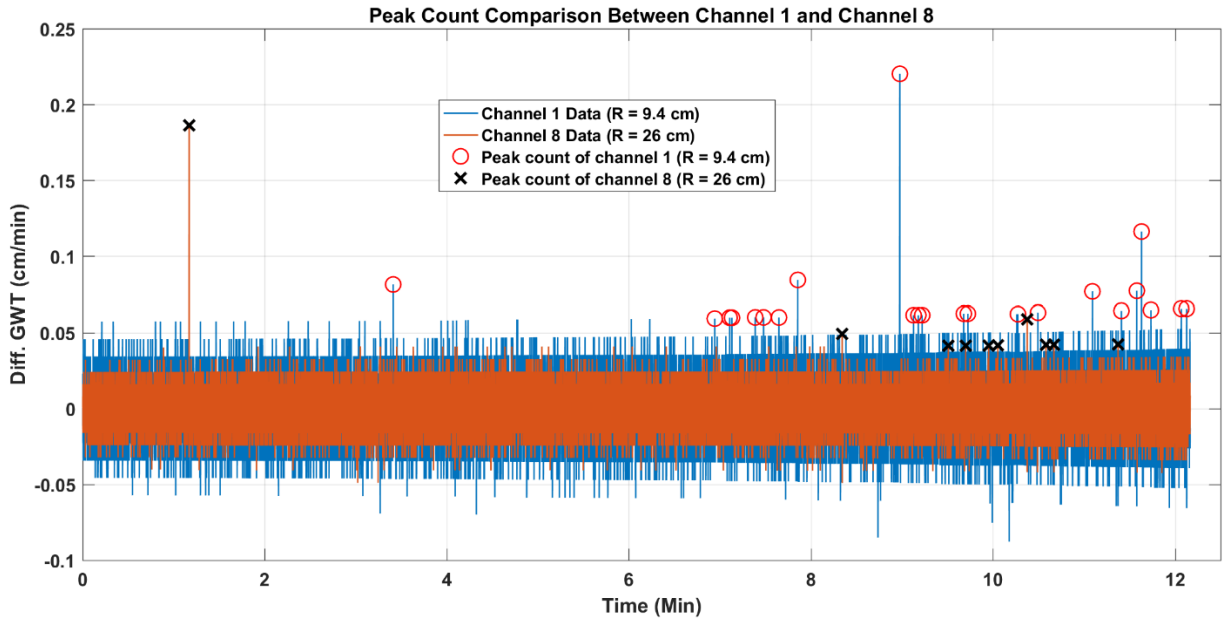

Figure 20: Comparison of peak count between Channel 1 (R = 9.4 cm) and Channel 8 (R = 26 cm) for soil thickness (h) = 150mm and ground water table (GWT) = 0.10h = 15mm

3.3.2 Spatial-Temporal Analysis

Twenty-four (24) tests, which were divided into eight cases, were performed. There were three tests with identical conditions in each case. The following results only show the cumulative results from those three tests in each case, so there are total eight cumulative graphs. The detailed plots for all tests are shown in Appendix C. In those analyses, curve fitting method was used to fit all data sets to produce surface plots. Three parameters in each data set were plotted, time, radial distance, and number of peak. One axis shows the normalized radial distance from the center of the mold to monitoring wells. The values of normalized distances range from 0.33 to 1.0 correspond to 8.6 cm to 26 cm from mold's center, respectively. The other axis shows duration from beginning of the tests until sinkhole had occurred. This axis divides equally into ten spaces,

so each space represents ten percent of the sinkhole time. The last axis shows the number of peak count corresponding to time and distance of the wells.

A series of preliminary analysis was used to find the equation that can be best fit the given data sets. From those analyses, peak count results from all tests can be fit by the following exponential equation. $f(x, y) = A \cdot exp(B \cdot x + C \cdot y) + A$, where A is magnitude of the peaks, B is slope in the x direction or normalized distance, and C is slope in the y axis or time domain. The slopes indicate how well the fitting equation converge to a critical corner where radial distance is smallest and time is largest. In most cases, slopes in both directions are high since there are more peaks around critical corner than other locations. However, in case 3, which has soil layer thickness equals 150 mm and ground water table from the surface equals 30 mm or twenty percent of soil thickness, the peaks are scattered and distributed at the middle of the graph as shown in Figure 23. All results proved that the exponential curves fit all data sets very well since the goodness of fit, R-square, for regression model range from 0.945 to 0.973 as shown in Table 3. R-square ranges from zero to one, with zero indicating that the proposed model does not improve prediction over the mean model and one indicating perfect prediction.

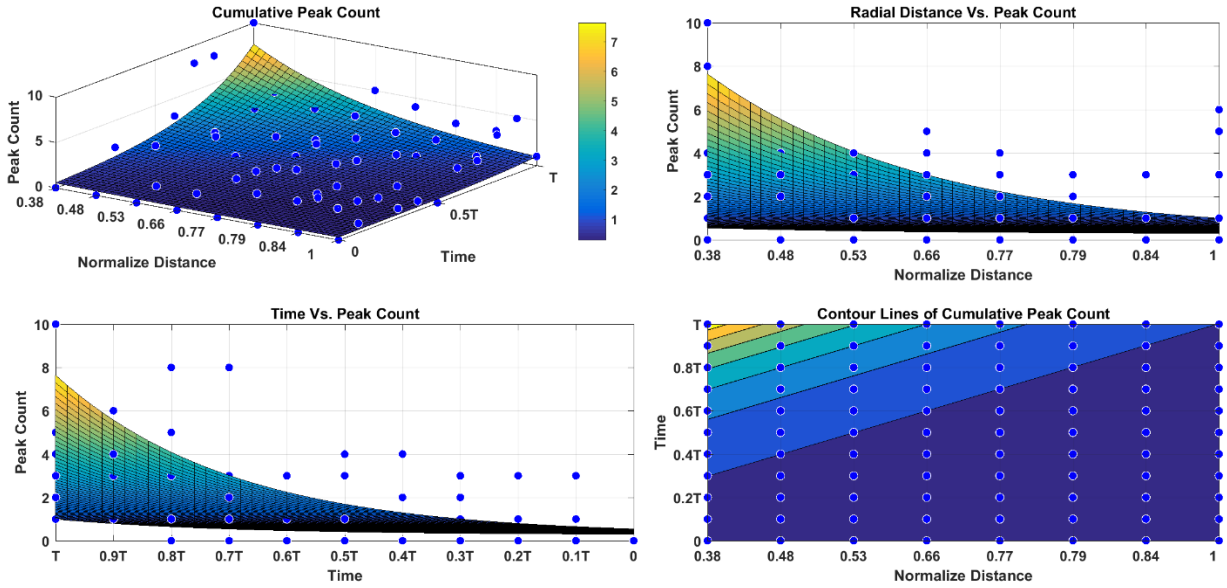

Figure 21: Cumulative peak count of special-temporal relationship for soil layer thickness (h) = 150mm and ground water table (GWT) = 0.10h = 15mm

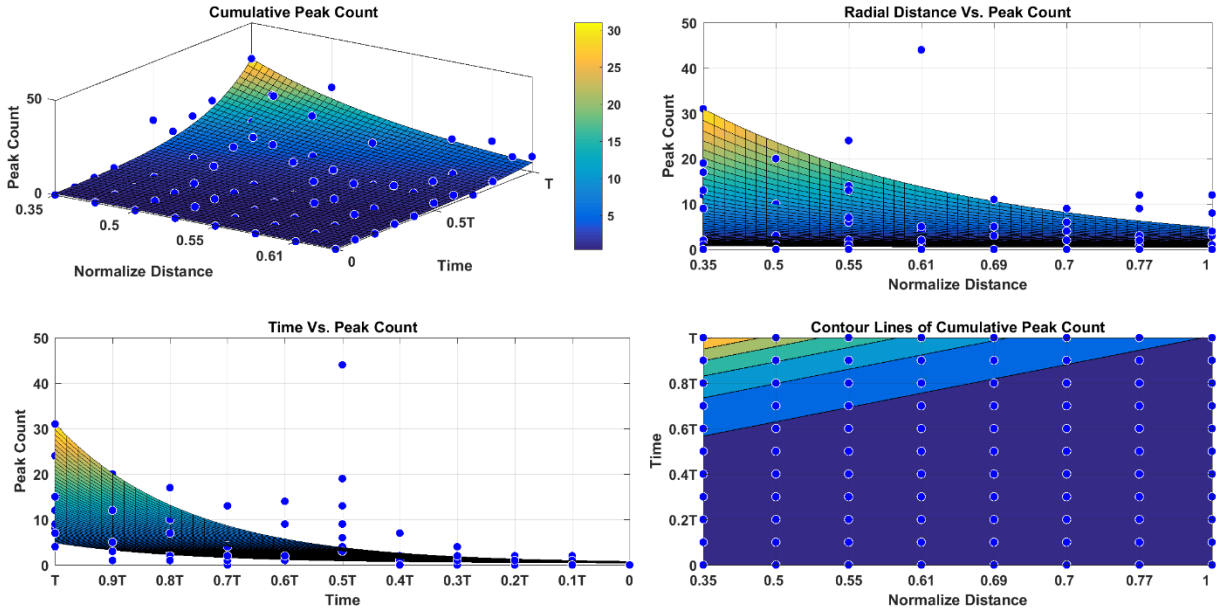

Figure 22: Cumulative peak count of special-temporal relationship for soil layer thickness (h) = 150mm and ground water table (GWT) = 0.15h = 22.5mm

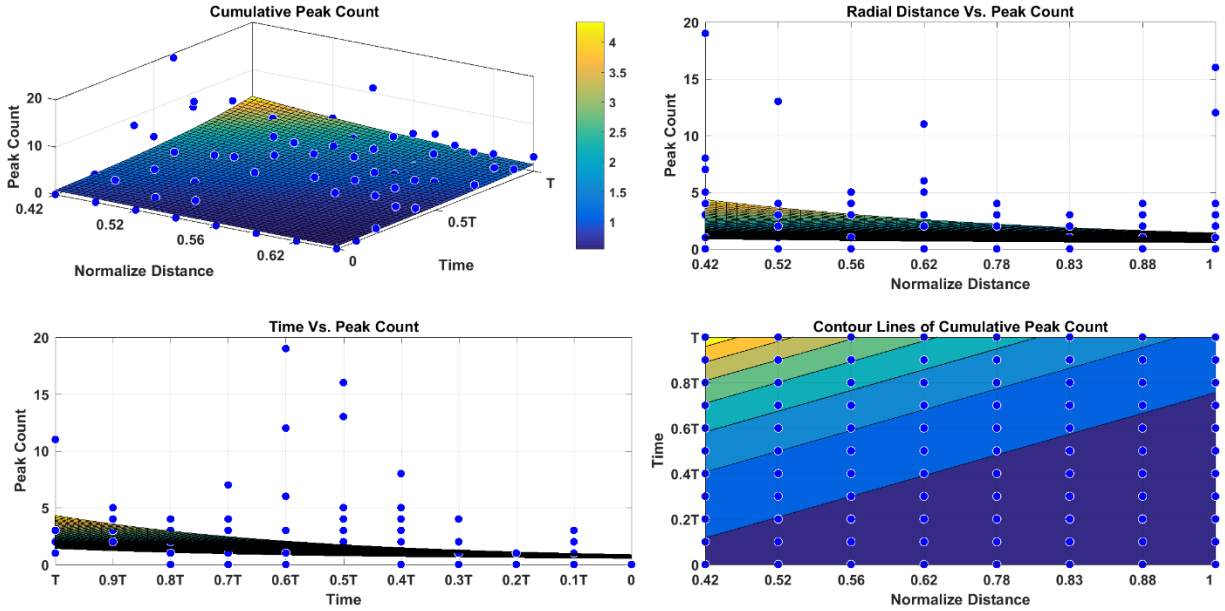

Figure 23: Cumulative peak count of special-temporal relationship for soil layer thickness (h) = 150mm and ground water table (GWT) = 0.20h = 30mm

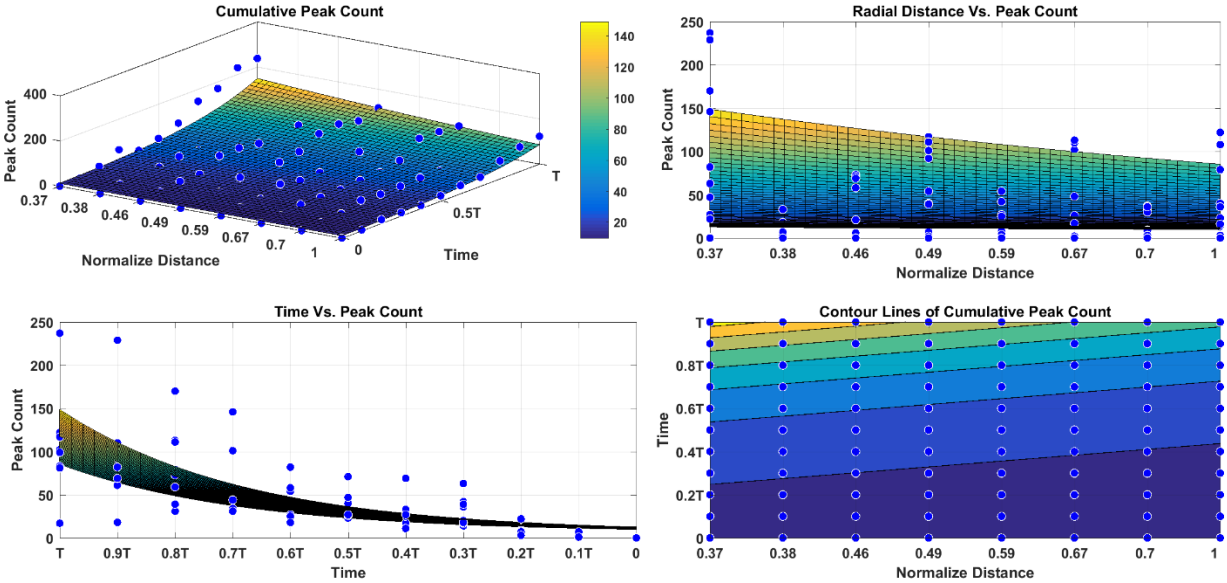

Figure 24: Cumulative peak count of special-temporal relationships for soil layer thickness (h) = 200mm and ground water table (GWT) = 0.10h = 20mm

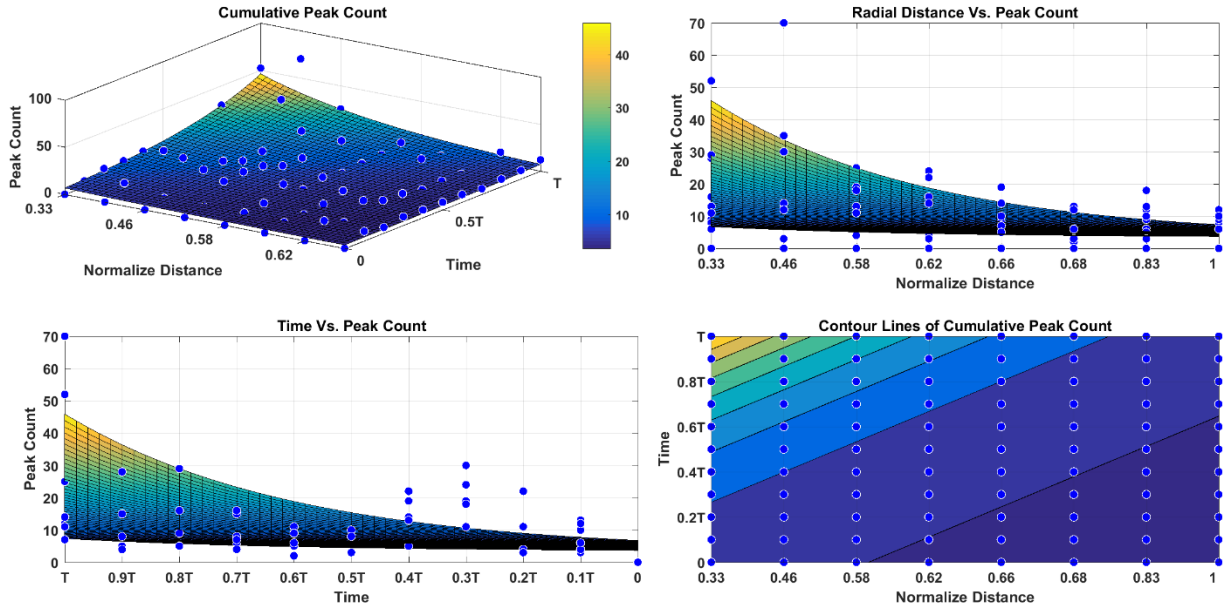

Figure 25: Cumulative peak count of special-temporal relationships for soil layer thickness (h) = 200mm and ground water table (GWT) = 0.15h = 30mm

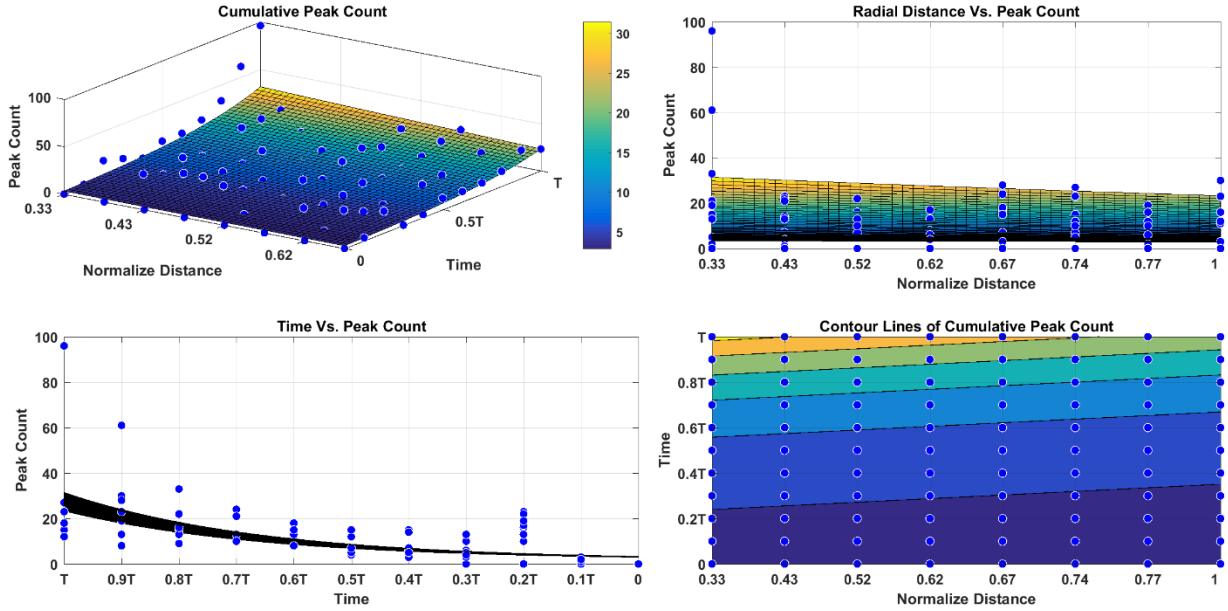

Figure 26: Cumulative peak count of special-temporal relationships for soil layer thickness (h) = 200mm and ground water table (GWT) = 0.20h = 40mm

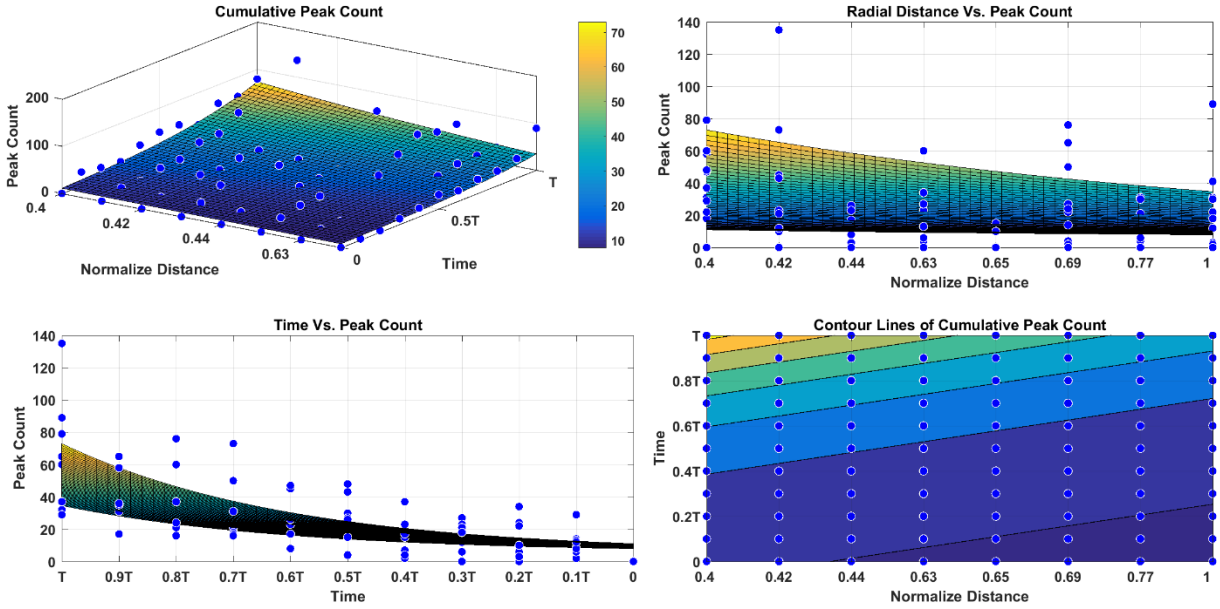

Figure 27: Cumulative peak count of special-temporal relationships for soil layer thickness (h) = 200mm and ground water table (GWT) = 0.30h = 60mm

Table 3: Table of coefficients from cumulative results

Cases	Soil Thickness (mm)	Ground Water Level (%)	Ground Water Level (mm)	Magnitude (A)	Slope x Direction (B)	Slope y Direction (C)	R-square
1	150	10	15	0.272	0.332	0.330	0.973
2		15	22.5	0.387	0.275	0.437	0.945
3		20	30	0.436	0.200	0.219	0.959
4		30	40	0.365	0.269	0.329	0.959
5	200	10	20	6.319	0.084	0.312	0.969
6		15	30	3.371	0.339	0.254	0.957
7		20	40	1.720	0.047	0.285	0.959
8		30	60	5.530	0.120	0.250	0.959

CHAPTER 4: SINKHOLE DETECTION FROM FIELD DATA

4.1 Introduction

The objective of this study is to develop a continuous monitoring system for the measurement of ground water table. The monitoring system will be operated with advance signal processing algorithm to detect any abnormal signature in the time histories of sensor data, which could be related to prior or posterior causes of sinkhole events.

Two very active sinkhole sites are selected. The first site is on the newly built road, Wekiva parkway (SR-429), about two thousand feet from State Road 46 connector. Interchange is located in Section 27, Township 19 South and Range 27 East of Lake County, Florida. Map of apparent relic sinkhole is shown in Figure 30. There are three bridges in this site in which two of them are overpass bridges for future traffic, and the other one, which was originally planned as roadway embankment, was constructed because subsurface karst conditions encountered during previous studies. The second site is FDOT's retention pond located on the south side of the junction of State Road 26 and County Road 235 in Newberry Florida. This site is selected because this is a well-known site since a lot of studies was conducted due to sinkhole activities. Locations of these sites are shown in Figure 28 and Figure 29.

Ground water level will be measured using piezometer sensors from Geokon. Thirty-six piezometers sensors will be installed in these two sites. There will be 20 sensors in Wekiva parkway site and 16 sensors in FDOT retention pond site. Signals from piezometer will be generated and acquired through datalogger. There will be five dataloggers in Wekiva pkwy site since the measuring area is large, approximately half of a square mile, and discontinuity by traffic flow. The remaining site will use only one 16-channel datalogger since it is a continuous zone and

the area is relatively small, approximately four acres. All works in this chapter are related to Wekiva parkway location since installation of sensors at FDOT retention pond in Newberry has not started by the time this thesis is written, and will be used for future researches.

Figure 28: Location of project at FDOT retention pond in Newberry, Florida

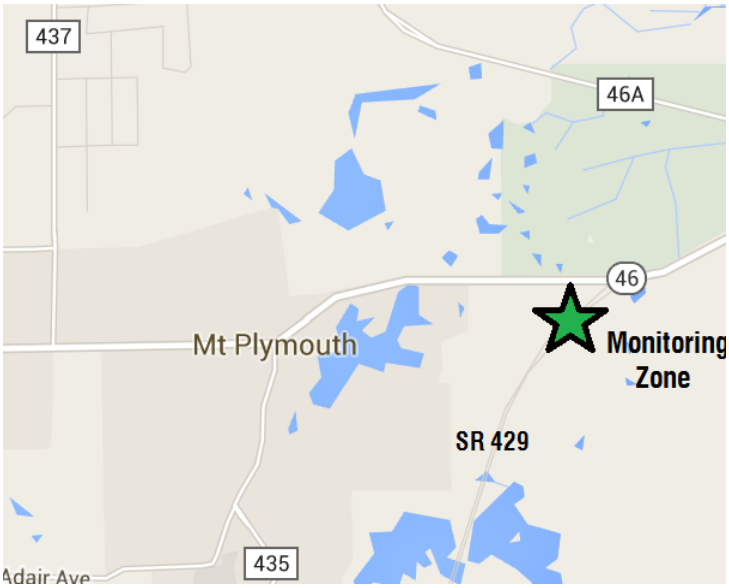

Figure 29: Location of project on Wekiva pkwy in Sorrento, Florida.

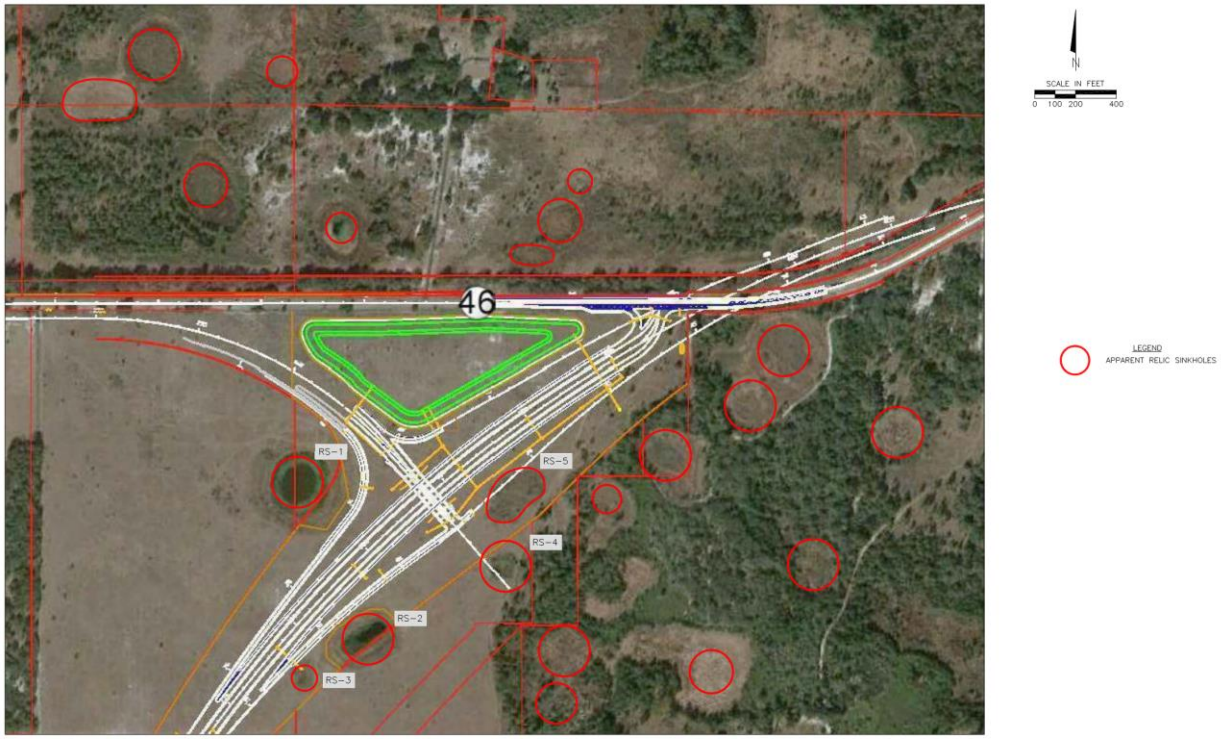

Figure 30: Apparent relic sinkhole in Wekiva pkwy vicinity (Professional Service Industries (PSI), 2014).

4.2 Soils Exploration for Wekiva Parkway (SR429) Site in Sorrento Florida

4.2.1 Surface Soil Exploration

The "Natural Resources Conservation Service (NRCS) Soil Survey of Lake County, Florida" was reviewed for general near-surface (from 0 to 80 inches from ground surface) soil information within the general project vicinity. This information indicates there are six primary mapping units within the vicinity of the proposed interchange. The soil units are as follows in Table 4. Details of sensors layout and near-surface soil map are shown in Figure 31. Most the sensors laid on Candler fine sand with 0 to 5 percent slopes.

Table 4: USDA Unified Soil Classification (United States Department of Agriculture (USDA), n.d.)

Soil Series	Depth (inches)	USDA Unified Soil Classification	USDA Seasonal High Groundwater Table Depth (feet)
(8) Candler fine sand, 0 to 5 percent slopes	0 to 80	SP, SP – SM, SM	>6
(38) Placid and Myakka sand, depressional	0 to 80	SP, SP – SM	(flooded) 0 for 12 months
(40) Placid and Myakka sand, depressional	0 to 80	SP, SP – SM, SM	+2 to 0
(41) Pomello sand, 0 to 5 percent slopes	0 to 80	SP, SP – SM, SM	30 - 40 inches SC (2.5-3.5')
(42) Pampano fine sand	0 to 80	SP, SP – SM	0 – 10 inches
(45) Tavares sand, 0 to 5 percent slopes	0 to 80	SP, SP – SM, SM	>6
(99) Water	0 to 80	-	-

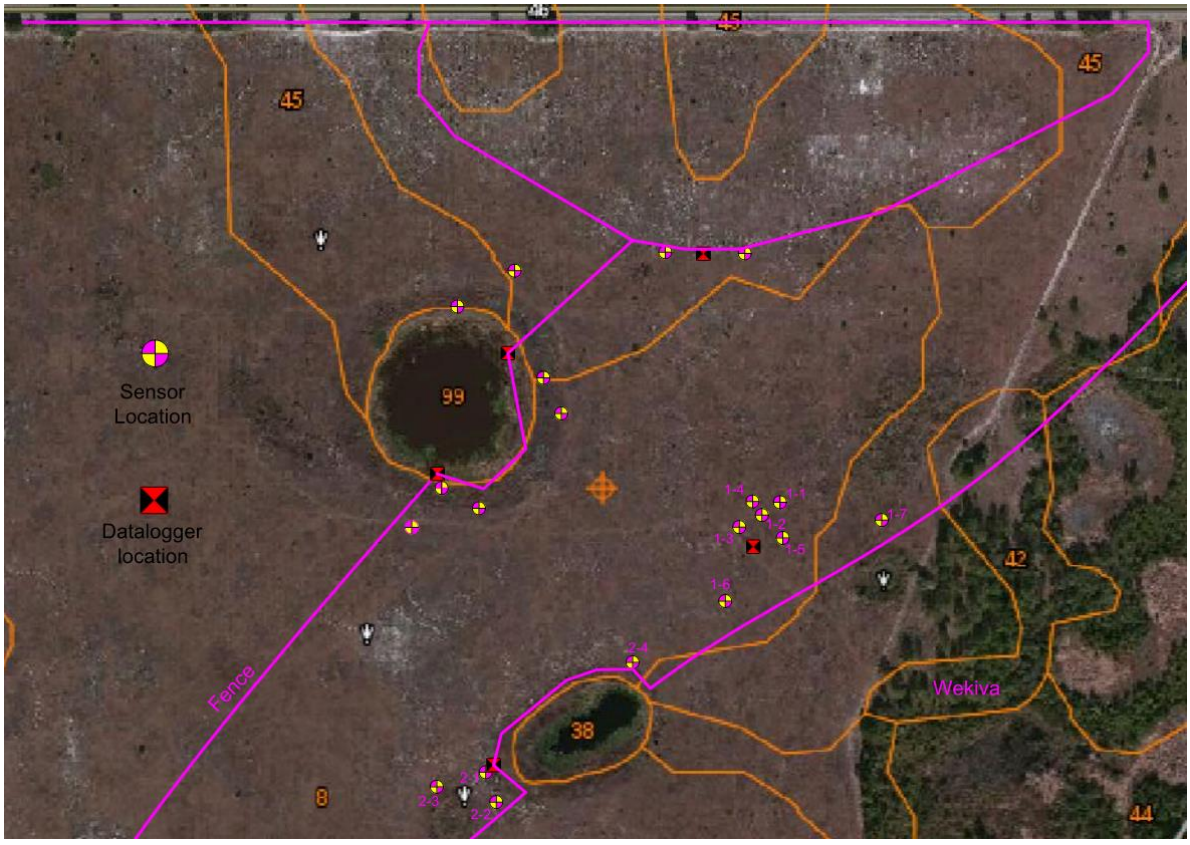

Figure 31: Map of USDA Unified Soil Classification, with sensors layout (United States Department of Agriculture (USDA), n.d.)

4.2.2 Subsurface Soil Explaration Using Standard Penetration Test (SPT) and Cone Penetration Test (CPT)

The sinkhole evaluation for this interchange included fourteen (14) Standard Peneration Test (SPT), seventy-four (74) Cone Penertration Test (CPT), Ground Peneratring Radar (GPR), and Electrical Resistivity Imaging (ERI). SPT borings were perfomed accordance to ASTM D-1586 by Professional Service Industries, Inc. (PSI). Soil samples were collected continuously for the first ten feet and every 2.5 feet thereafter to the termiation depths. During the sampling process, bentonite-based mud was used as the circulating fluid to stabilize the boreholes. Upon completion, a mixed of Porland cement and betonite clay was filled into boreholes to the existing grade. SPT boring locations are shown in Figure 32. CPT soundings were performed by FDOT accordance to ASTM specification D5778-2012. The penetrometer, which has base diameter approximately 35.56 mm and total area approximately 993 mm^2, was driven into the soil by means of a hydraulic thrust system at a constant rate of 24 to 48 inches per minute (Professional Service Industries (PSI), 2014).

Results from SPT borings indicated very loose to medium dense sands (SP, SP-SM) in the upper 15 to 20 feet followed by 15 to 20 feet of alternating layers of clayey fine sands (SC) and clays (CL). Below the depth of 30 to 40 feet raveled soil conditions are consisting of silty fine sands (SM) and clayey fine sands (SC) with W/H and W/R (Weight of Hammer and Weight of Rod) N-values was encountered. The loose raveled soils extended to the surface of the existing limestone formation. In addition, 100 percent loss of drilling fluid was also evident during drilling through depth intervals above the limestone formation and within it (Professional Service Industries, 2014). Based on the field results, Professional Service Industries , Inc ranked this site as moderate to high risk for sinkhole formation. Details of soil profiles presented in Appendix A

from Figure 80 to Figure 85. Goundwater levels varied from 10 to 12 feet from ground surface or 66 to 72 feet above mean sea level at the time SPT borings performed. It may change upon the changes of seasonal conditions, estimated seasonal heigh are shown in Table 5.

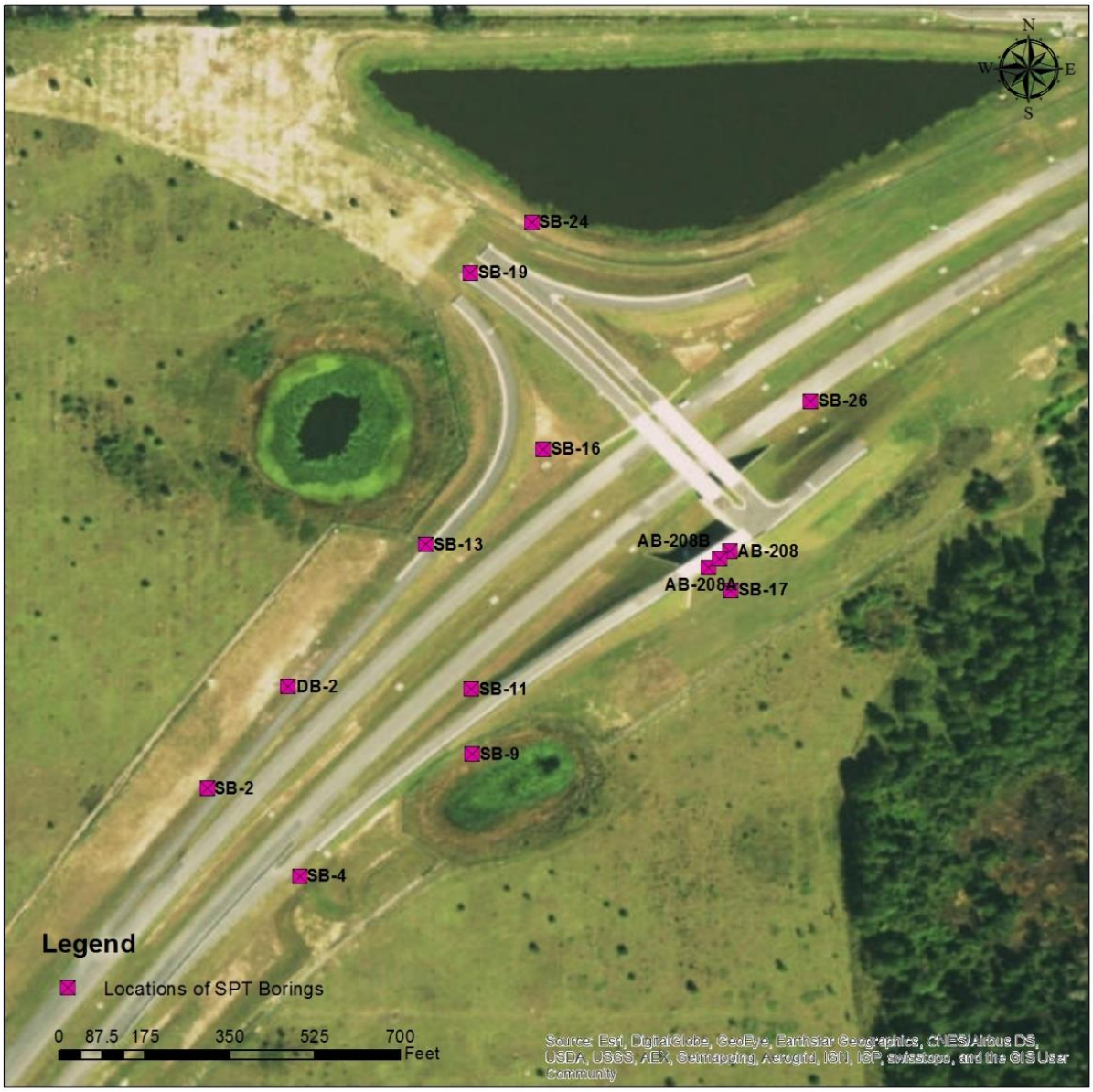

Figure 32: Locations of existing Standard Penetrating Test (SPT) borings (Base Image from ESRI)

Table 5: Existing Standard Penetration Test (SPT) data and ground water elevation (Professional Service Industries (PSI), 2014)

SPT Boring No	Latitude	Longitude	Surface elevation (ft)	Height of water (ft)	Reading date	Estimated seasonal height (ft)
SB-4	28.807819	-81.51048	75.0	67.0	2/21/2013	69.0
DB-2	28.808887	-81.51054	80.0	67.0	2/19/2013	70.0
SB-9	28.808507	-81.50950	72.0	64.1	3/5/2013	66.0
SB-11	28.808876	-81.50951	76.0	64.1	3/12/2013	67.0
SB-13	28.80969	-81.50976	75.0	65.8	2/22/2013	69.0
SB-17	28.809432	-81.50805	75.0	66.0	3/12/2013	70.0
AB-208A	28.80956	-81.50817	75.5	66.5	12/13/2012	71.5
AB-208	28.80965	-81.50805	75.2	65.4	12/3/2013	71.2
AB-208B	28.80961	-81.50811	74.8	65.8	12/13/2012	70.8
SB-26	28.810499	-81.50760	74.0	64.0	3/13/2013	69.0
SB-2	28.808315	-81.51100	80.0	70.5	2/22/2013	70.0
SB-16	28.810228	-81.50910	77.0	68.1	3/4/2013	71.0
SB-19	28.811223	-81.50951	74.0	63.0	3/13/2013	66.0
SB-24	28.811508	-81.50917	77.0	65.0	3/21/2013	69.0

4.2.3 Subsurface Soil Explaration Using Ground Penetrating Radar (GPR) and Electrical Resistivity Imaging (ERI)

In addition to Standard Penetration Test (SPT) and Cone Penetration Test (CPT), Ground Penetrating radar (GPR) and Electrical Resistivity Imaging (ERI), which performed by Geoview under a contract from PSI, was also used for subsurface soil exploration. These geophysical investigation helped characterize subsurface geological conditions within the project vicinity and identify abnormal features that may associate with sinkhole activities. GPR and ERI tests were performed along a series of parallel transects, which spaced 25 feet between GPR and ERI transects. Details of geophysical survey area, locations of transects and anomalies are shown in Figure 33.

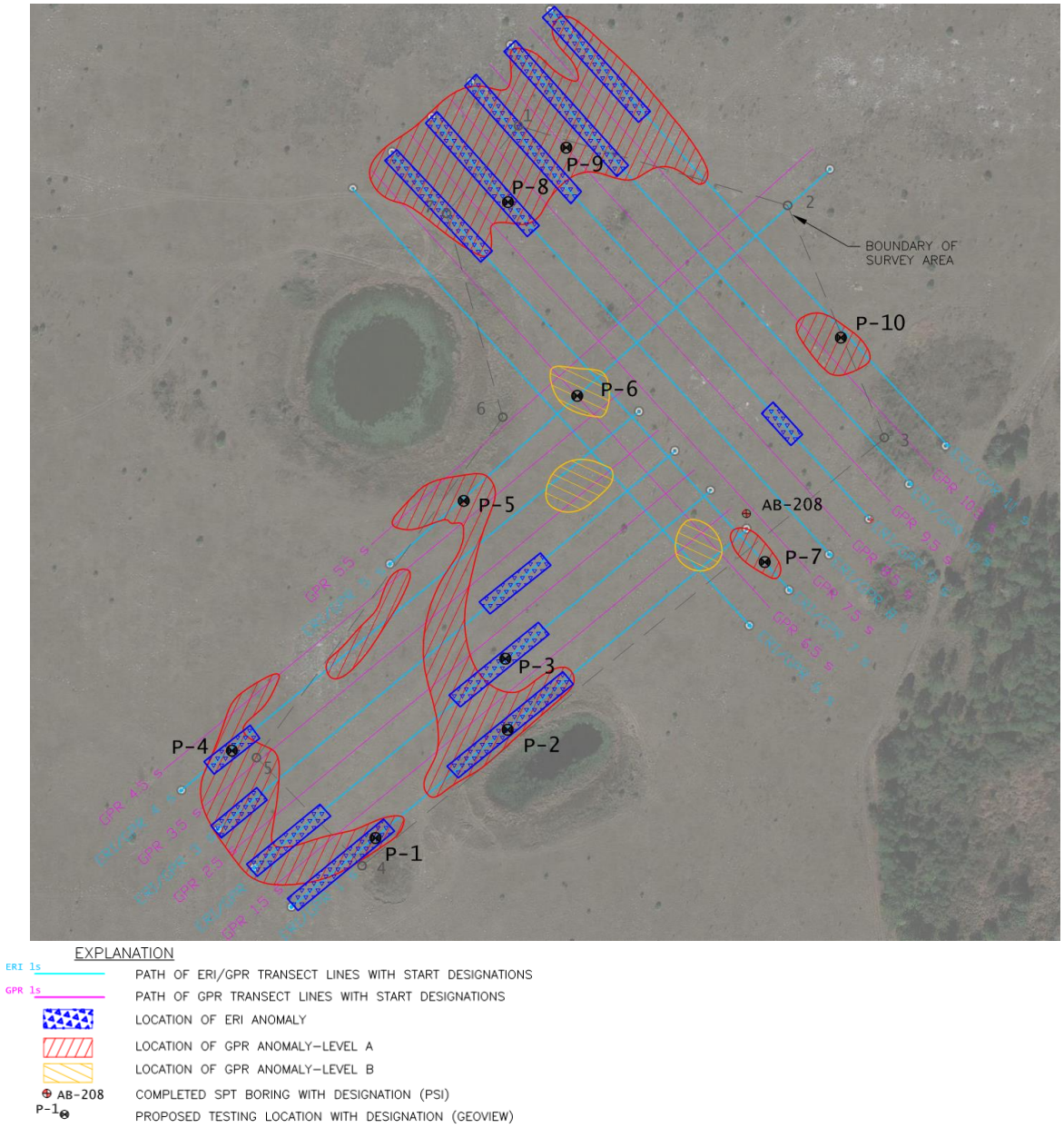

Figure 33: Map of Ground Penetrating Radar (GPR) and Electrical Resistivity Imaging (ERI) survey in Sorrento, Florida (Professional Service Industries (PSI), 2014)

Initially, only ERI method was used for geophysical exploration. However, because of the uncertainty of the ERI's results, GPR was used to confirm results from ERI. This chapter only focus on results from GPR while result from ERI is presented in APPENDIX D. Nine GPR

anomalies were identified within the survey area as shown from Figure 34 to Figure 41. These anomalies were arranged into two levels, A and B, where level A anomaly is the most severe and level B anomaly is the least severe. In the report to FDOT, Geoview defined “Level A anomalies are characterized by a steep downwarping towards a common center of the upper and, where observed, the lower GPR reflector sets. A localized significant increases in the both the depth of the penetration and/or amplitude of the GPR signal response was also observed. The increase in GPR signal penetration depth or amplitude is often associated with either a localized increase in sand content or decrease in soil density at depth.” And “ Level B anomalies were characterized by a less-steep downwarping of the upper GPR reflector set and a lack of corresponding increase in the amplitude and depth of penetration of the GPR signal. This type of anomaly has a high probability for being associated with either erosional/depositional activity or a stabilized karst related feature.”

Table 6: Summary of GPR Anomaly Classification (Professional Service Industries (PSI), 2014)

Test Location	GPR Anomaly Level	Easting	Northing
1	A	492751	1626809
2	A	492998	1627011
3	NONE	492996	1627144
4	A	492484	1626971
5	A	492918	1627440
6	B	493129	1627636
7	A	493481	1627324
8	A	493000	1627999
9	A	493109	1628099
10	A	493622	1627744

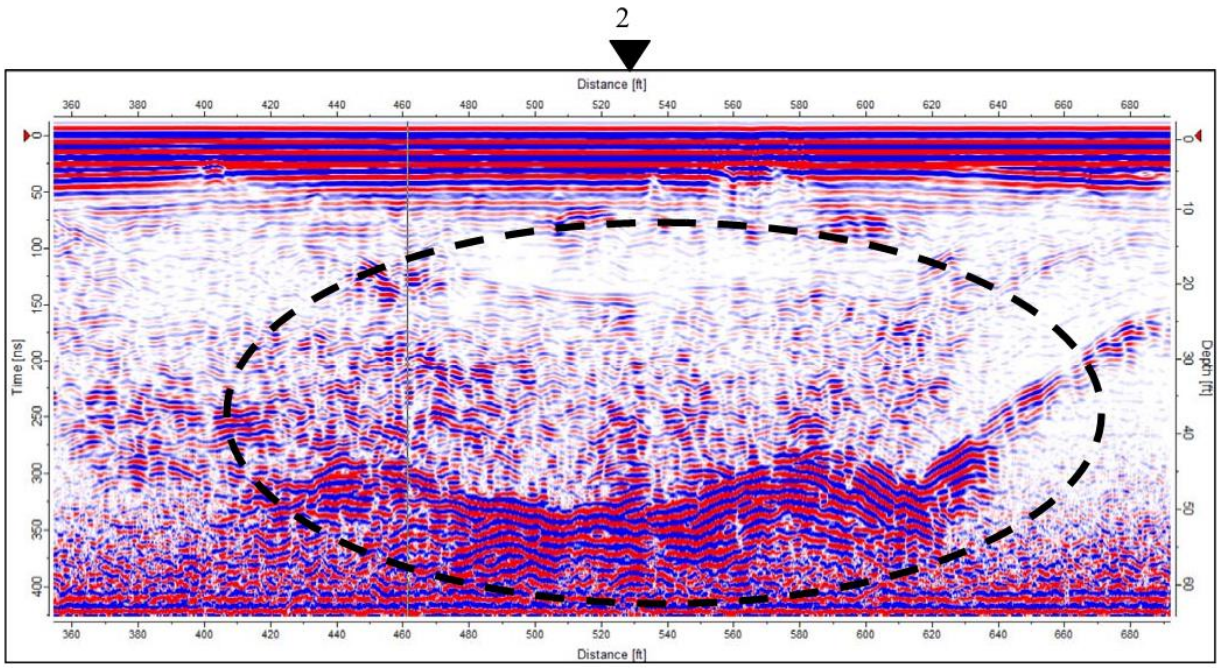

Figure 34: Level A GPR Anomaly Transect 1 (Professional Service Industries (PSI), 2014)

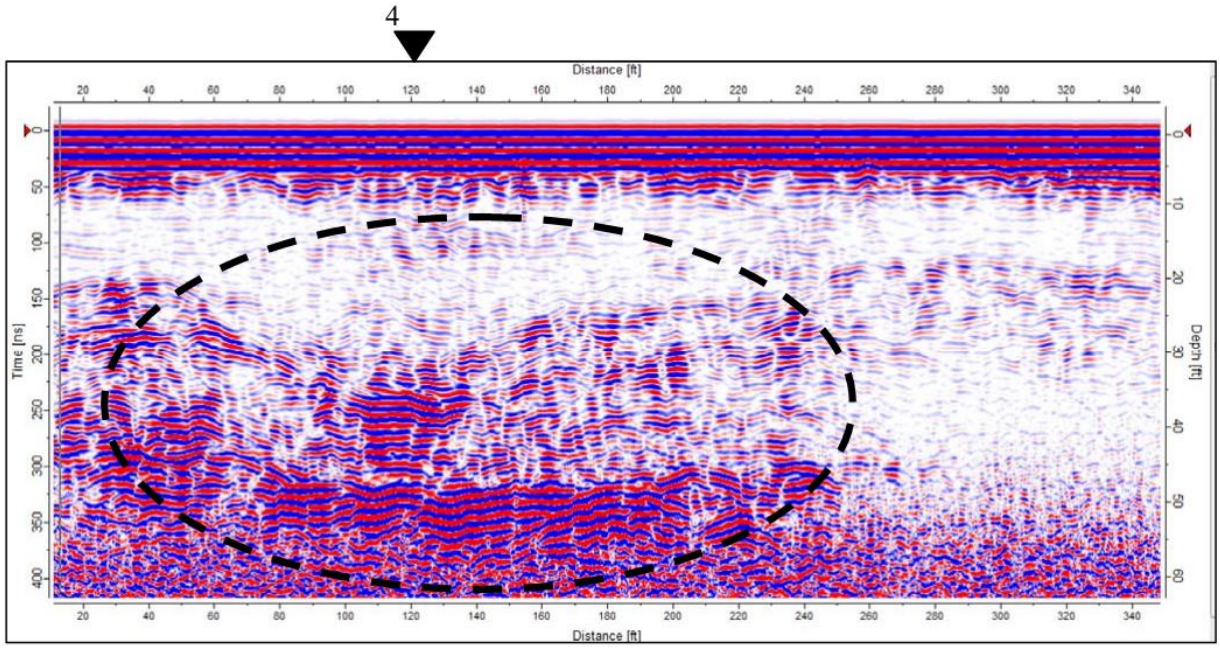

Figure 35: Level A GPR Anomaly Transect 4 (Professional Service Industries (PSI), 2014)

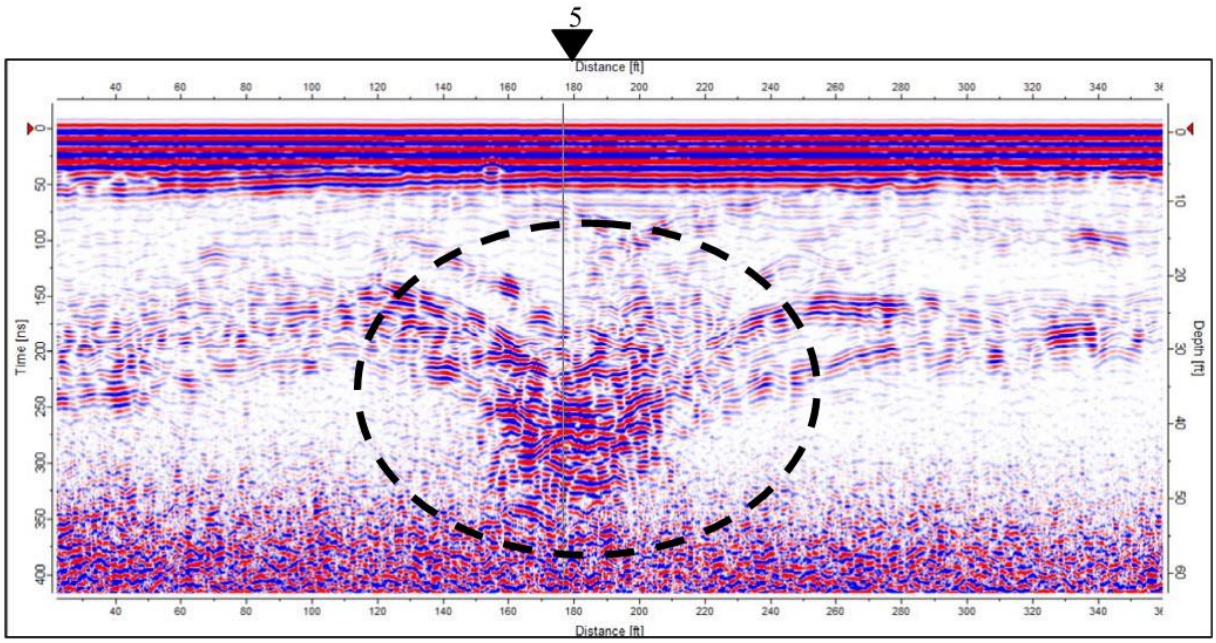

Figure 36: Level A GPR Anomaly Transect 5 (Professional Service Industries (PSI), 2014)

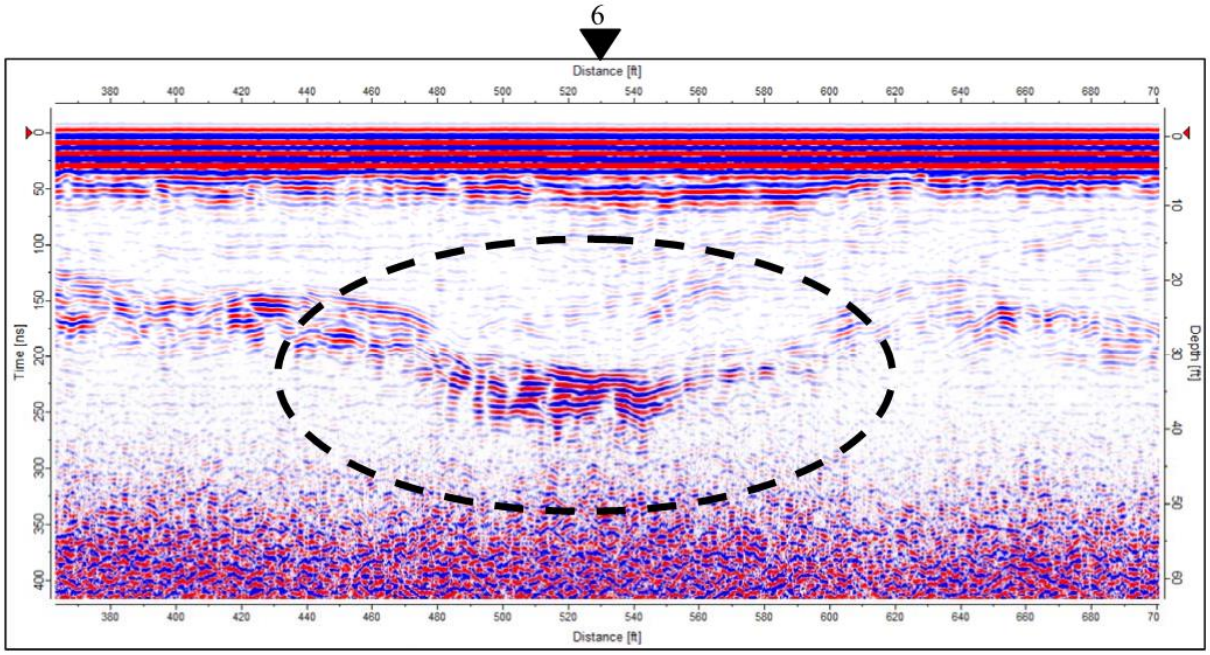

Figure 37: Level B GPR Anomaly Transect 6.5 (Professional Service Industries (PSI), 2014)

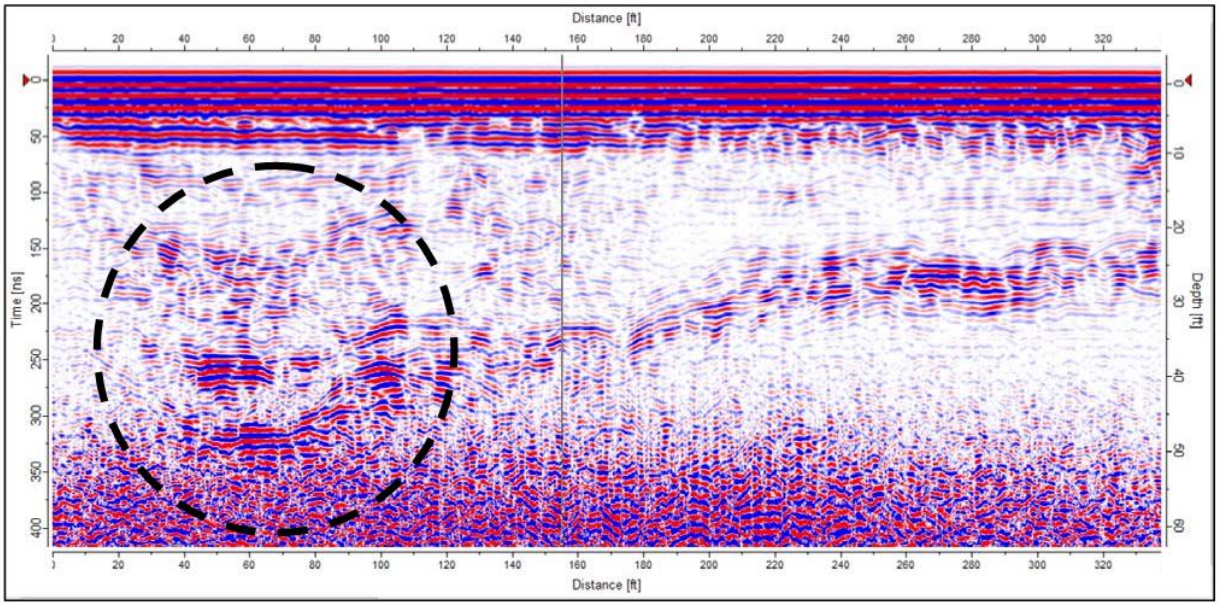

Figure 38: Level A GPR Anomaly Transect 7 (Professional Service Industries (PSI), 2014)

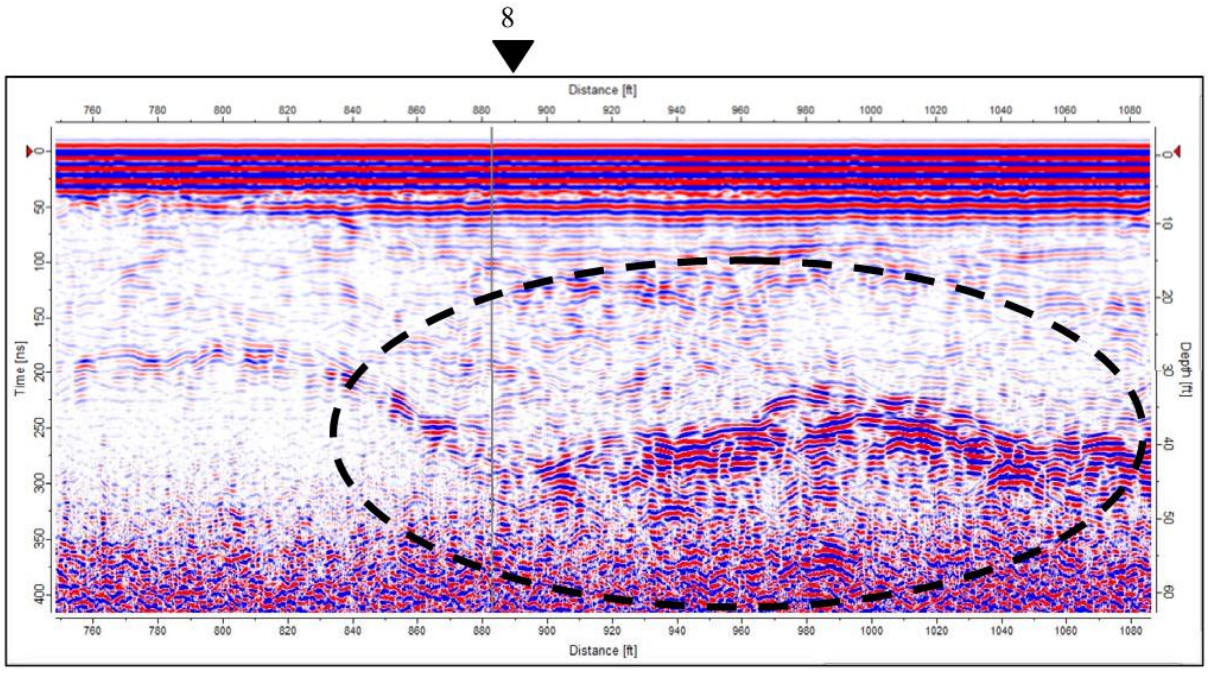

Figure 39: Level A GPR Anomaly Transect 8 (Professional Service Industries (PSI), 2014)

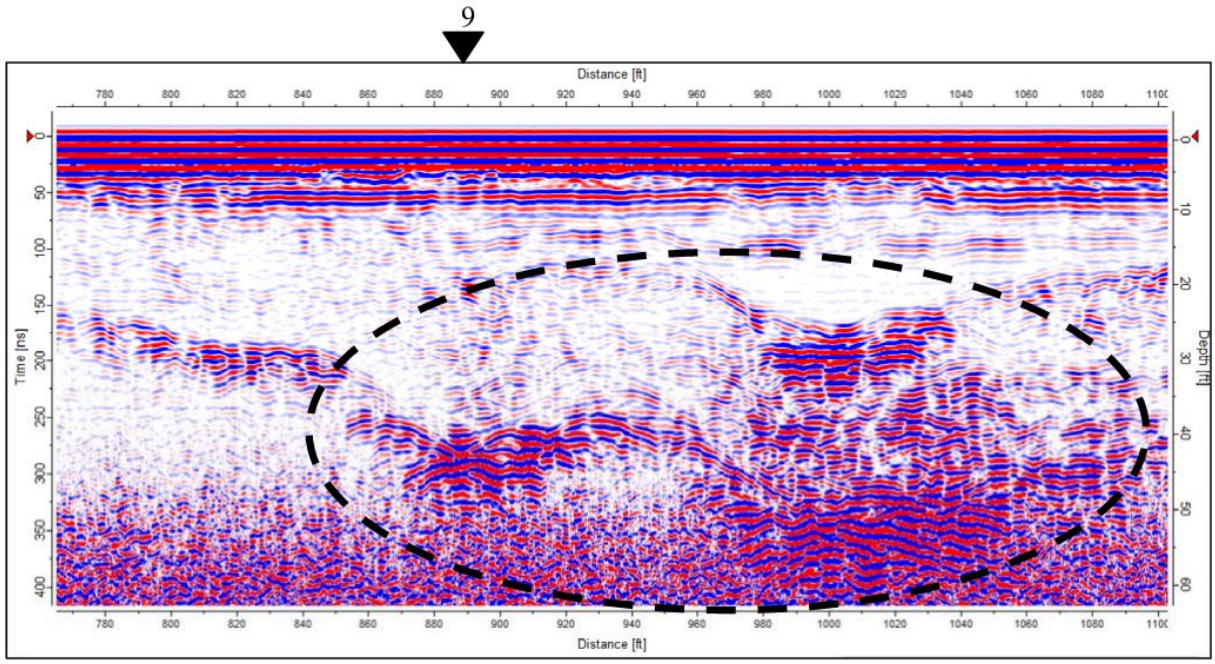

Figure 40: Level A GPR Anomaly Transect 9 (Professional Service Industries (PSI), 2014)

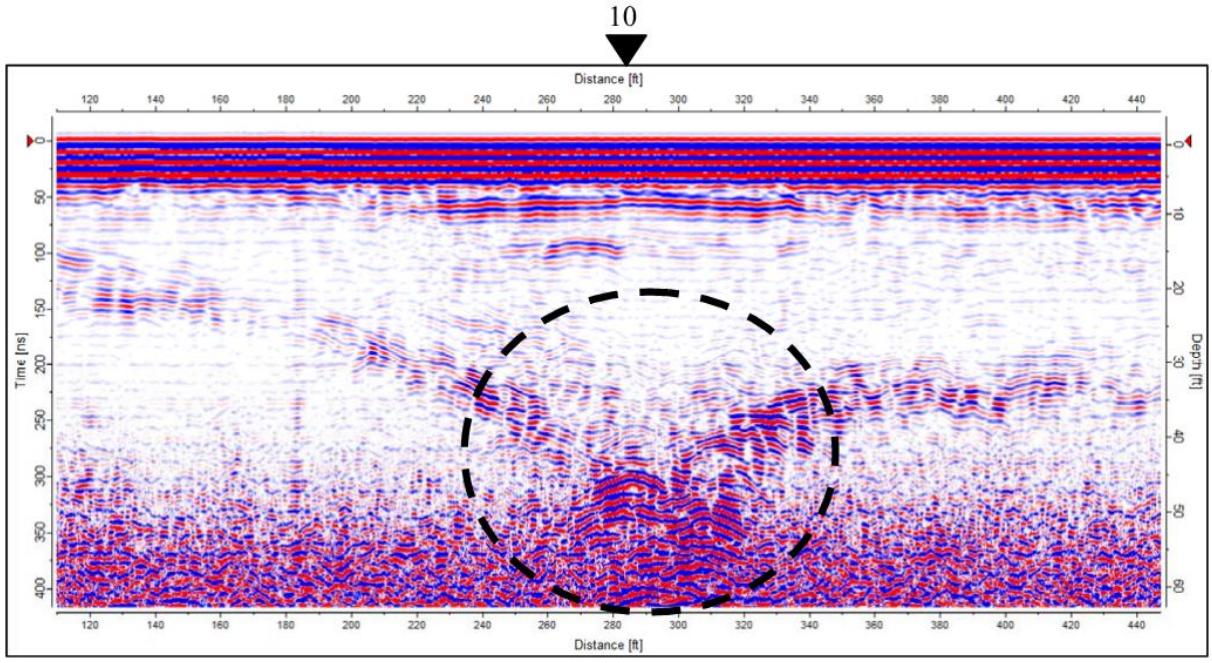

Figure 41: Level A GPR Anomaly Transect 10 (Professional Service Industries (PSI), 2014)

4.3 Equipment

In this study, piezometer model 4500S-350kPa from Geokon was used to measure water level. Model 4500S vibrating wire piezometer designs for long – term measurements of fluid pressures such as ground water elevations and pore pressures when buried directly in embankments, fills, etc. Also for installation inside boreholes, observation wells and standard (>19 mm diameter) piezometer riser pipe (Geokon, 2016). The selected sensors have very high resolution and accuracy 0.025 percent and ± 0.1 percent of Full Scale (F.S) reading, respectively. Assumes the specific weight of water is 9.81 kN/m^3 and the sensor is placed 10-m underwater, the theoretical reading pressure is 98.1-kPa. The resolution of the sensor in this case is $0.025\% \times 98.1kPa = 0.0245kPa$ or 2.5mm. It means the sensor be able to detect any changes in water level when this change is larger than or equal to 2.5mm. The accuracy of the sensor is ± 0.1 percent of Full Scale reading that means the actual pressure reading of the sensor may range from 98.00kPa to 98.2kPa. Details of sensors' specifications are listed in Table 7.

Table 7: Specification of Model 4500S-350kPa piezometer

Model	Rated pressure	Over range	Resolution	Accuracy	Temperature range	Length x Diameter
4500S	350kPa	$2 \times 350kPa$	0.025%F.S	$\pm 0.1\% F.S$	$-20℃ \; to \; 80℃$	133x19.1mm

As mention earlier, sensors will be installed at two active relic sinkhole sites. The input pulse train to the sensors and the output signal from the sensors will be transmitted and received by dataloggers. There are five dataloggers at the first site, intersection of State Road 46 and State Road 429 located in Sorrento Florida, in which four of them are four-channels dataloggers and the last one is sixteen-channels datalogger as shown in Figure 42. The second site is a retention pond located in Newberry Florida has only one sixteen – channels datalogger. There are two type of

signals are received by dataloggers. The first and most important type of signal is called “Digits”. The “Digits” for vibrating wire transducer output when using linear conversion is calculated based on the following equation: $Digits = Frequency^2 \times 10^{-3}$. The frequency in this equation is resonant frequency of transducer measures in Hertz which is determined by dataloggers. For example, a piezometer sensor reading 9000 digits corresponds to a frequency 3000 Hz. The second type of signal is temperature from thermistors embedded in piezometer sensors. Temperature at depth where sensors located is used for pressure calibration since specific gravity of water varies over temperature. Measured data will be stored in 320K bytes of EEPROM memory, which translates into a memory storage capacity of 10666 arrays for 4 – channel datalogger and 3555 arrays for 16 – channel. Each array consists of the datalogger ID, day, time battery voltage, datalogger temperature, vibrating wire sensor reading, and the sensor temperature. If data is sampled with rate of 30 minutes per sample, it takes 222 days for the 4 – channel and 74 days for the 16 – channel to fill the memory in full.

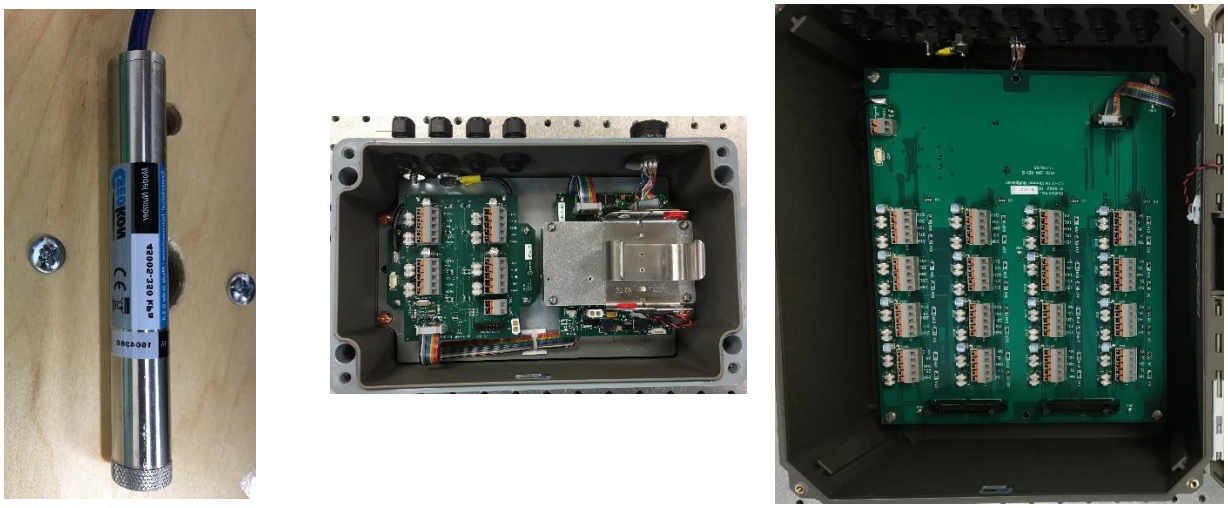

Figure 42: Sensor and dataloggers. Left: Geokon piezometer Model *4500S-350kPa*. Middle: Geokon Datalogger Model *8002-4*. Right: Geokon Datalogger Model *8002-16*

The last thing of this puzzle is a software called “Logview”, which uses to control dataloggers. All of the test paramters such as sampling rate, duration of measurement, data types, date, and time can be set and load to dataloggers for operation. This software is also capable to calculate displace water pressure at the location of sensor using the following equation:

$Pressure = Calibration\ factor \times (Current$ "digits" $reading - Initial$ "digits" $reading)$ or $P = G \times (G_1 - G_0)$. Calibration factor (G) is unique for each sensor, which can be found in the calibration report from manufacture. Since piezometers are installed in the field, which is uncontrolled environment, the temperature may vary; hence, temperature correction is necessary. The pressure equation with accounted for the temperature change is:

$$P = G(G_1 - G_0) + K(T_1 - T_0)$$

Where: G is vibrating wire gate factor

K is themostor factor

G_1 and G_0 are current and initial “Digits” readings

T_1 and T_0 are current and initial temperature readings

After water pressures are determined, the high of water column obove the sensors can be calculated easily by divides measured pressure for specific gravity of water.

4.4 Installation Process of Piezometer Sensors

The ideal soil's types to place piezometer sensor are sandy soils since it has high hydraulic conductivity, so any changes in water level can be measured faster and more accurate. In the oposite, clayey soils are tried to avoid because it has very fine soil particles, which passed 200 size sieve, so it may clog the piezometer's filter and leading to wrong reading results.

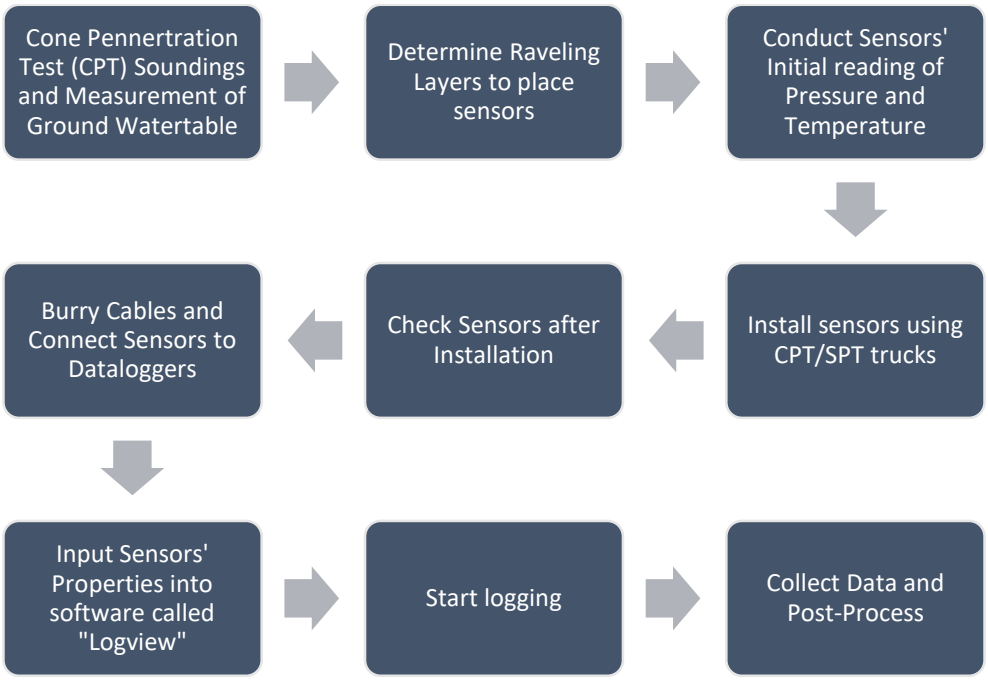

Figure 43: Flow Chart of Sensors Installation

As mentioned previously, fourteen SPTs and seventy-four CPTs were performed by PSI and FDOT District 5, respectively. In order to determine depths of raveled zones, the first step in this process was to perform CPT soundings. There were 20 CPT soundings, which performed by State Materials Office, in this site. Locations of these CPTs are in Figure 45.These CPT soundings performed accordance to ASTM D-5778-12 (Standard Test Method for Electronic Friction Cone and Piezocone Penetration Testing of Soils) with the cone tip size of 10 cm^2. Details of 20 CPT soundings present in Appendix B. The depth ranged from 51.18 feet to 81.36 feet with depth

increment of 0.164 feet. CPT results indicated mostly sandy to silty sand in the upper 20 feet followed by 20 to 30 feet of alternating layers of sand, clayey fine sands, and clays with maximum tip resistance of 370 tsf. Below the depth of 45 to 55 feet raveled soil conditions consisting of sandy silt, clayey silt, and silty clay. The second step was to determine raveling layers to place sensors. Results from previous and current CPT sounding indicated a raveled zone at the bottom of soil profile as shown in Figure 46, so sensors were placed in this zone. The third step in this process was to read initial values of pressure and temperature. This step needed to be handled with care while performing since all of the following values will use these initial values as references. Sensors were lower down to near but not touch GWT in holes created by CPT soundings then let it stabilized at that position for about 10 – 15 minutes then using handheld device to read initial values of pressure and temperature, which used to calibrate the pressure since specific weight of water varies with temperature. The fourth step was install sensors into predetermined depth using CPT or SPT trucks. During the installation process, sensors were protected by an adapter. One end of the adapter connected to rods from CPT/SPT trucks the other end was sealed by a sacrificial cone-tip, which connected with sensors via a small cable (fishing leader was used in this case). Details of adapter's dimensions and image are shown in Figure 44. When desired depth was achieved, adapter and sensors were held in place for about 15 minutes before detaching sacrificial cone-tip from adapter by lifting up the adapter. Boreholes' walls collapsed and held the sacrificial cone-tip in position after waiting time, so sensor was kept in place since it connected with the cone-tip via a small cable. To make sure all sensors worked sufficiently after installation, it was checked using handheld reader device; then, compared these values to the theoretical pressure for each sensor. The next steps were to burry cables and connect sensors to dataloggers, input sensors'

properties into software called "logview", start logging, and collect data and perform post-processing.

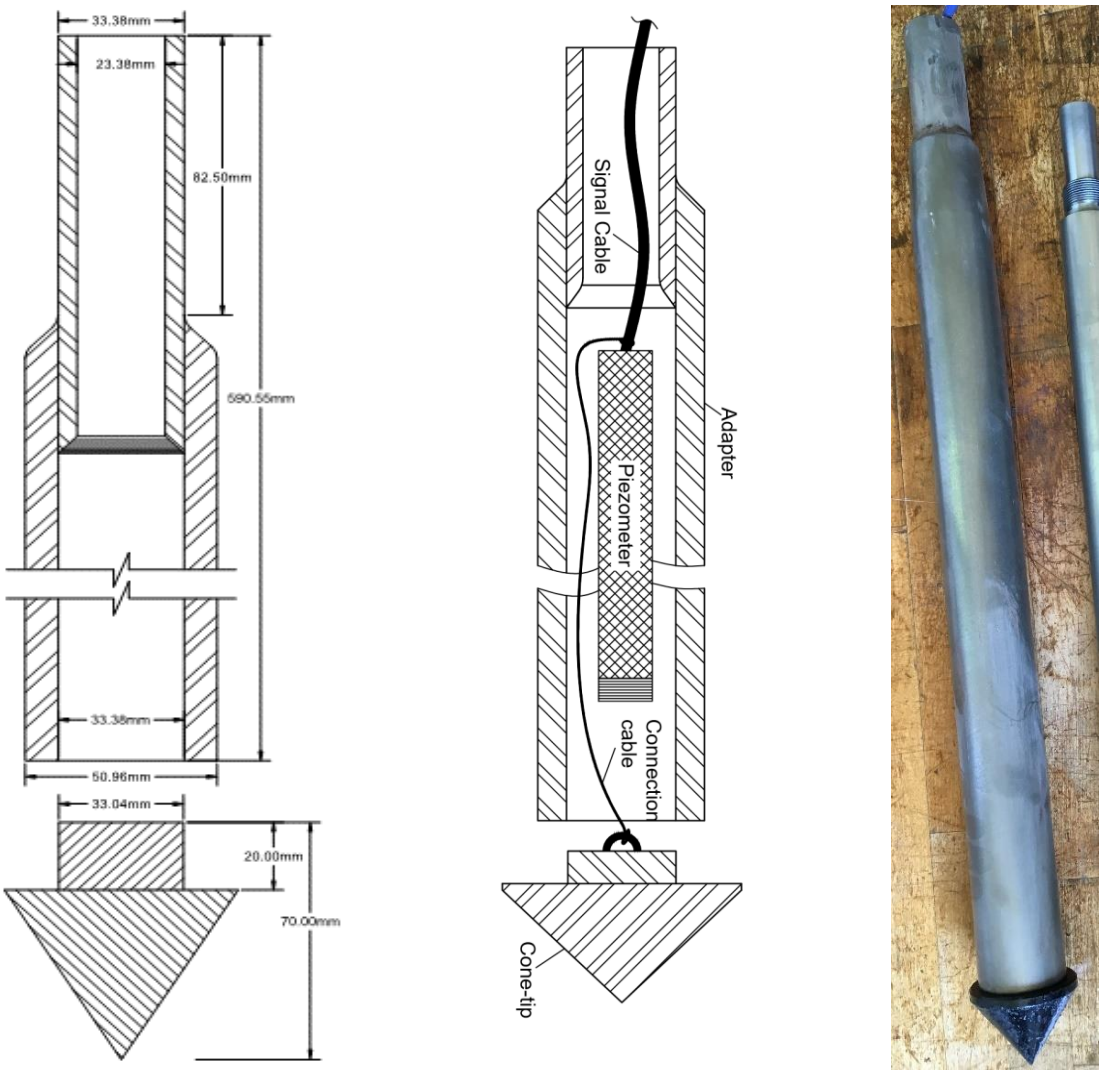

(a) (b) (c)

Figure 44: (a)-Schematic drawing of the adapter. (b) detail connections of sensor and sacrificial cone-tip. (c) Actual image of the adapter

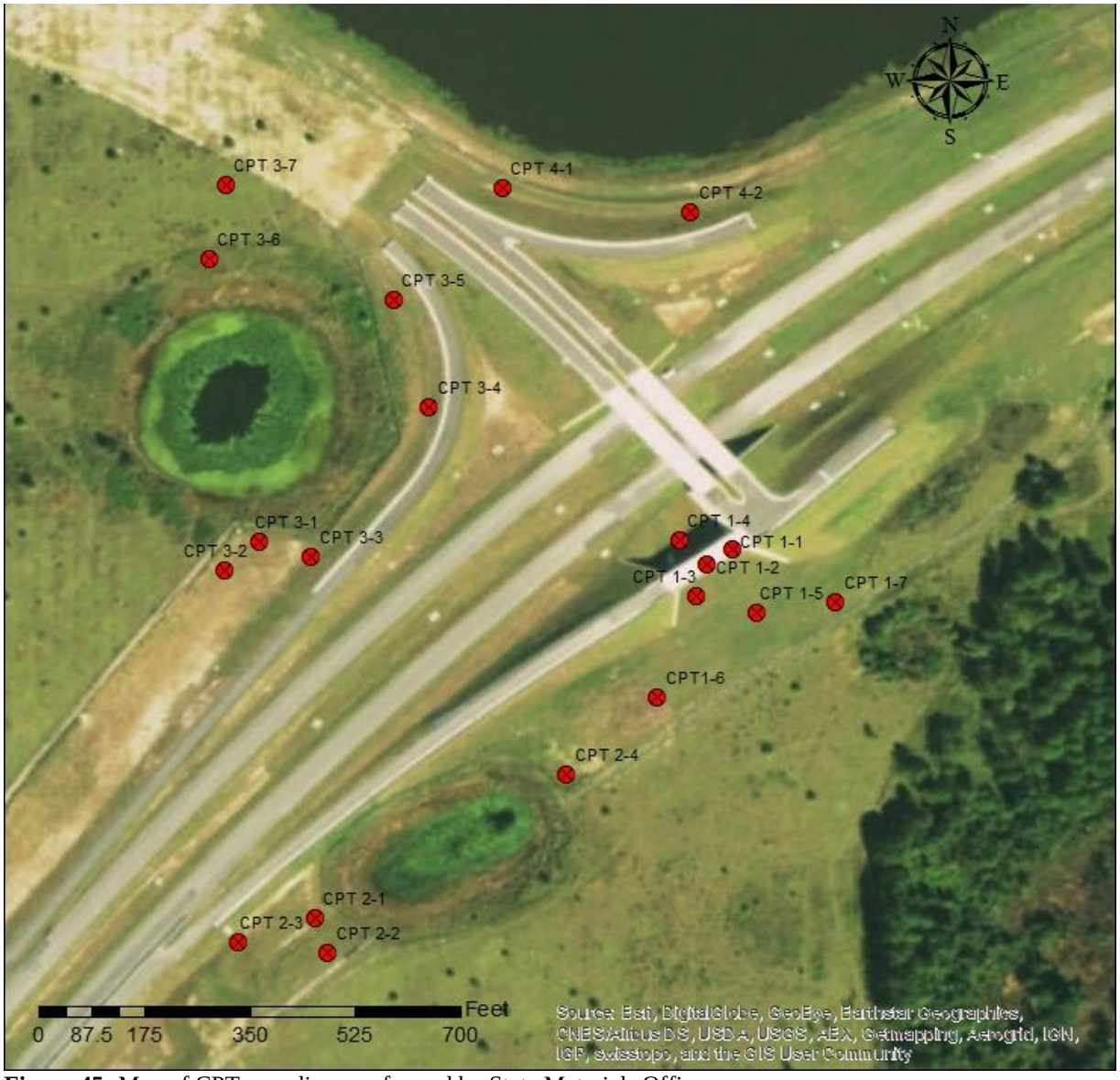

Figure 45: Map of CPT soundings performed by State Materials Office

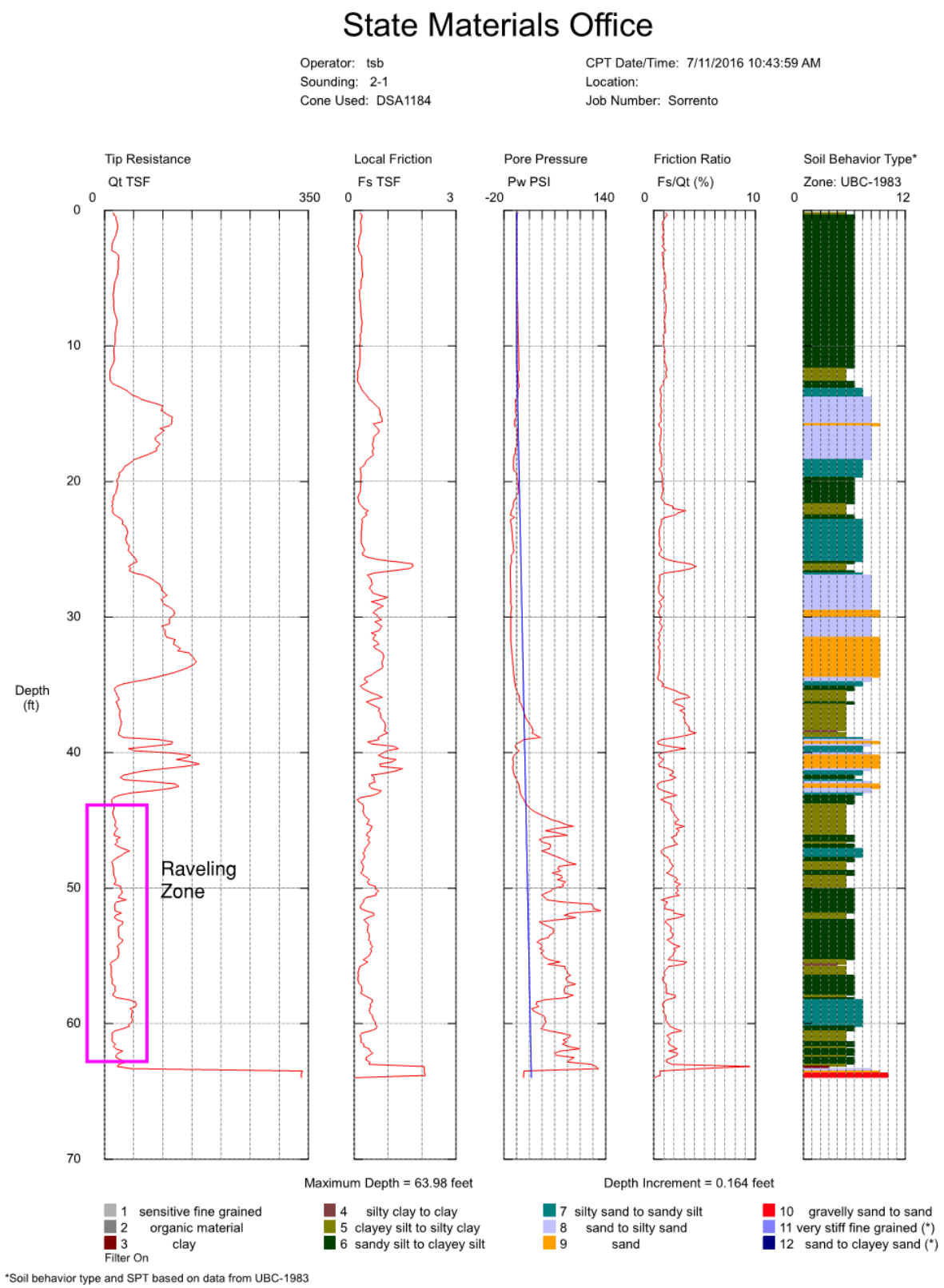

Figure 46: Result of CPT Sounding for sensor 2-1

4.5 Development of Sensor Layout

Result from existing Standard Penetration Test (SPT) as shown in Table 5, which performed by Professional Service Industries (PSI), was used to plot the ground elevation contours as shown in the transparent area in Figure 47. The lowest and highest water table were 63 and 70.5 feet from mean sea level (MSL), respectively. The bluish colors represented for the low water table level areas while the reddish colors represented for the high water table level areas. The GWT contours were generated by the interpolation function in ArcGIS. There were two wet ponds in the relic sinkhole zones, which have magenta color in Figure 47. Because location of future sinkhole even is unknown, sensors' positions are distributed randomly with one constraint that two sensors in the same region make a perpendicular line to the contour lines.

Sensors are divided into four zones. Zone 1 is located on the east side of Figure 47. This zone has seven sensors named 1-1 through 1-7. Zone 2 is located on the south east of Figure 47, and contains four sensors named 2-1 to 2-4. The next zone is Zone 3 which is located on the west side of Figure 47. This zone has seven sensors named 3-1 to 3-7. The last zone is Zone 4 which has two sensors and is located on the north side of Figure 47. These four zones are located on both sides of Wekiva Parkway. By evaluate different scenarios, it turned out that the most economical way is using five dataloggers for these zones. Signals from sensors in Zone 1 will be generated and acquired by a 16-channel datalogger. Similarly, sensors in Zone 2 will be connected to a 4-channel datalogger. Two dataloggers will be used in Zone 3. Sensors 3-1 to 3-3 will be connected to a 4-channel datalogger, and the remaining sensors of Zone 3 will be connected to the other 4-channel datalogger. Two sensors in Zone 4 will be connected to another 4-channel datalogger.

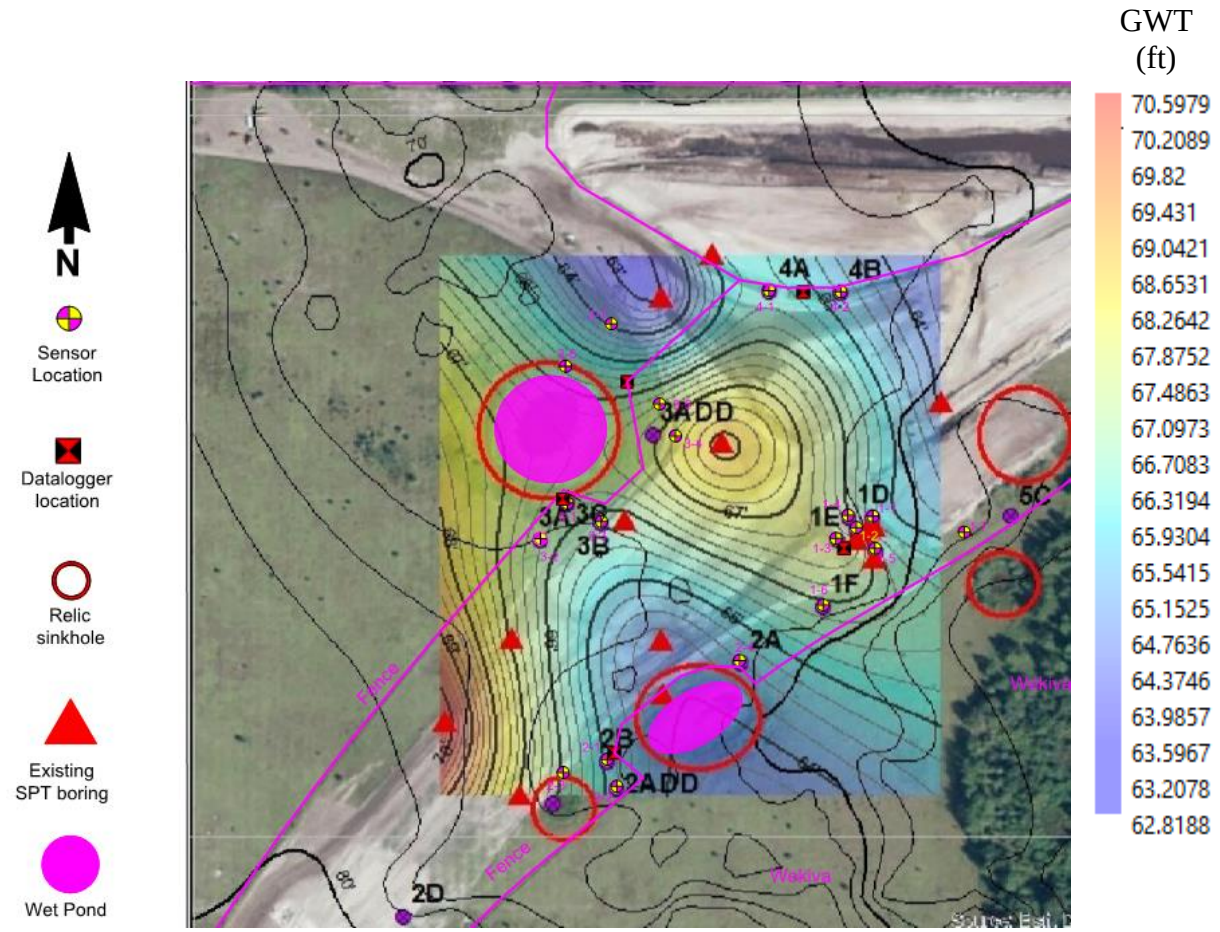

Figure 47: Ground water table and sensor layout of Wekiva Parkway in Lake County, Florida

4.6 Surveying

Depth of ground water was measured twice for each sensor location, the first time right after each CPT sounding, and the second time right after the installation of each sensor. The depths of GWT presented in Table 8 were the average values between the two trails. Ground surface elevation was measured using total station method. In this survey, a theodolite model DT-100 manufactured by Topcon and its accessories were used. A point with known elevation (75ft) located in the south retaining wall of the bridge on Ramp O as shown in Figure 48 (a) was used as a benchmark. Five total stations were set up during the survey process. The first station was set at

position of sensor 1-5. From this station, Elevations and directions of all sensors in Zone 1 and sensor 2-4 in Zone 2 were measured. The second station was set at position of sensor 2-4 since elevation of this location was determined from the first station. Elevations and directions (compare to the north direction) of the remaining three sensors of Zone 2 was determined. The next station was set in Zone 3 as shown in Figure 48 (b). Elevations and directions of five out of seven sensors in Zone 3, except sensors 3-6 and 3-7 were determined. Because sensors 3-6 and 3-7 located beyond the fences, another station was created to do the measurement for these sensors. The last station was setup in Zone 4 since all two sensors in this zone was out of sight from the other zones. After surface elevations of the desired locations had been known, elevations of ground water table and sensors were calculated and presented in Table 8.

(a) (b)

Figure 48: (a) Location of benchmark. (b) Image of station in Zone 3

Table 8: Summary Elevations of GWT and Sensors

Zones	Sensor No.	S/N	Sensor depth (ft)	Depth of GWT (ft)	Surface Elevation (ft)	Elevation of GWT (ft)	Elevation of Sensors (ft)
1	1-1	1337248	51.70	10.30	74.47	64.17	22.77
	1-2	1608973	58.30	10.60	75.47	64.87	17.17
	1-3	1617085	73.00	10.57	75.63	65.06	2.63
	1-4	1609795	28.80	10.70	75.375	64.68	46.58
	1-5	1609797	44.00	10.70	74.45	63.75	30.45
	1-6	1617091	46.00	10.60	76.25	65.65	30.25
	1-7	1617088	42.00	10.10	71.68	61.58	29.68
2	2-1	1604360	55.11	3.24	70.065	66.83	14.96
	2-2	1609794	60.14	7.69	74.745	67.06	14.61
	2-3	1617095	68.44	4.00	70.605	66.61	2.17
	2-4	1617098	49.70	8.15	73.225	65.08	23.52
3	3-1	1617087	41.03	4.63	71.405	66.78	30.38
	3-2	1617094	41.22	4.51	71.785	67.28	30.56
	3-3	1617092	76.00	5.85	72.485	66.64	-3.52
	3-4	1617097	45.97	7.83	73.375	65.55	27.40
	3-5	1617084	45.18	8.80	74.315	65.52	29.13
	3-6	1617093	61.04	5.34	71.935	66.60	10.89
	3-7	1617096	24.25	9.75	75.155	65.41	50.91
4	4-1	1617086	45.72	13.00	76.655	63.66	30.93
	4-2	1617089	60.63	12.55	75.825	63.28	15.20

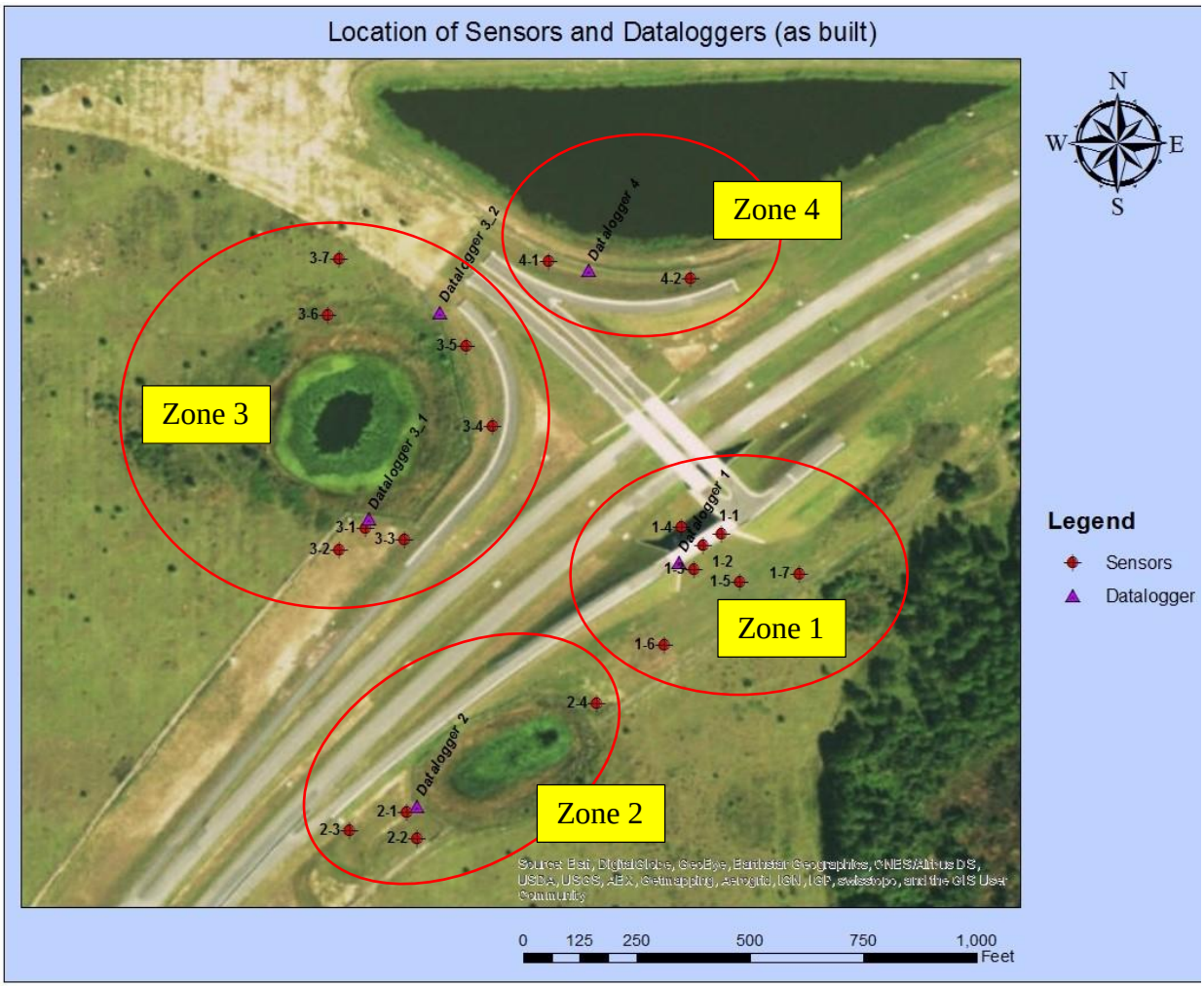

Figure 49: Location of sensors and datalogger (as built) base map from ESRI

4.7 Signal Processing

Moving average technique is used to show the change in piezometric levels of water over time. This method helps smooth out the input signals by filtering out the noises from random signals' fluctuation. Output data is presented by frames. Each frame shows the mean values of one day piezometric data. The next frame is four hours apart from the preceded frame. Thus a day data will be shared by six frames as shown in Figure 50. If there are any abnormal signals occurred, it will be repeated six times; so missing valuable signal can be minimized.

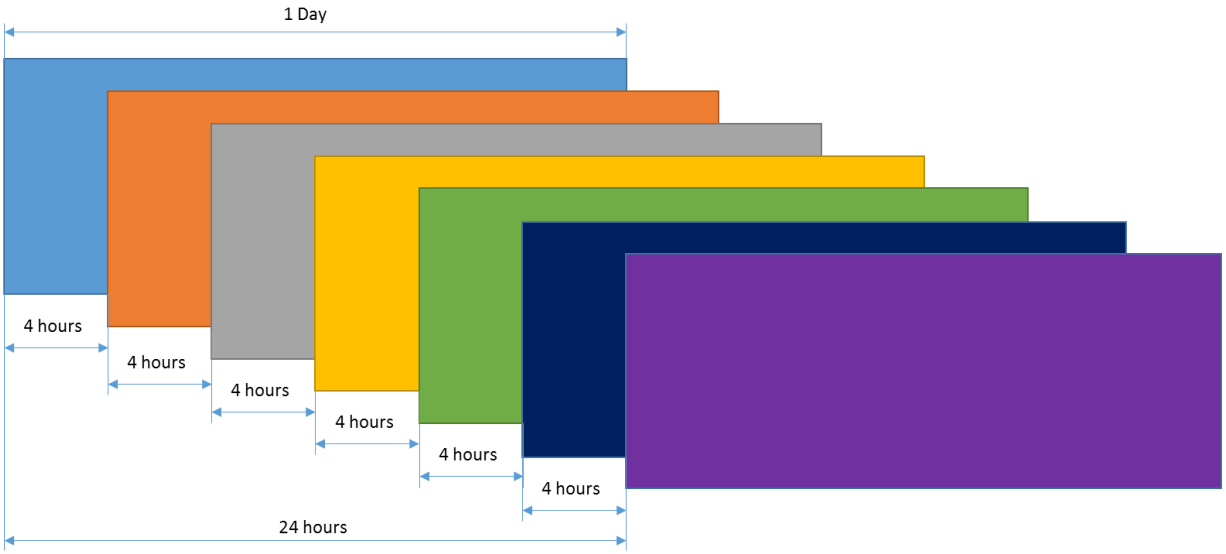

Figure 50: Flow chart of moving average technique

ArcGIS software from Environmental Systems Research Institute (ESRI) is used to analyze piezometric data from 20 sensors. In the first step, sensors' information such as latitude, longitude, depth of sensors, identification of sensors, as well as the fluctuations of piezometric pressure over time are imported into the program. Based on the sensors' identification, ArcGIS can sort and match sensors' coordinate and piezometric data at a desired time frame then the mean values can be calculated using statistics toolbox. In the next step, twenty mean values of piezometric data from twenty sensors are served as known point. Information from all points other than these 20 known points were interpolated using Inverse Distance Weighting (IDW) method. IDW is multivariate interpolation technique. To predict a value for any unmeasured location, IDW searches known values surrounding the prediction location. The measured values closer to the prediction location have more influence to the predicted values than those further away. This technique assumes each measured point has a local influence and diminishes with distance. The weight for each unknown point is proportion to the inverse distance raised to the power value *p*. if p = 0, there is no decrease with distance. The predicted value will be the mean values in the

searched neighborhood. The weights for the distant points decrease substantially when p increase. The illustrations of search neighborhood and decrease of weight with distance are shown in Figure 51(a) and Figure 51(b), respectively. (Environmental Systems Research Institute (ESRI), 2016). The mathematical expression for this method is shown in the following equation.

$$z_j = \frac{\sum_{i=0}^{n} \left(\frac{z_i}{d_{ij}^p} \right)}{\sum_{i=0}^{n} \left(\frac{1}{d_{ij}^p} \right)}$$

Where: $z_j =$ prediction value

$p =$ power of the interpolation function

$z_i =$ measured value at point i

$d_{ij} =$ distance from point i to point j

From the result of IDW interpolation method, equivalent piezometric contour lines can be generated easily for the interest intervals. Equipotential line is a line along which the potential head at all points is equal. If piezometers are placed at different points along the equipotential line, the water level will rise to the same level in all of them. Contour interval of 2 feet is used for this paper. Final result for each frame includes transparent color map of IDW, piezometric contour lines, and base map of the site. When all created frames put together and play in the sequence of time, fluctuation of piezometric pressures over time can be represented in form of 2D images video.

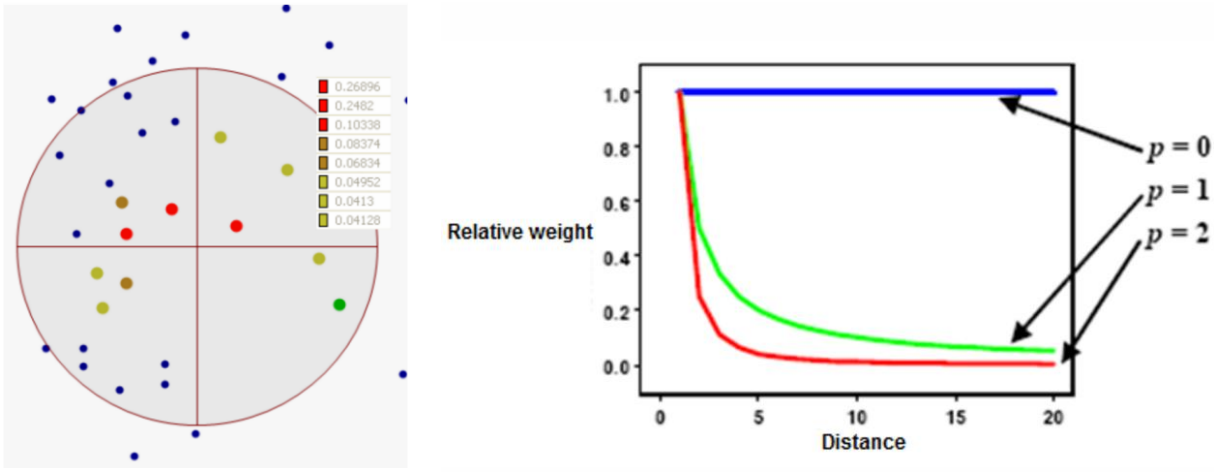

(a) (b)

Figure 51: (a) IDW search neighborhood illustration. (b) Decrease of weight with distance illustration (Environmental Systems Research Institute (ESRI), 2016)

In addition to 1D and 2D signal processing of piezometric data, velocity or rate of change in piezometric pressure can also be quantified by taking numerical differentiation of piezometric data. This rate of change is referred as drops or peaks in water level. Results from scaled models in chapter 3 have proved that a sinkhole even has spatial-temporal relationships. It means that if the sensor closer to sinkhole location, it will have more peaks than those further away. Similarly, the number of peaks will accelerate when sinkhole formation stage is approaching. Since field test also uses groundwater as an indicator for sinkhole monitoring, it is expecting to have the same behaviors as scaled model. However, we have to note that it is a lot more complicated in field conditions compare to laboratory conditions. As discovered from subsurface exploration, there are multiple soil layers from loose to dense sand in the first few layers follow by clayey fine sand then clay layers thereafter. The thickness of these soil layers are also varied from point to point. Unlike scaled model in the laboratory with point of discharge is predetermined, the locations of points of discharges are unclear. Sometimes, there are multiple points of discharges close to each other, so one point of discharge can influence the others.

4.8 Results

In order to relate changes in piezometric elevations to rain evens, precipitation information for period from 08/17/2016 to 10/11/2016 for rain gage located in Lake Sylvan near Paola, Florida, which is about 7 miles toward the southeast from project site, is also presented in Figure 52. The sampling rate of this rain gage is 15 minutes. Three major rainfall evens occurred during this period. The first even occurred from 08/29 to 09/03 with the cumulative precipitation of 3.5 inches while precipitation of more than one inch was recorded in the second even in 09/18. The last even occurred during 10/01 and 10/08 (Hurricane Matthew) with the cumulative rain fall of almost 9 inches.

Plots of piezometric pressure elevations compare to Mean Sea Level (MSL) in each zone (refers to Figure 49 for details of zoning map) are shown from Figure 53 to Figure 56. Data from all sensors have the same trend and almost the same fluctuating magnitude except for sensor 2-1, 2-2, and 2-3 in zone 2. By investigating on maps and daily working on the field for more than a month during the sensor installation process, it is identified that there is a huge concrete pipe serves as point of discharge right above sensor 2-3 that dumps runoff water from Wekiva Parkway into this region. As a result, changes in magnitude of those sensors are stiffer than the others. In the first rainfall even, piezometric pressures start increasing from 08/29 and reach its peak on 09/06. The change in piezometric pressure during the second rainfall even is smaller since its cumulative precipitation only one inch. Because of the high precipitation in a short period of time in the third rainfall even, slopes of piezometric pressure profiles in this area are stiffer than the ones in the other areas. Overall, at the location of sensor 3-3 has the lowest piezometric elevation while the highest piezometric elevation occurs at location of sensor 3-7.

Figure 57 to Figure 76 show fluctuation of piezometric elevations and velocities over time in the order of sensor by sensor. Data of 20 piezometers sensors are shown in the 20 paired graphs. In each pair, the top graph is piezometric elevation while the bottom graph is its corresponding velocity, which is calculated by taking numerical differentiation of piezometric data. The numerical differentiation calculates differences between adjacent elements. The magnitude of velocity is high or low depends on the difference in magnitude between 2 adjacent elements of piezometric data since the change in time is always 30 minutes (sampling frequency). Velocity bounds up and down along the x-axis of velocity graph. Negative velocity means piezometric elevation has decreased from the previous data point. While in the positive velocity case, piezometric elevation has increased from previous data point. As a result of fluctuating groundwater during the day under effects of diurnal cycles, velocity is also fluctuating over time. It is easily to identify the two regions that have the highest peaks in velocity corresponding to the first and third rain evens in the precipitation data as shown in Figure 52. The maximum velocity is in sensor 1-2 with the magnitude of 30 ft/min. There are portions in sensors 1-6, 1-7, and 3-5 where piezometric pressures are constant and velocities are zero because connecting cables from sensors to dataloggers accidently got cut by a trencher while Young's Communication Co. Inc. installing optic cable along the road way.

Figure 77 and Figure 78 show the mean values of low and high piezometric elevations for one-day data between 8/28/2016 – 8/29/2016 and 9/7/2017 – 9/8/2016. The sampling frequency for those piezometer sensors is 30-minutes, so mean values for one-day at each sensor are average of 48 data points as presented in Table 9. To see the fluctuations of piezometric elevation over time, the means values of one-day data are generated every 4 hours (frame rate equals 4-hour). For example, if the current frame is representing mean values of piezometric data from 8/28/1016

4:00:00AM to 8/29/2016 4:00:00AM, the next frame will represent for the mean values between 8/28/2016 8:00:00AM and 8/29/2016 8:00:00AM. Then those frames put into the sequence of time to see how water fluctuates over time. Even though levels of piezometric elevations are increased between two data frames in Figure 77 and Figure 78, sensor 3-3 and sensor 3-7 remain its lowest and highest potentiometric elevations among 20 sensors, respectively. The values change from 43.838 feet to 44.857 feet in the lowest potentiometric case and from 64.869 feet to 66.049 feet in the highest potentiometric case. A constant interval of 2-foot between contour lines is used in Figure 77, Figure 78 and Figure 79. When distance between two contours is small, there is stiffer slope in that area. On the other hand, the stiffness of slope decrease when distance between contours increases. Area with lowest piezometric pressures, which represents in pink colors, is distributed in the middle of the maps, so water will flow from other areas to this area.

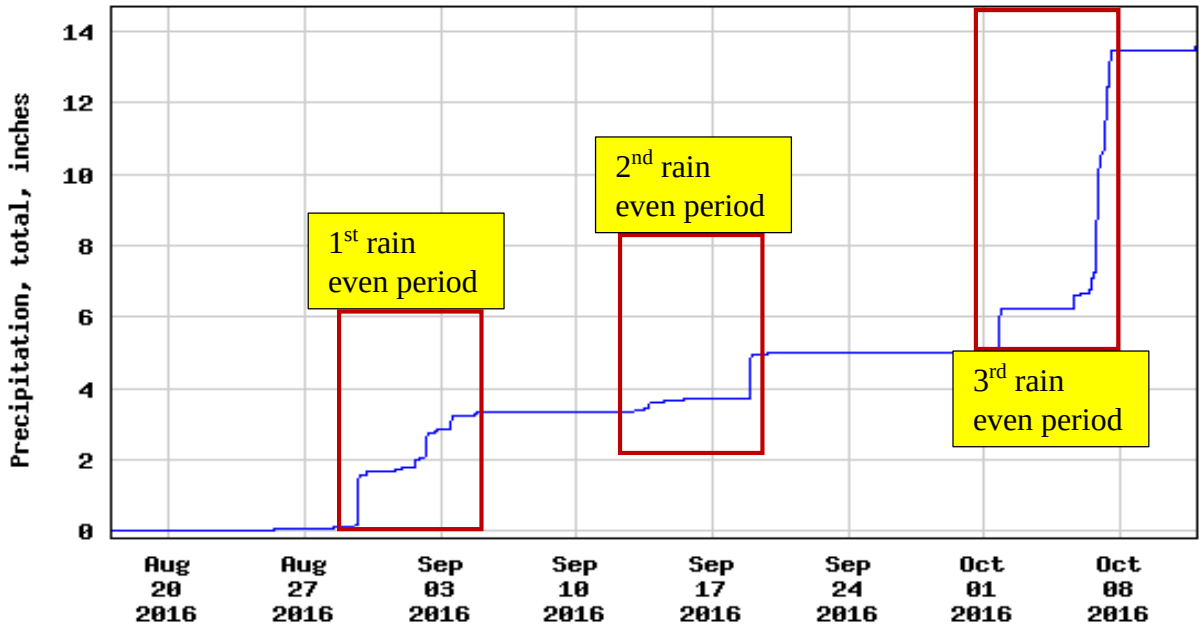

Figure 52: Precipitation data (08/17/2016 – 10/11/2016) for rain gage located in Lake Sylvan near Paola, Florida (U.S Geological Survey, 2016)

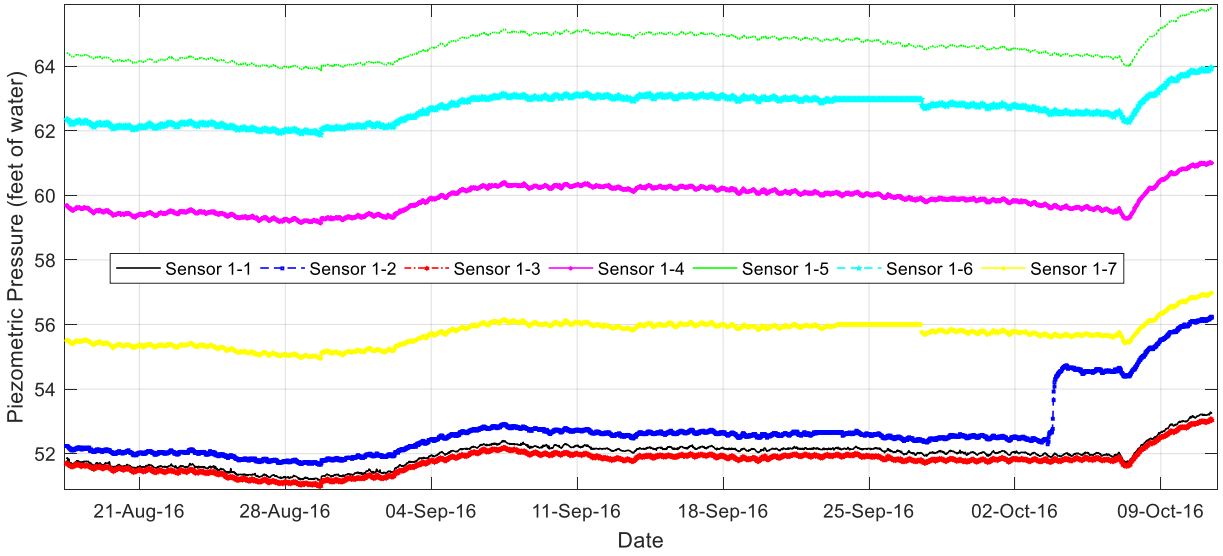

Figure 53: Fluctuation of piezometric pressure over time in Zone 1

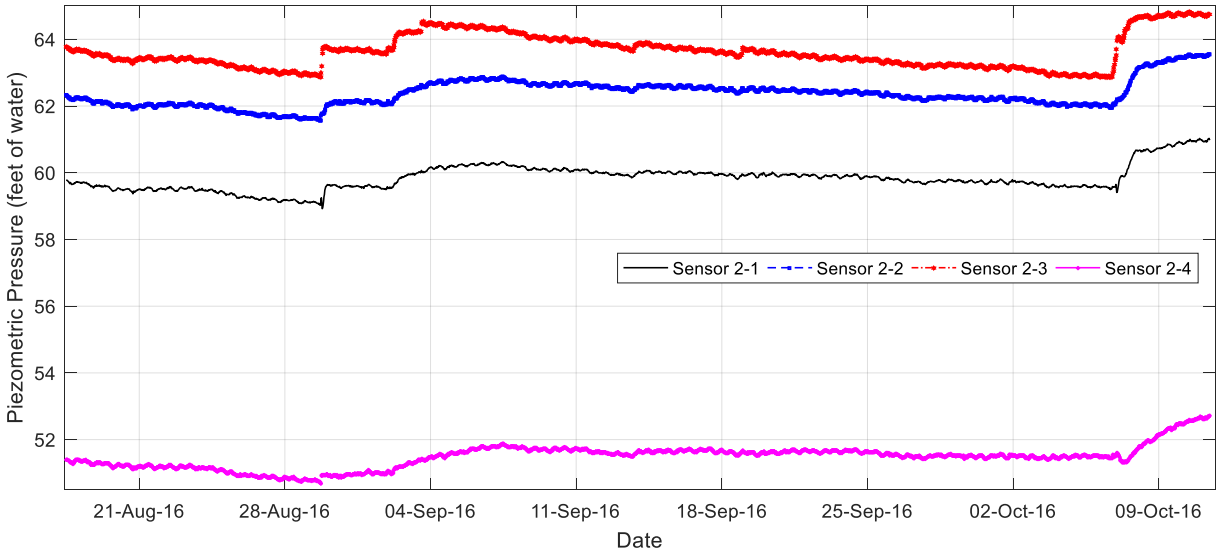

Figure 54: Fluctuation of piezometric pressure over time in Zone 2

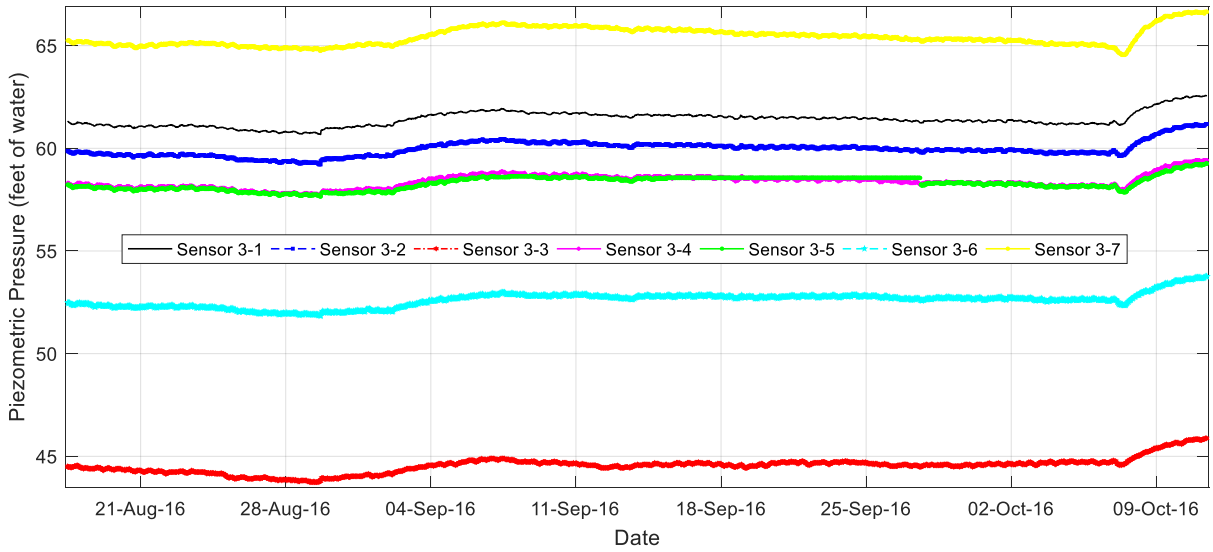

Figure 55: Fluctuation of piezometric pressure over time in Zone 3

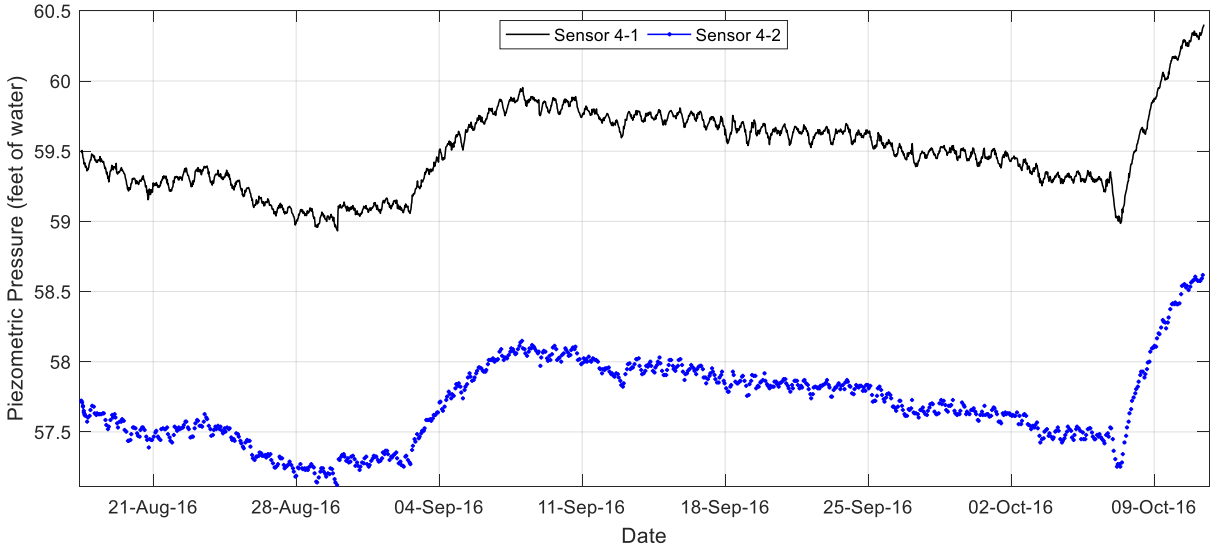

Figure 56: Fluctuation of piezometric pressure over time in Zone 4

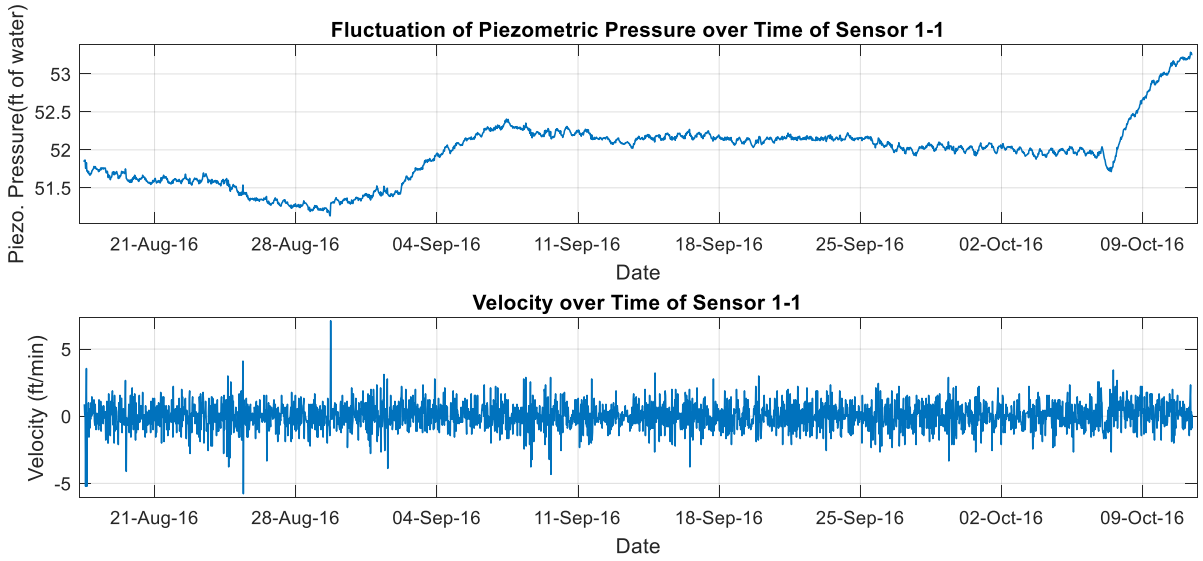

Figure 57: Fluctuation of piezometric pressure and velocity over time of Sensor 1-1

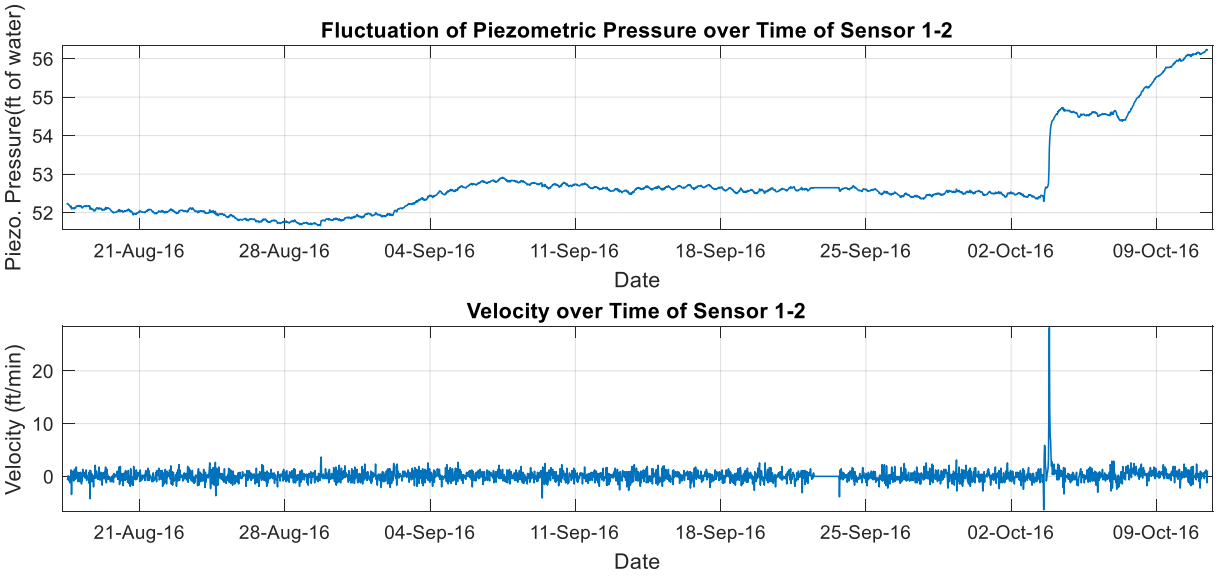

Figure 58: Fluctuation of piezometric pressure and velocity over time of Sensor 1-2

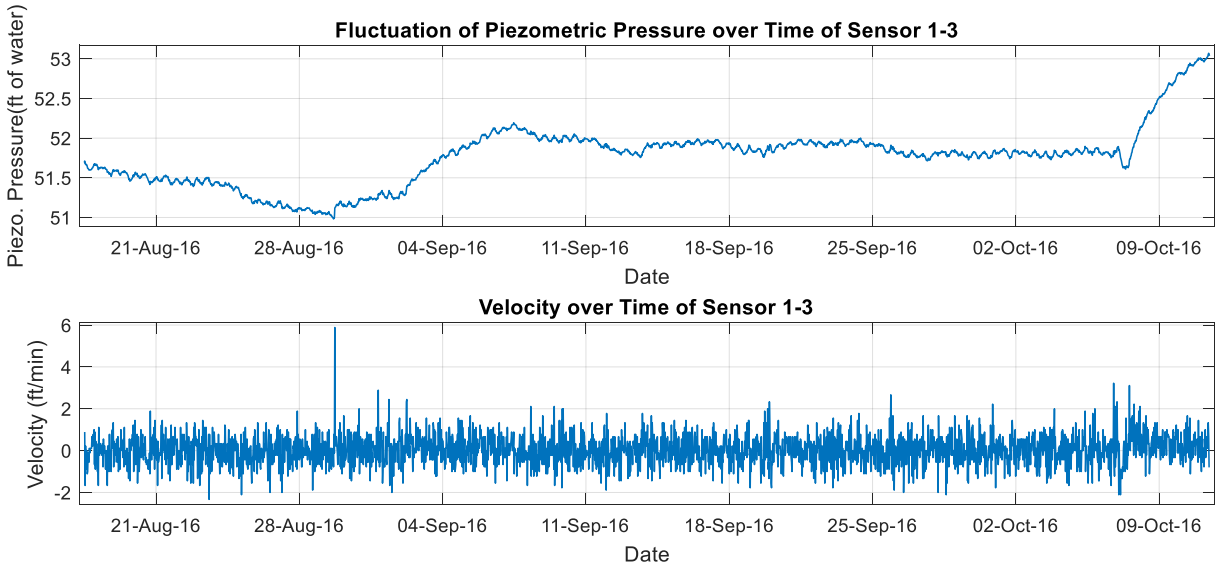

Figure 59: Fluctuation of piezometric pressure and velocity over time of Sensor 1-3

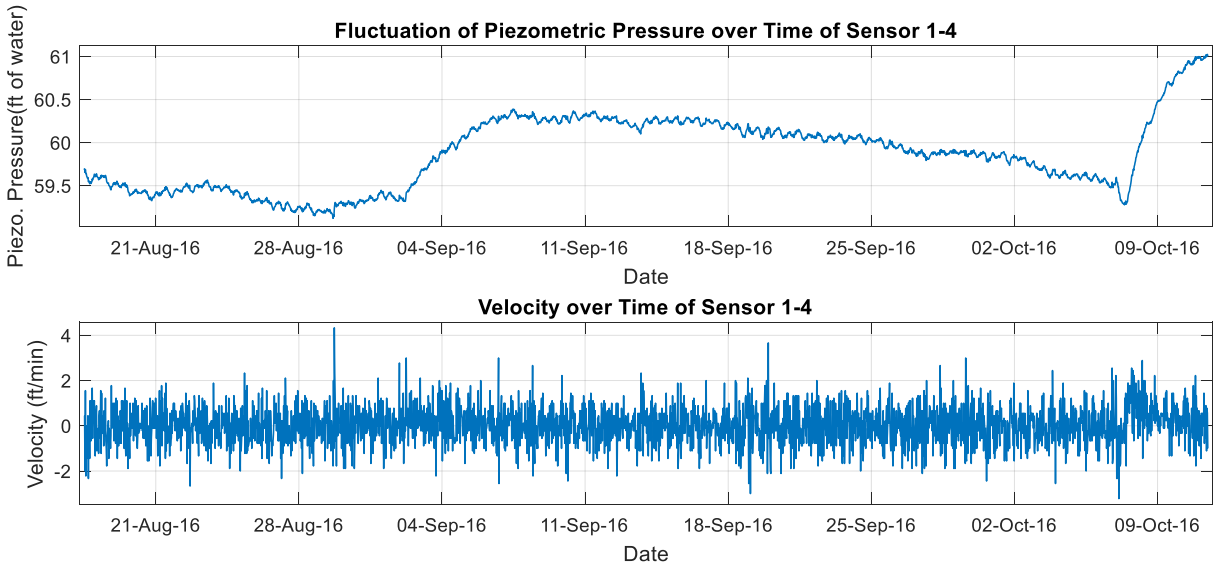

Figure 60: Fluctuation of piezometric pressure and velocity over time of Sensor 1-4

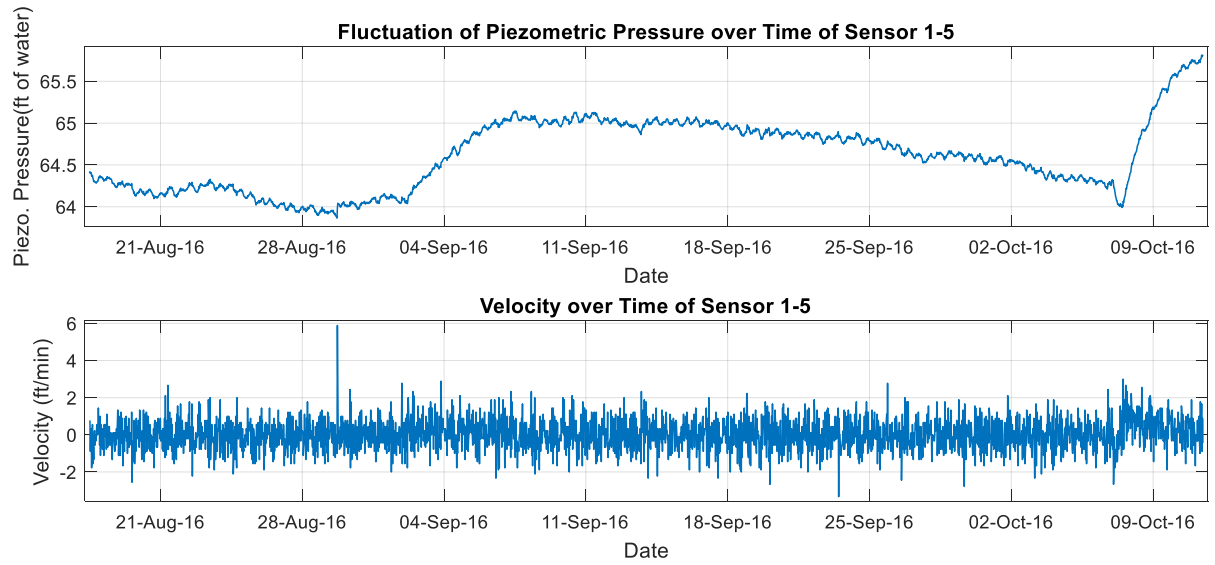

Figure 61: Fluctuation of piezometric pressure and velocity over time of Sensor 1-5

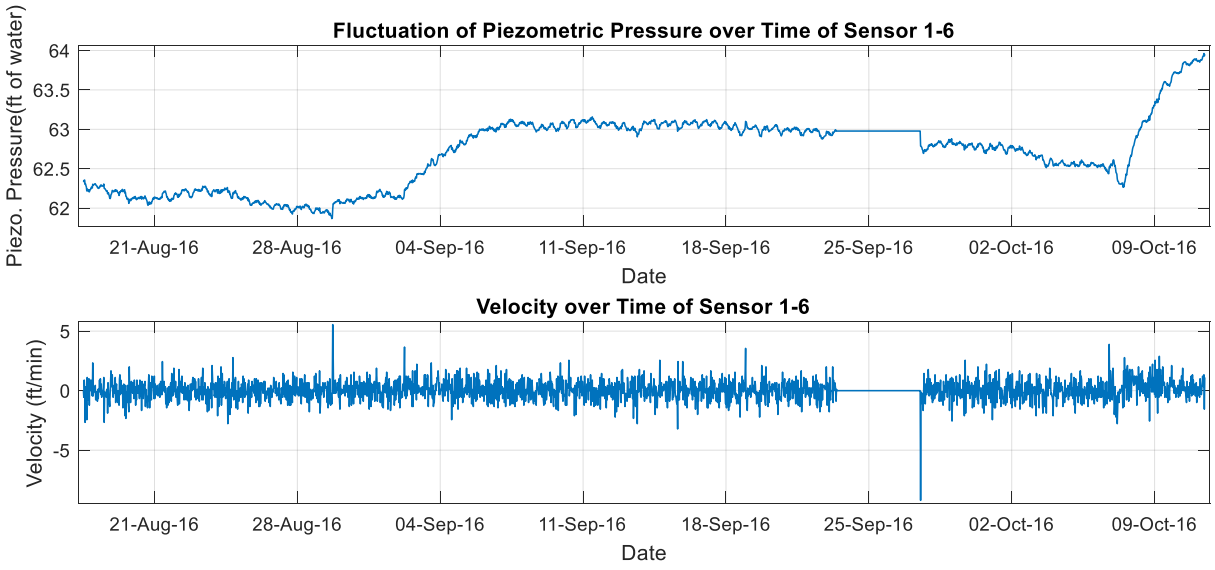

Figure 62: Fluctuation of piezometric pressure and velocity over time of Sensor 1-6

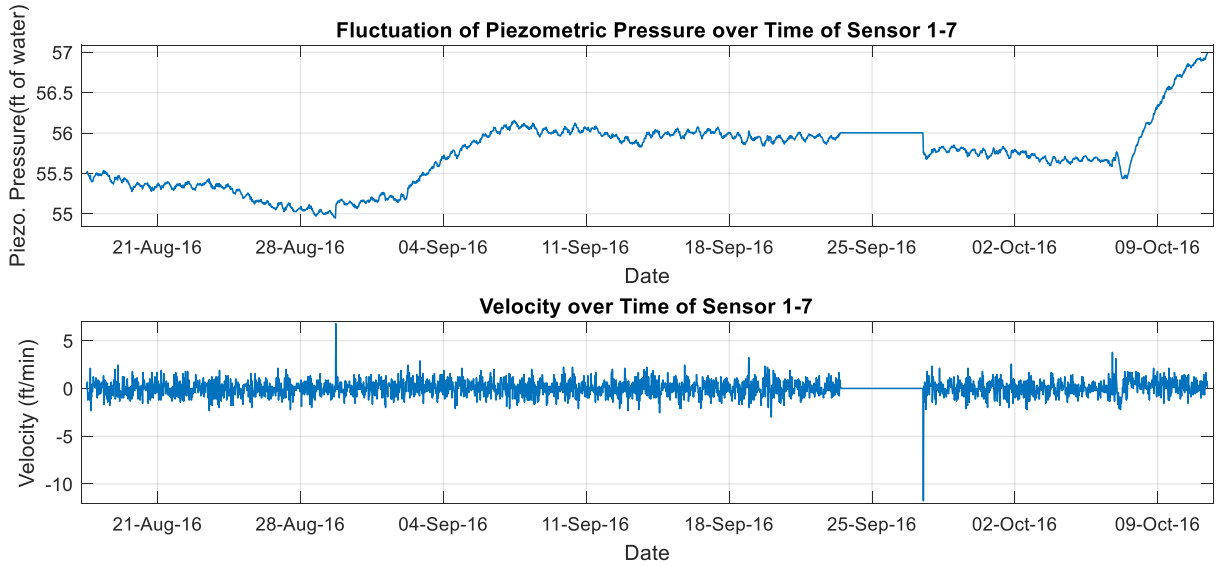

Figure 63: Fluctuation of piezometric pressure and velocity over time of Sensor 1-7

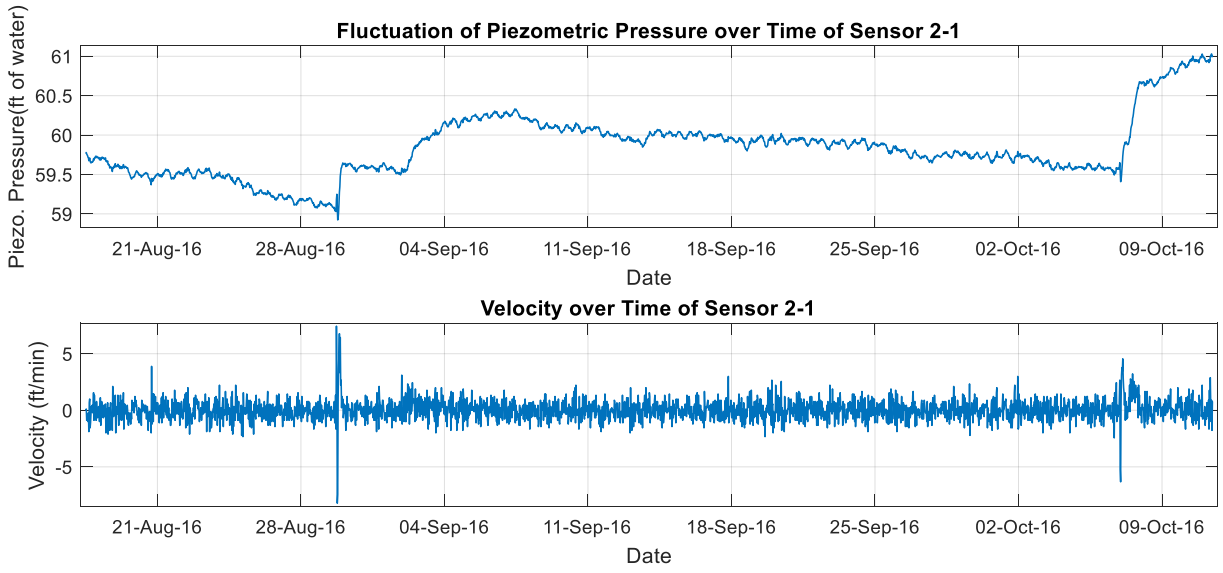

Figure 64: Fluctuation of piezometric pressure and velocity over time of Sensor 2-1

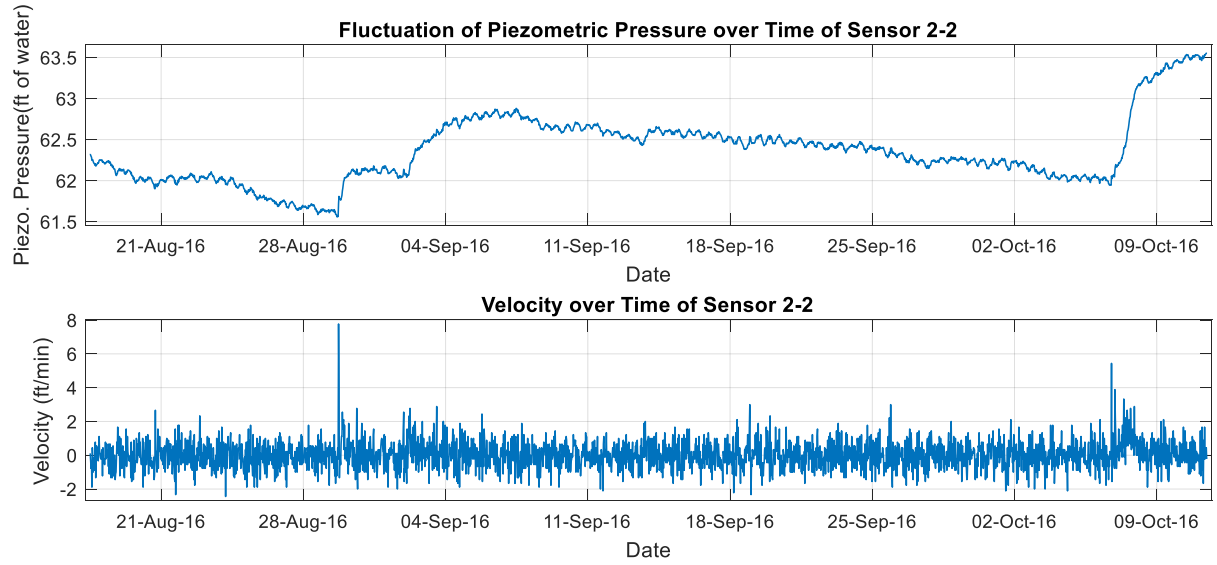

Figure 65: Fluctuation of piezometric pressure and velocity over time of Sensor 2-2

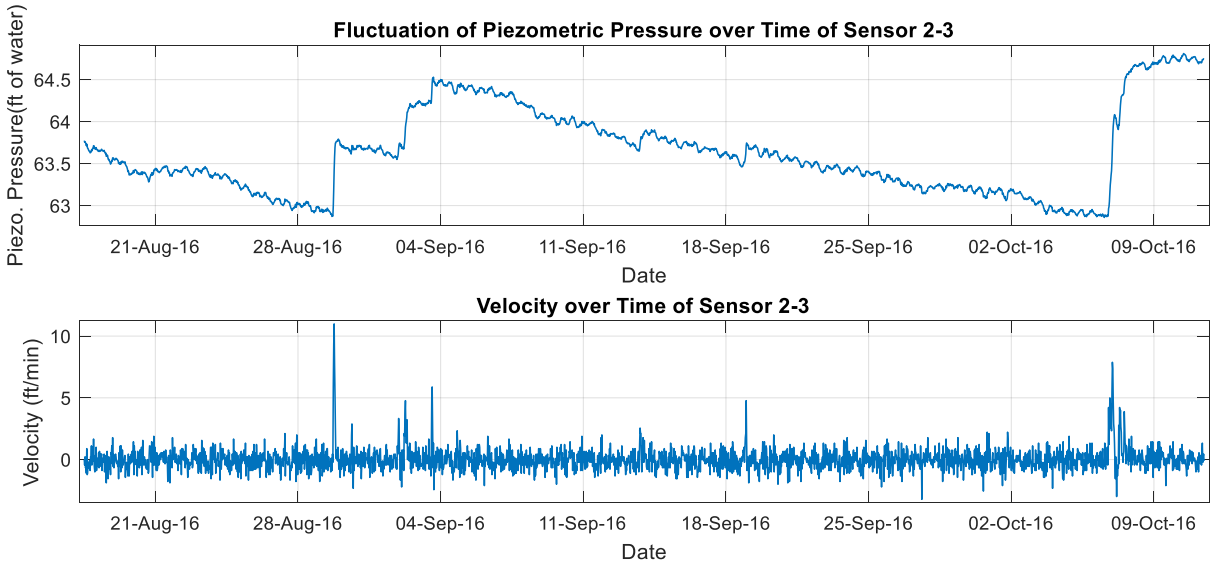

Figure 66: Fluctuation of piezometric pressure and velocity over time of Sensor 2-3

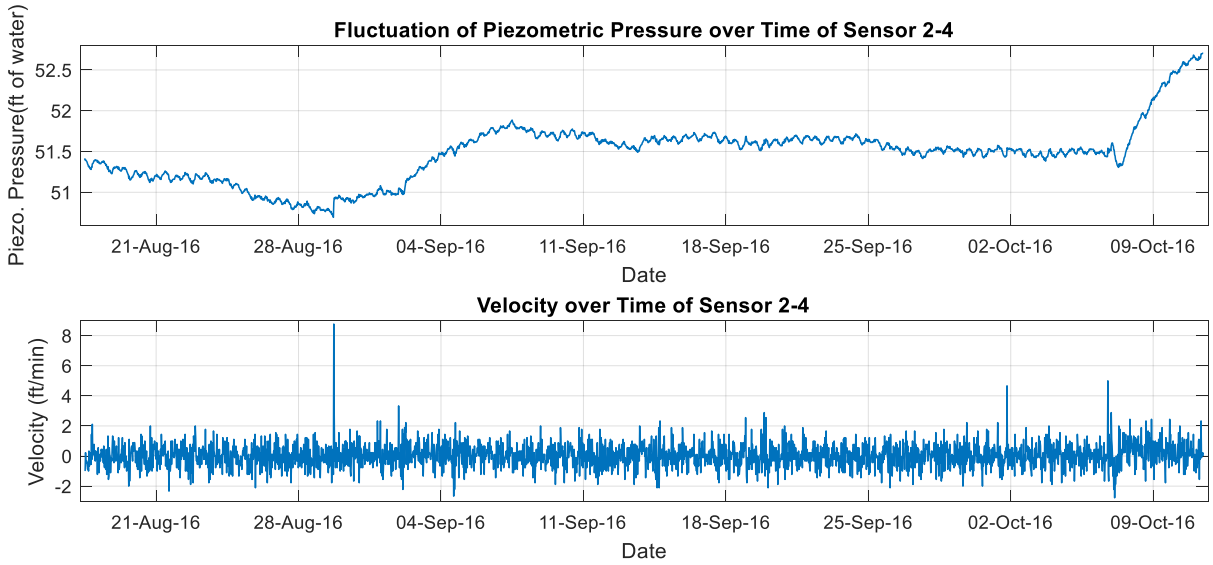

Figure 67: Fluctuation of piezometric pressure and velocity over time of Sensor 2-4

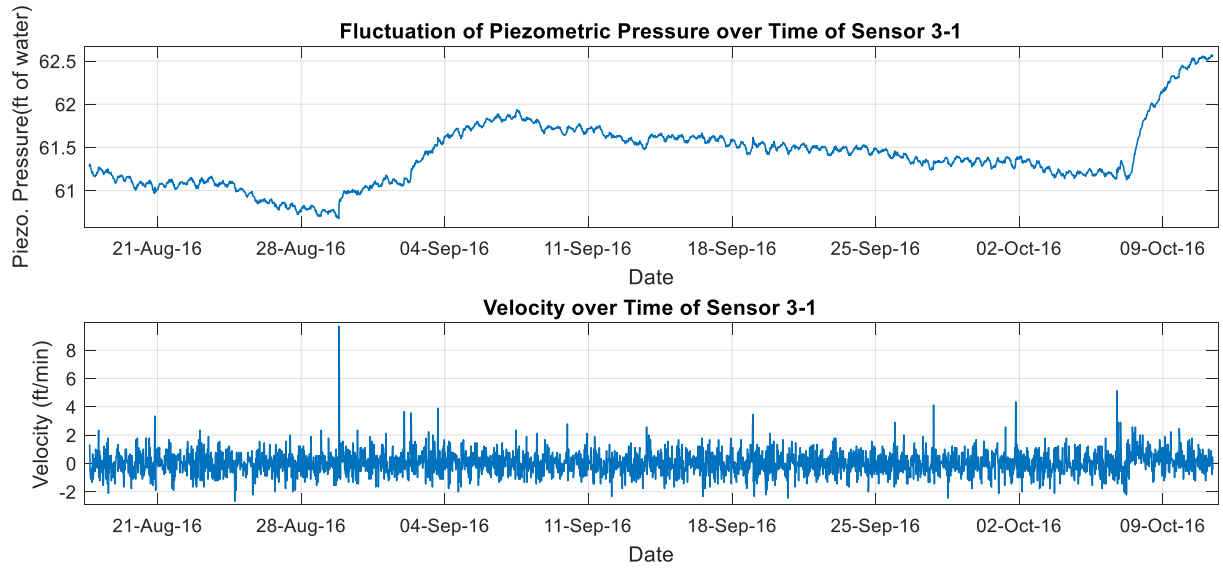

Figure 68: Fluctuation of piezometric pressure and velocity over time of Sensor 3-1

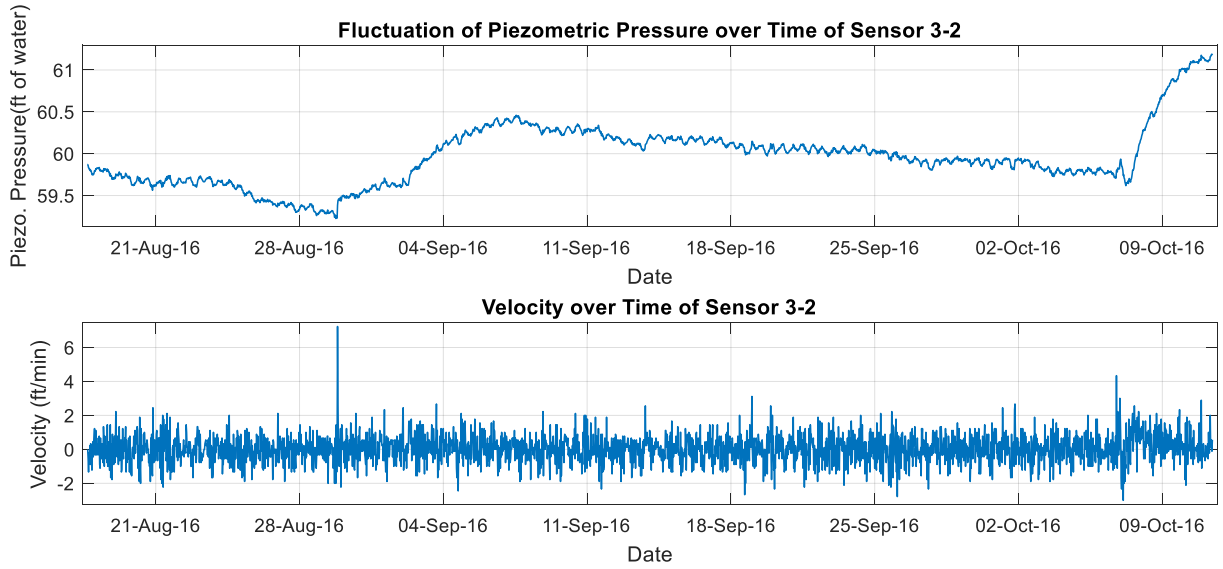

Figure 69: Fluctuation of piezometric pressure and velocity over time of Sensor 3-2

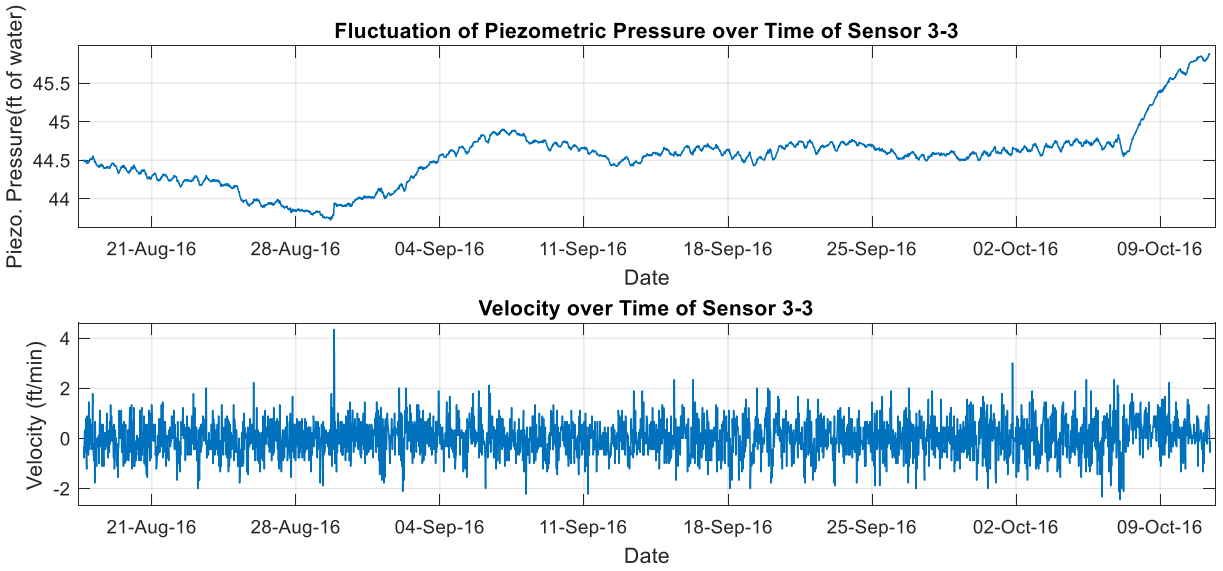

Figure 70: Fluctuation of piezometric pressure and velocity over time of Sensor 3-3

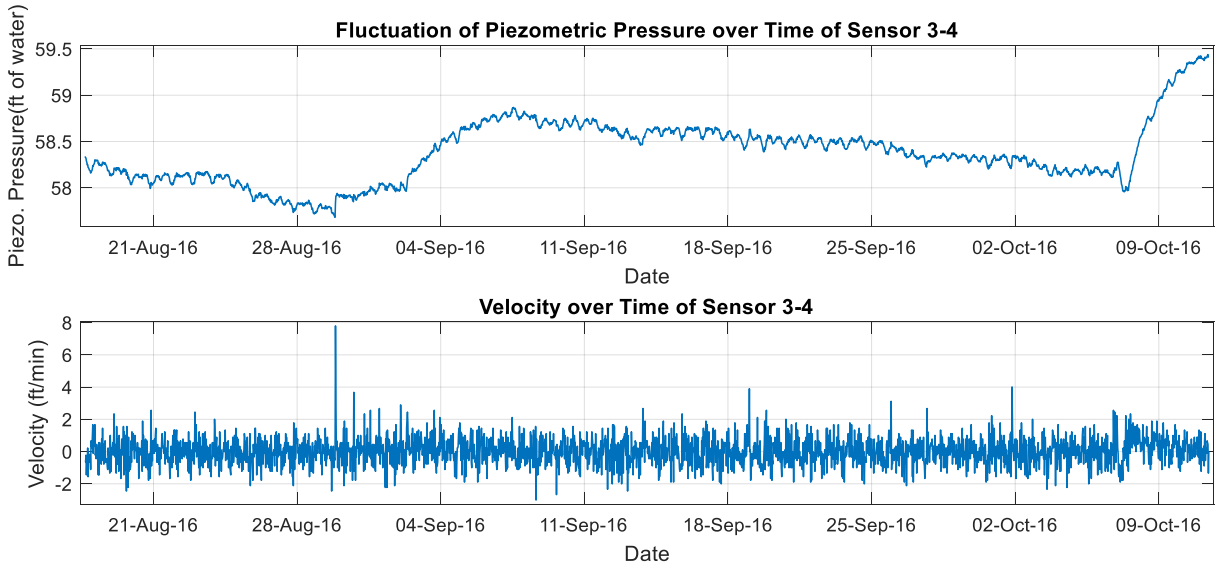

Figure 71: Fluctuation of piezometric pressure and velocity over time of Sensor 3-4

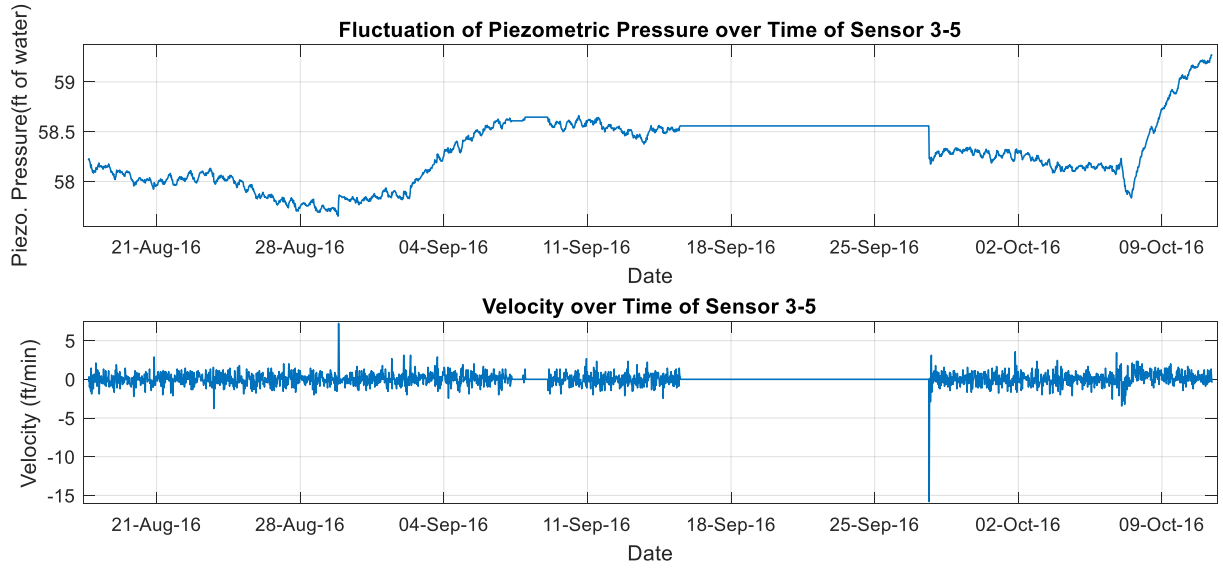

Figure 72: Fluctuation of piezometric pressure and velocity over time of Sensor 3-5

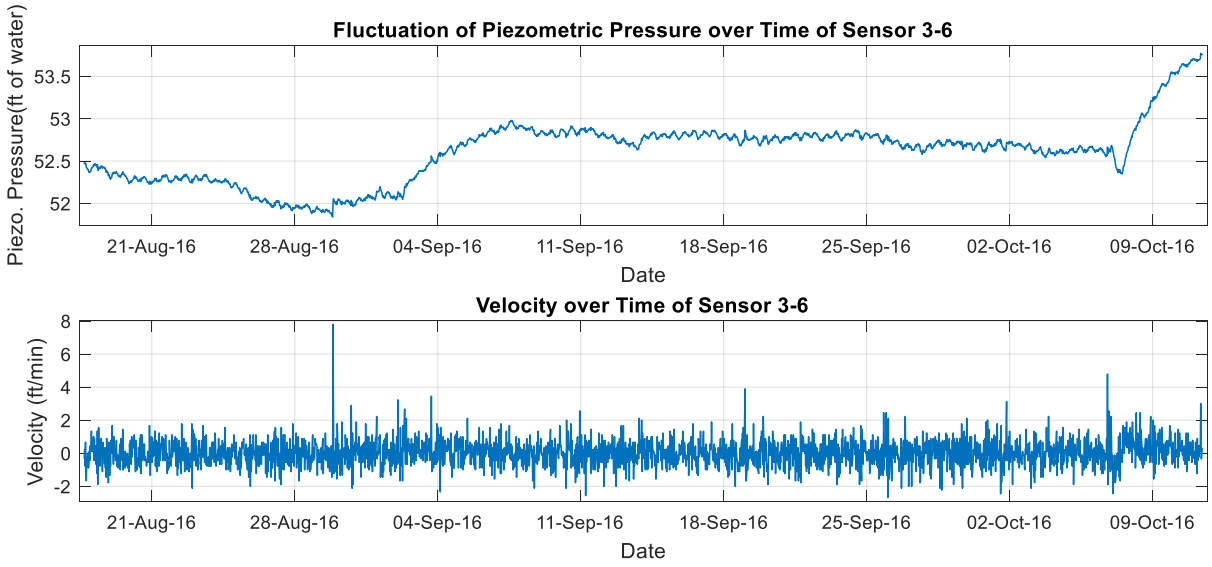

Figure 73: Fluctuation of piezometric pressure and velocity over time of Sensor 3-6

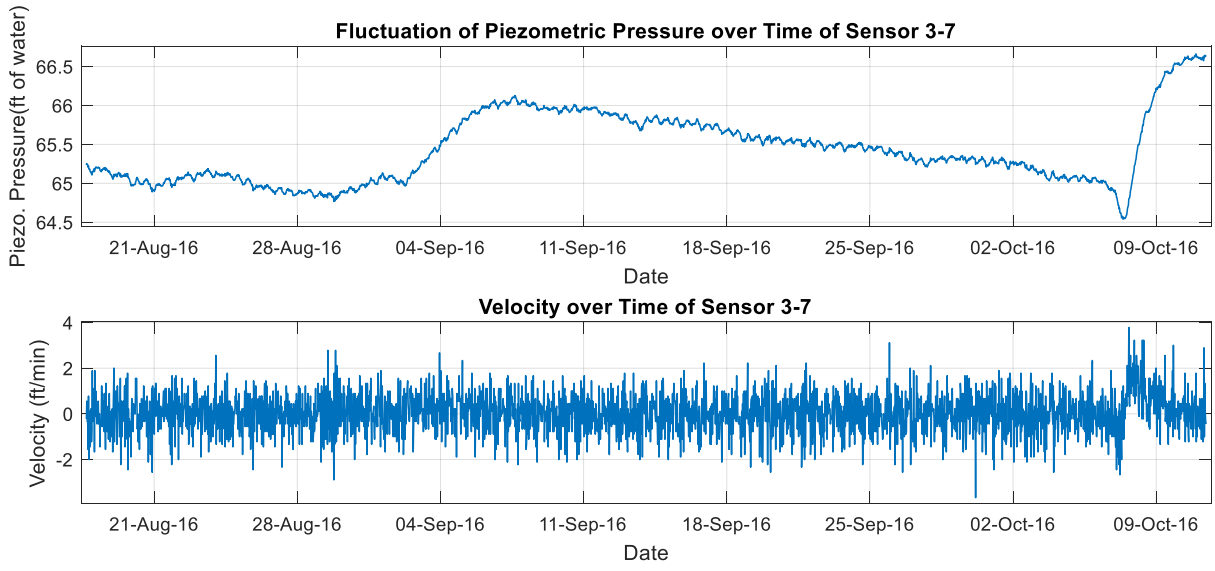

Figure 74: Fluctuation of piezometric pressure and velocity over time of Sensor 3-7

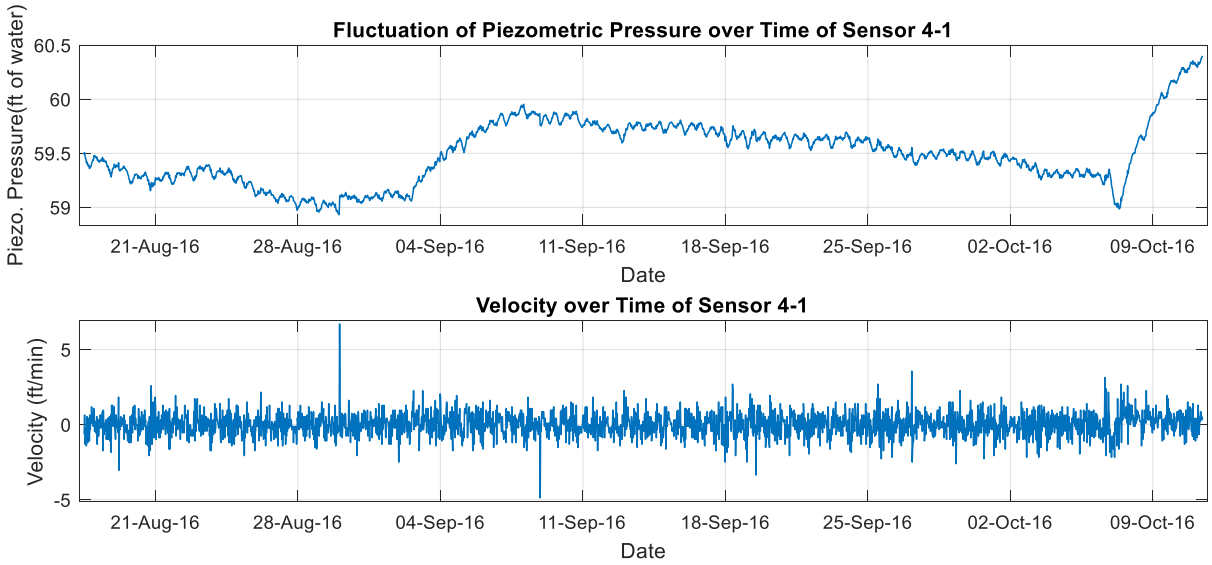

Figure 75: Fluctuation of piezometric pressure and velocity over time of Sensor 4-1

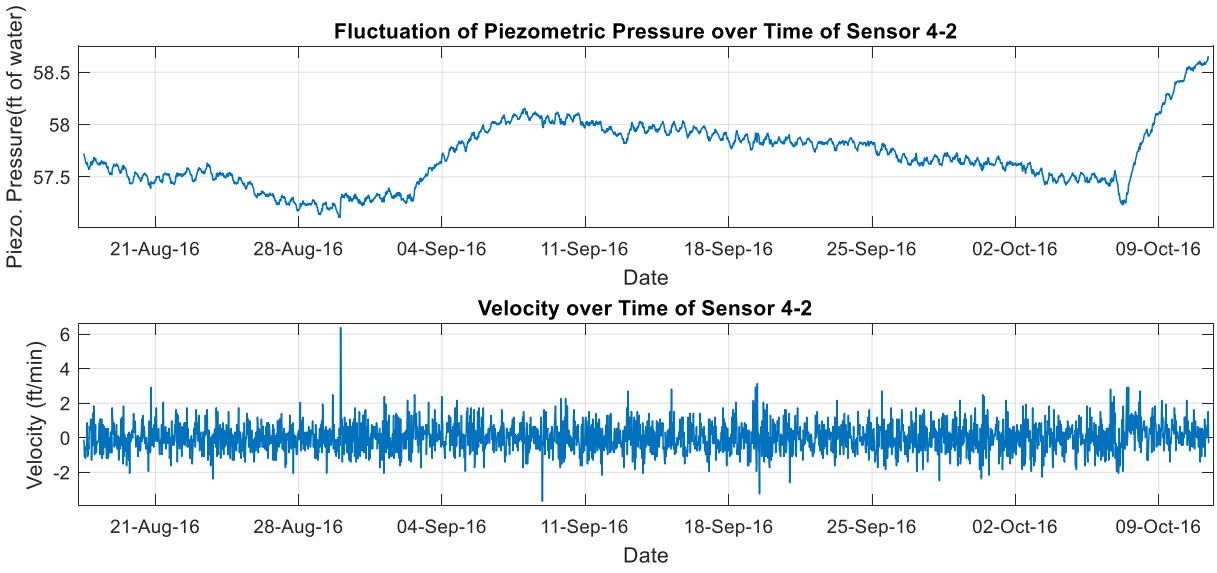

Figure 76: Fluctuation of piezometric pressure and velocity over time of Sensor 4-2

Table 9: Summary of Mean Piezometric Elevations for Periods of 8/28/2016 – 8/29/2016 and 9/7/2016 – 9/8/2016

Zones	Sensor No.	Mean piezometric elevations between 8/28-08/29 (ft)	Mean piezometric elevations between 9/7-9/8 (ft)	Change in piezometric elevations (ft)
1	1-1	51.254	52.322	1.067
	1-2	51.746	52.843	1.097
	1-3	51.087	52.130	1.043
	1-4	59.220	60.317	1.097
	1-5	63.966	65.068	1.102
	1-6	61.997	63.075	1.078
	1-7	55.042	56.093	1.051
2	2-1	59.144	60.252	1.108
	2-2	61.657	62.800	1.143
	2-3	62.983	64.279	1.296
	2-4	50.822	51.815	0.993
3	3-1	60.767	61.850	1.083
	3-2	59.341	60.403	1.062
	3-3	43.838	44.857	1.020
	3-4	57.805	58.803	0.998
	3-5	57.758	58.615	0.857
	3-6	51.948	52.920	0.972
	3-7	64.869	66.049	1.180
4	4-1	59.043	59.883	0.840
	4-2	57.220	58.086	0.867

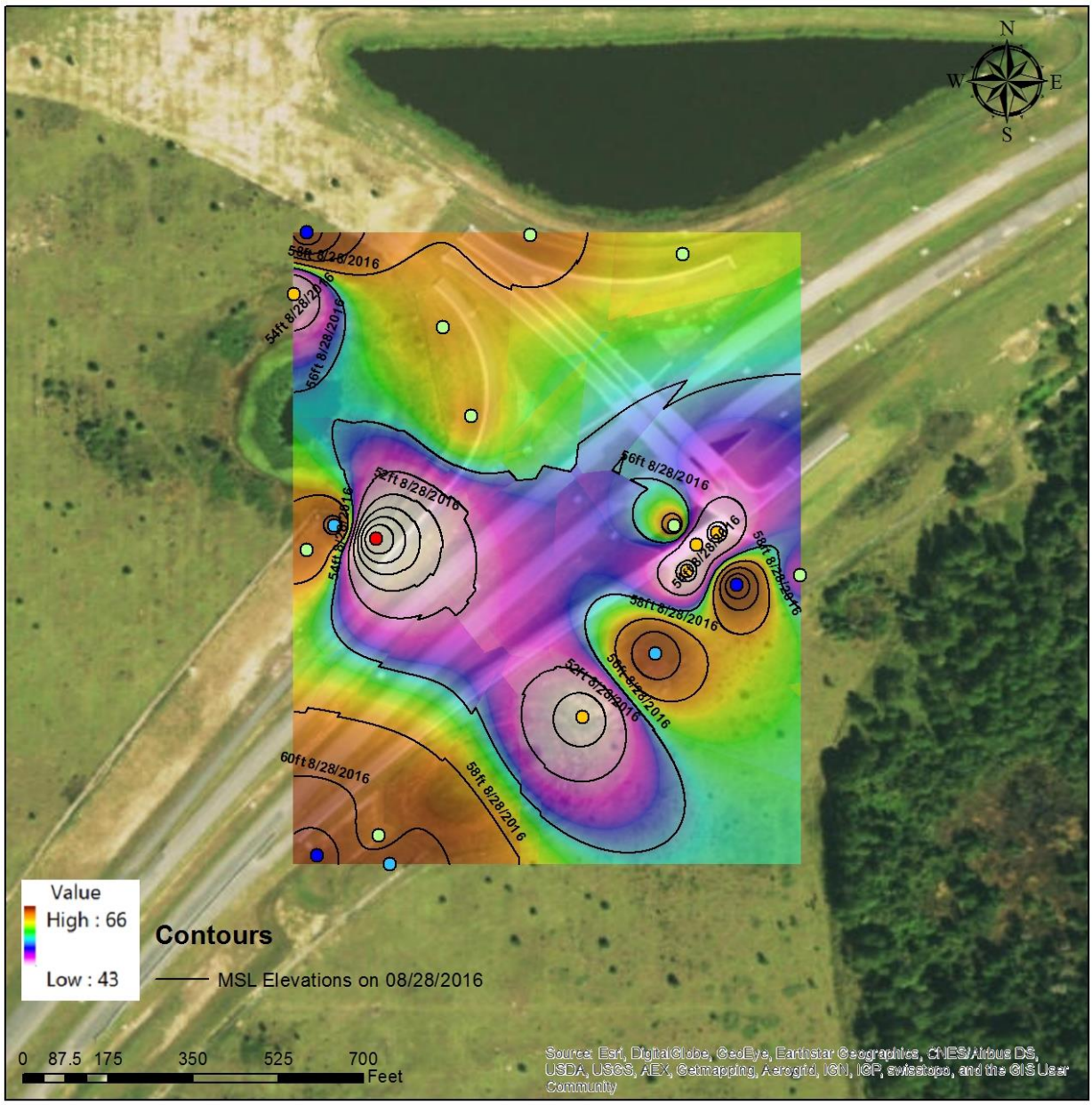

Figure 77: Contours of mean piezometric pressure between 8/28/2016 – 8/29/2016 (Low piezometric pressure)

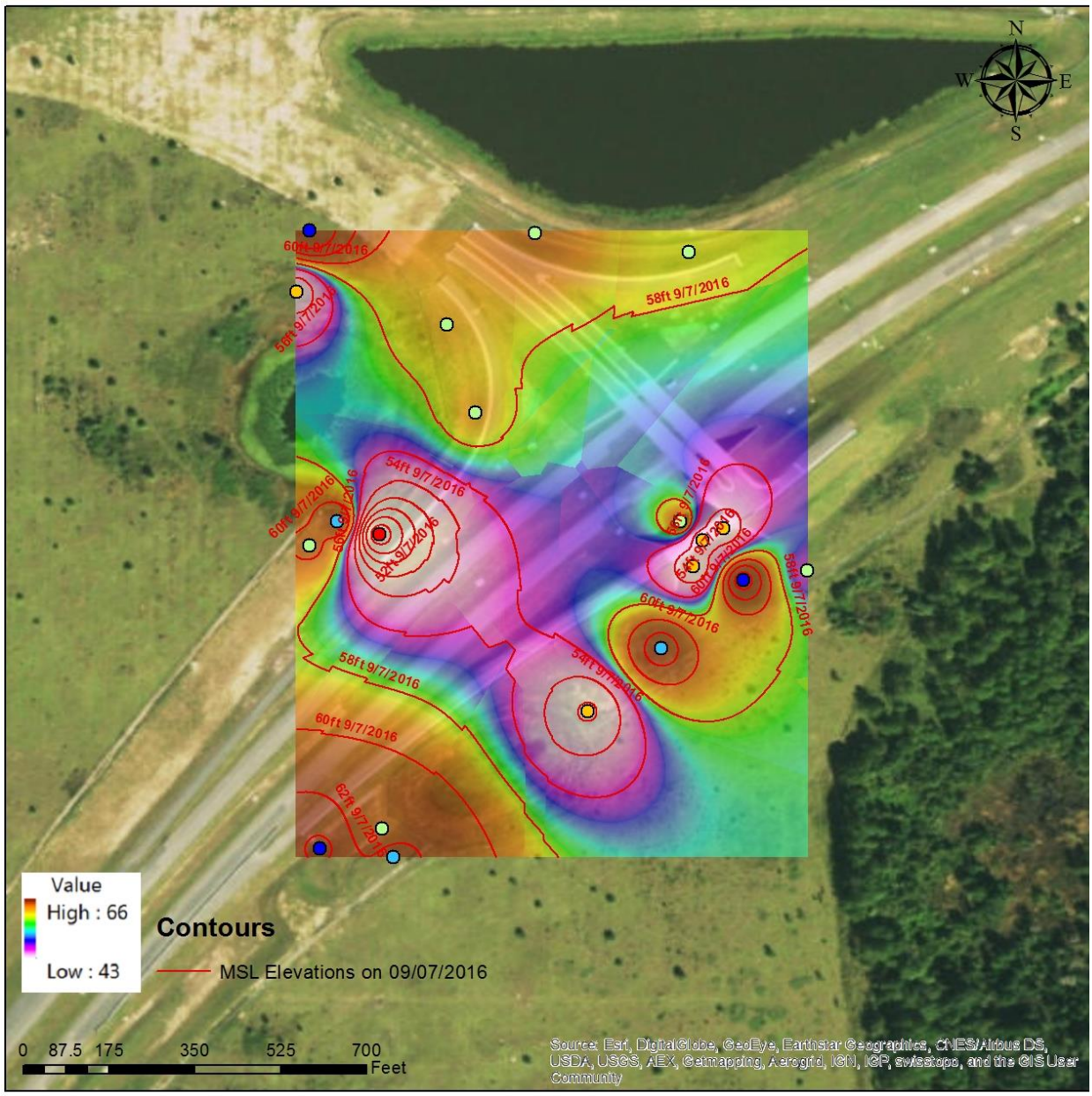

Figure 78: Contours of mean piezometric pressure between 9/7/2016 – 9/8/2016 (High piezometric pressure)

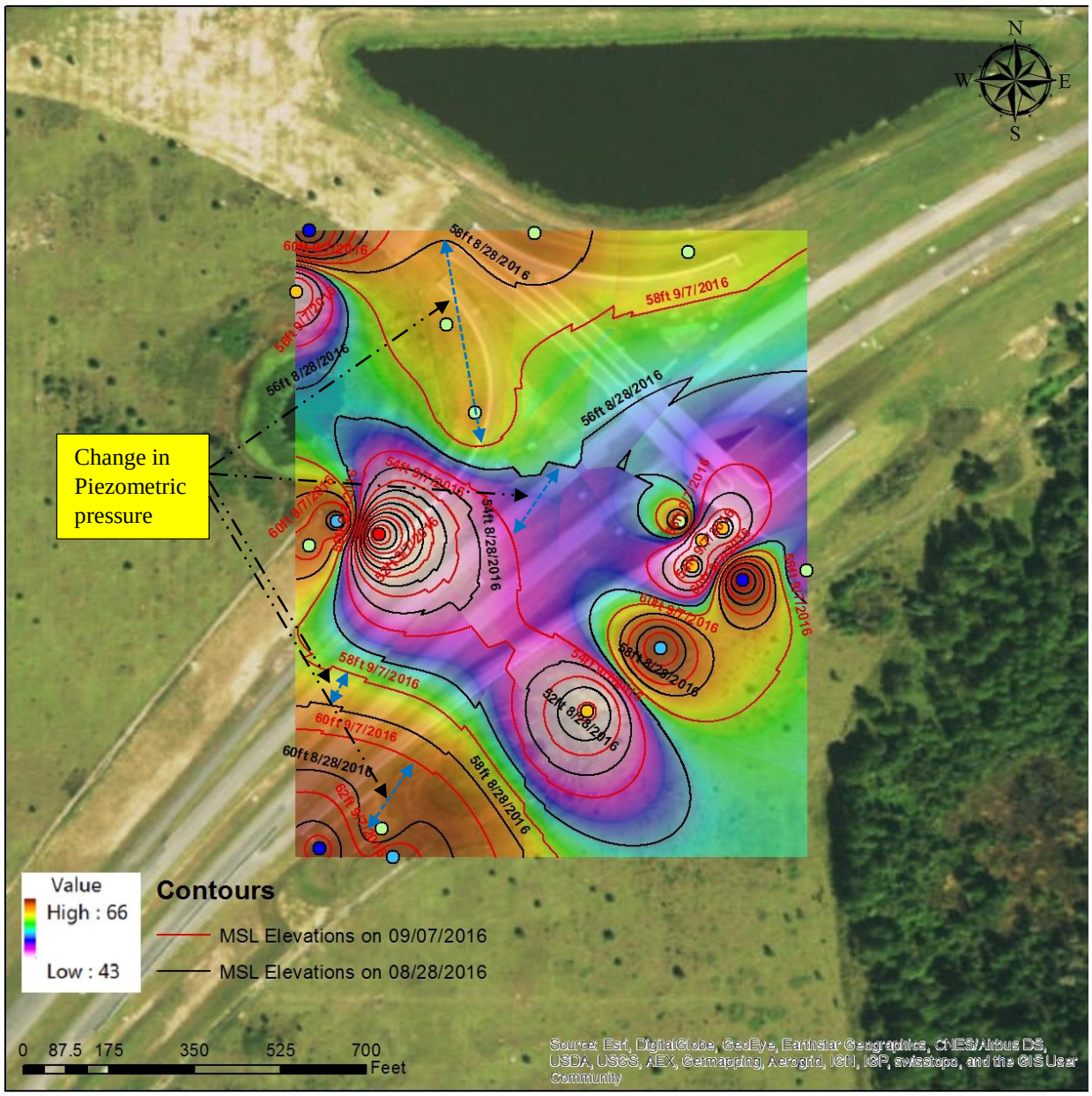

Figure 79: Comparison between low and high piezometric pressure data sets

CHAPTER 5: SUMMARY AND CONCLUSIONS

5.1 Summary and Conclusions

As discussed in the previous chapters, the work presented in this thesis is aimed to use piezometer sensors to monitor groundwater as well as locate points of water breaches. In order to prepare for the field test, 24-tests were performed in the lab. The first 12 tests used soil thickness (h) of 150 mm, and the other 12 tests used soil thickness (h) of 200 mm. In each soil thickness, three tests for each groundwater table level, which was to 0.1h, 0.15h, 0.2h, and 0.30h, were performed. The hypothesis of this study was that sinkhole and fluctuation of ground water table have spatial – temporal relationships. Peak count analysis showed that at the same time sensors closer to the predetermine sinkhole had more peaks than those further away. The result also confirmed that more peaks were appeared during the sinkhole formation stage. Curve fitting method was used to fit all peak count data sets to produce surface plots. Peak count results from all tests can be fit by the following exponential equation. $f(x,y) = A \cdot exp(B \cdot x + C \cdot y) + A$ where A is magnitude of the peaks, B is slope in the x direction or normalized distance, and C is slope in the y axis or time domain. With the R-square ranged from 0.94 to 0.97, this exponential equation was a good representation for given data sets in scaled model. Results from scaled model in chapter 3 have proved the correctness of the hypothesis.

In a research project between University of Central Florida (UCF) and Florida Department of Transportation, two sites were selected based on its historic sinkhole activities. The first site located near the intersection of State Road 429 and State Road 46 in Lake county, Florida while the second site located in FDOT's retention pond in Newberry, Florida. This thesis only presented

works of the site which located in near State Road 429 and State Road 26 Interchange. Twenty piezometric sensors made by Geokon were installed to monitor piezometric elevations. Sensors were intended to install into raveled zones. In order to identify exact depths of the raveled zones for each location, Twenty CPT soundings were performed at the locations of proposed sensors as shown in Appendix B. Sensors were divided into 4 zones, 7 sensors in zones 1 and 3, 4 sensors in zones 2, and 2 sensors in zone 4. Those sensors were connected to 5-dataloggers and sampled with the frequency of 30 minutes/sample. When compared piezometric fluctuation profiles with precipitations of rainfall evens, it indicated that there were strong correlations between these two data sets. Increases in piezometric elevations were proportional to the magnitudes of precipitations. When it started raining, water needed some time to percolate through soil layers so that sensors could sense the change in ground water levels. As a result, there was delay time between precipitation and fluctuation of groundwater. Fluctuation of groundwater elevations got its peaks after the rainfall events had gotten its maximum precipitations.

Fluctuations of piezometric elevations over time were presented in a series of 2D images using moving average signal processing technique Each frame showed the mean values of one day piezometric data. Frequency between two adjacent frames was set at 4 hours. After all frames had been generated, frames were put into sequence of time to see how water fluctuated over time.

One of the most important results when using piezometer sensor is that points of active breaches can be determined while GPR's results can only indicate points of anomalies. In addition, results from piezometer sensors also agreed with results of GPR. GPR results (P5) indicated a huge point breach with approximate diameter of 120 feet near location of sensor 3-3 (Figure 36). At the same time, sensor 3-3 showed its lowest piezometric elevation among sensors. The low

piezometric elevations were also occurred in sensors 1-1, 1-2 and 1-3 corresponding to GPR's result a long transect 7 (Figure 38). Sensor 2-4 had the second lowest piezometric pressure among 20 sensors, but there was no GPR data at that location (out of GPR survey area). The existence of a point of breach probably located at or near location of sensor 2-4 based on the well matched between the two methods.

5.2 Limitations

Limitations in this study include:

1. Field exploration needs to be done preceding to the installation of sensors
2. Length of field data in this study is short
3. There is no existence of actual data set during a sinkhole even
4. Locations of piezometer sensors may affect the results

5.3 Recommendations for Future Research

The following recommendations could be used for future studies:

1. Sensor 2-4 had the second lowest piezometric pressure among 20 sensors, but it has not confirmed by GPR images. To give better confident on the result of sensor 2-4, GPR survey is recommended.
2. There were total 94 CPT soundings performed by FDOT District 5 and State Materials Office (SMO). However, these data sets have not used to do the analysis other than identifying reveled zone during the sensor installation process. Together, results from CPT, GPR, and piezometer sensor will yield the confidents over the evaluation of sinkhole.
3. Similar to the scaled model, field test could use the same peak count technique as a "sign" to predict a sinkhole even. An actual set of data that occurs during a sinkhole even can be used as a reference to calibrate peak count parameters.

APPENDIX A: SOIL PROFILES OF STANDARD PENETRATION TEST (SPT)

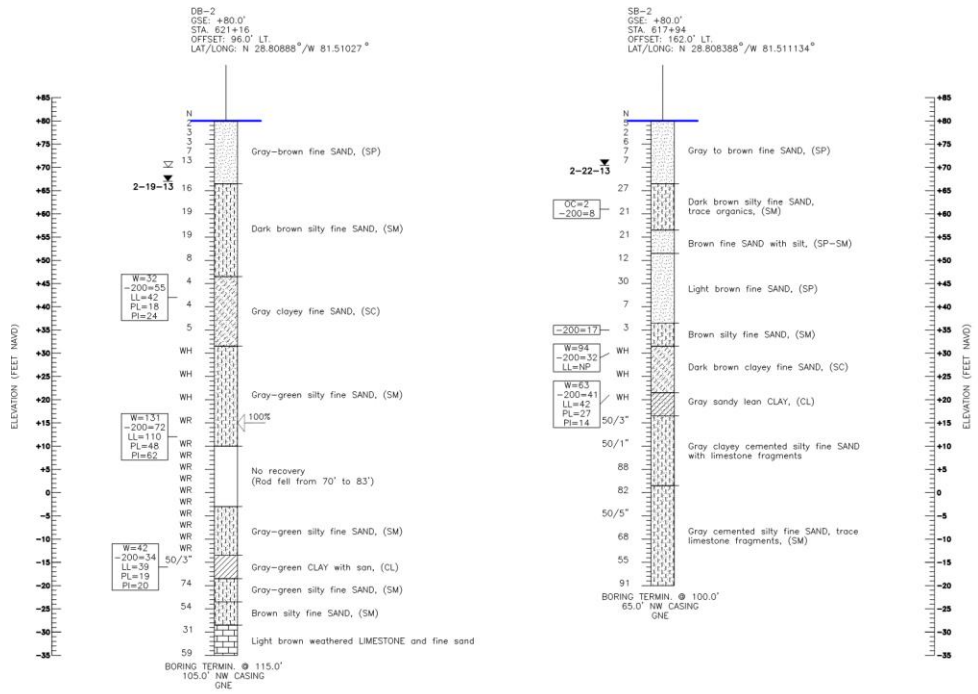

Figure 80: Soil profiles from SPT for boreholes DB -2 and SB-2 (Professional Service Industries (PSI), 2014)

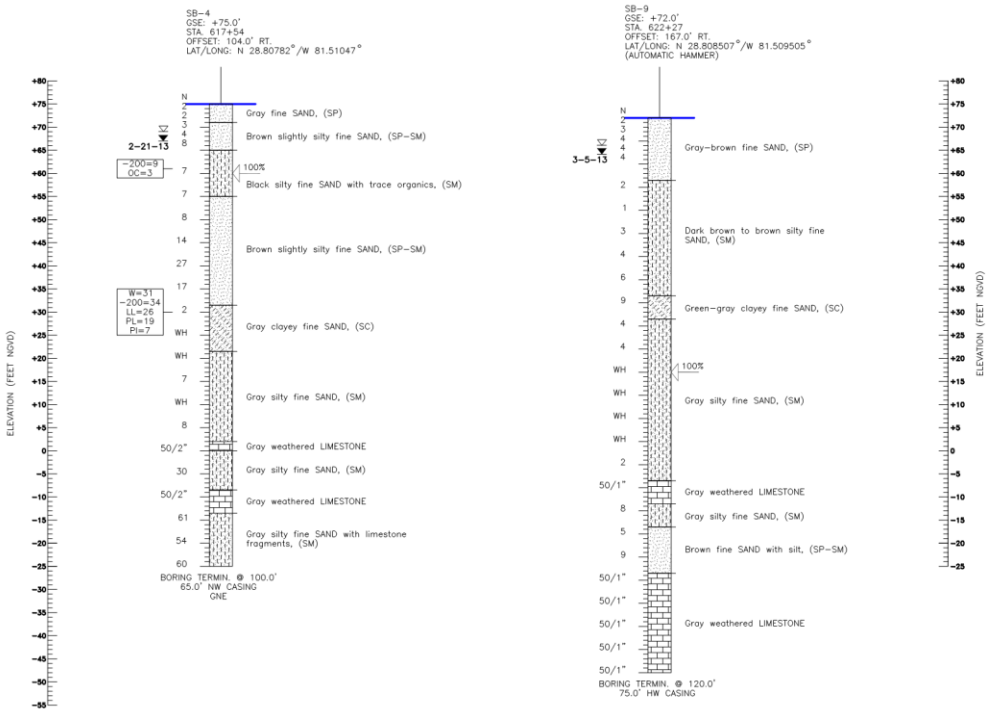

Figure 81: Soil profiles from SPT for boreholes SB -4 and SB-9 (Professional Service Industries (PSI), 2014)

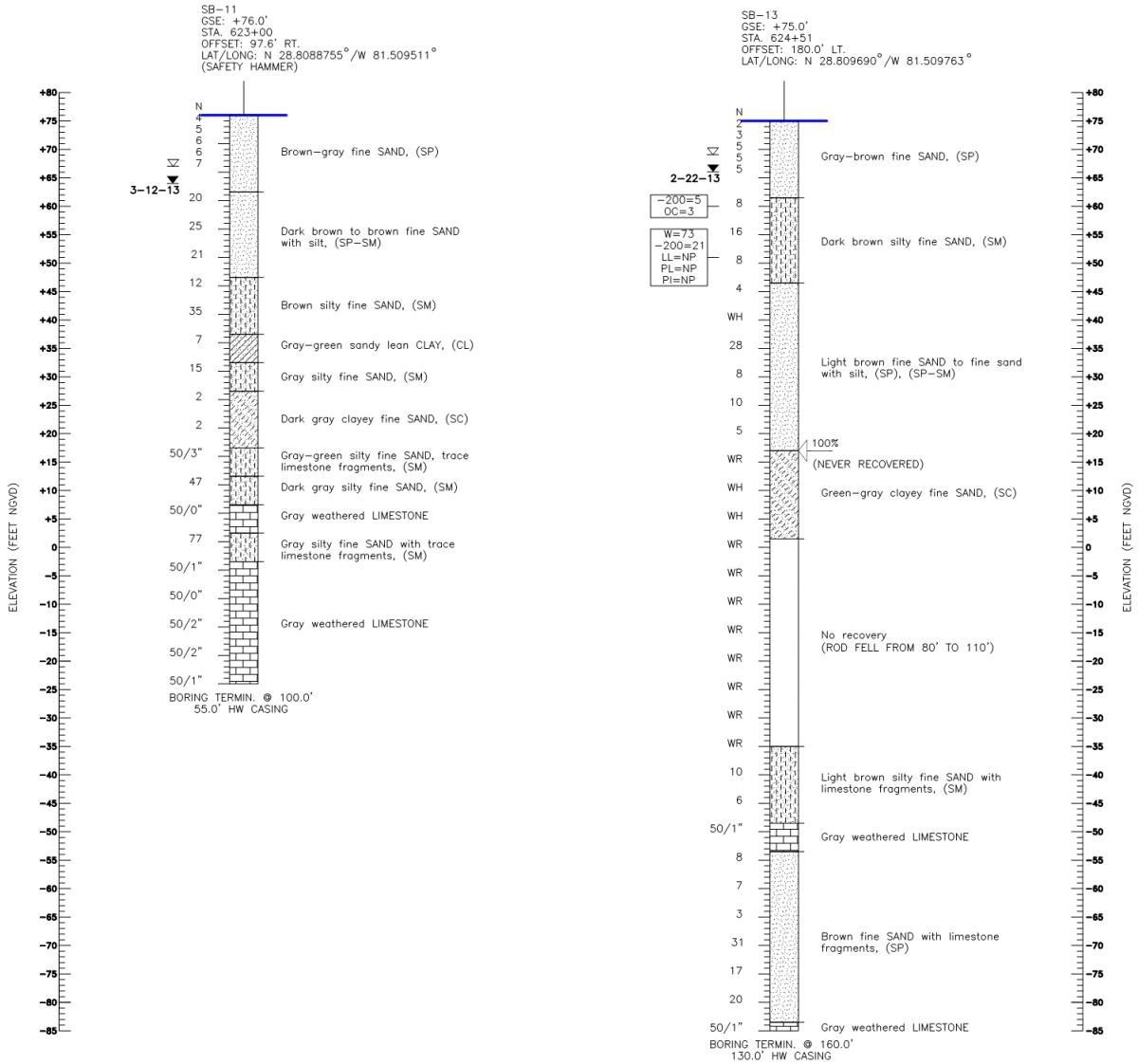

Figure 82: Soil profiles from SPT for boreholes SB -11 and SB-13 (Professional Service Industries (PSI), 2014)

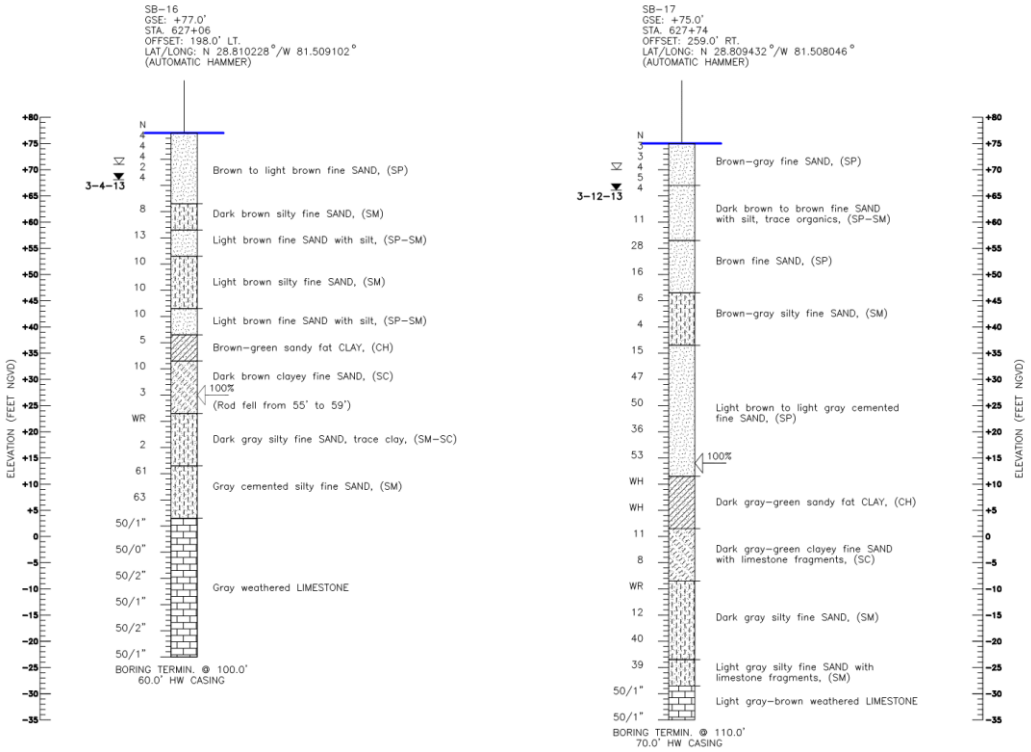

Figure 83: Soil profiles from SPT for boreholes SB -16 and SB-17 (Professional Service Industries (PSI), 2014)

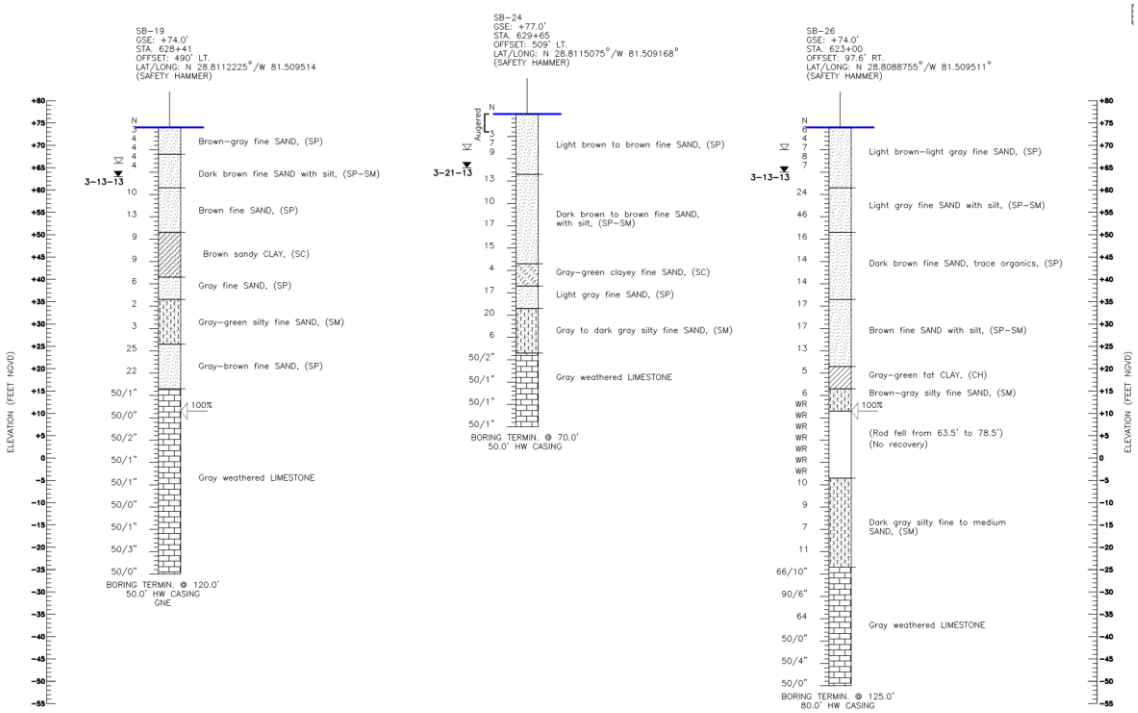

Figure 84: Soil profiles from SPT for boreholes SB -19, SB -24, and SB-26 (Professional Service Industries (PSI), 2014)

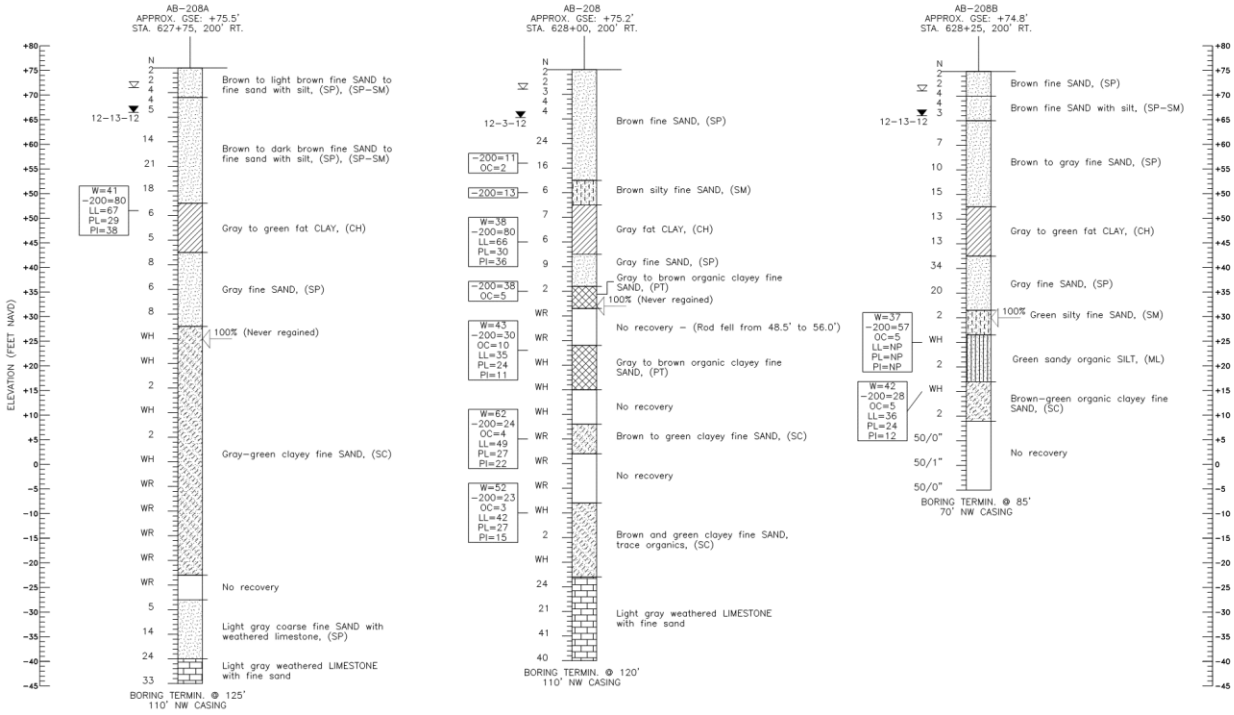

Figure 85: Soil profiles from SPT for boreholes AB-208A, AB-208, and AB-208B (Professional Service Industries (PSI), 2014)

APPENDIX B: RESULTS OF CONE PENETRATION TEST (CPT)

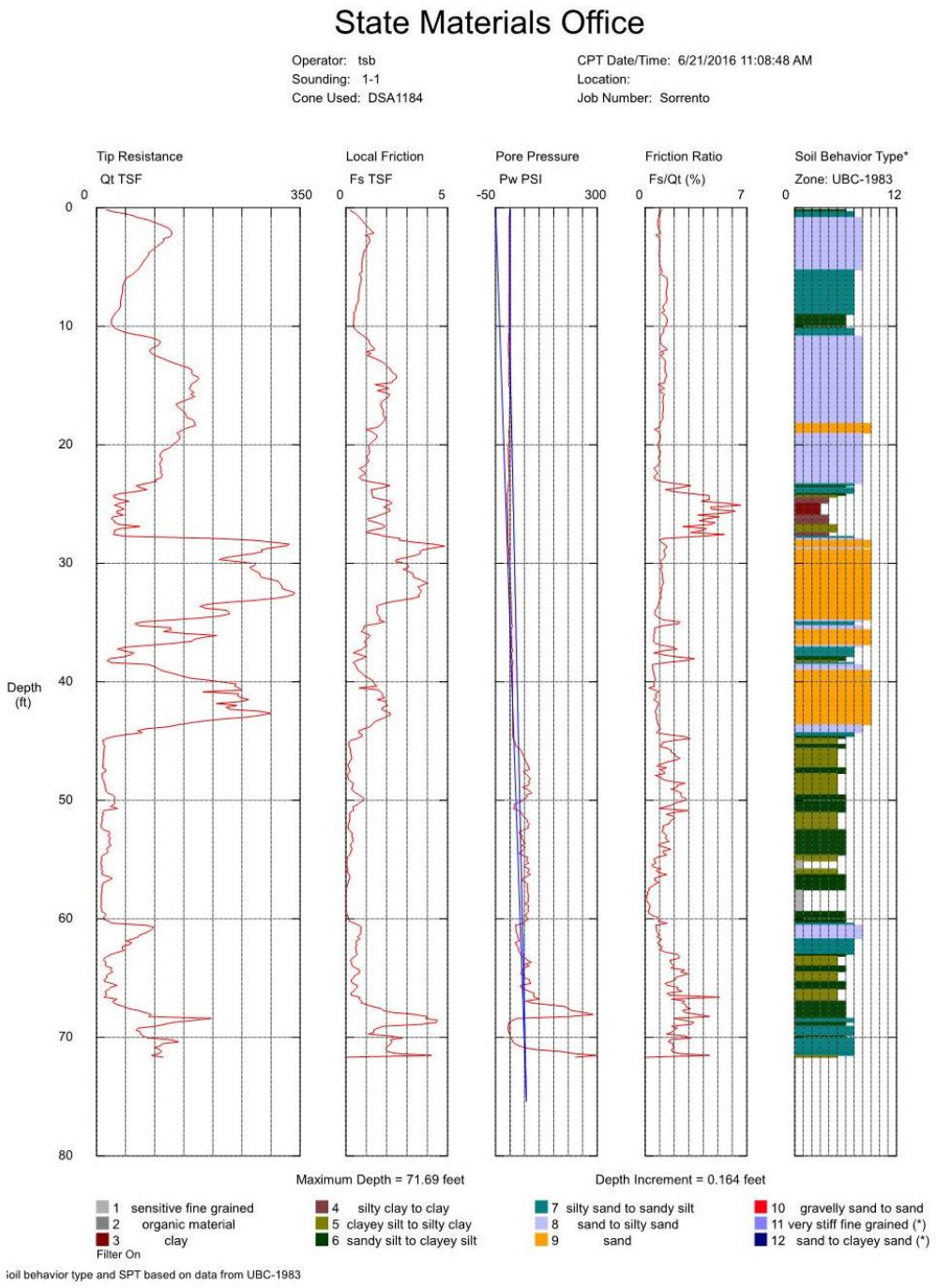

Figure 86: Result of CPT sounding for location of sensor 1-1 performed by Florida State Materials Office

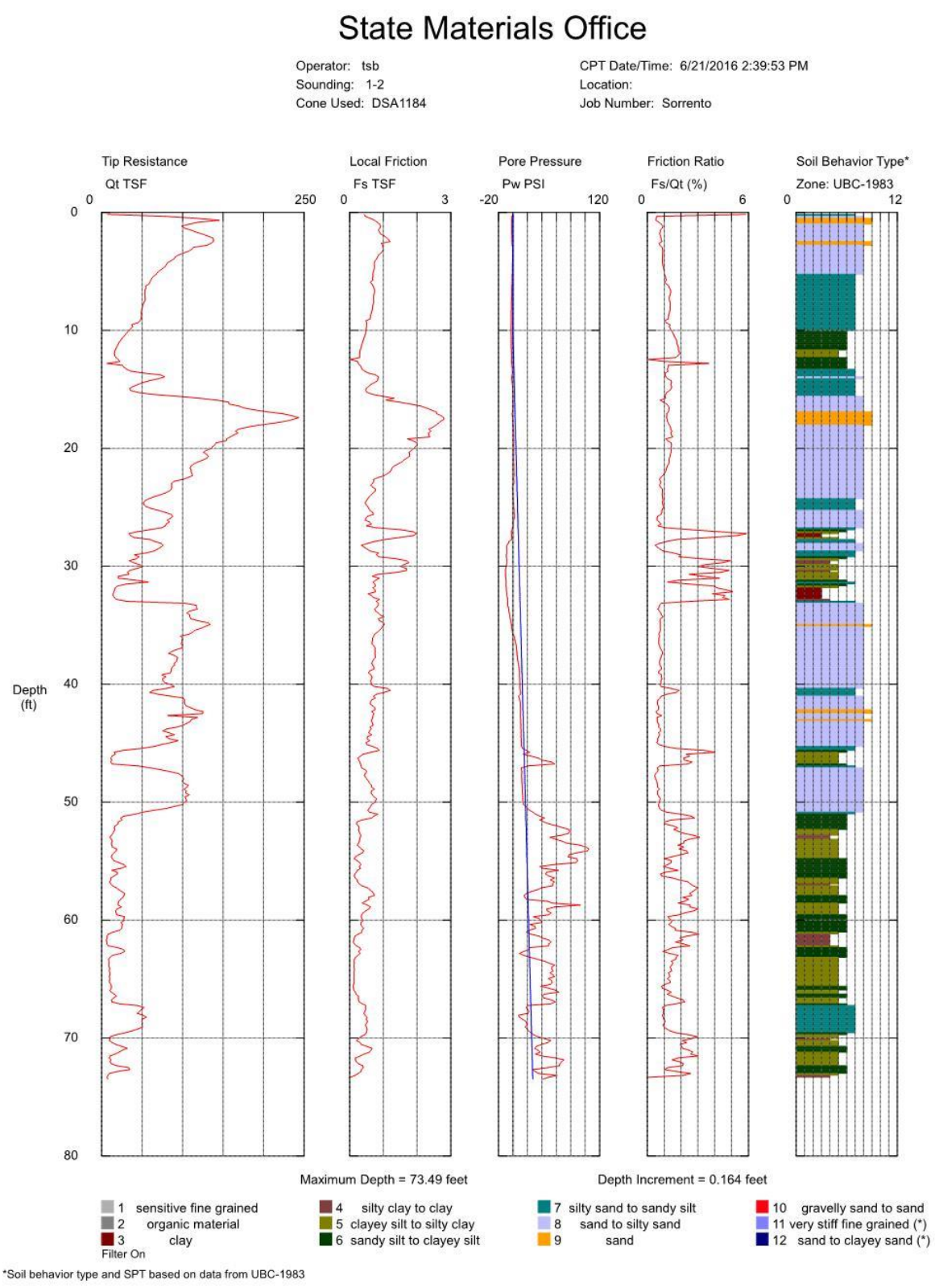

Figure 87: Result of CPT sounding for location of sensor 1-2 performed by Florida State Materials Office

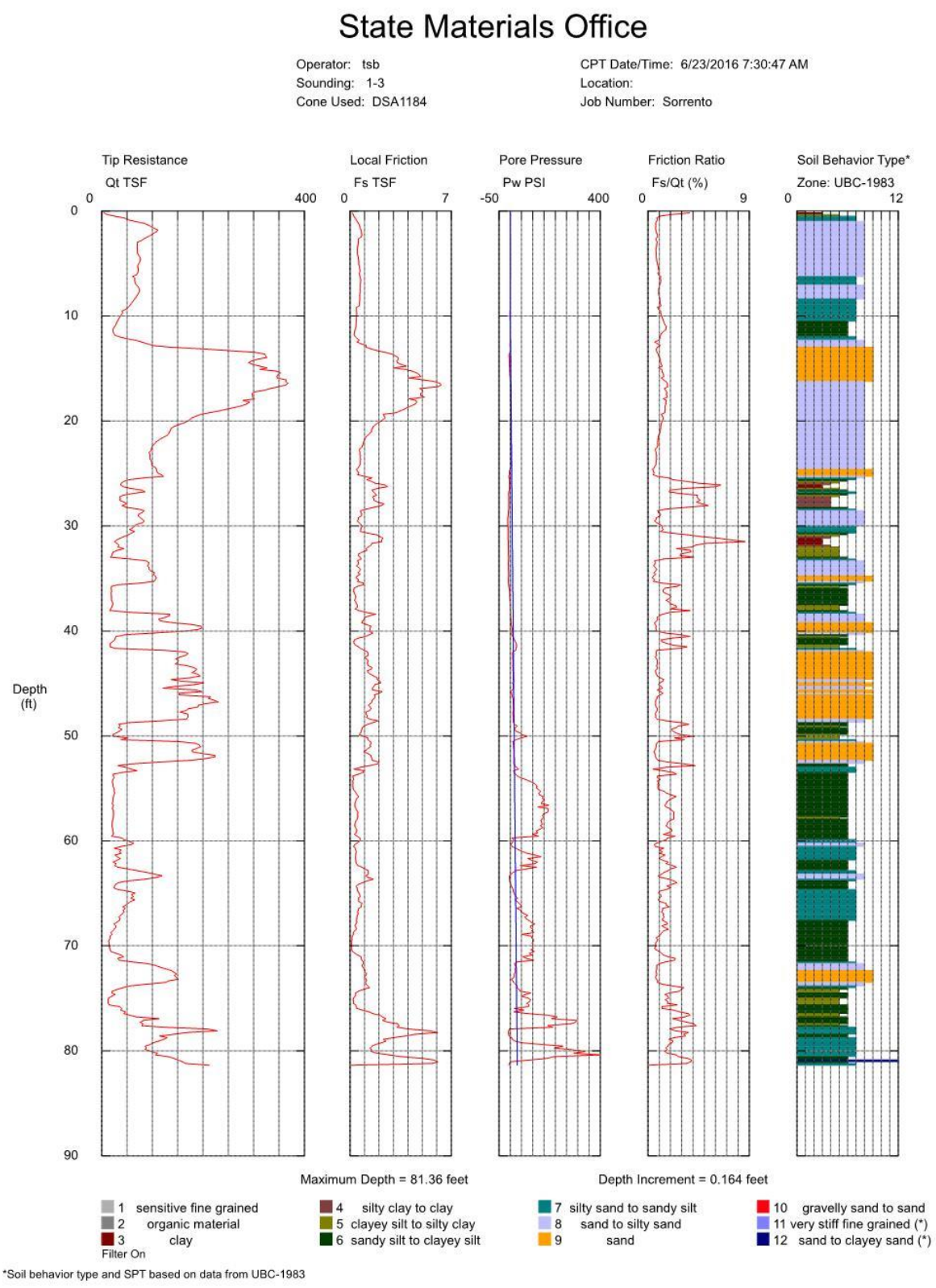

Figure 88: Result of CPT sounding for location of sensor 1-3 performed by Florida State Materials Office

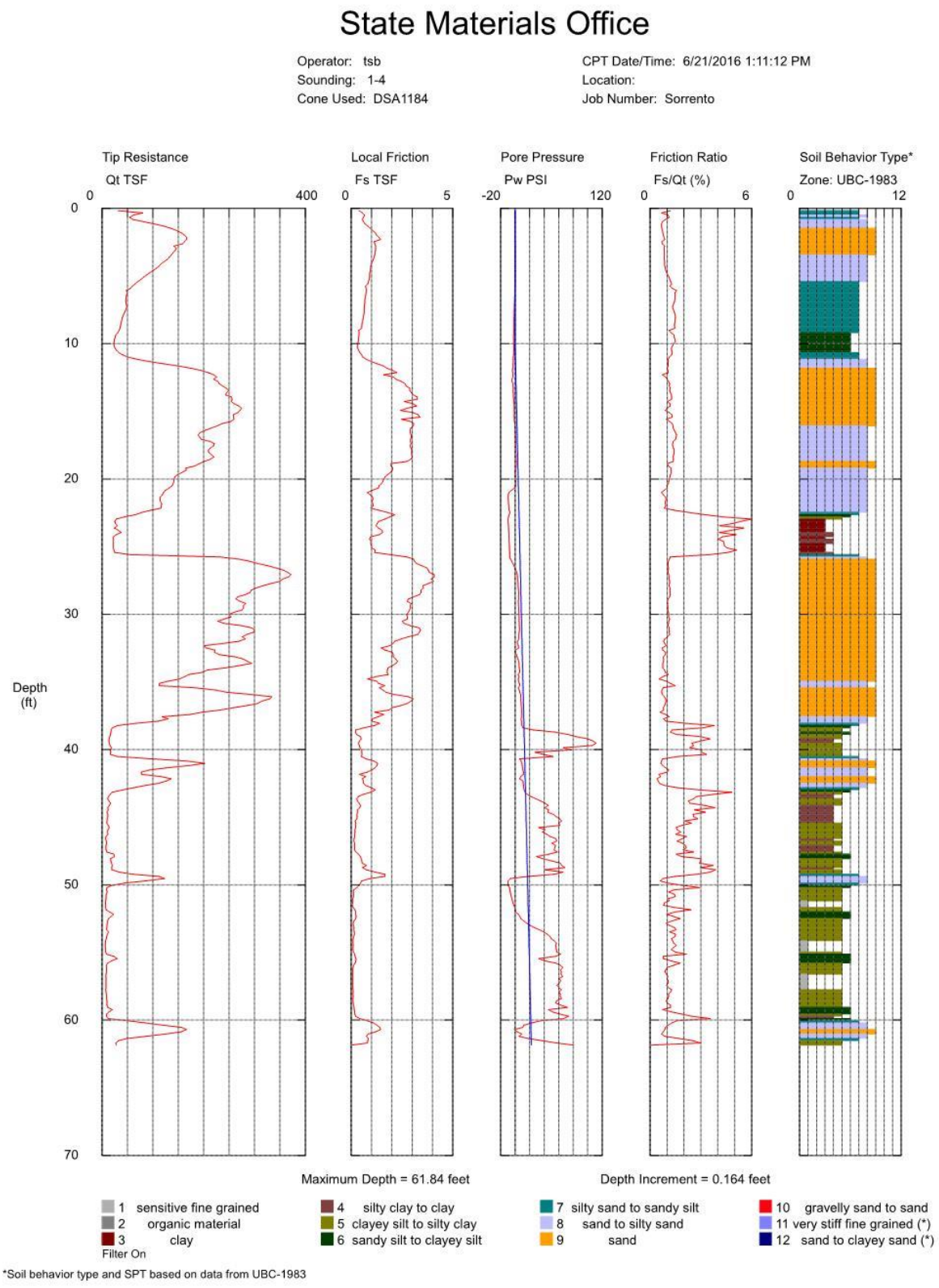

Figure 89: Result of CPT sounding for location of sensor 1-4 performed by Florida State Materials Office

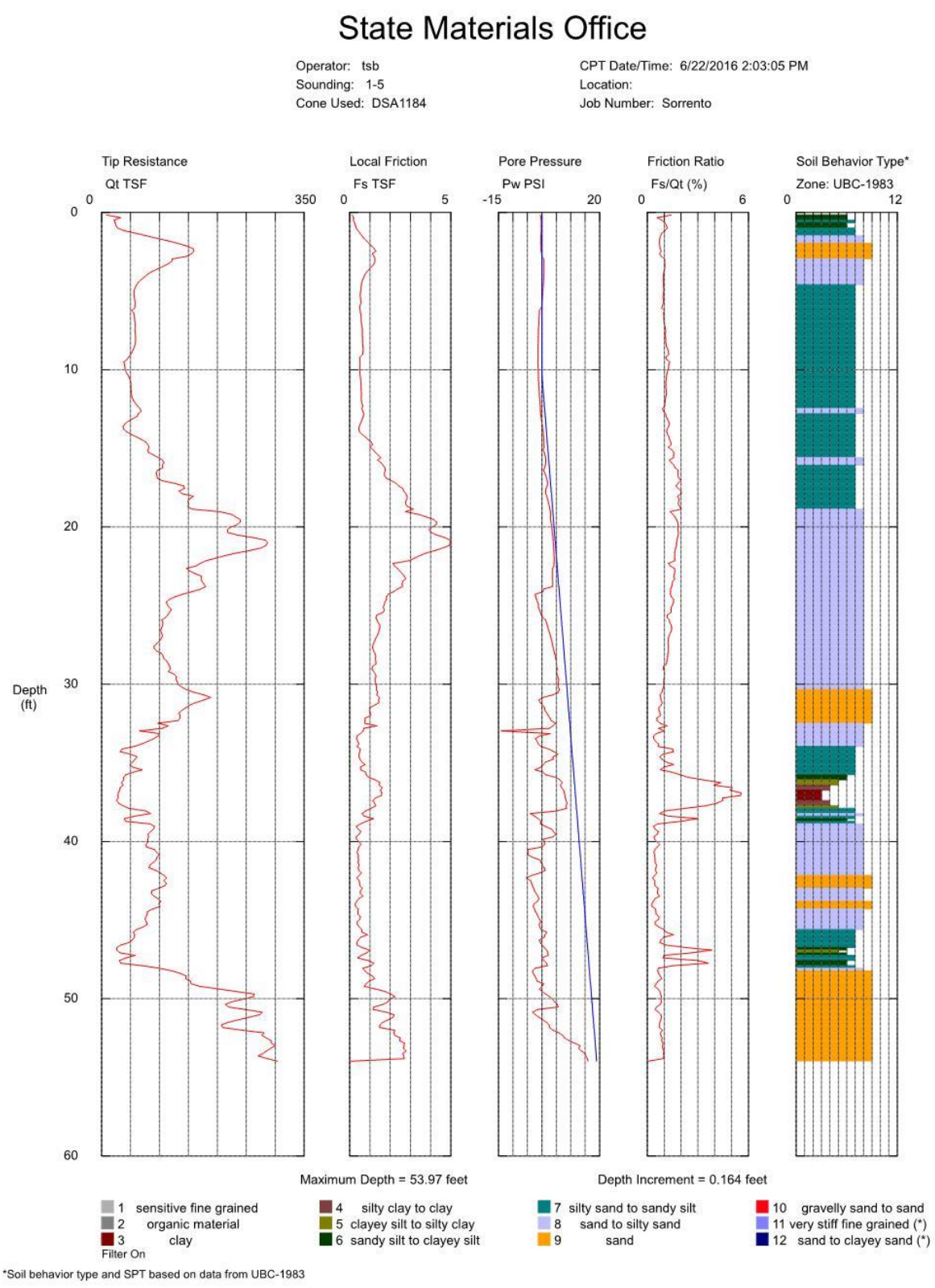

Figure 90: Result of CPT sounding for location of sensor 1-5 performed by Florida State Materials Office

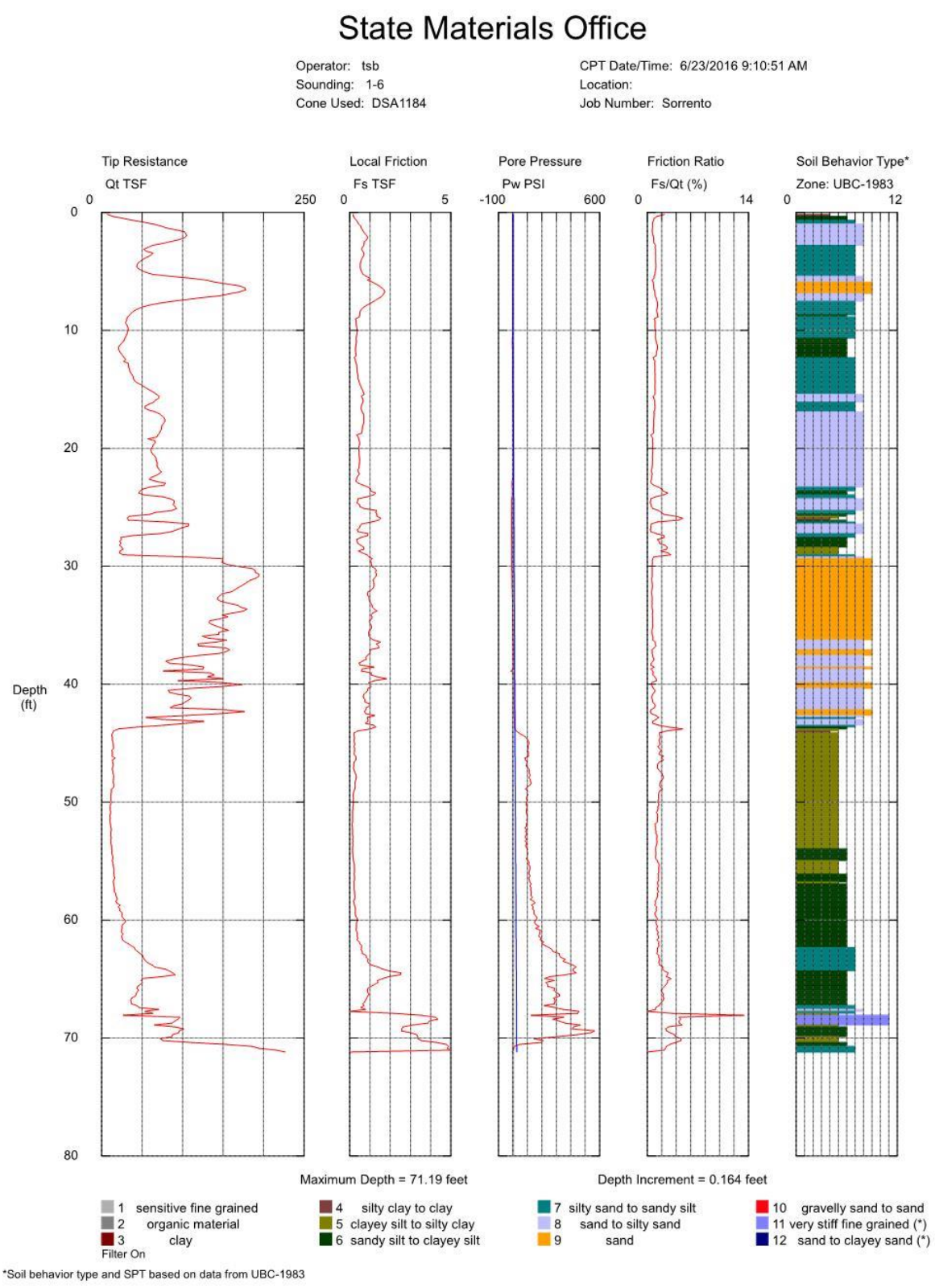

Figure 91: Result of CPT sounding for location of sensor 1-6 performed by Florida State Materials Office

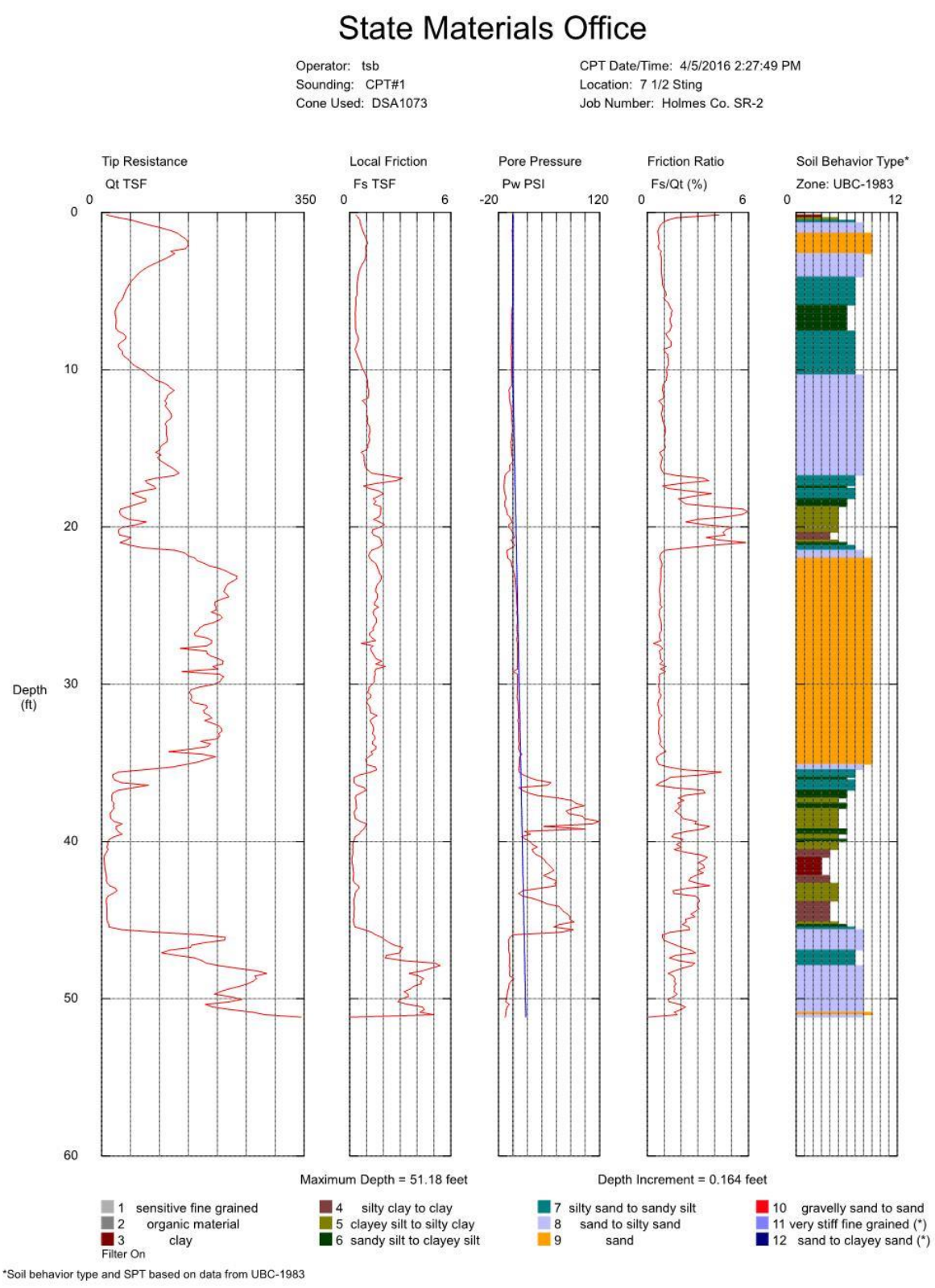

Figure 92: Result of CPT sounding for location of sensor 1-7 performed by Florida State Materials Office

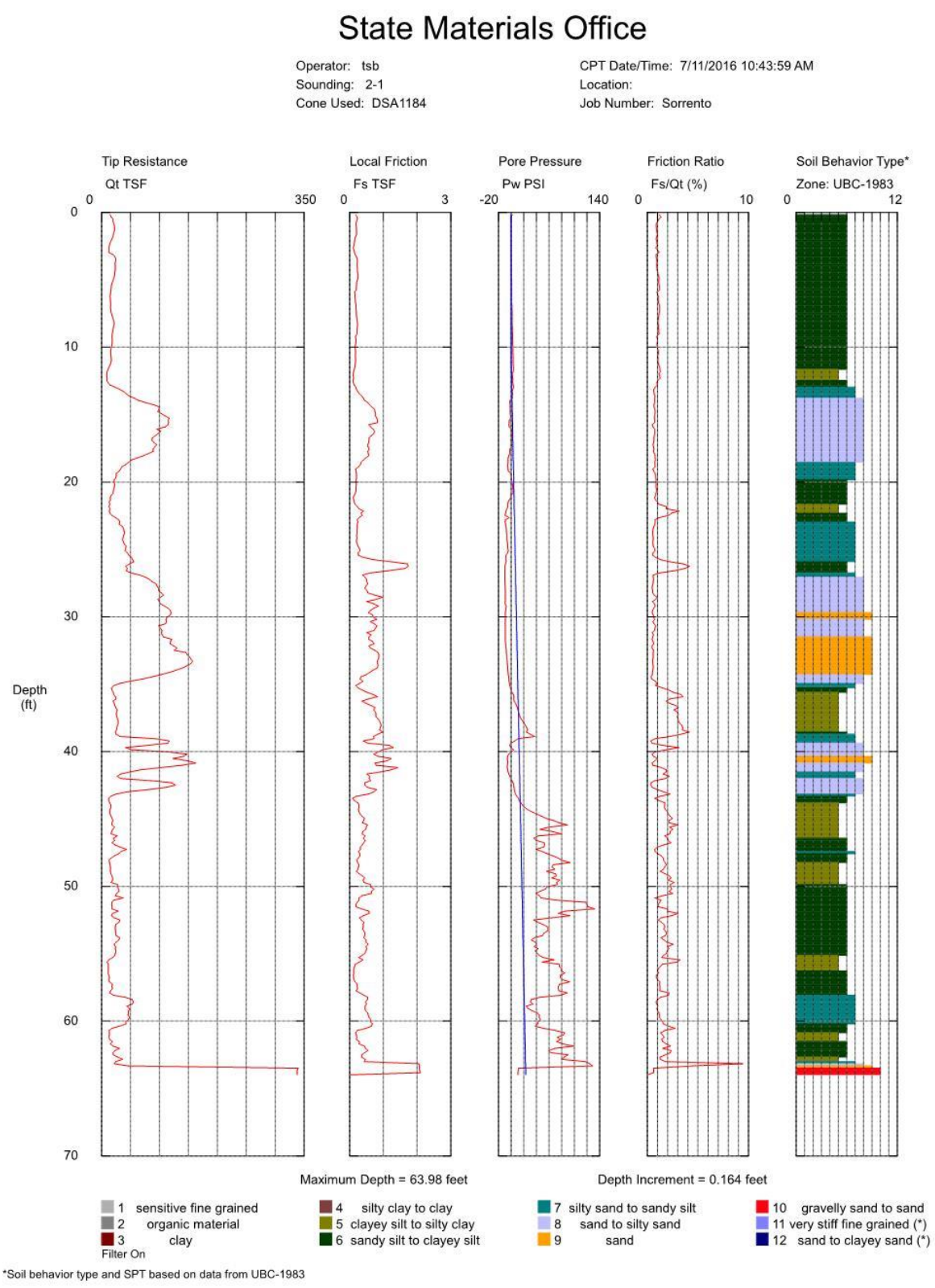

Figure 93: Result of CPT sounding for location of sensor 2-1 performed by Florida State Materials Office

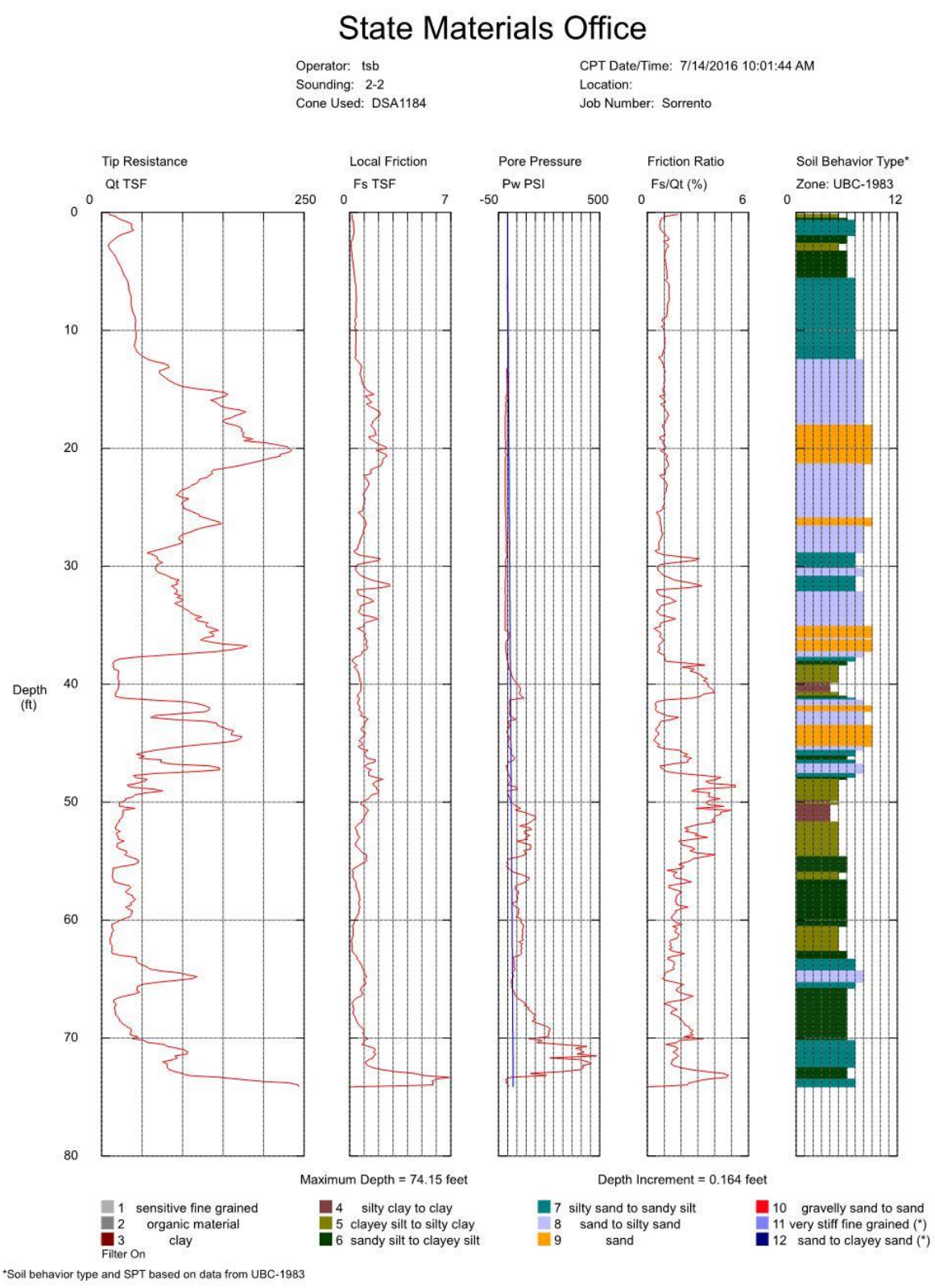

Figure 94: Result of CPT sounding for location of sensor 2-2 performed by Florida State Materials Office

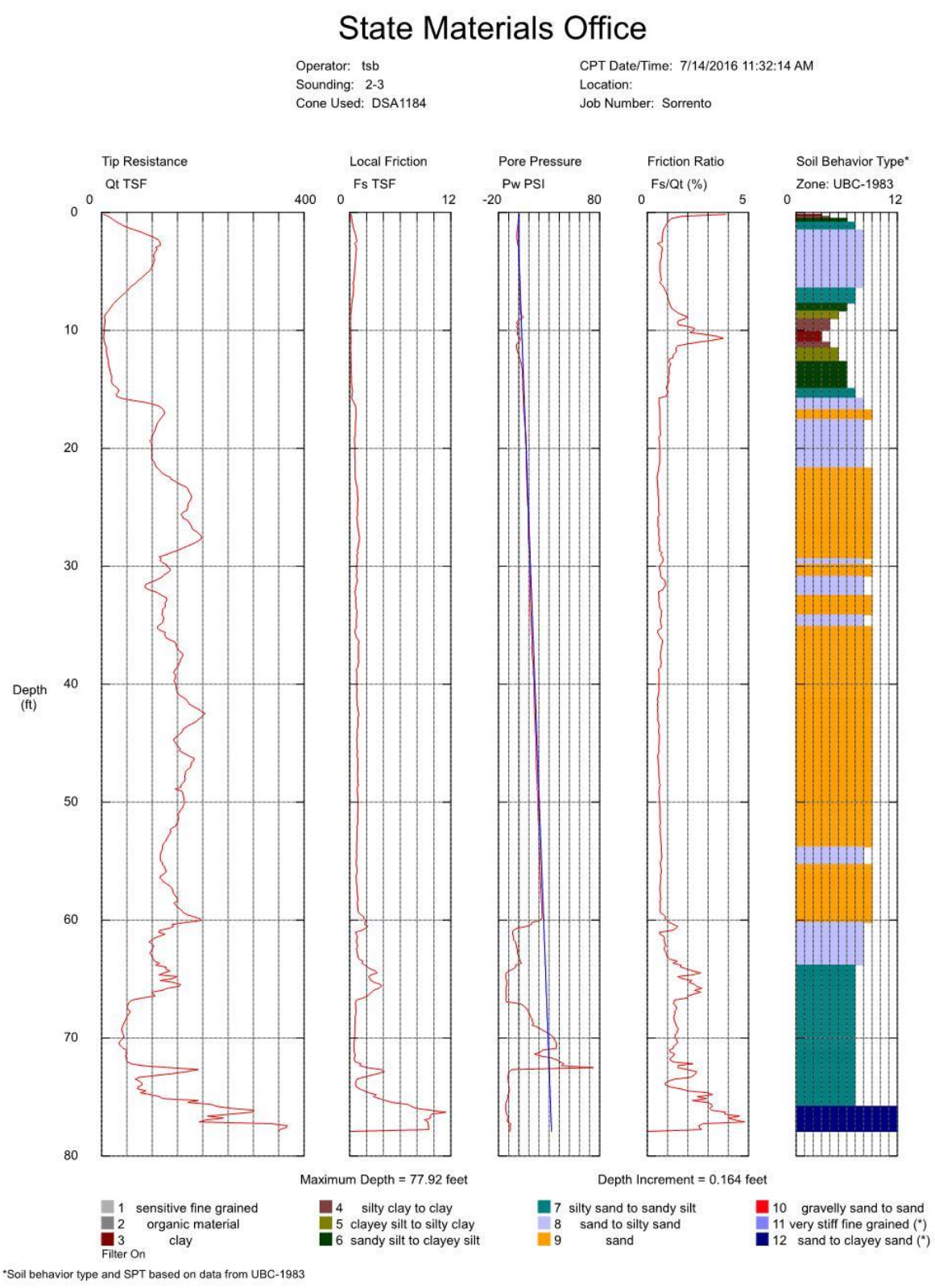

Figure 95: Result of CPT sounding for location of sensor 2-3 performed by Florida State Materials Office

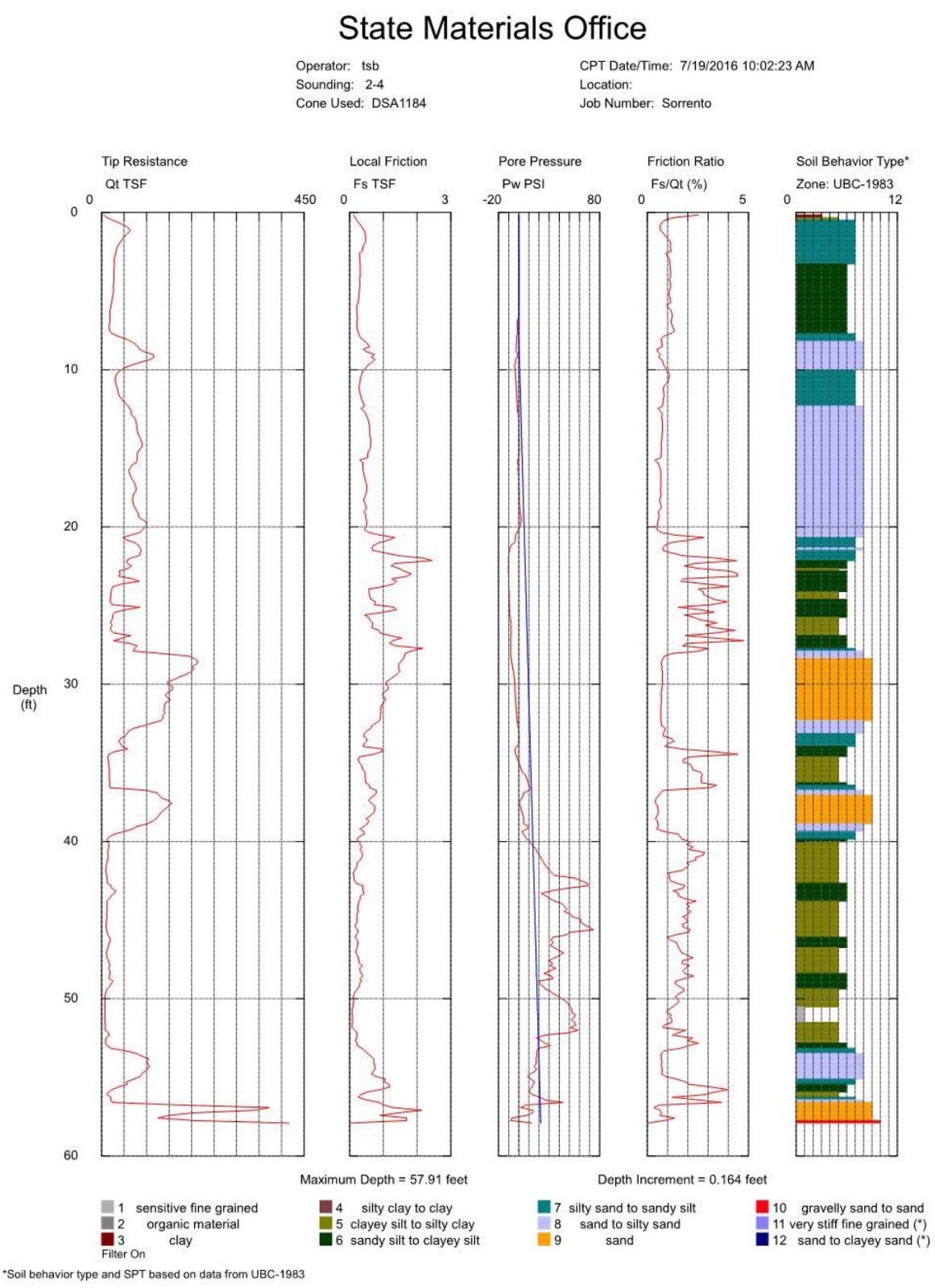

Figure 96: Result of CPT sounding for location of sensor 2-4 performed by Florida State Materials Office

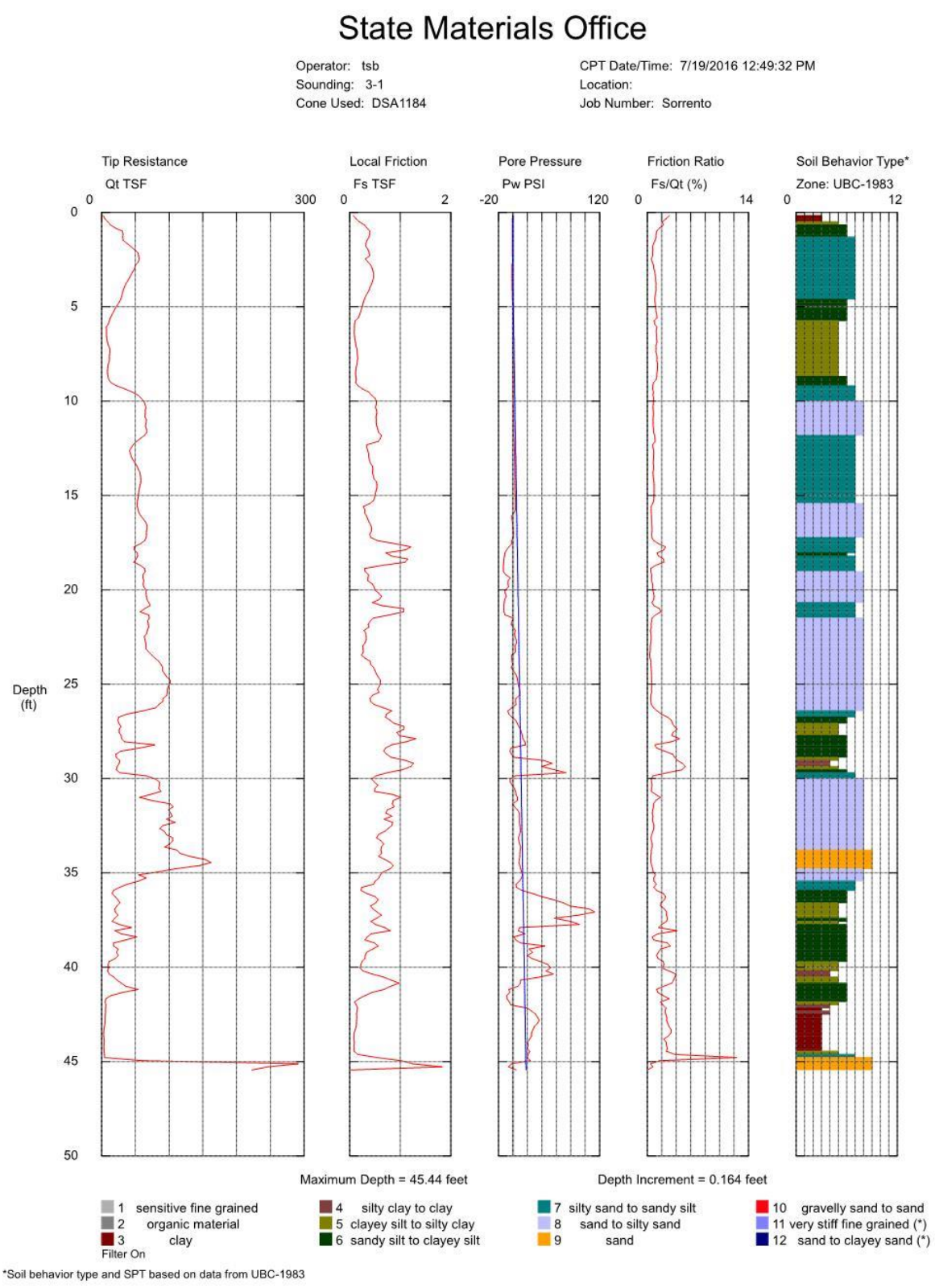

Figure 97: Result of CPT sounding for location of sensor 3-1 performed by Florida State Materials Office

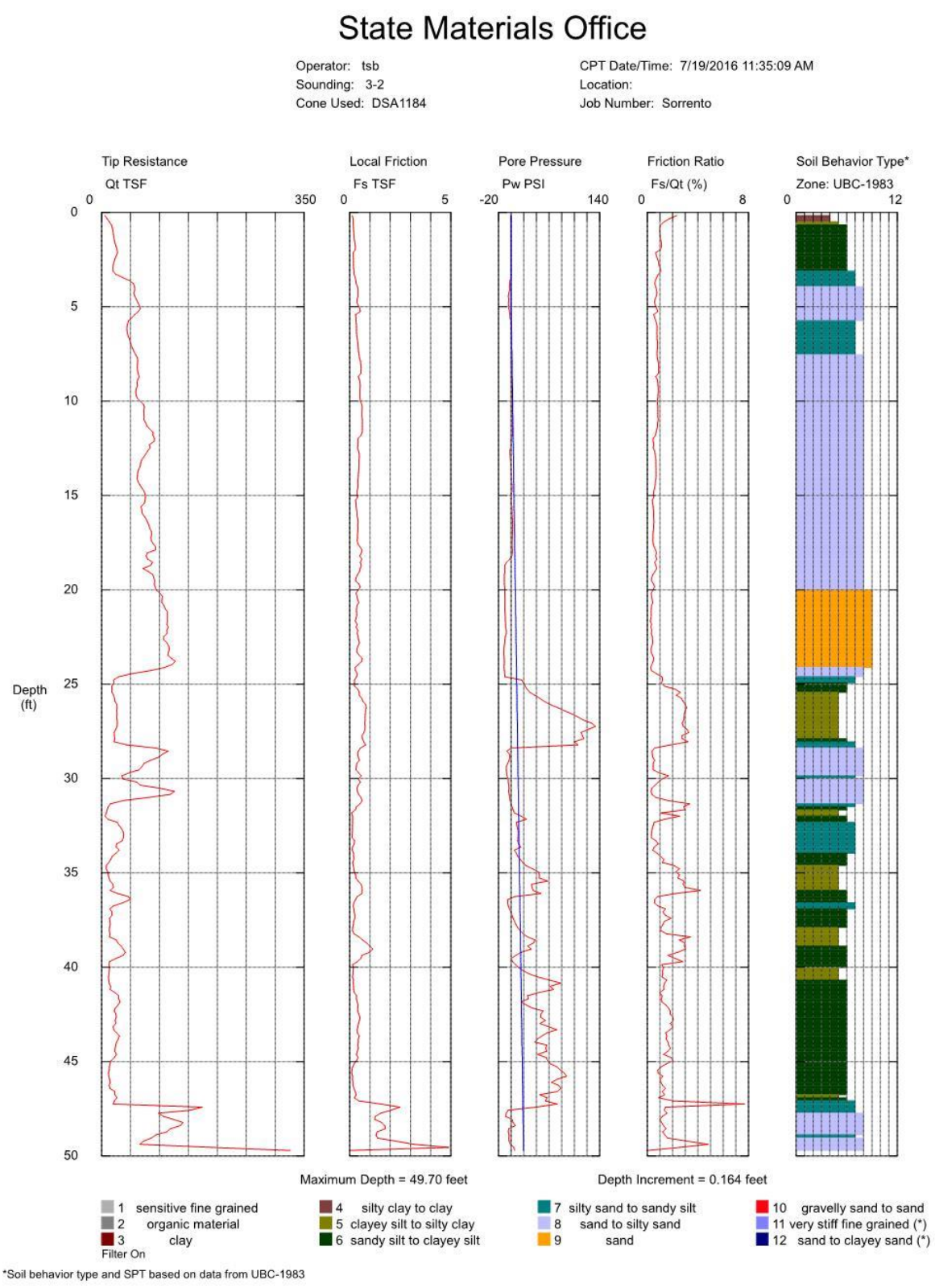

Figure 98: Result of CPT sounding for location of sensor 3-2 performed by Florida State Materials Office

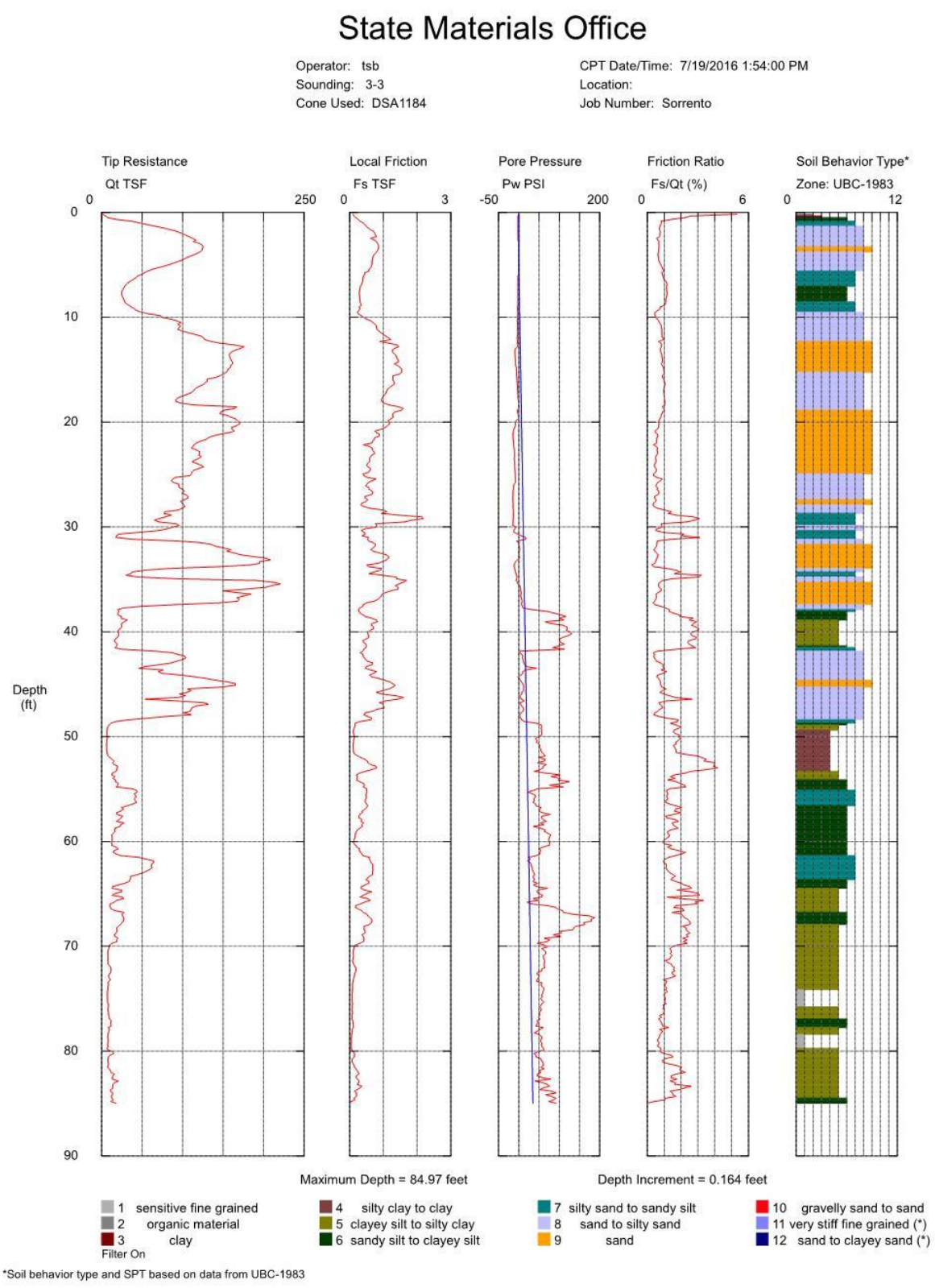

Figure 99: Result of CPT sounding for location of sensor 3-3 performed by Florida State Materials Office

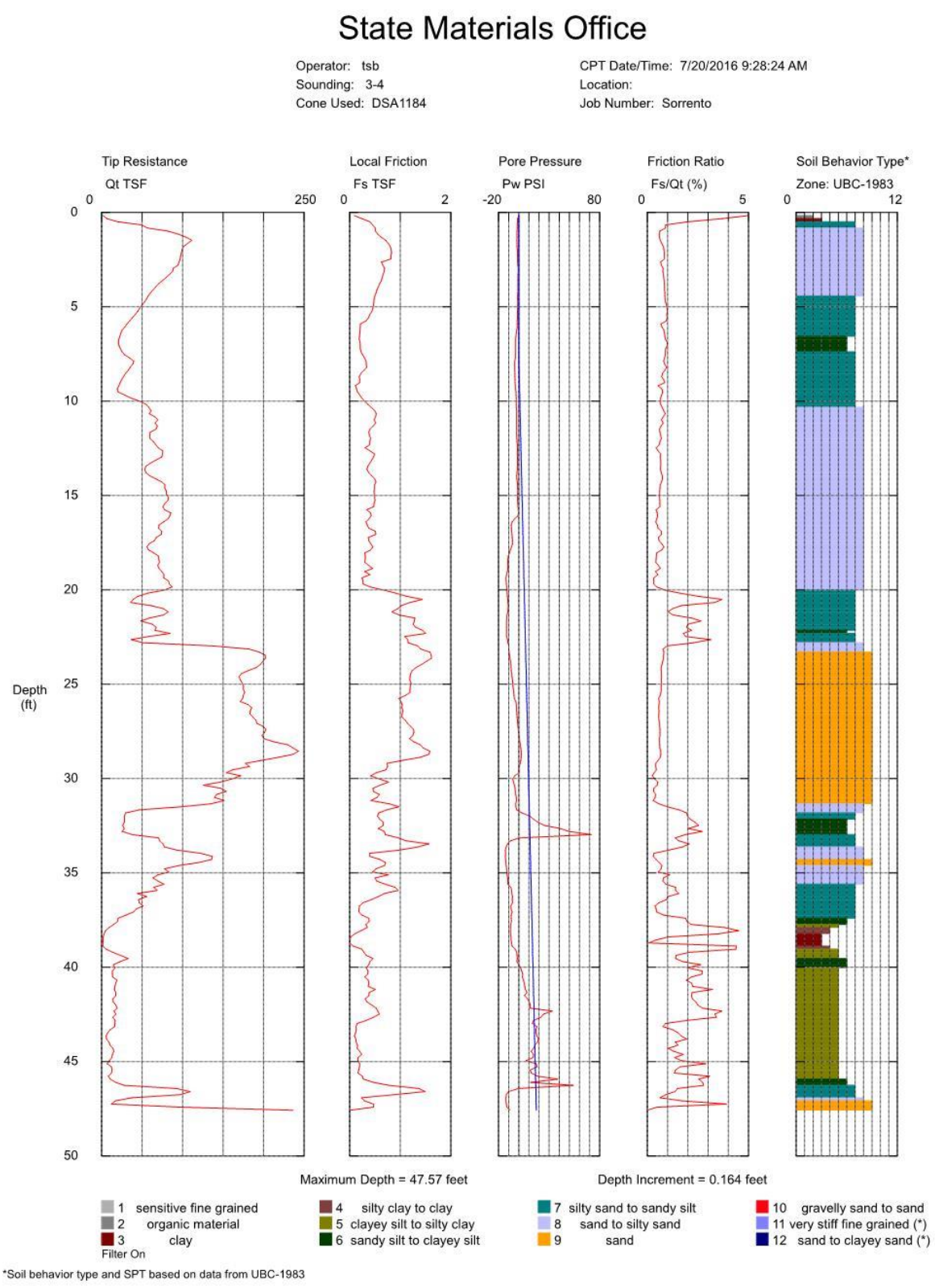

Figure 100: Result of CPT sounding for location of sensor 3-4 performed by Florida State Materials Office

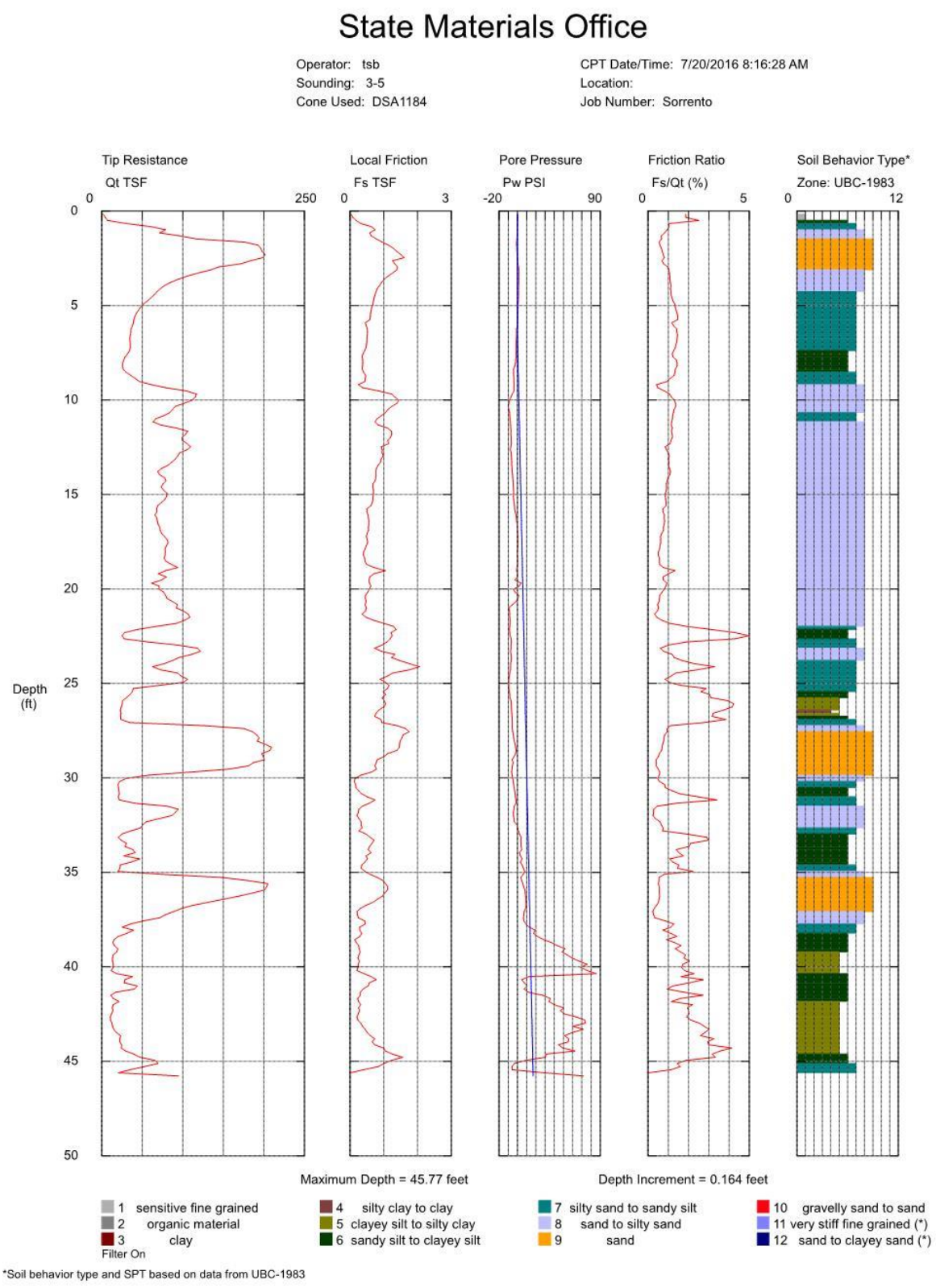

Figure 101: Result of CPT sounding for location of sensor 3-5 performed by Florida State Materials Office

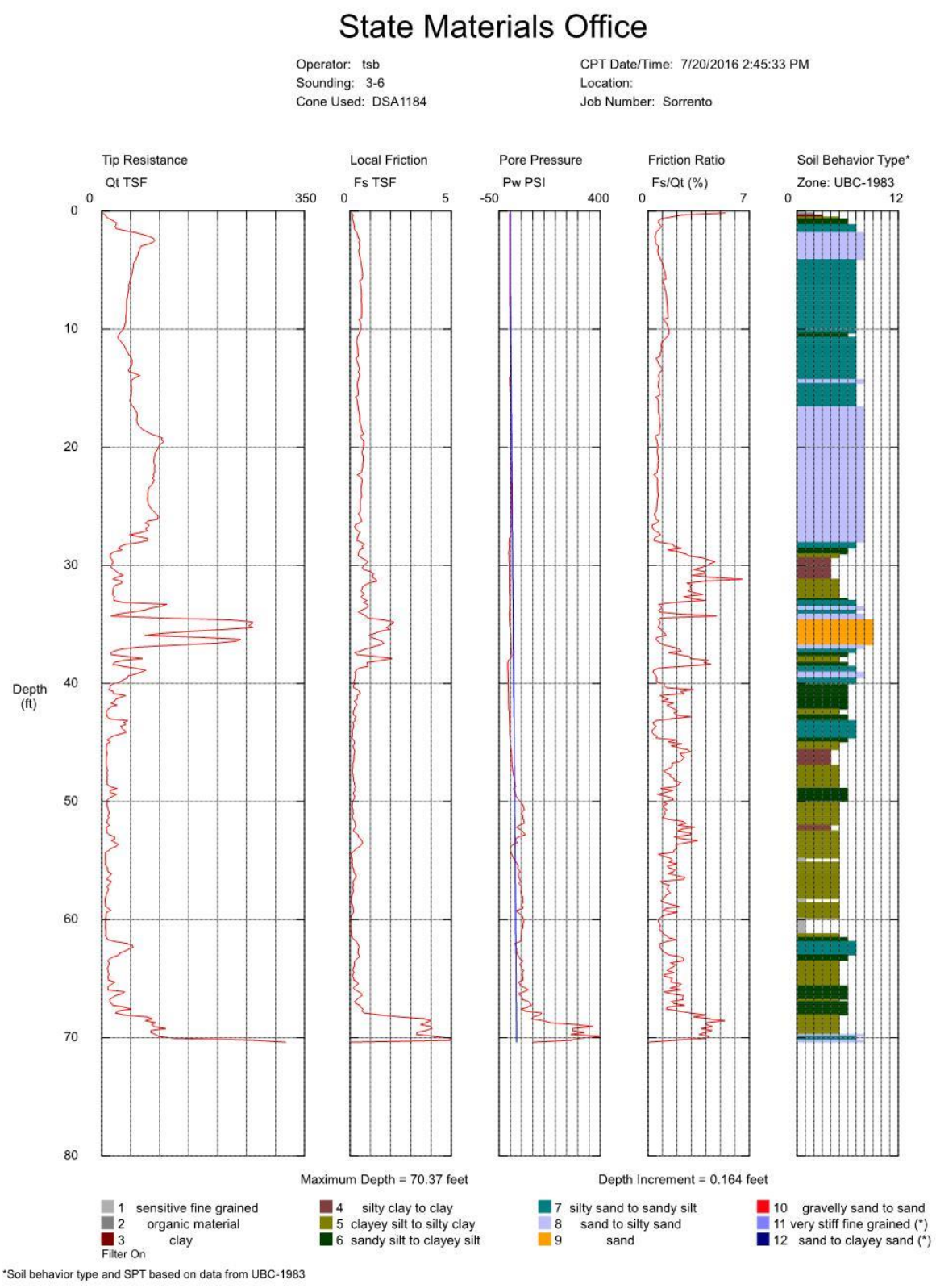

Figure 102: Result of CPT sounding for location of sensor 3-6 performed by Florida State Materials Office

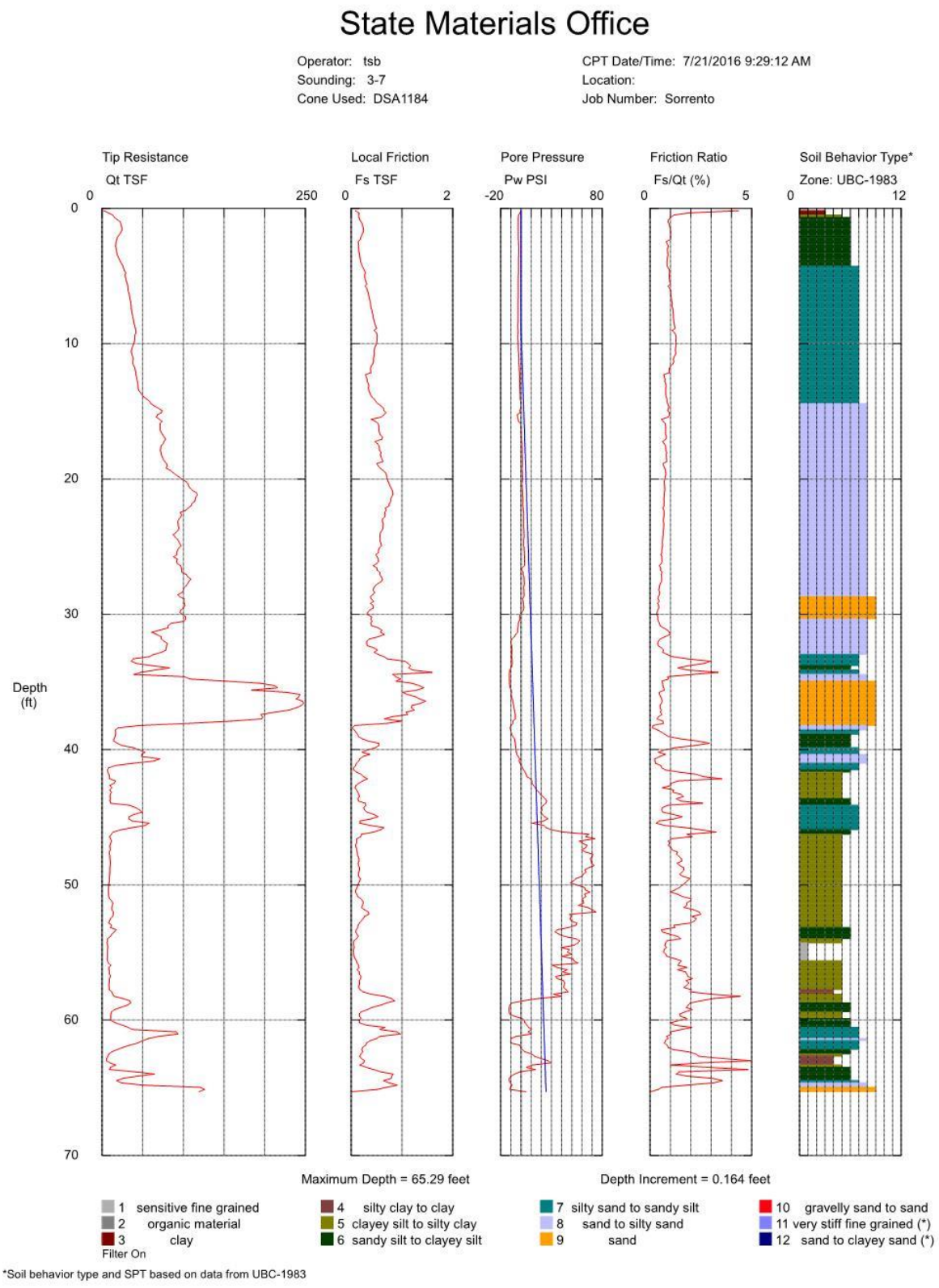

Figure 103: Result of CPT sounding for location of sensor 3-7 performed by Florida State Materials Office

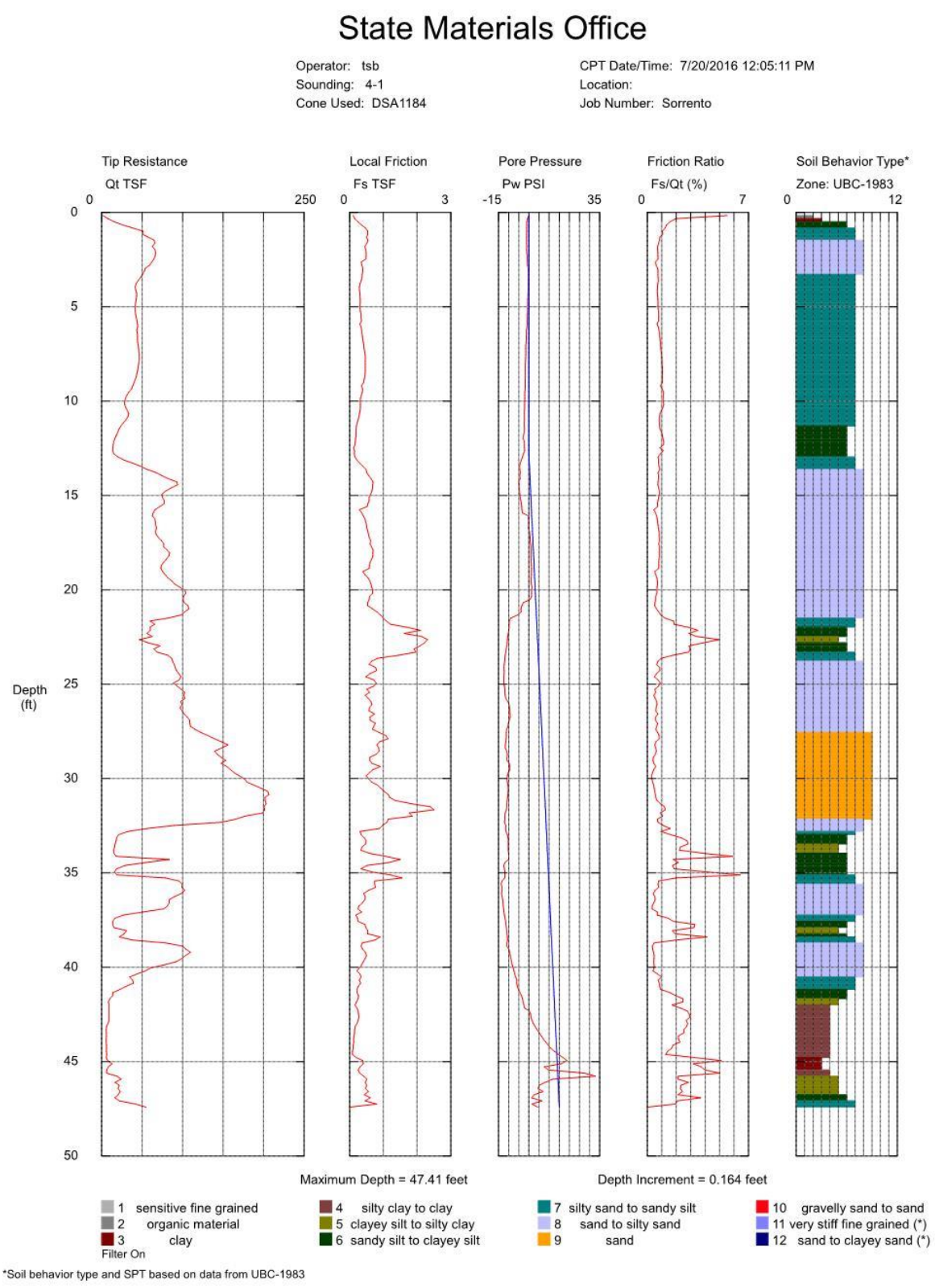

Figure 104: Result of CPT sounding for location of sensor 4-1 performed by Florida State Materials Office

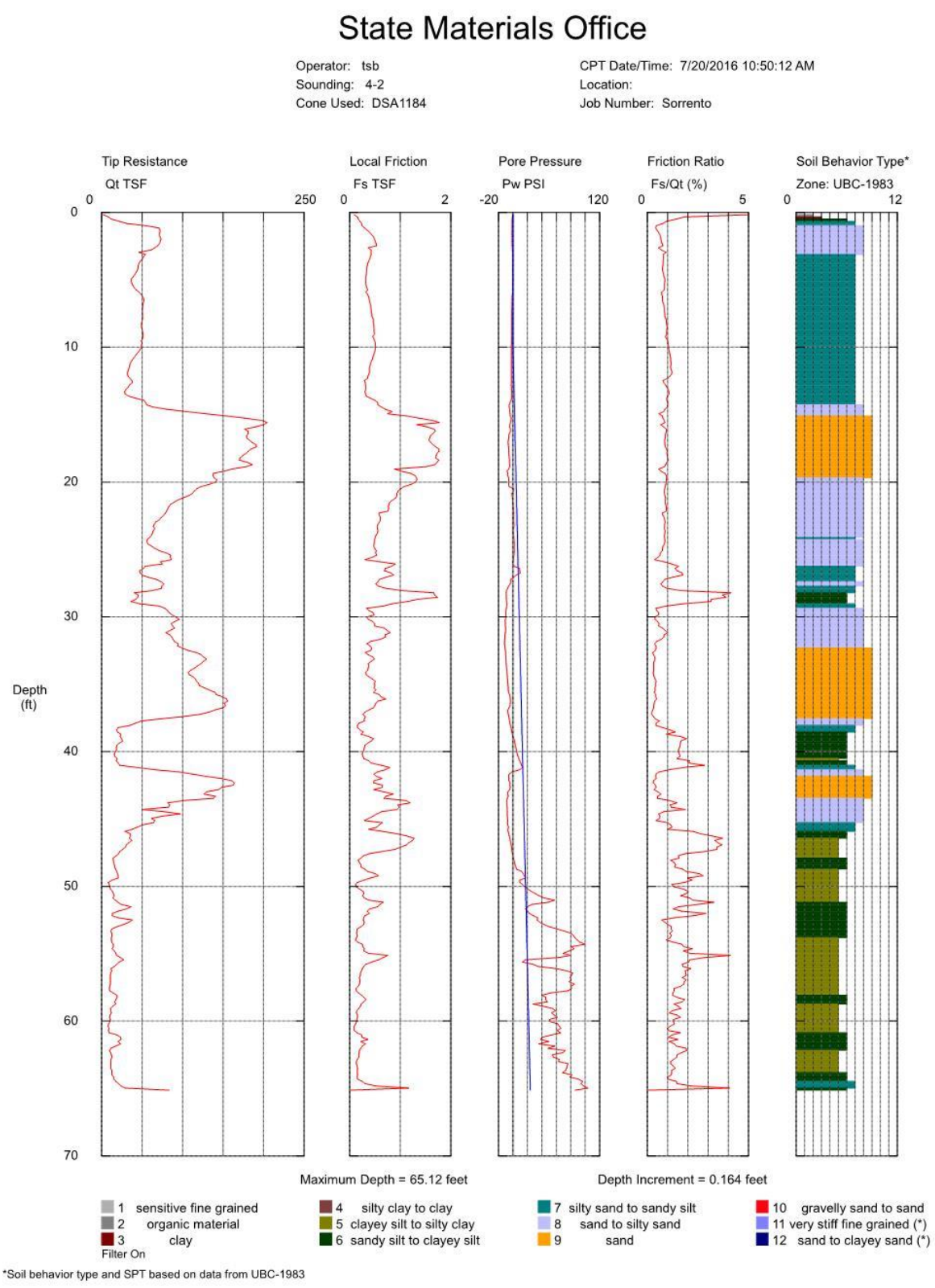

Figure 105: Result of CPT sounding for location of sensor 4-2 performed by Florida State Materials Office

APPENDIX C: RESULTS OF SCALED MODEL

Sample 1 (Thickness = 150mm G.W.T = 15mm)

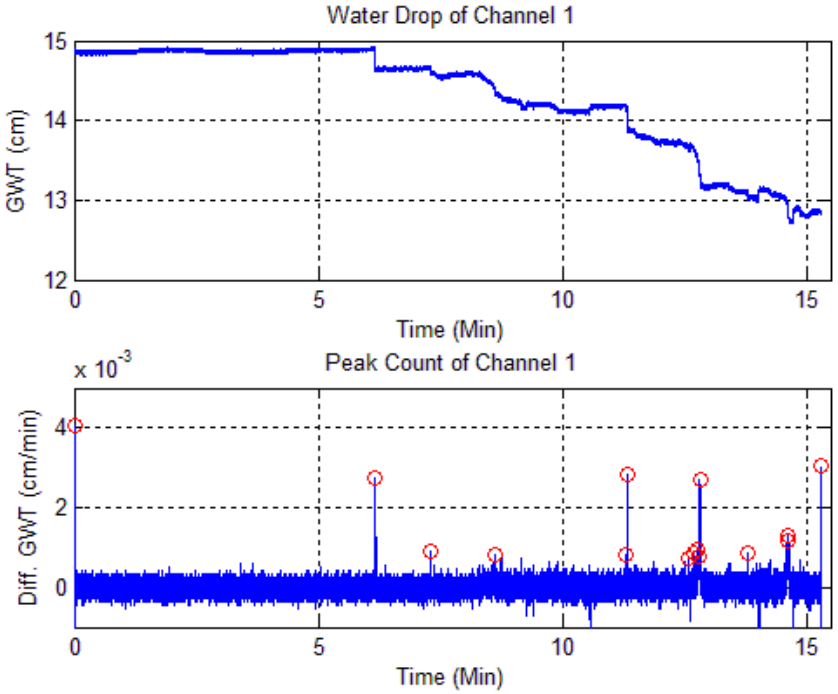

Figure 106: Peak counting of sample 1 with thickness of 150mm, G.W.T = 15mm, and radius (R) = 9.4cm

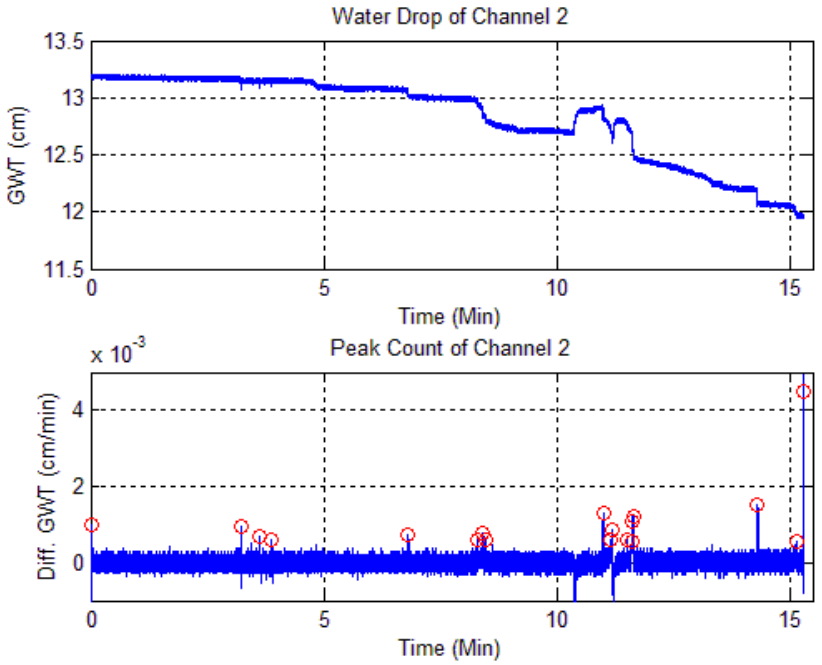

Figure 107: Peak counting of sample 1 with thickness of 150mm, G.W.T = 15mm, and radius (R) = 12.5cm

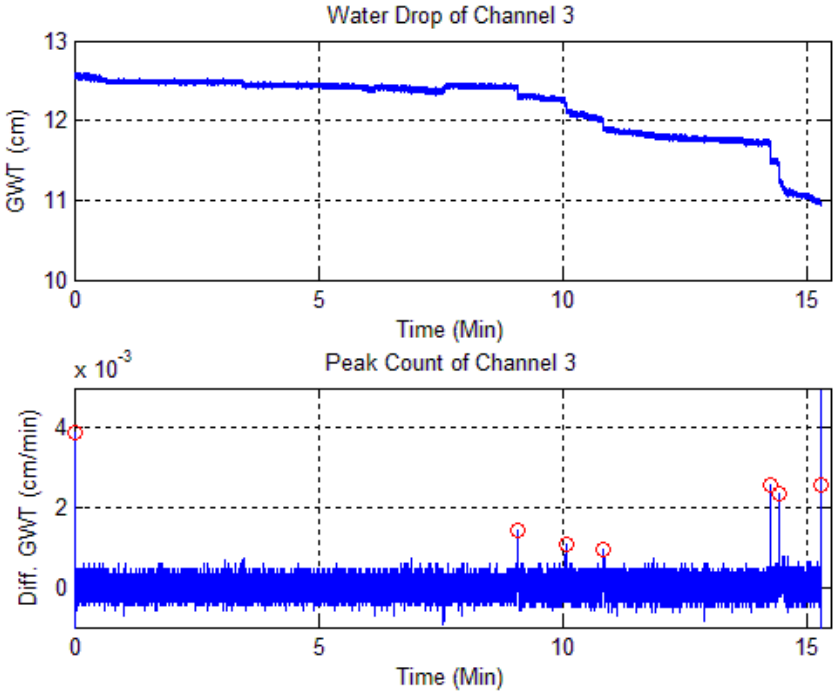

Figure 108: Peak counting of sample 1 with thickness of 150mm, G.W.T = 15mm, and radius (R) = 13.5cm

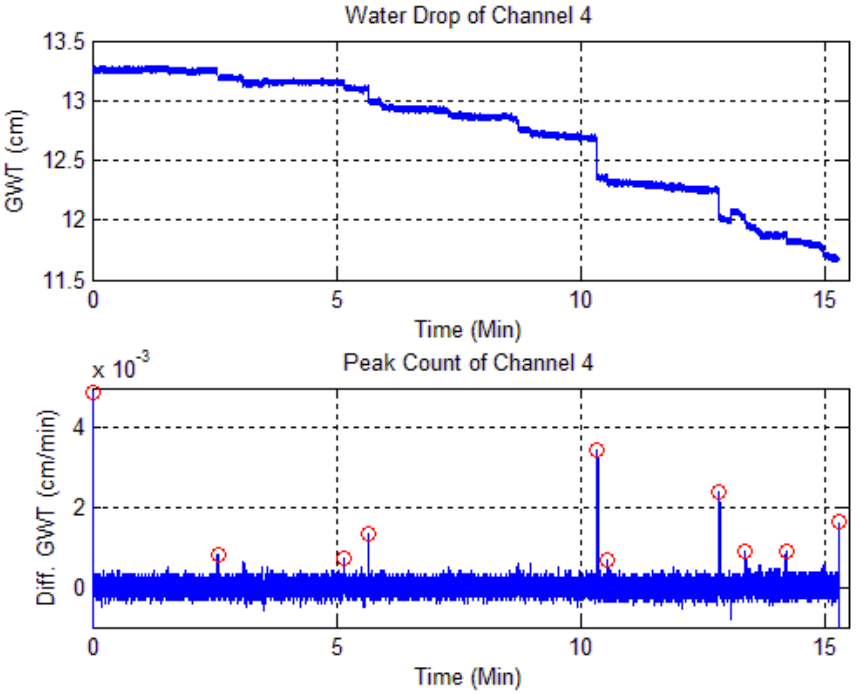

Figure 109: Peak counting of sample 1 with thickness of 150mm, G.W.T = 15mm, and radius (R) = 15cm

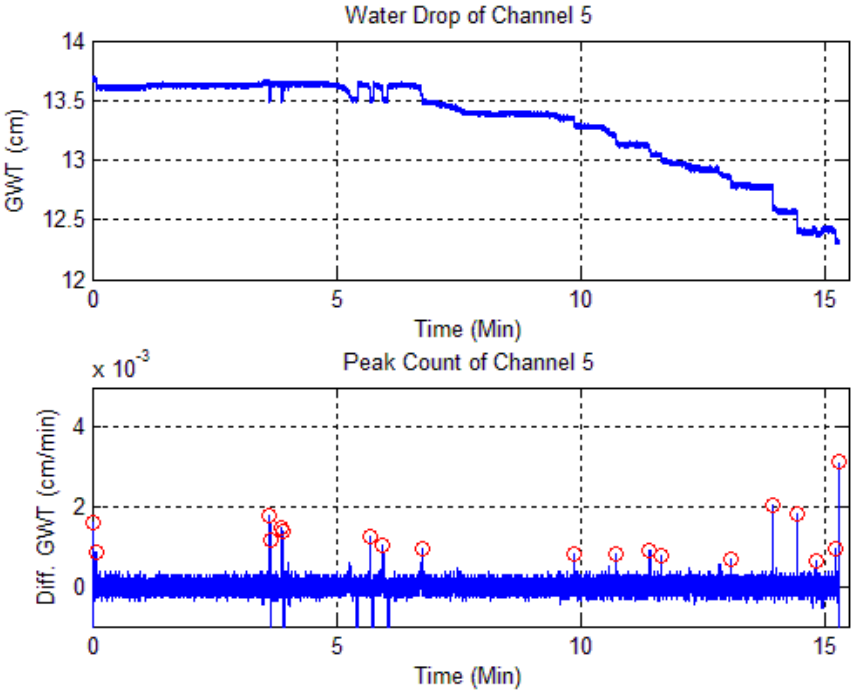

Figure 110: Peak counting of sample 1 with thickness of 150mm, G.W.T = 15mm, and radius (R) = 17cm

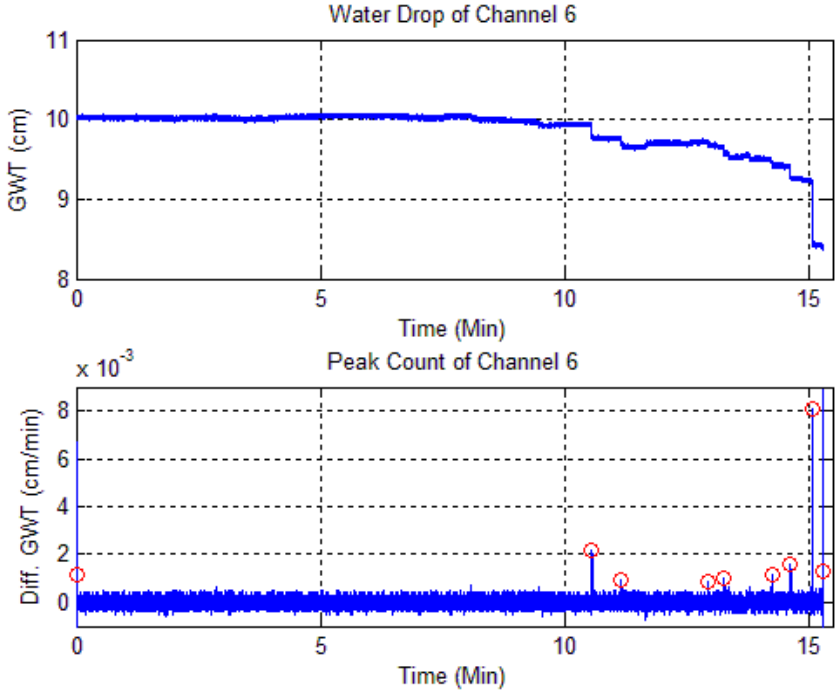

Figure 111: Peak counting of sample 1 with thickness of 150mm, G.W.T = 15mm, and radius (R) = 18.2cm

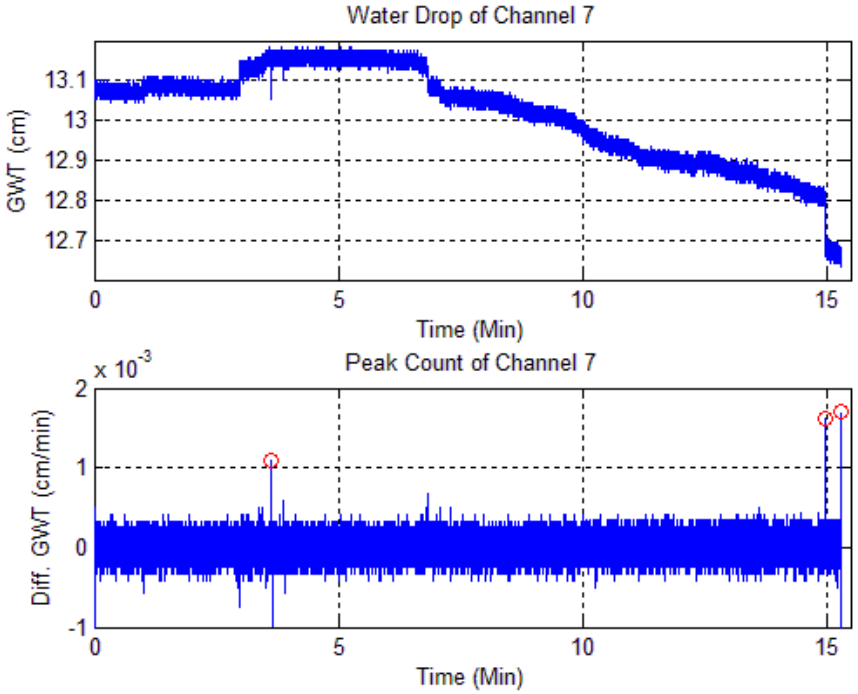

Figure 112: Peak counting of sample 1 with thickness of 150mm, G.W.T = 15mm, and radius (R) = 20.2cm

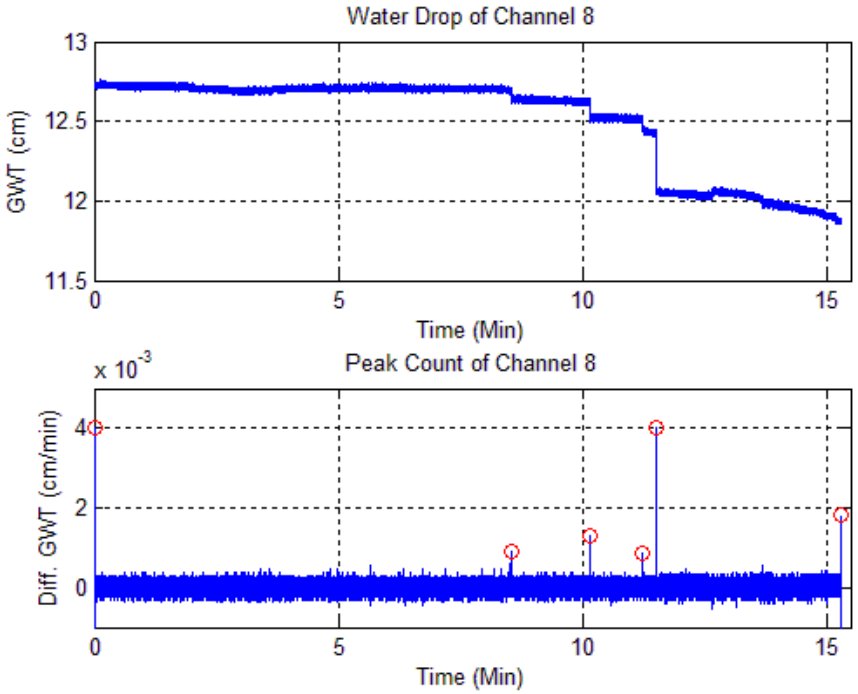

Figure 113: Peak counting of sample 1 with thickness of 150mm, G.W.T = 15mm, and radius (R) = 26cm

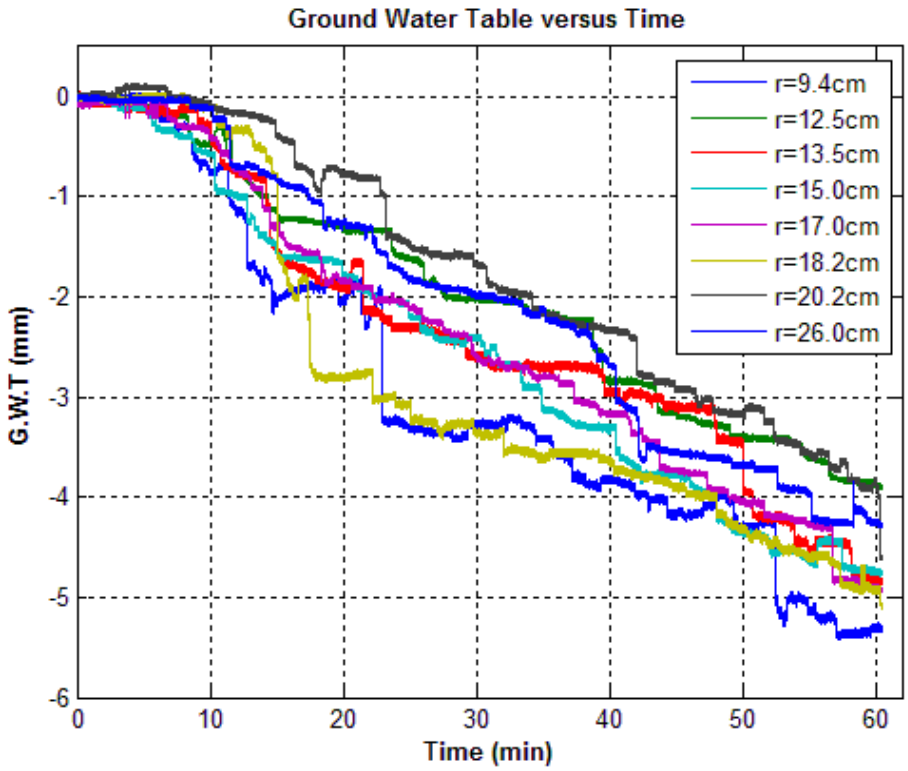

Figure 114: G.W.T over time of sample 1 with thickness of 150mm, G.W.T = 15mm

Sample 2 (Thickness = 150mm G.W.T = 15mm)

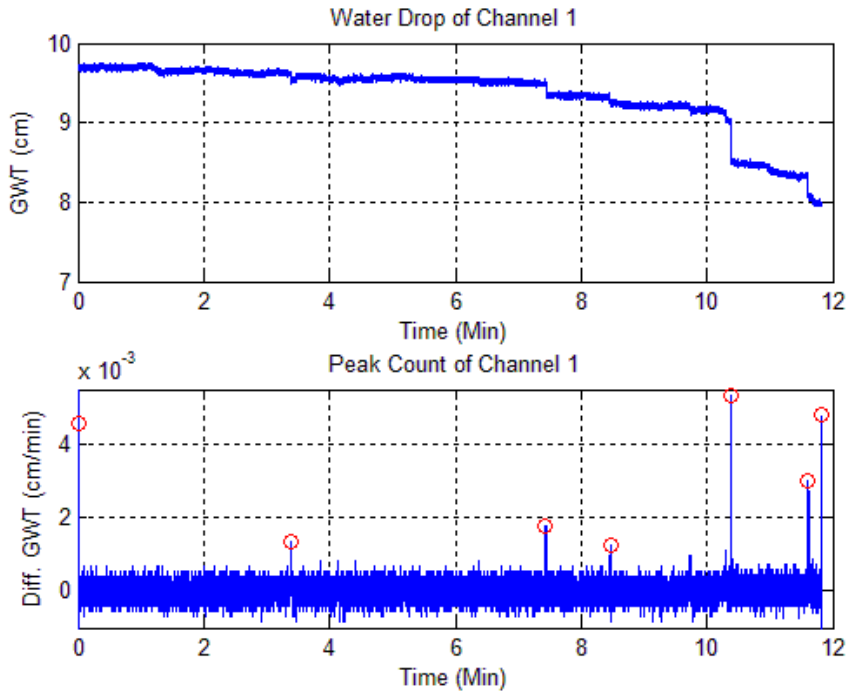

Figure 115: Peak counting of sample 2 with thickness of 150mm, G.W.T = 15mm, and radius (R) = 11.0cm

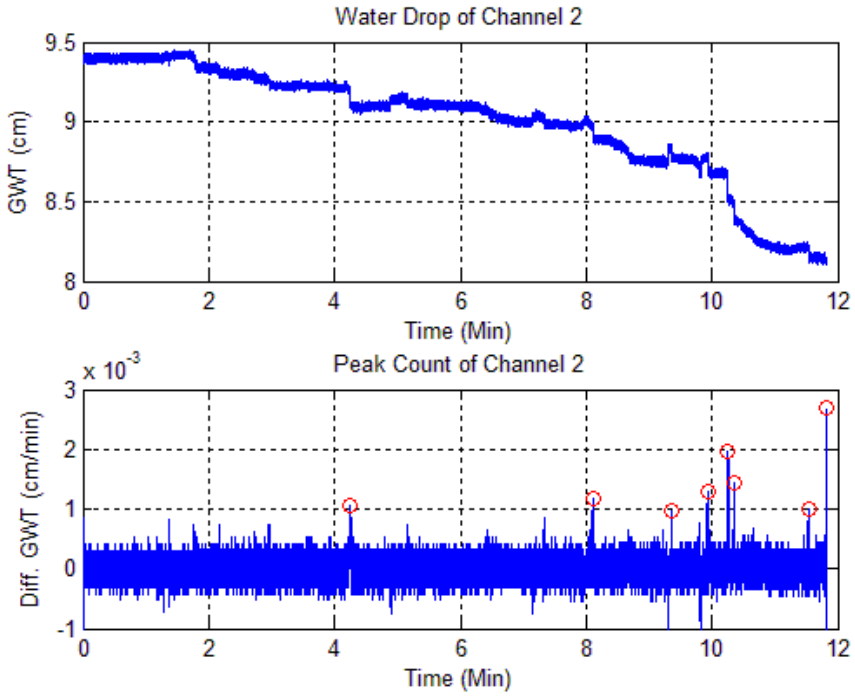

Figure 116: Peak counting of sample 2 with thickness of 150mm, G.W.T = 15mm, and radius (R) = 13.0cm

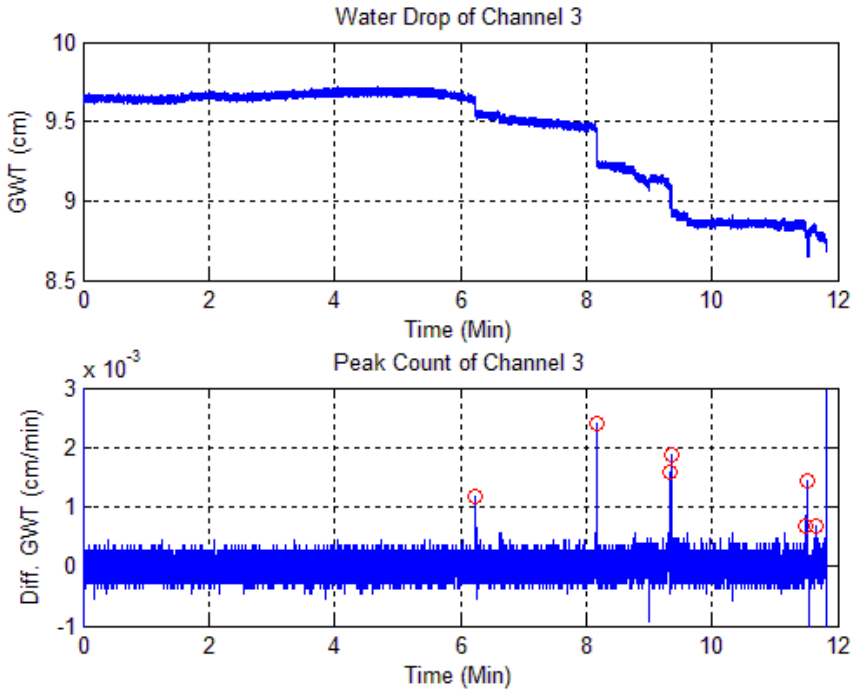

Figure 117: Peak counting of sample 2 with thickness of 150mm, G.W.T = 15mm, and radius (R) = 15.0cm

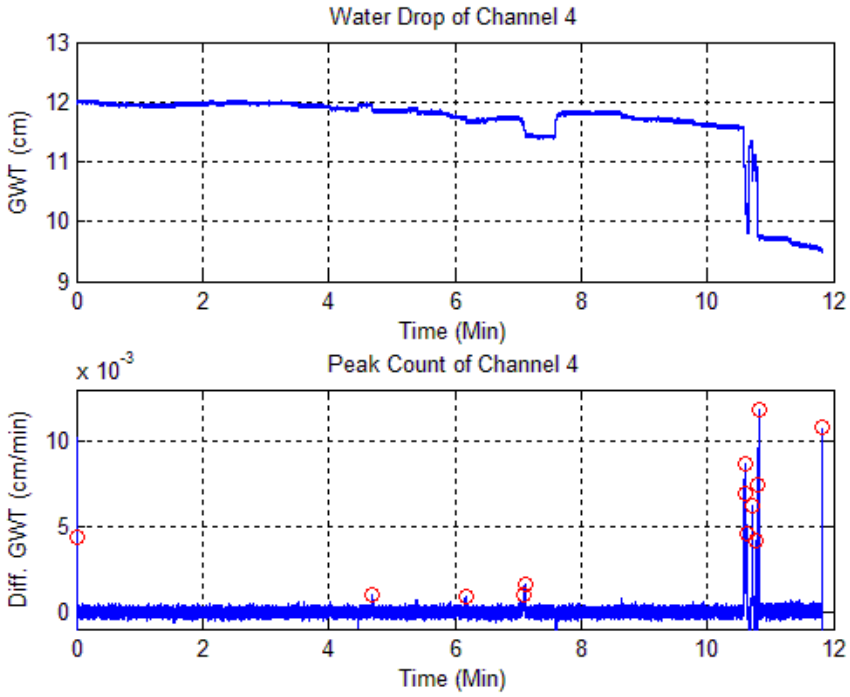

Figure 118: Peak counting of sample 2 with thickness of 150mm, G.W.T = 15mm, and radius (R) = 17.0cm

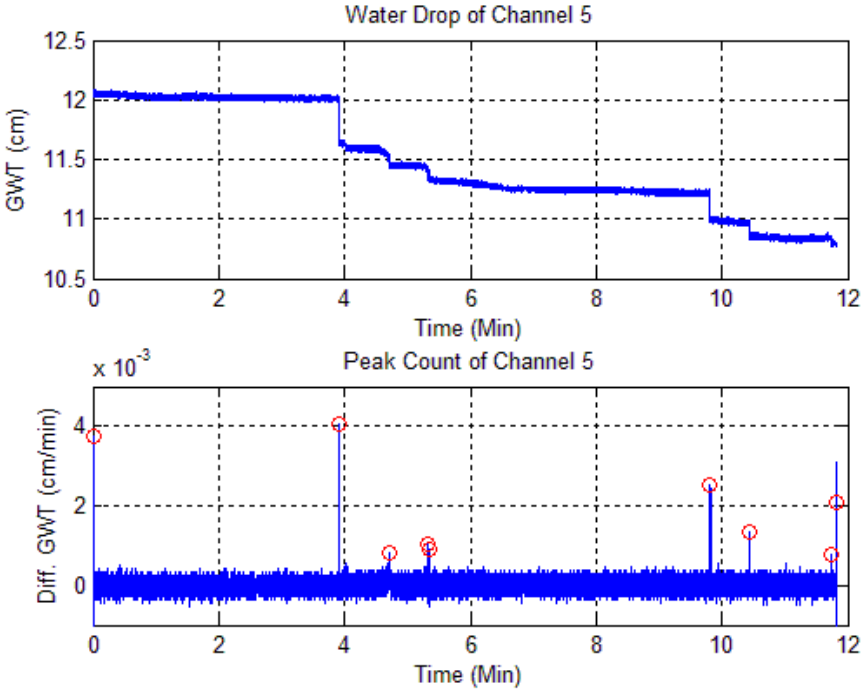

Figure 119: Peak counting of sample 2 with thickness of 150mm, G.W.T = 15mm, and radius (R) = 20.5cm

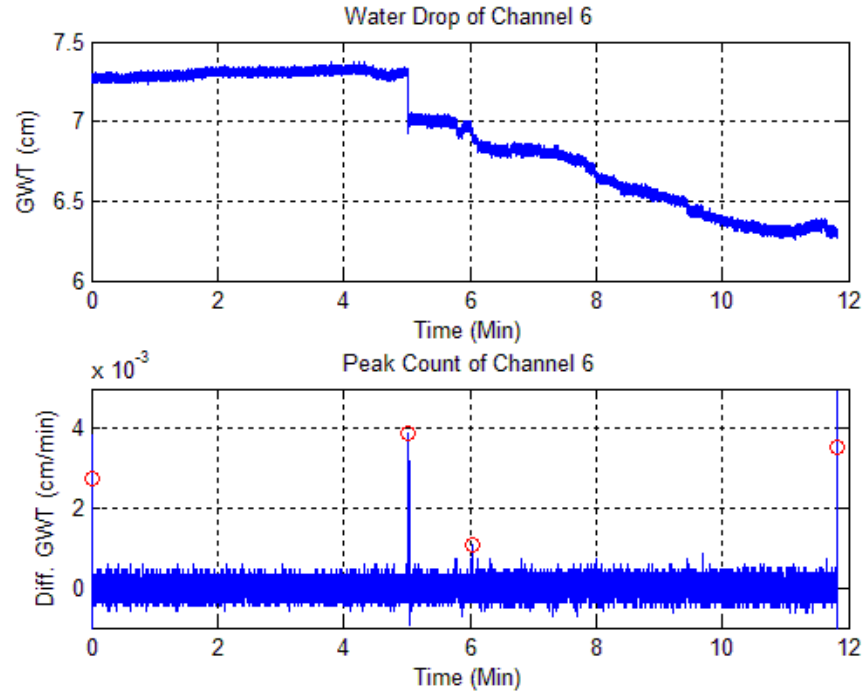

Figure 120: Peak counting of sample 2 with thickness of 150mm, G.W.T = 15mm, and radius (R) = 21cm

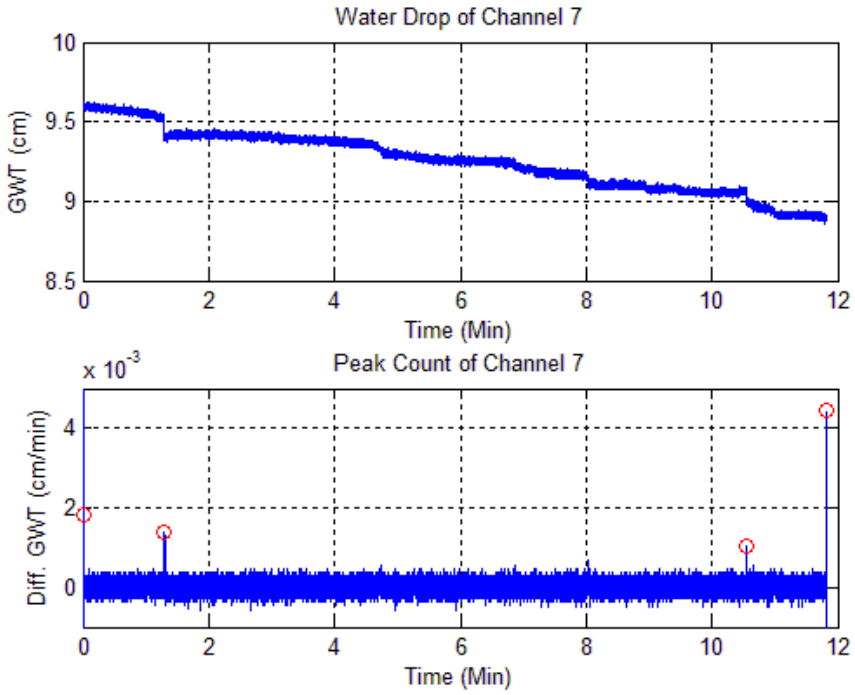

Figure 121: Peak counting of sample 2 with thickness of 150mm, G.W.T = 15mm, and radius (R) = 24.0cm

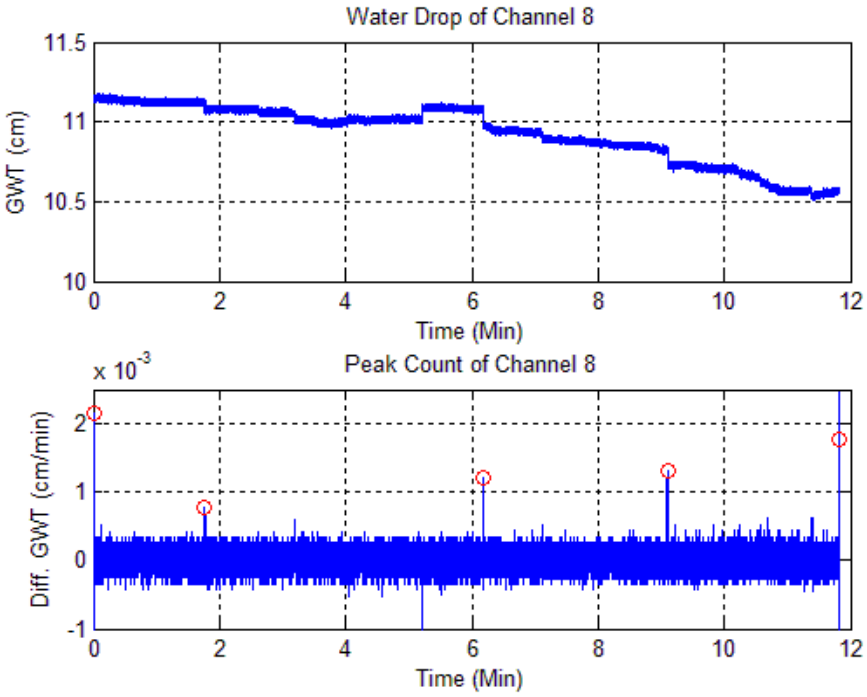

Figure 122: Peak counting of sample 2 with thickness of 150mm, G.W.T = 15mm, and radius (R) = 26.0cm

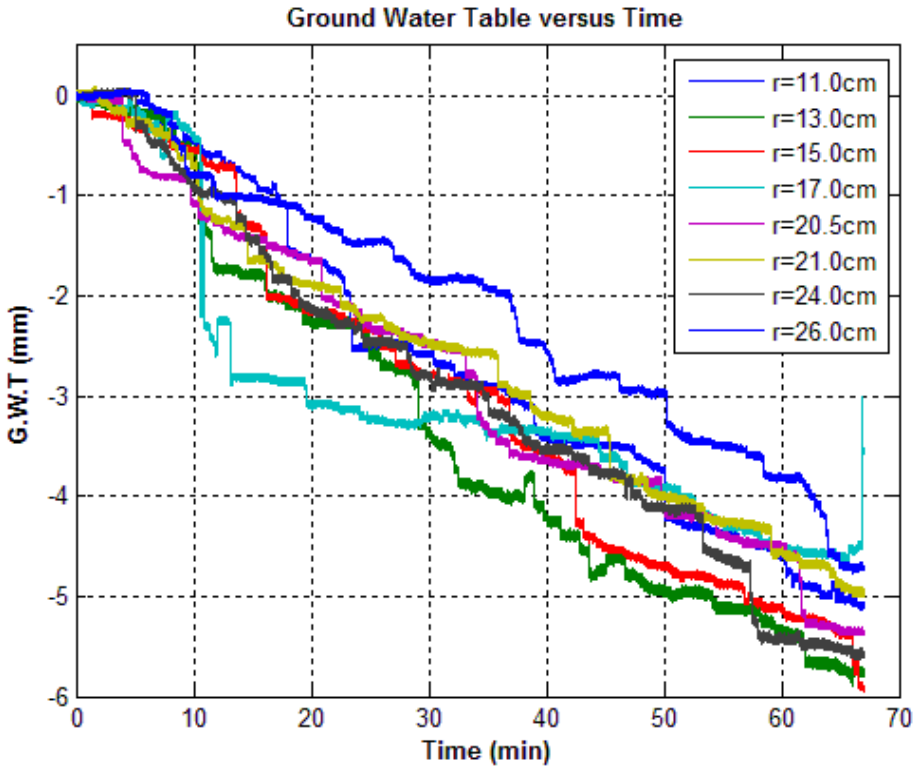

Figure 123: G.W.T over time of sample 2 with thickness of 150mm, G.W.T = 15mm

Sample 3 (Thickness = 150mm G.W.T = 15mm)

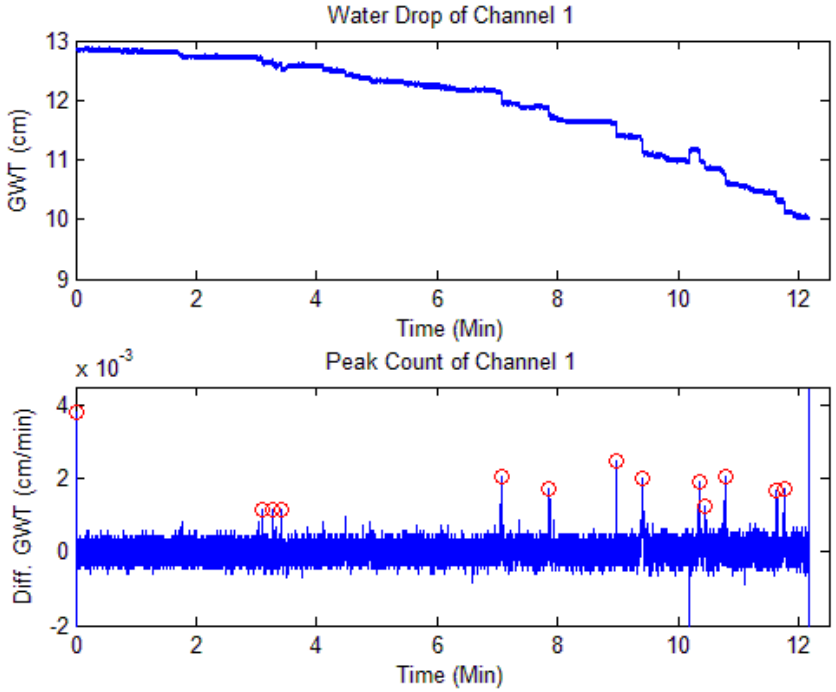

Figure 124: Peak counting of sample 3 with thickness of 150mm, G.W.T = 15mm, and radius (R) = 10cm

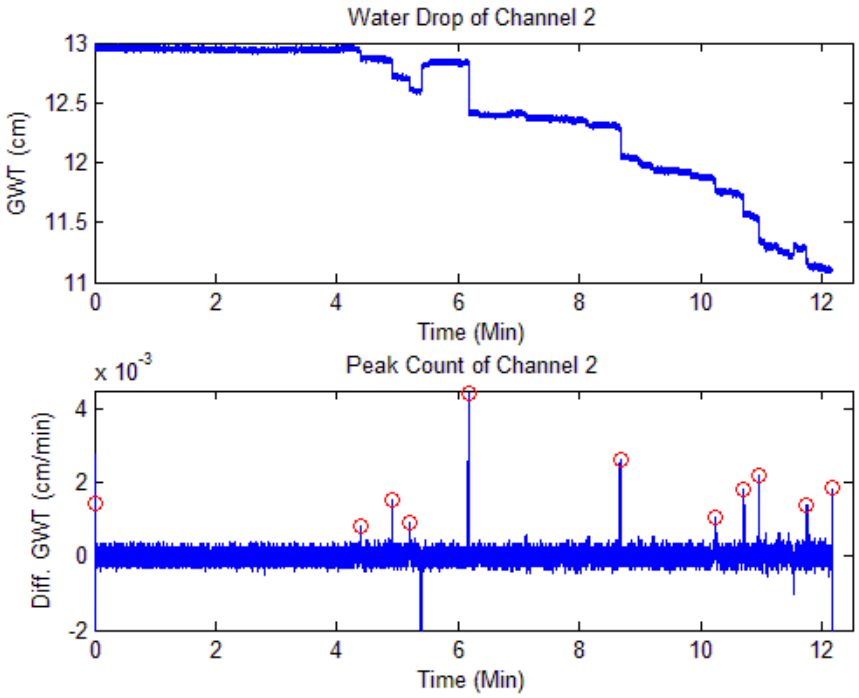

Figure 125: Peak counting of sample 3 with thickness of 150mm, G.W.T = 15mm, and radius (R) = 12.5cm

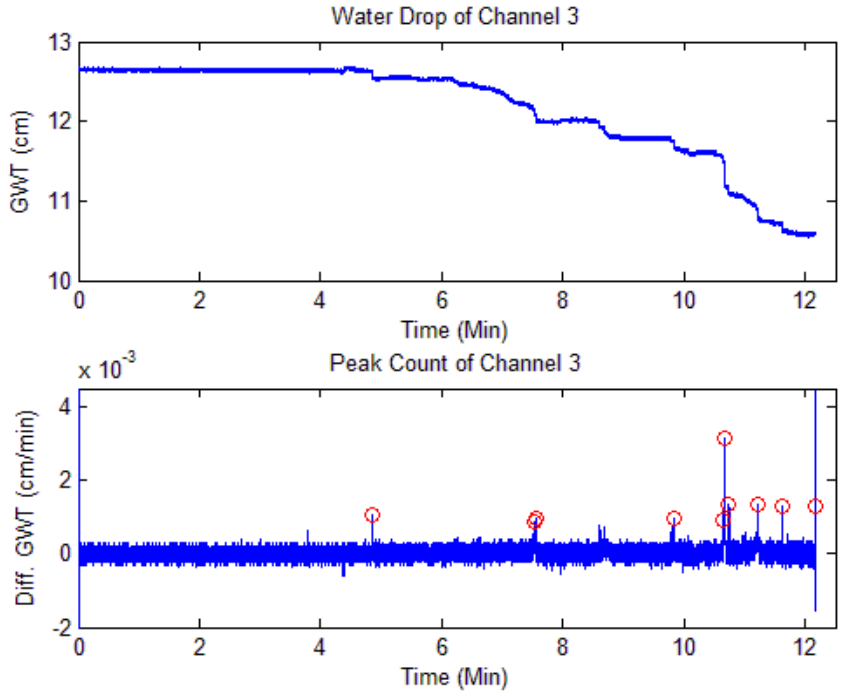

Figure 126: Peak counting of sample 3 with thickness of 150mm, G.W.T = 15mm, and radius (R) = 13.8cm

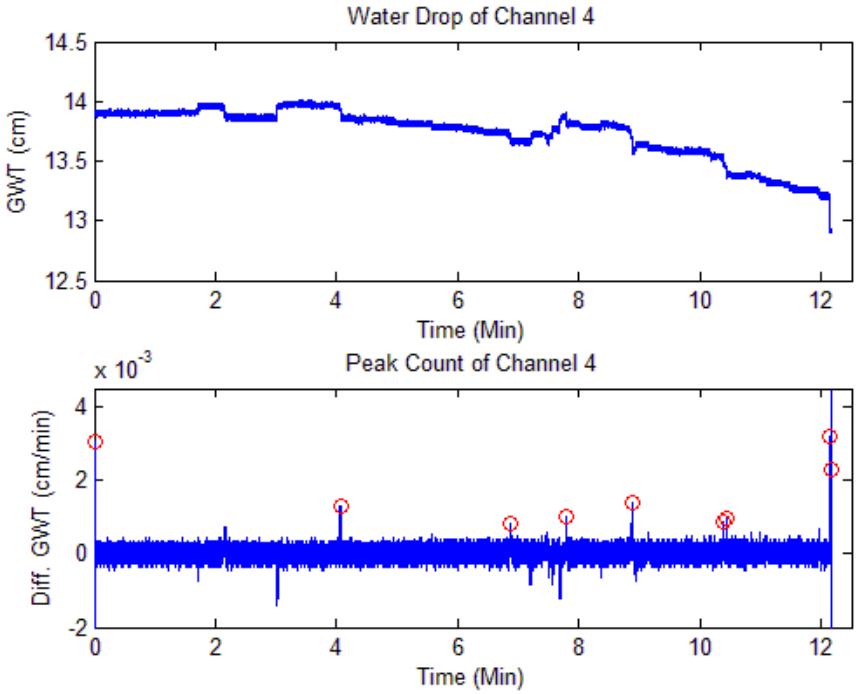

Figure 127: Peak counting of sample 3 with thickness of 150mm, G.W.T = 15mm, and radius (R) = 17.2cm

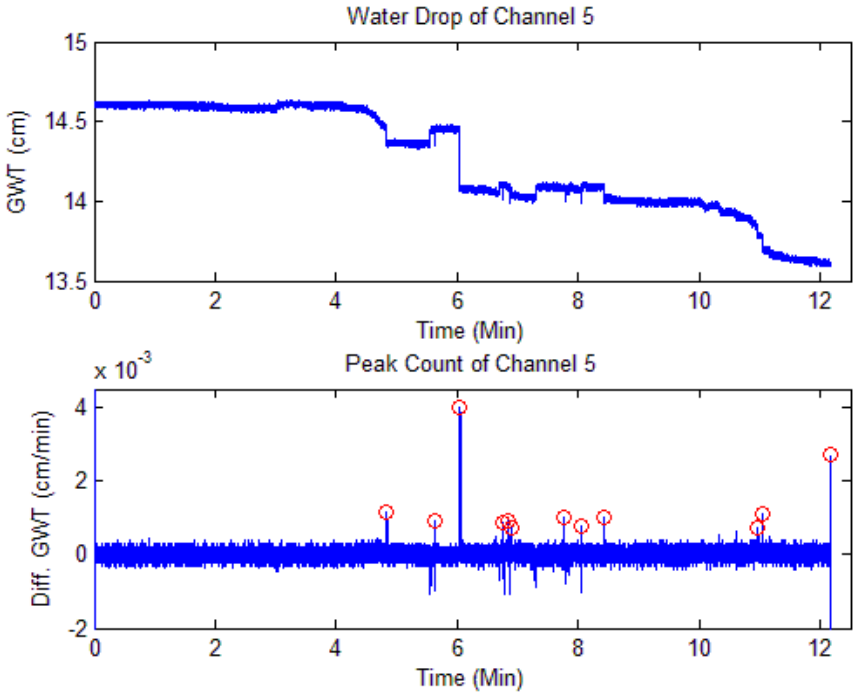

Figure 128: Peak counting of sample 3 with thickness of 150mm, G.W.T = 15mm, and radius (R) = 20cm

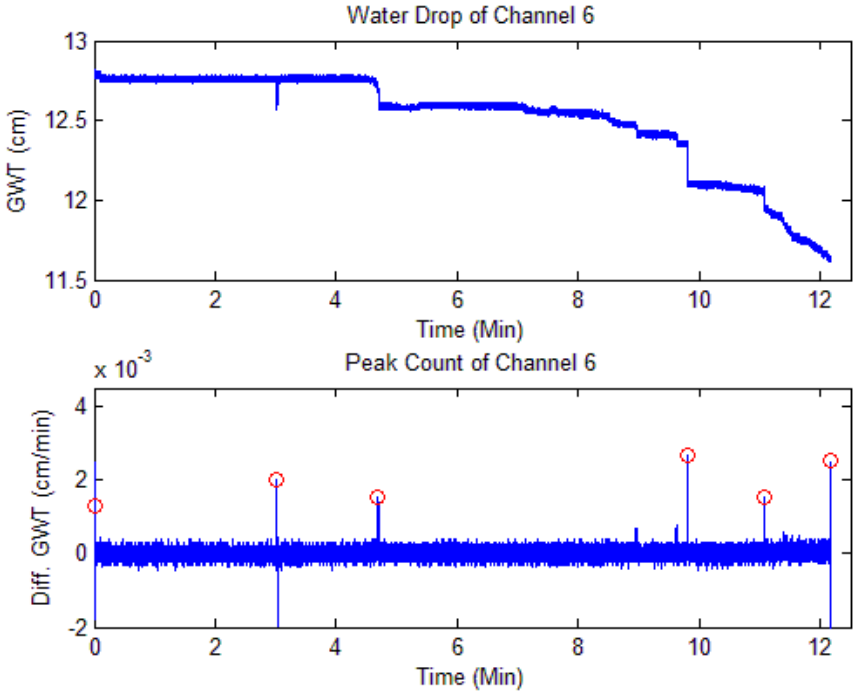

Figure 129: Peak counting of sample 3 with thickness of 150mm, G.W.T = 15mm, and radius (R) = 20.5cm

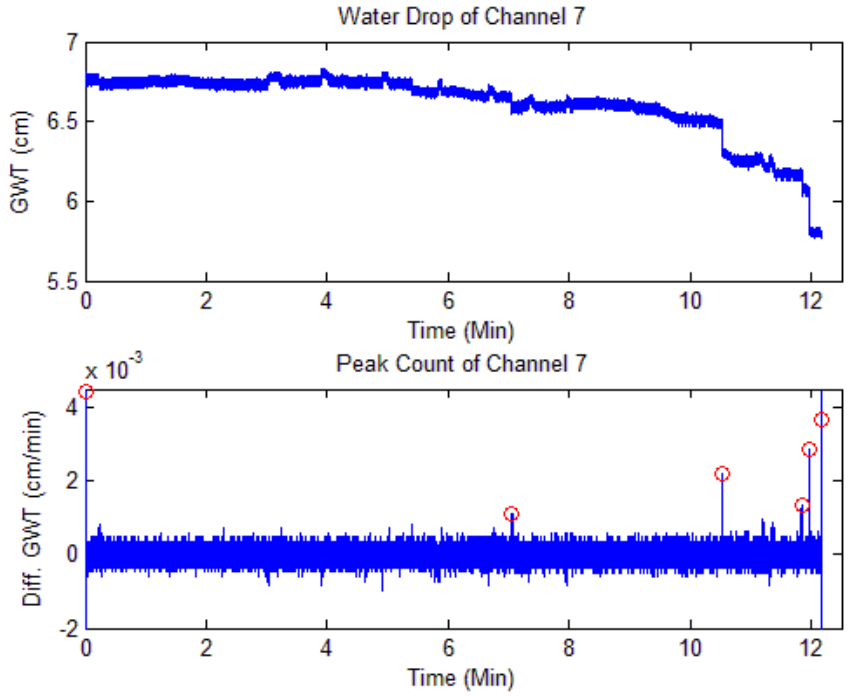

Figure 130: Peak counting of sample 3 with thickness of 150mm, G.W.T = 15mm, and radius (R) = 21.8cm

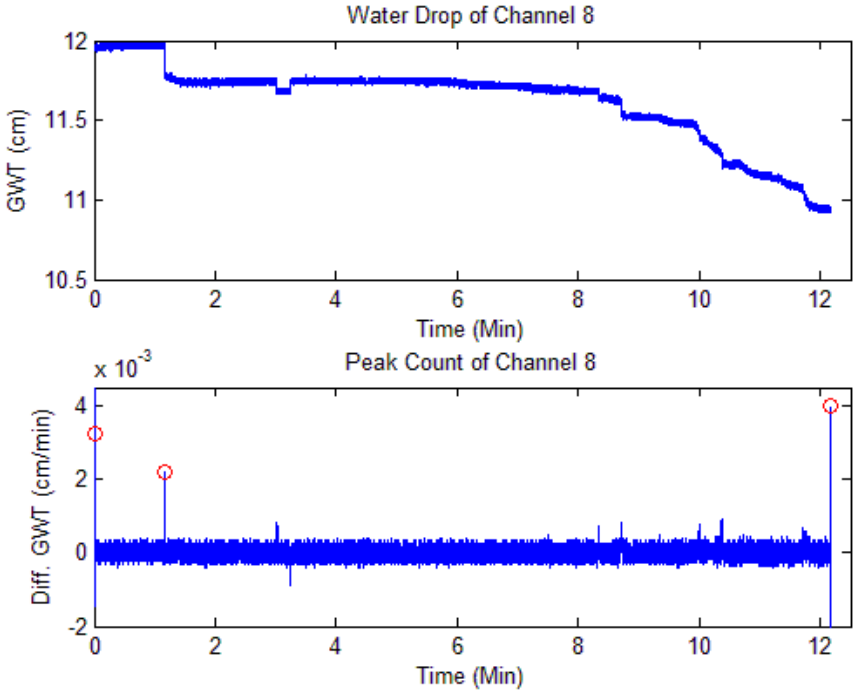

Figure 131: Peak counting of sample 3 with thickness of 150mm, G.W.T = 15mm, and radius (R) = 26cm

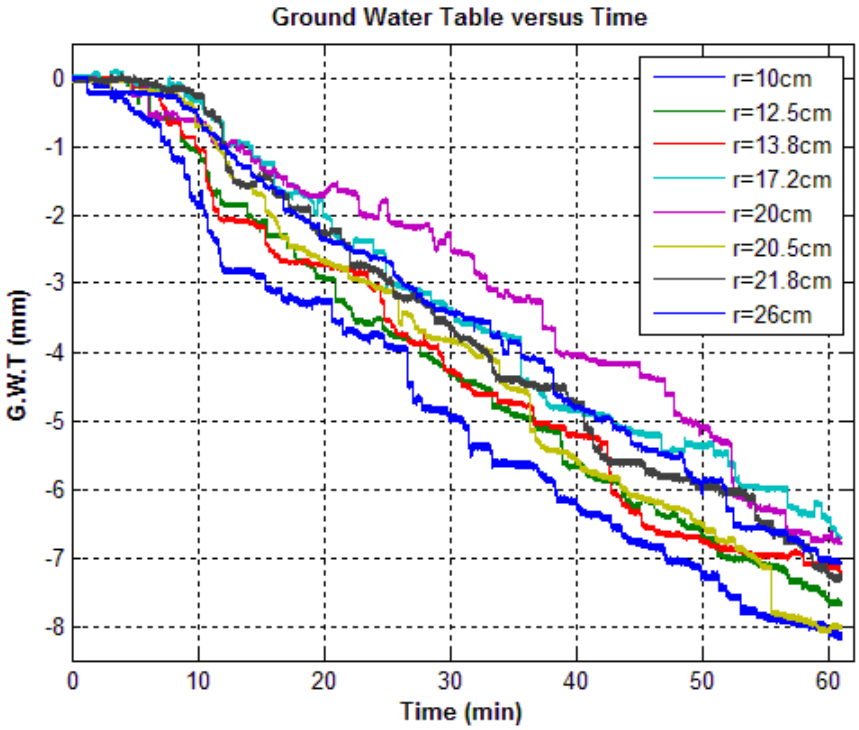

Figure 132: G.W.T over time of sample 3 with thickness of 150mm, G.W.T = 15mm

Sample 1 (Soil Thickness = 150mm G.W.T = 22.5mm)

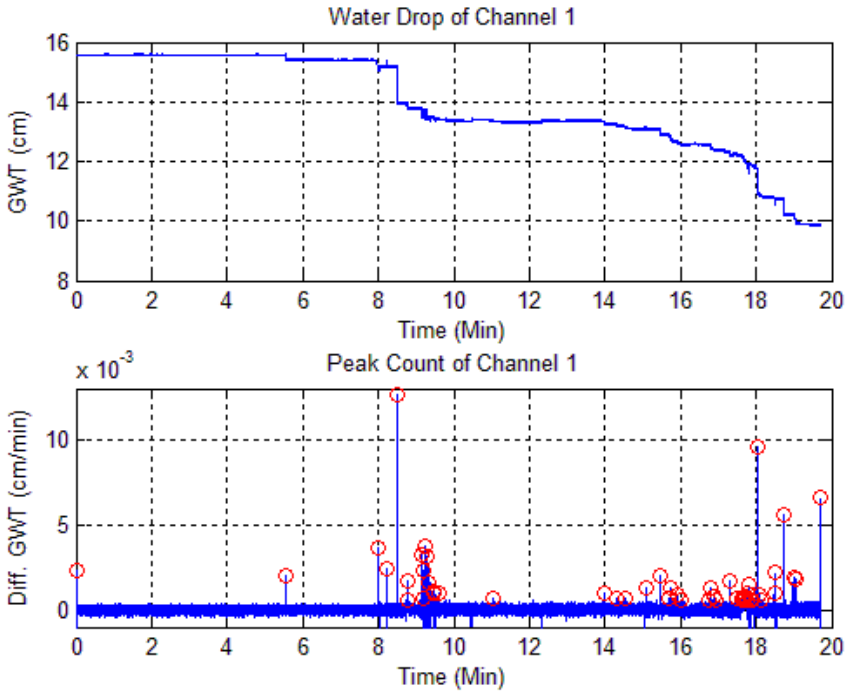

Figure 133: Peak counting of sample 1 with thickness of 150mm, G.W.T = 22.5mm, and radius (R) = 10.4cm

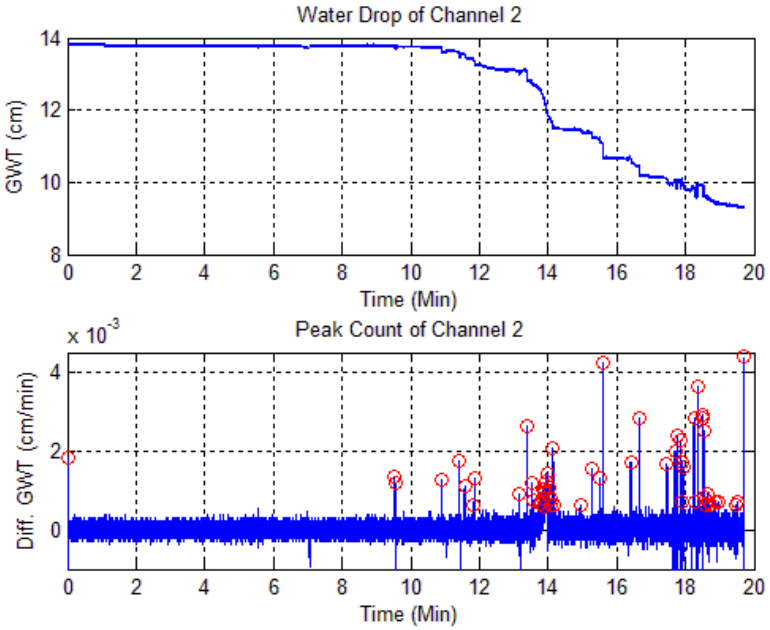

Figure 134: Peak counting of sample 1 with thickness of 150mm, G.W.T = 22.5mm, and radius (R) = 13.3cm

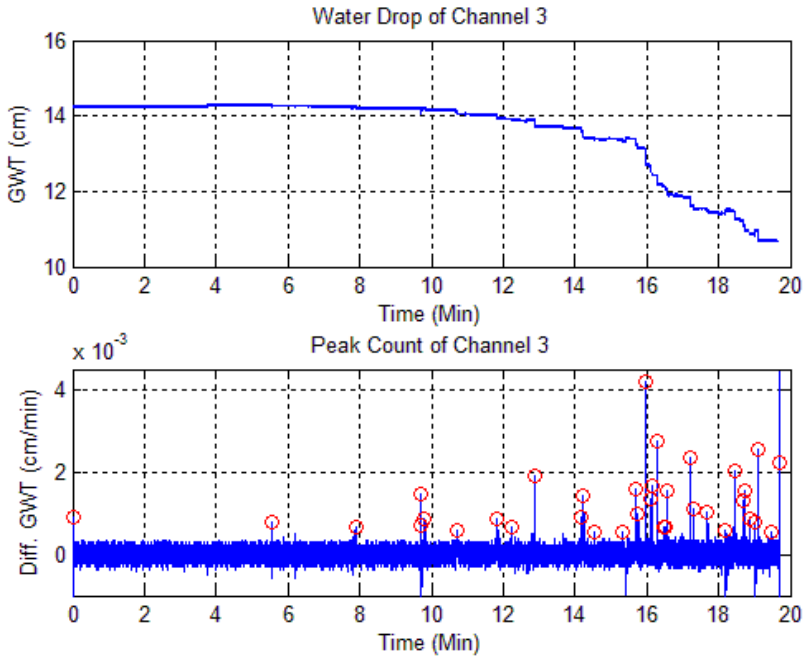

Figure 135: Peak counting of sample 1 with thickness of 150mm, G.W.T = 22.5mm, and radius (R) = 13.9cm

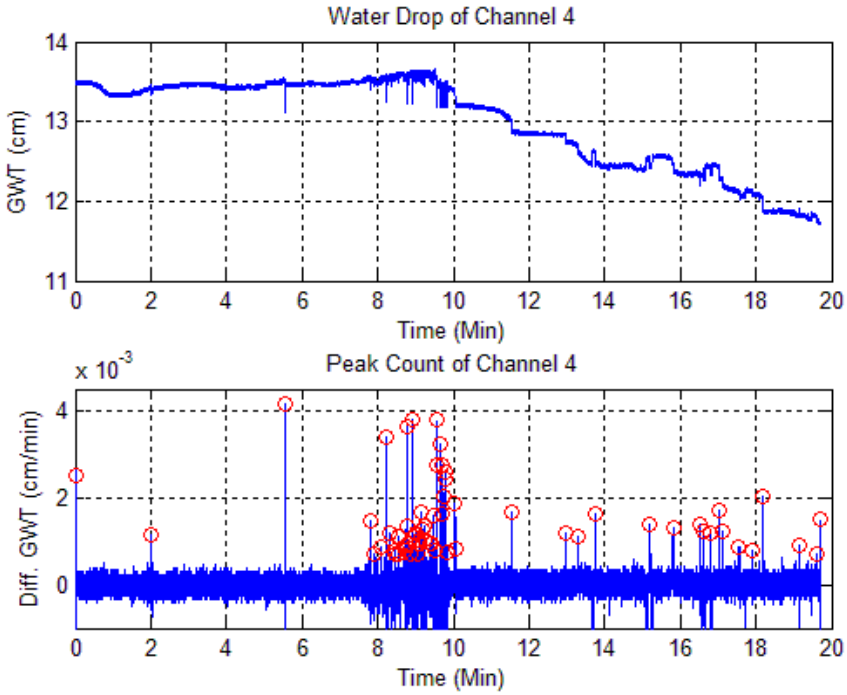

Figure 136: Peak counting of sample 1 with thickness of 150mm, G.W.T = 22.5mm, and radius (R) = 16cm

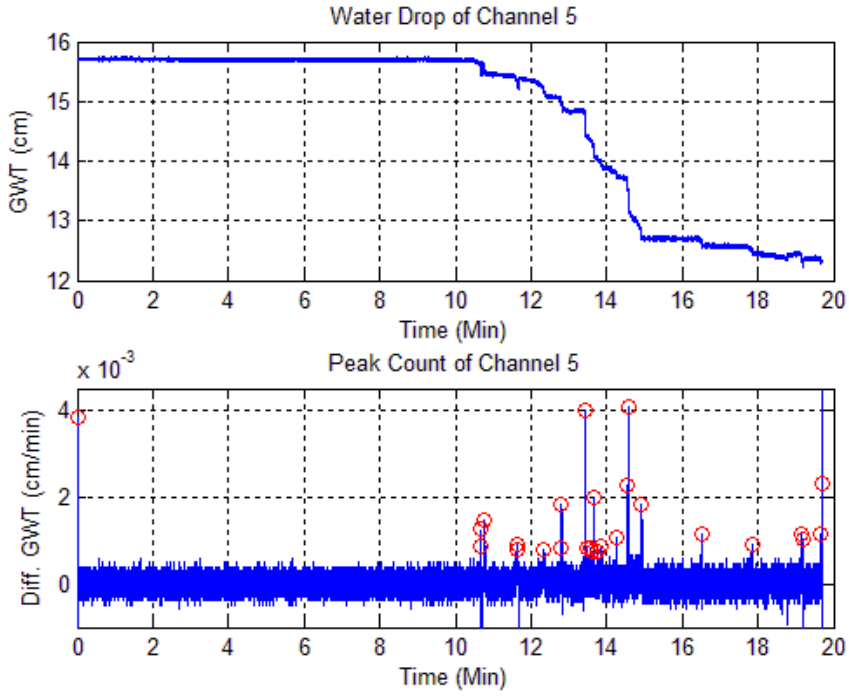

Figure 137: Peak counting of sample 1 with thickness of 150mm, G.W.T = 22.5mm, and radius (R) = 17.3cm

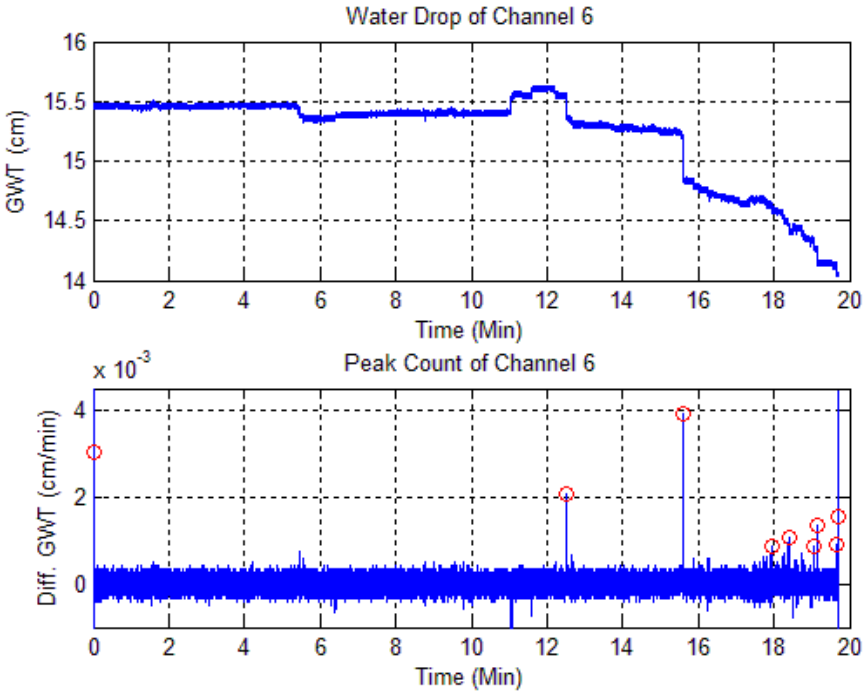

Figure 138: Peak counting of sample 1 with thickness of 150mm, G.W.T = 22.5mm, and radius (R) = 20.4cm

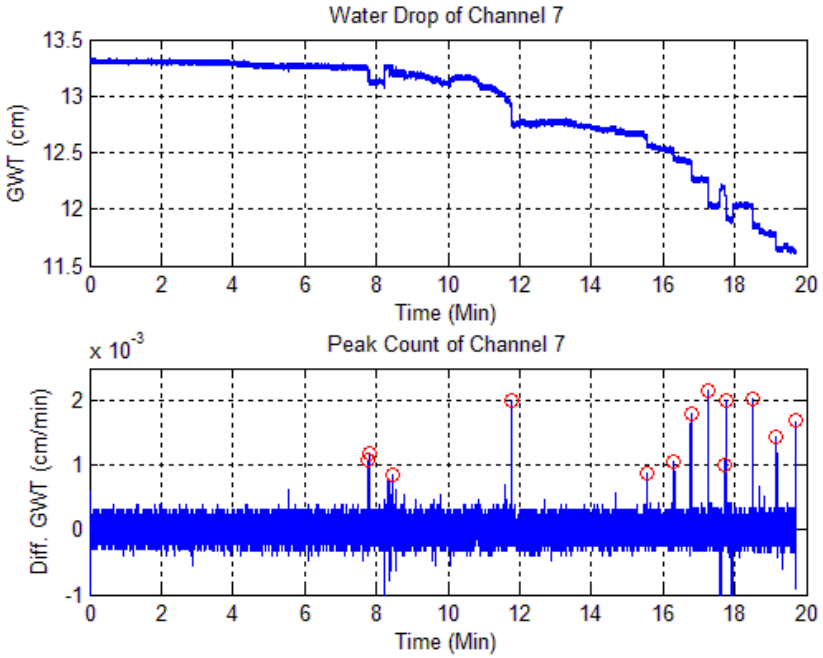

Figure 139: Peak counting of sample 1 with thickness of 150mm, G.W.T = 22.5mm, and radius (R) = 22.9cm

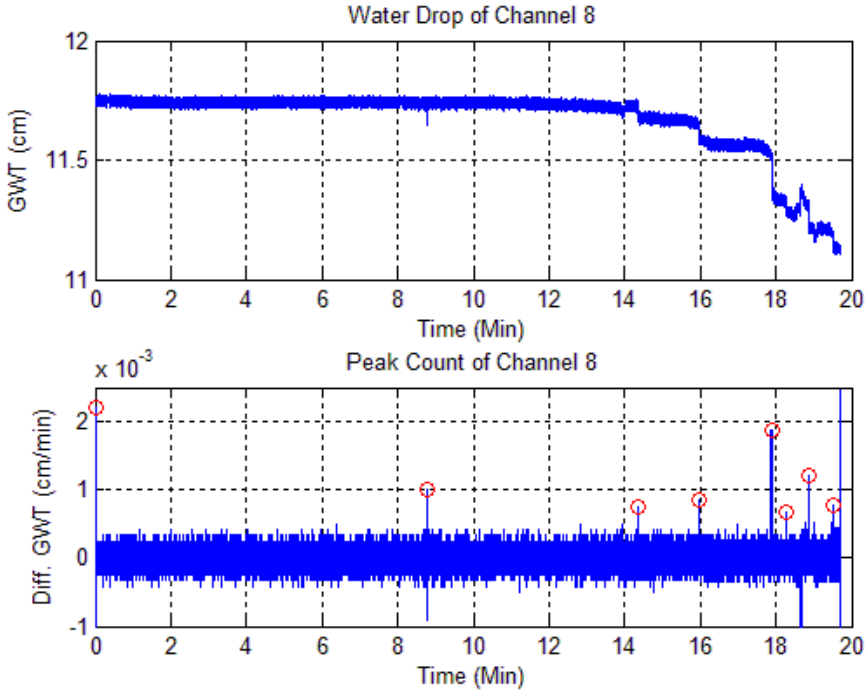

Figure 140: Peak counting of sample 1 with thickness of 150mm, G.W.T = 22.5mm, and radius (R) = 26.1cm

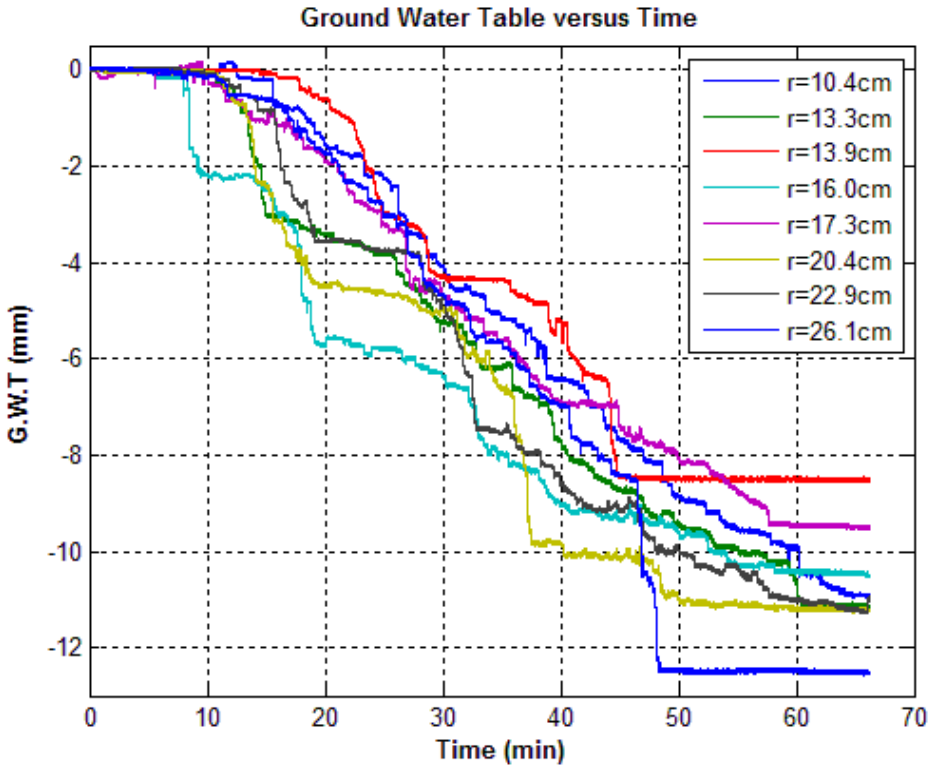

Figure 141: G.W.T over time of sample 1 with thickness of 150mm, G.W.T = 22.5mm

Sample 2 (Soil Thickness = 150mm G.W.T = 22.5mm)

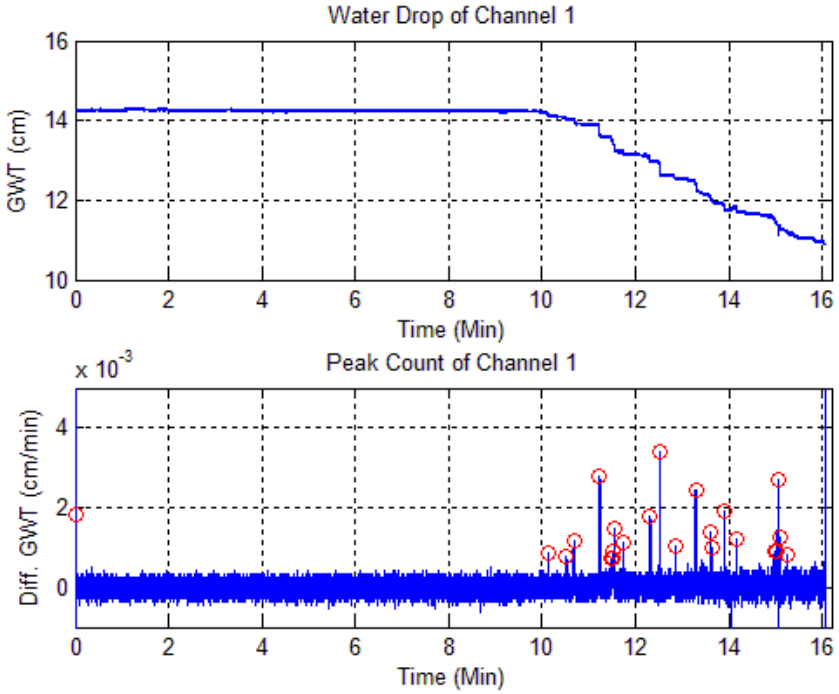

Figure 142: Peak counting of sample 2 with thickness of 150mm, G.W.T = 22.5mm, and radius (R) = 10.0cm

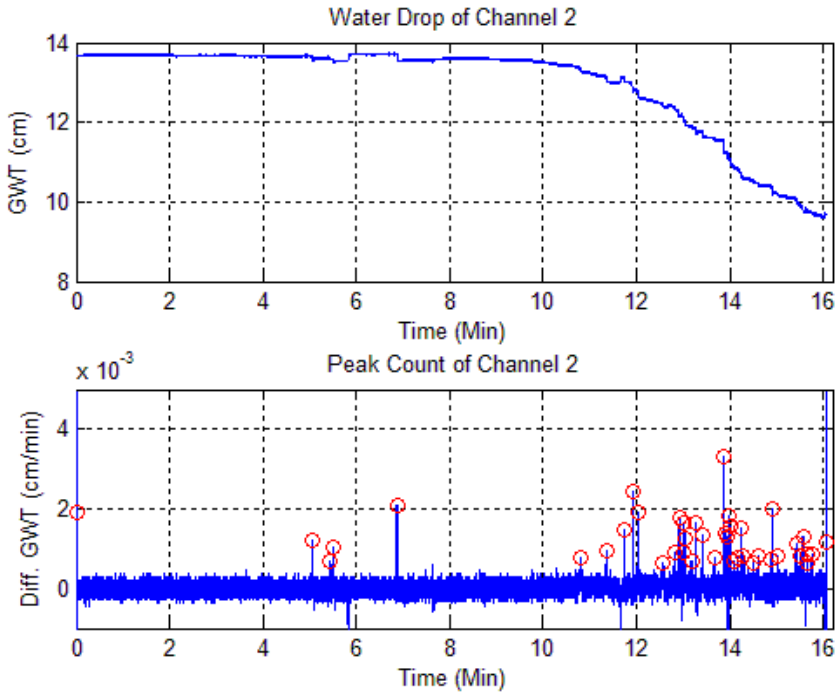

Figure 143: Peak counting of sample 2 with thickness of 150mm, G.W.T = 22.5mm, and radius (R) = 10.5cm

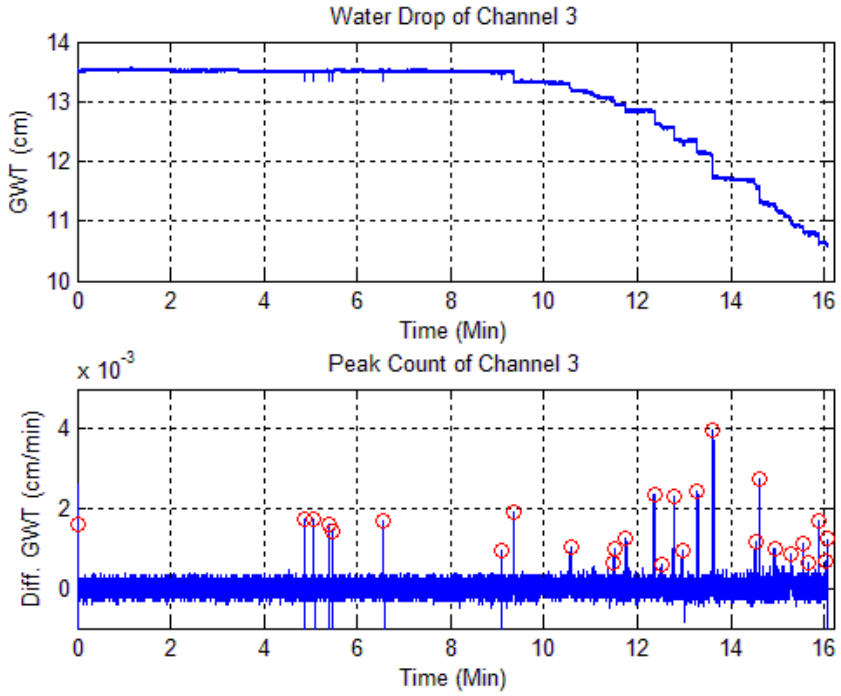

Figure 144: Peak counting of sample 2 with thickness of 150mm, G.W.T = 22.5mm, and radius (R) = 13.3cm

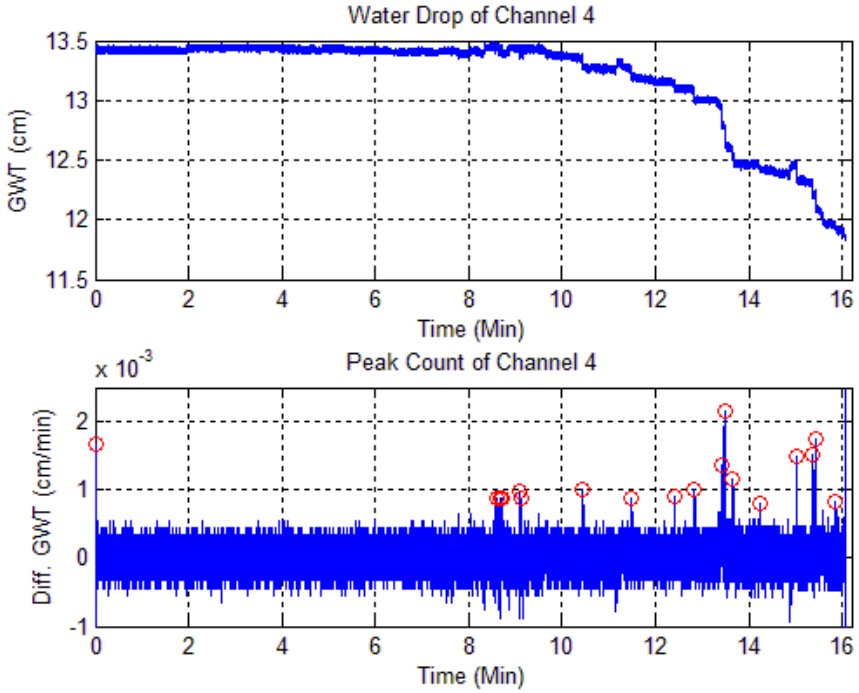

Figure 145: Peak counting of sample 2 with thickness of 150mm, G.W.T = 22.5mm, and radius (R) = 16.8cm

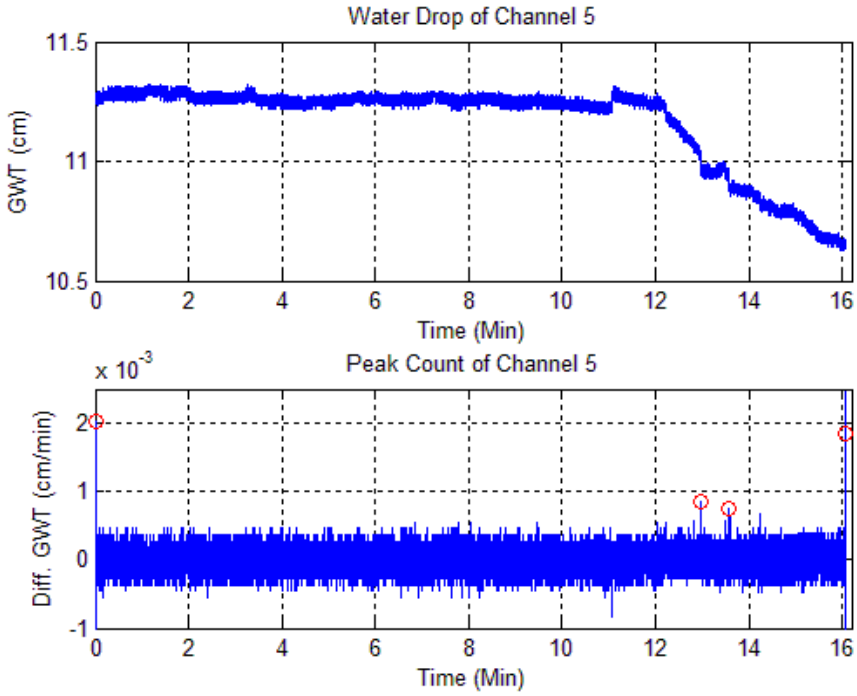

Figure 146: Peak counting of sample 2 with thickness of 150mm, G.W.T = 22.5mm, and radius (R) = 17.5cm

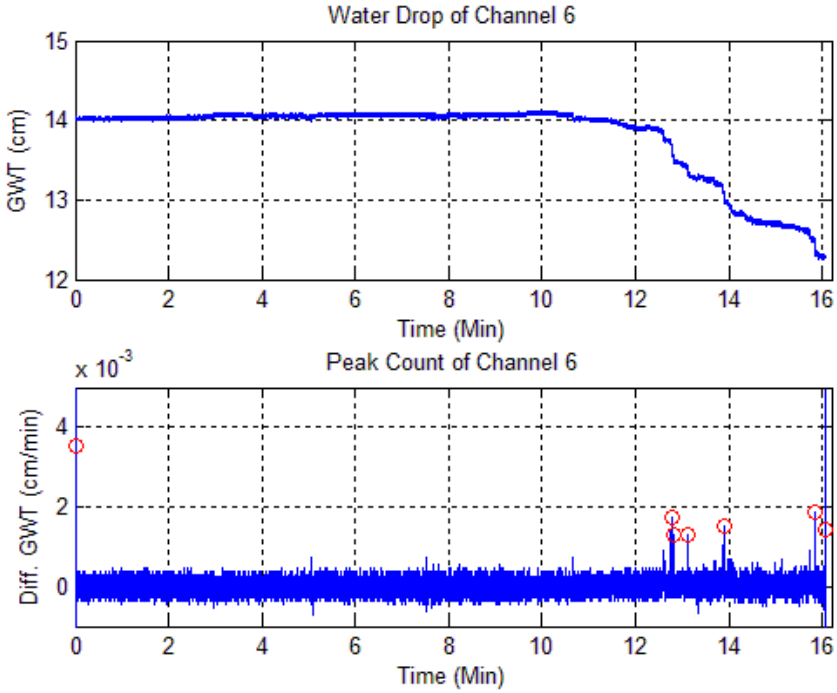

Figure 147: Peak counting of sample 2 with thickness of 150mm, G.W.T = 22.5mm, and radius (R) = 20.5cm

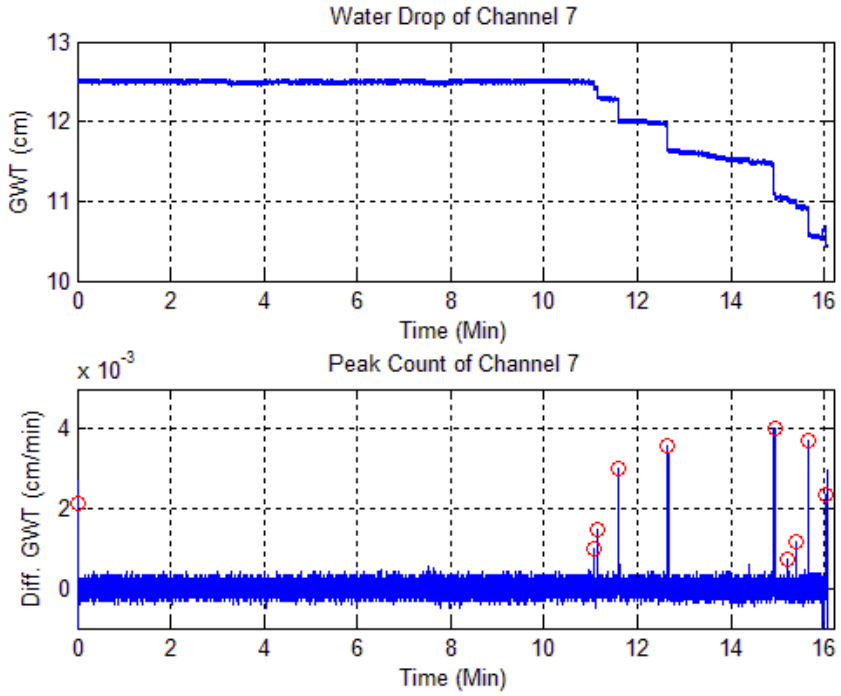

Figure 148: Peak counting of sample 2 with thickness of 150mm, G.W.T = 22.5mm, and radius (R) = 22.7cm

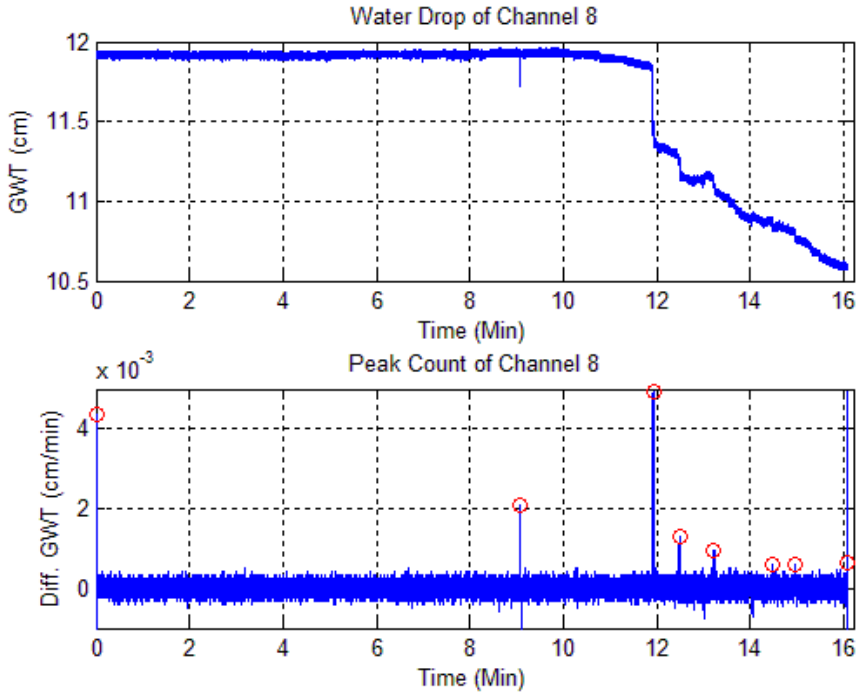

Figure 149: Peak counting of sample 2 with thickness of 150mm, G.W.T = 22.5mm, and radius (R) = 26.1cm

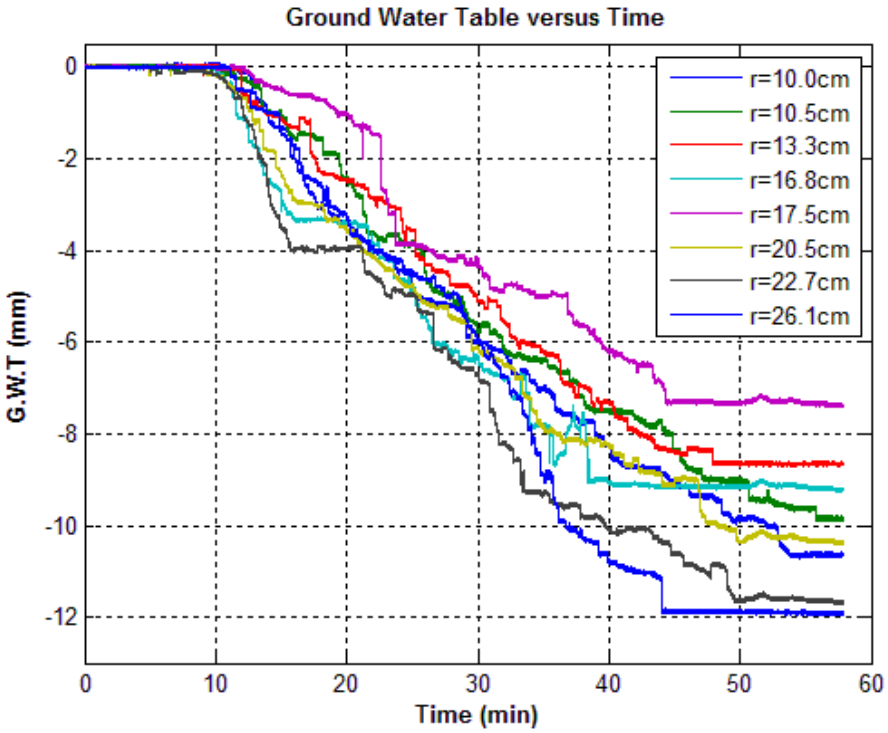

Figure 150: G.W.T over time of sample 2 with thickness of 150mm, G.W.T = 22.5mm

Sample 3 (Soil Thickness = 150mm G.W.T = 22.5mm)

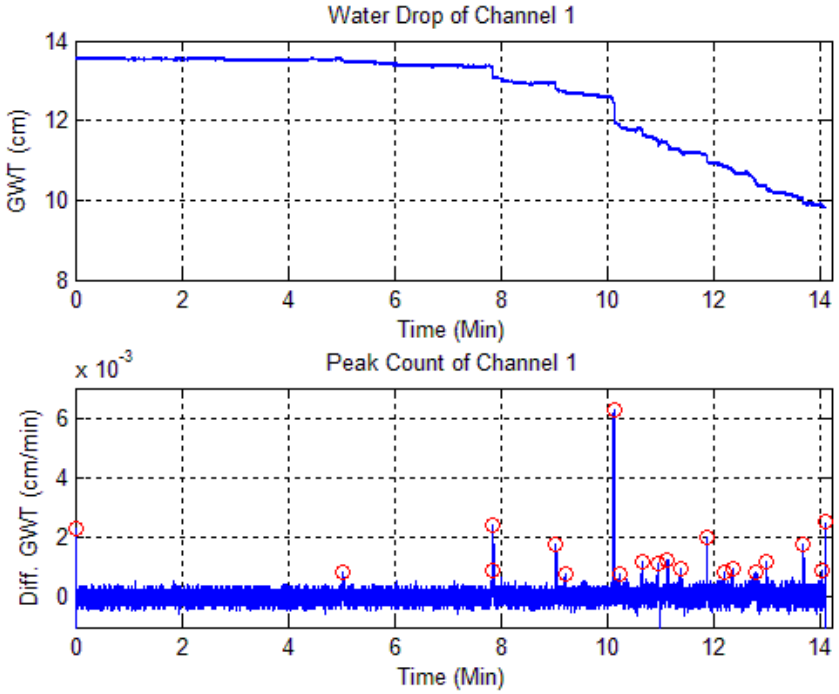

Figure 151: Peak counting of sample 3 with thickness of 150mm, G.W.T = 22.5mm, and radius (R) = 9.2cm

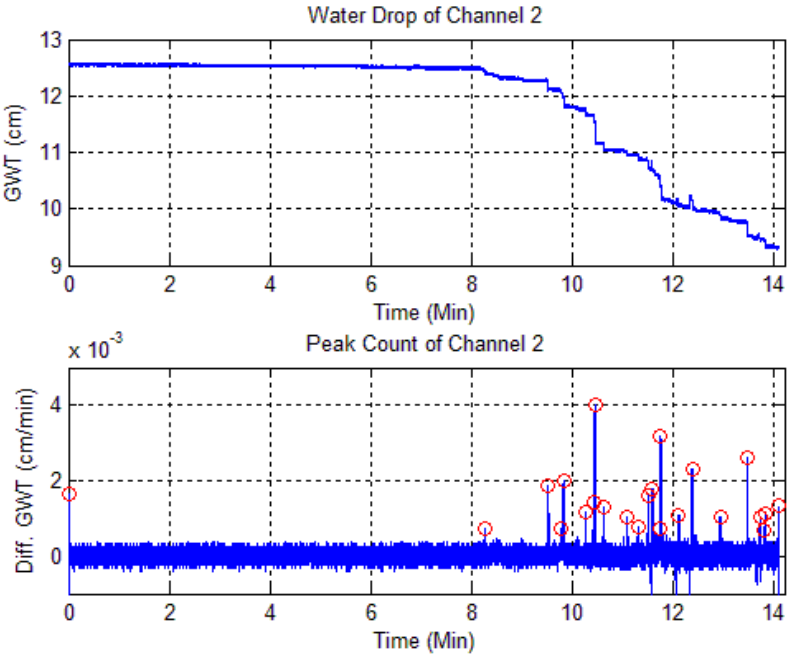

Figure 152: Peak counting of sample 3 with thickness of 150mm, G.W.T = 22.5mm, and radius (R) = 13cm

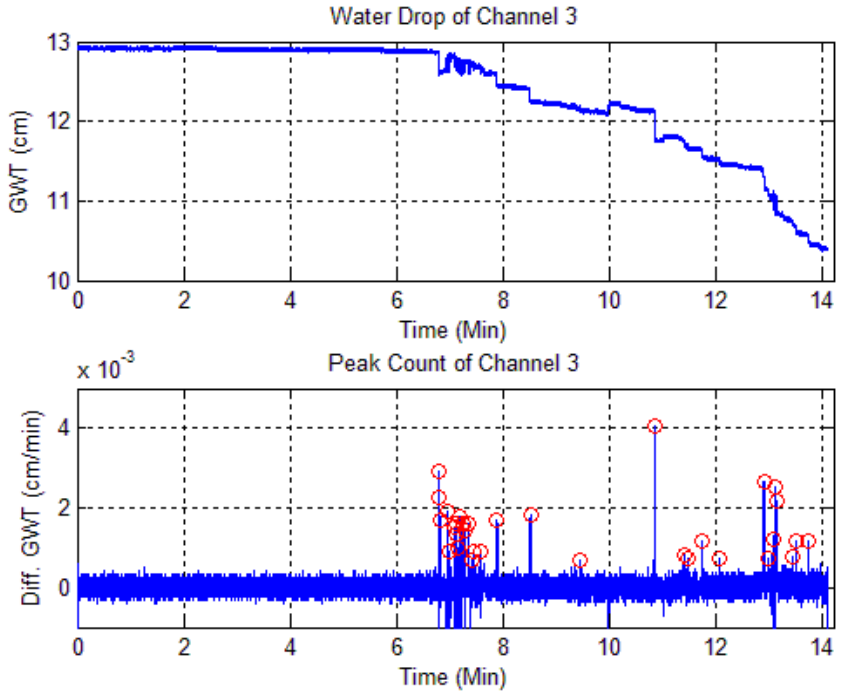

Figure 153: Peak counting of sample 3 with thickness of 150mm, G.W.T = 22.5mm, and radius (R) = 14.5cm

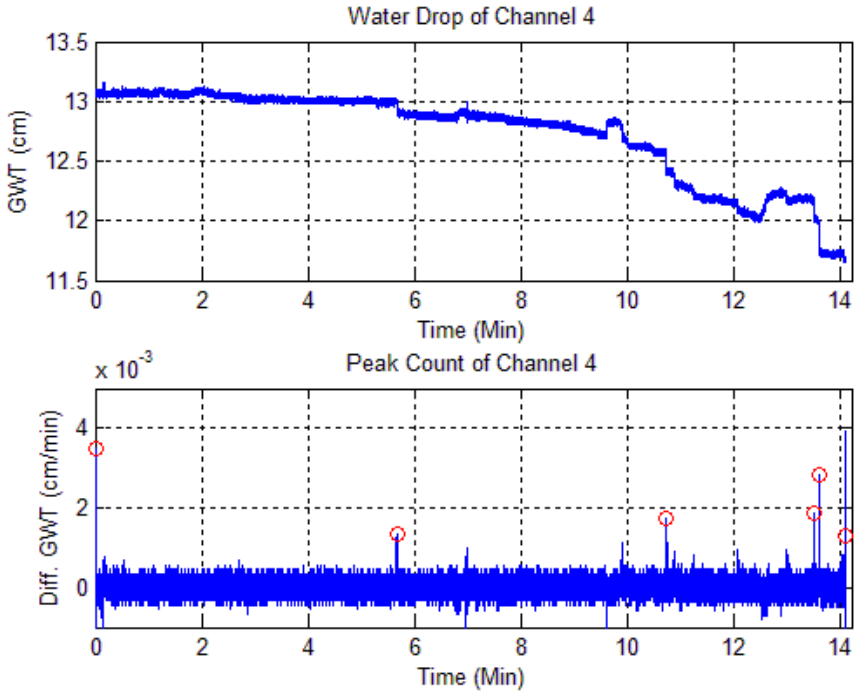

Figure 154: Peak counting of sample 3 with thickness of 150mm, G.W.T = 22.5mm, and radius (R) = 16.0cm

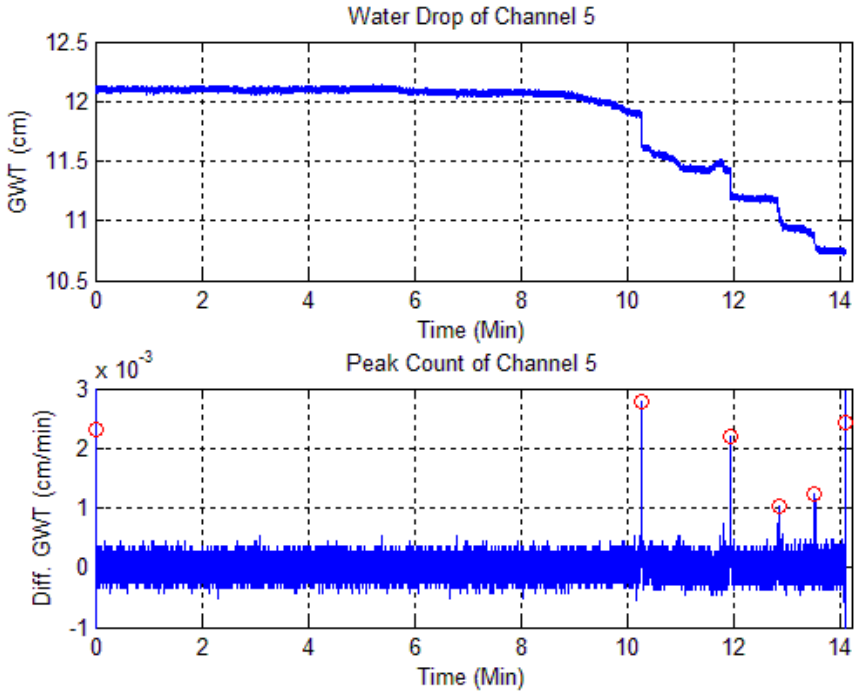

Figure 155: Peak counting of sample 3 with thickness of 150mm, G.W.T = 22.5mm, and radius (R) = 18.0cm

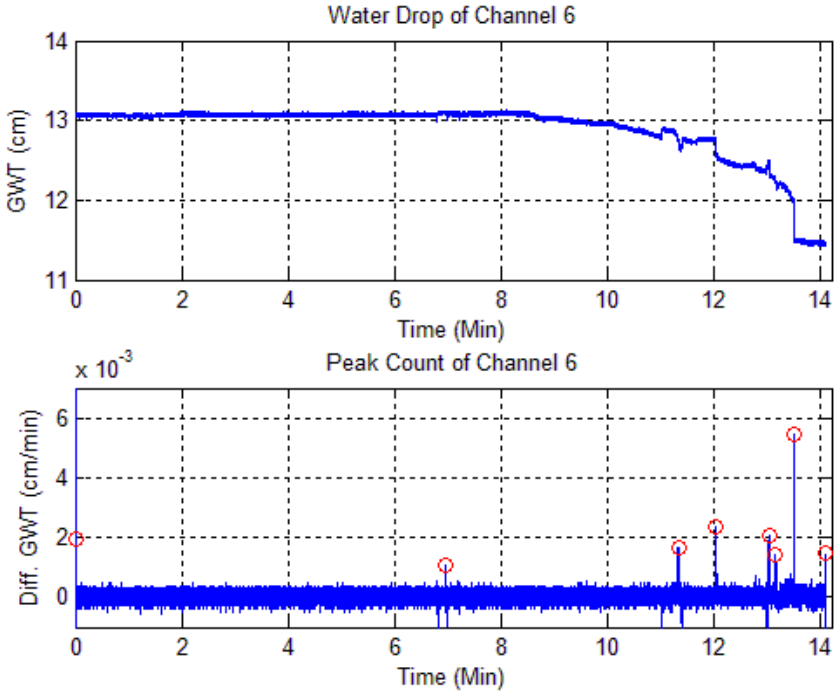

Figure 156: Peak counting of sample 3 with thickness of 150mm, G.W.T = 22.5mm, and radius (R) = 18.4cm

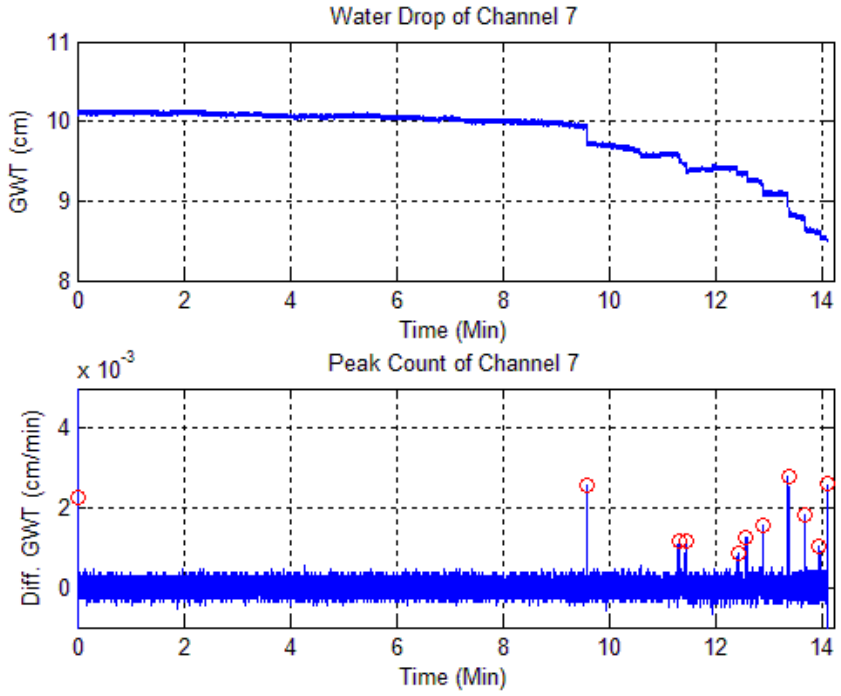

Figure 157: Peak counting of sample 3 with thickness of 150mm, G.W.T = 22.5mm, and radius (R) = 20.3cm

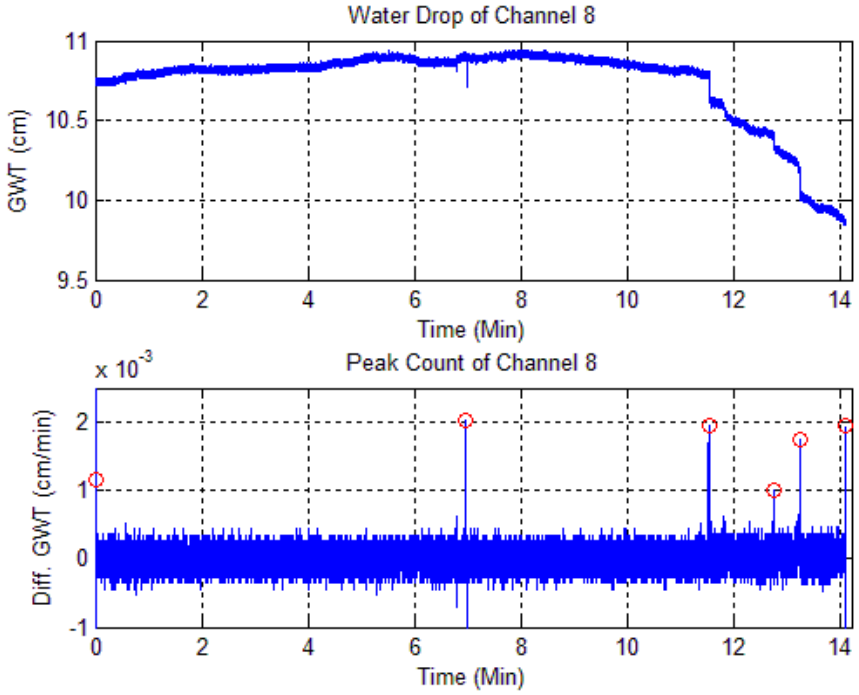

Figure 158: Peak counting of sample 3 with thickness of 150mm, G.W.T = 22.5mm, and radius (R) = 26.2cm

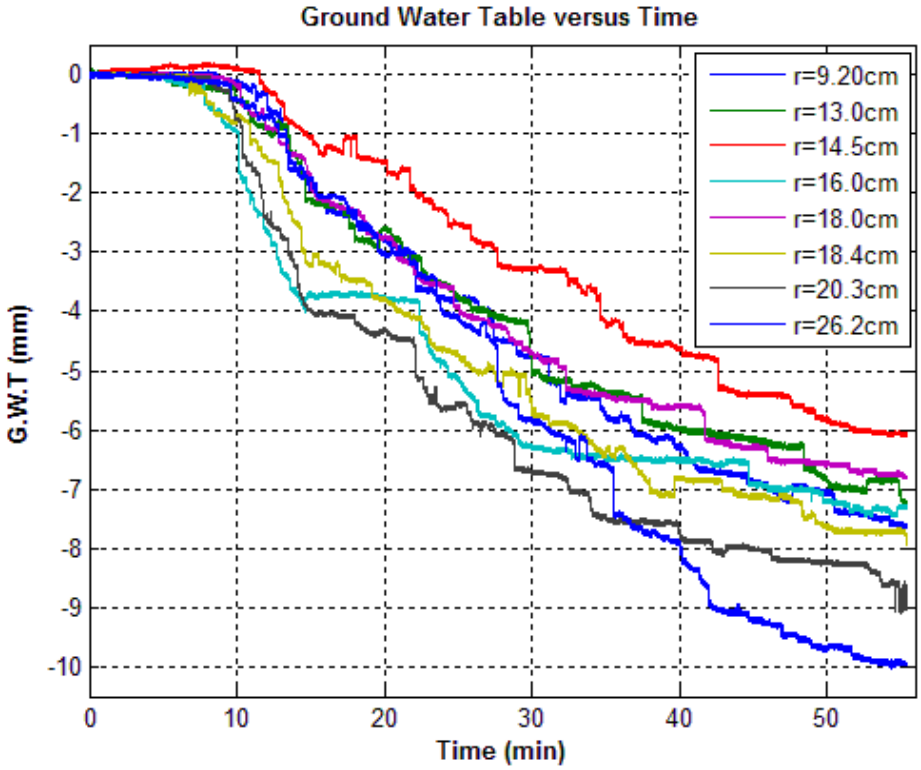

Figure 159: G.W.T over time of sample 3 with soil thickness of 150mm, G.W.T = 22.5mm

Sample 1 (Soil Thickness = 200mm G.W.T = 20mm)

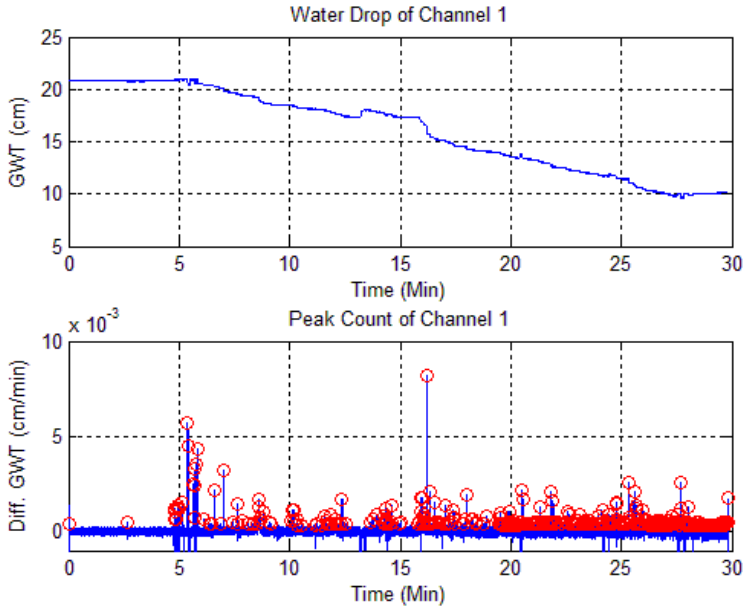

Figure 160: Peak counting of sample 1 with thickness of 200mm, G.W.T = 20mm, and radius (R) = 8.6cm

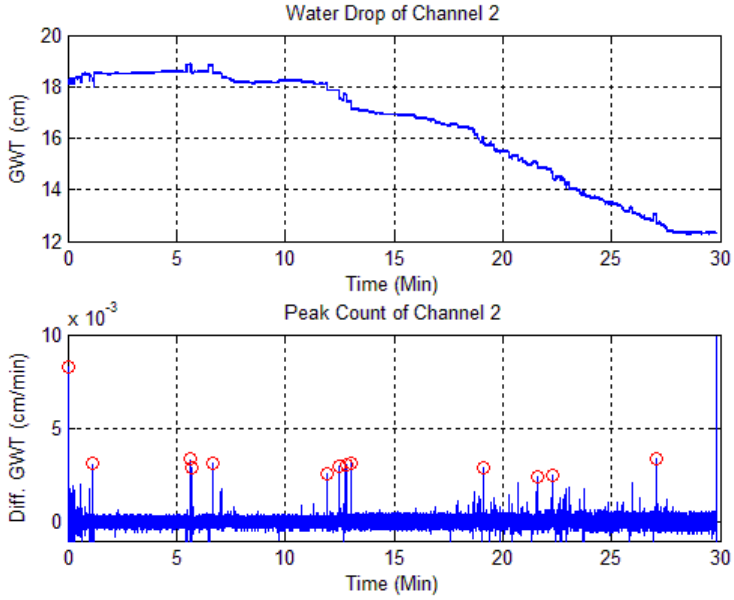

Figure 161: Peak counting of sample 1 with thickness of 200mm, G.W.T = 20mm, and radius (R) = 10cm

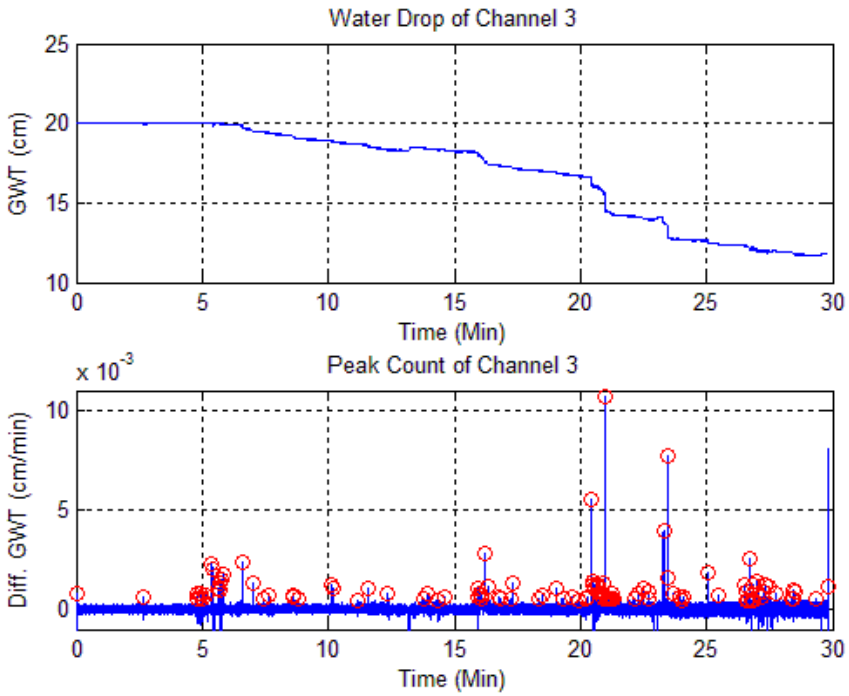

Figure 162: Peak counting of sample 1 with thickness of 200mm, G.W.T = 20mm, and radius (R) = 15.5cm

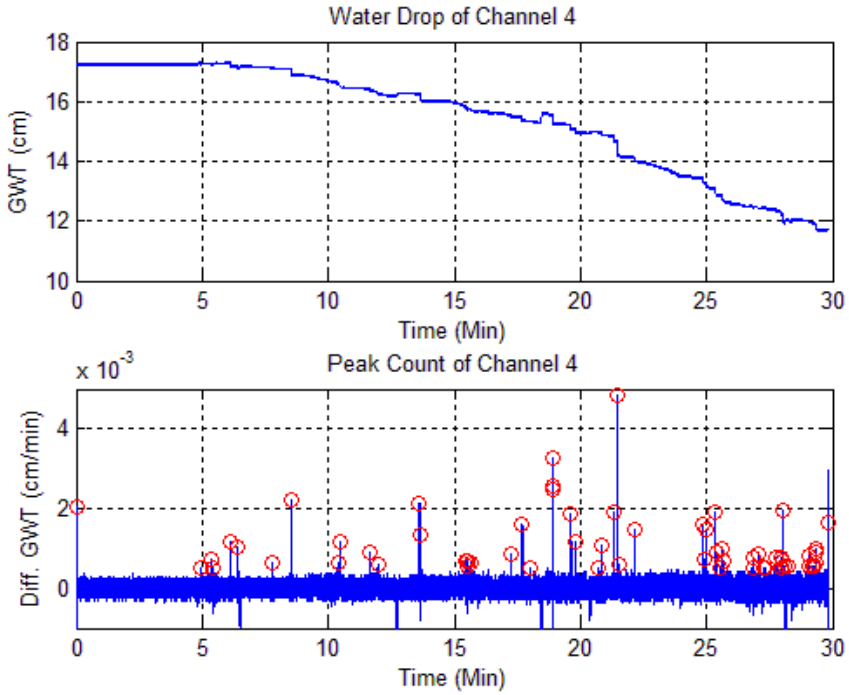

Figure 163: Peak counting of sample 1 with thickness of 200mm, G.W.T = 20mm, and radius (R) = 15.5cm

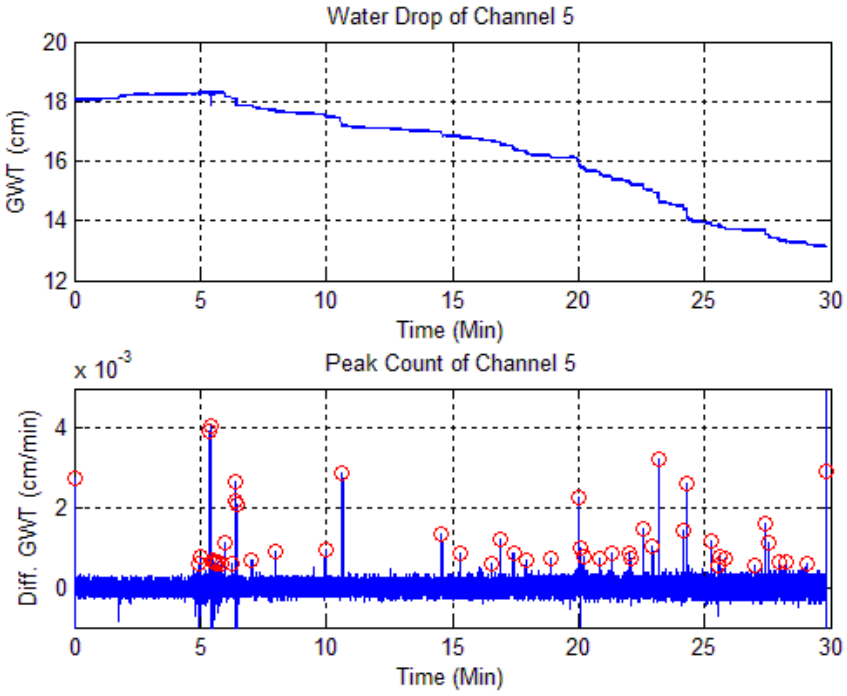

Figure 164: Peak counting of sample 1 with thickness of 200mm, G.W.T = 20mm, and radius (R) = 16.0cm

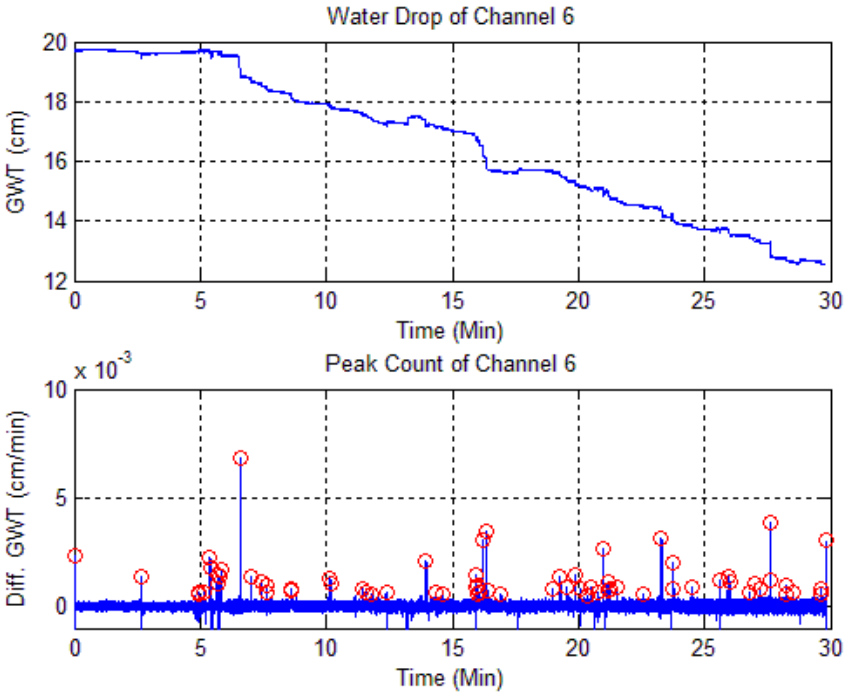

Figure 165: Peak counting of sample 1 with thickness of 200mm, G.W.T = 20mm, and radius (R) = 18.8cm

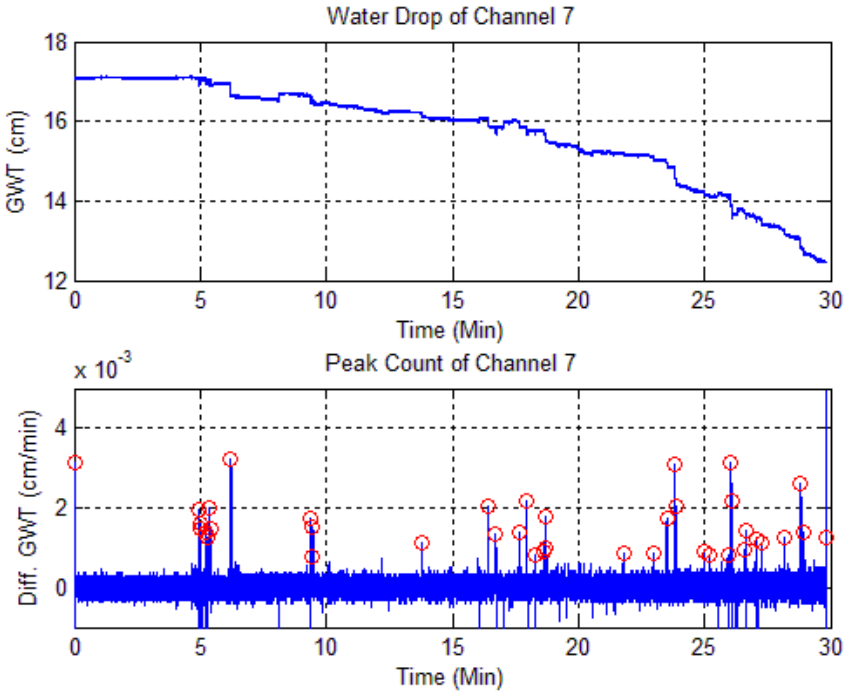

Figure 166: Peak counting of sample 1 with thickness of 200mm, G.W.T = 20mm, and radius (R) = 21.0cm

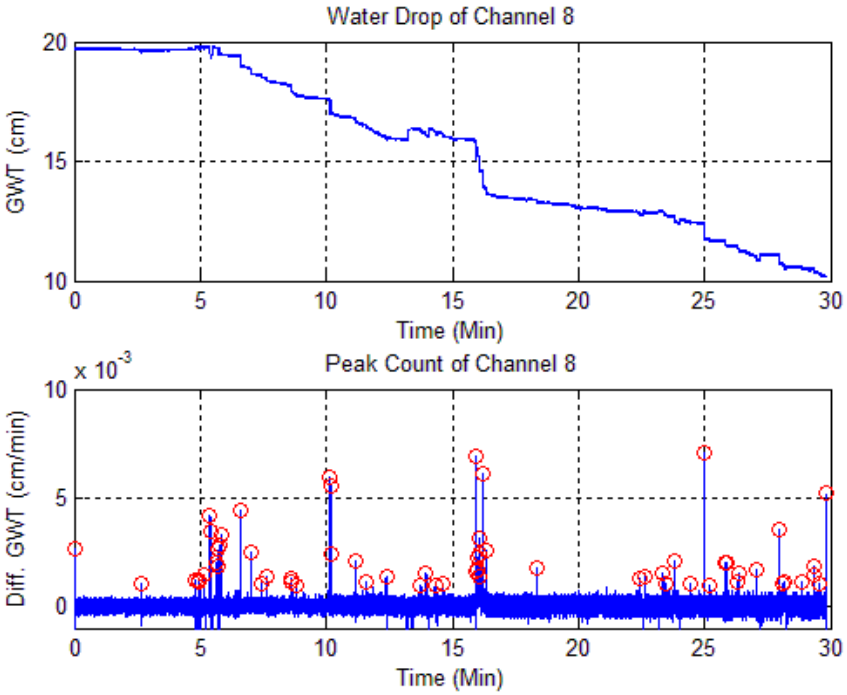

Figure 167: Peak counting of sample 1 with thickness of 200mm, G.W.T = 20mm, and radius (R) = 26.0cm

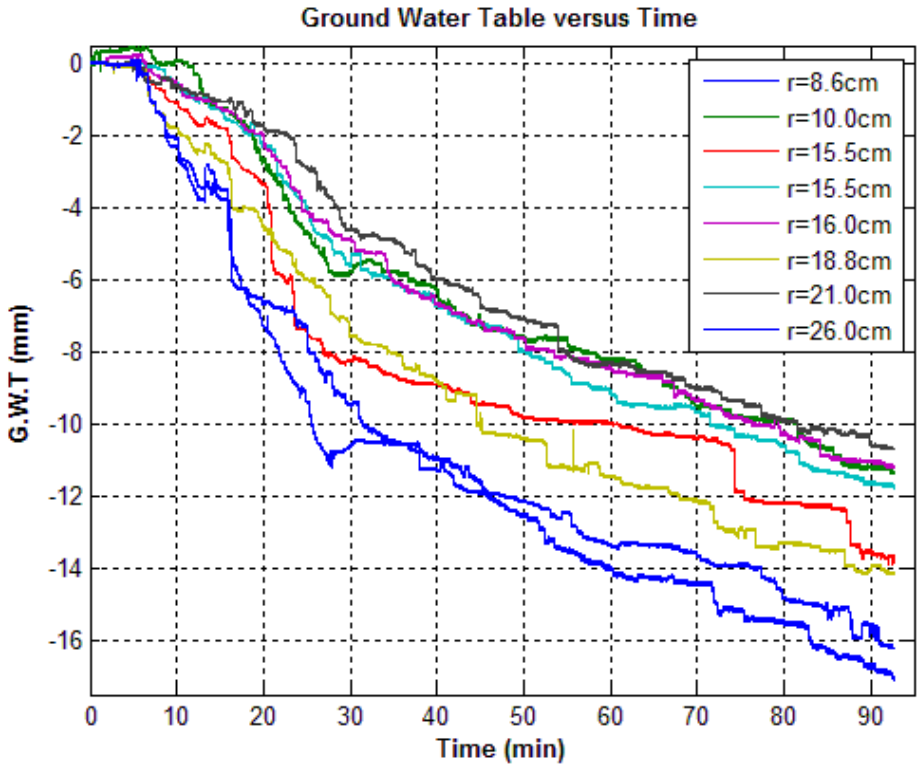

Figure 168: G.W.T over time of sample 1 with soil thickness of 200mm, G.W.T = 20mm

Sample 2 (Soil Thickness = 200mm G.W.T = 20mm)

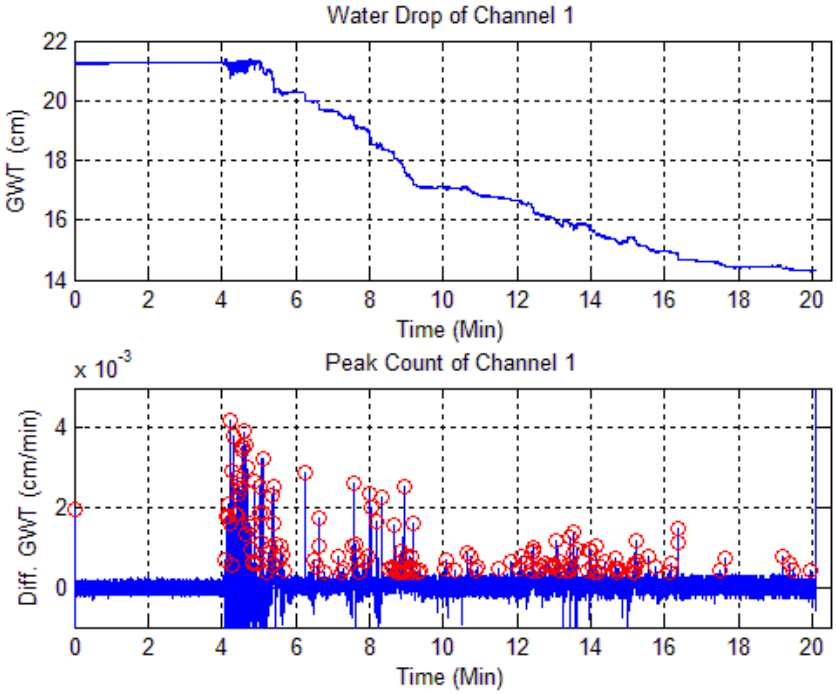

Figure 169: Peak counting of sample 2 with thickness of 200mm, G.W.T = 20mm, and radius (R) = 9.2cm

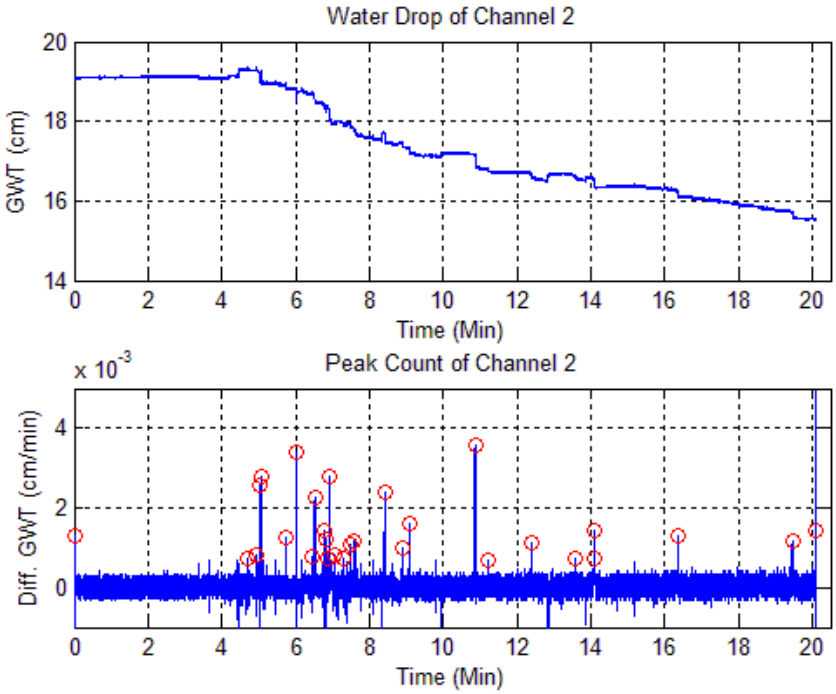

Figure 170: Peak counting of sample 2 with thickness of 200mm, G.W.T = 20mm, and radius (R) = 11.0cm

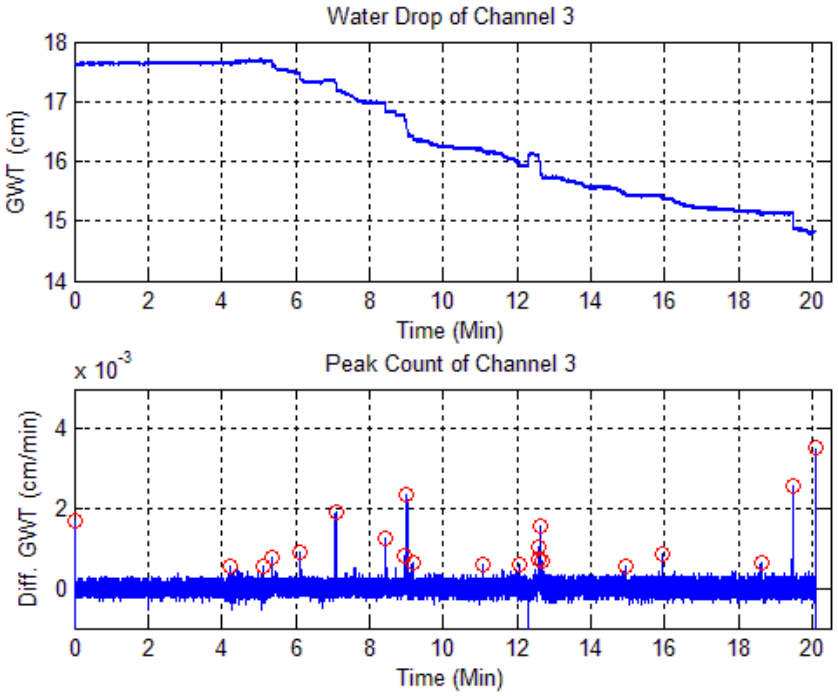

Figure 171: Peak counting of sample 2 with thickness of 200mm, G.W.T = 20mm, and radius (R) = 14.0cm

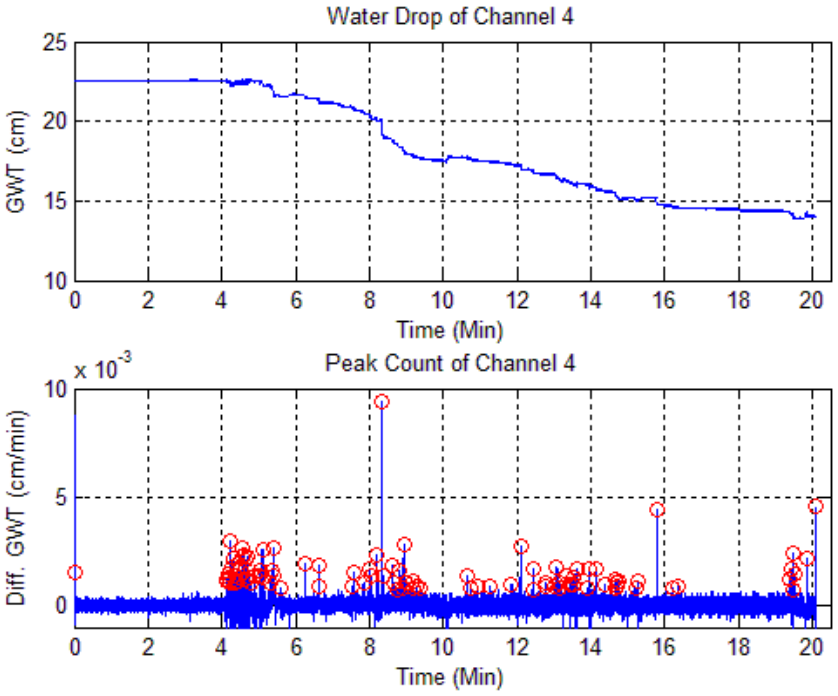

Figure 172: Peak counting of sample 2 with thickness of 200mm, G.W.T = 20mm, and radius (R) = 15.0cm

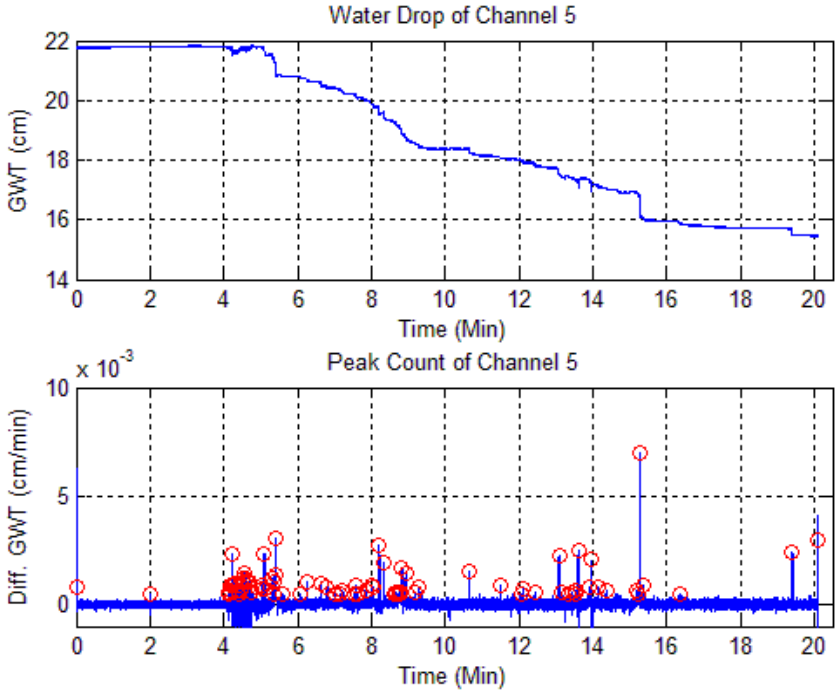

Figure 173: Peak counting of sample 2 with thickness of 200mm, G.W.T = 20mm, and radius (R) = 16.8cm

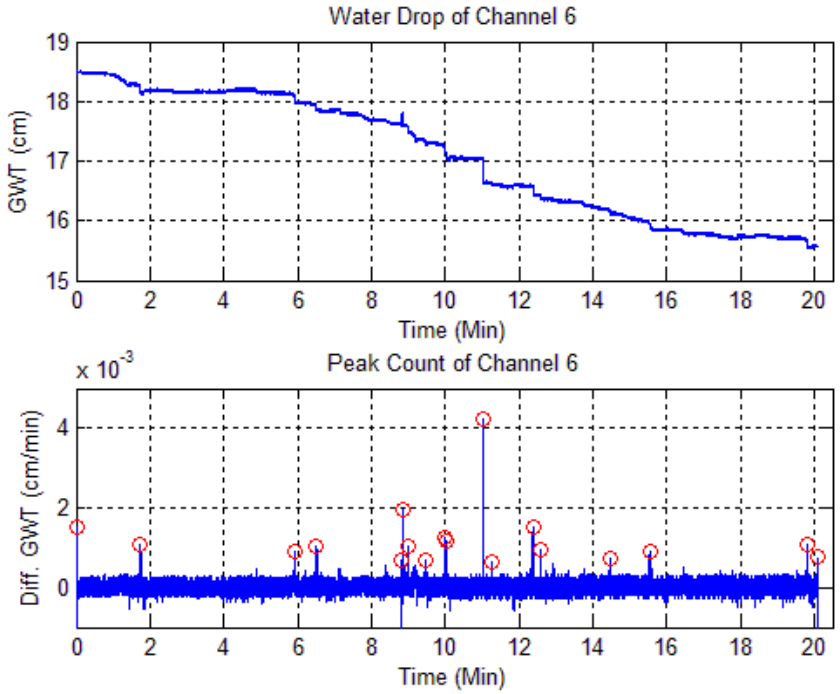

Figure 174: Peak counting of sample 2 with thickness of 200mm, G.W.T = 20mm, and radius (R) = 18.5cm

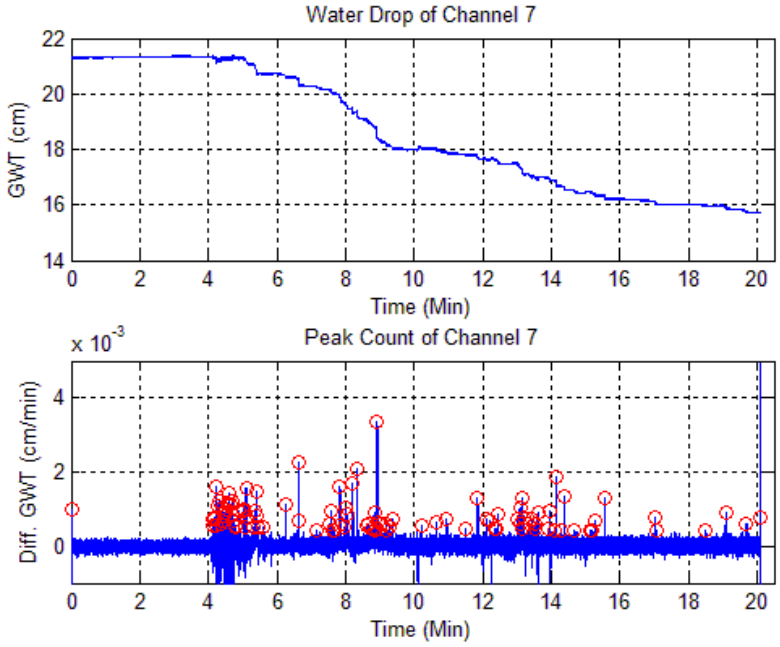

Figure 175: Peak counting of sample 2 with thickness of 200mm, G.W.T = 20mm, and radius (R) = 19.5cm

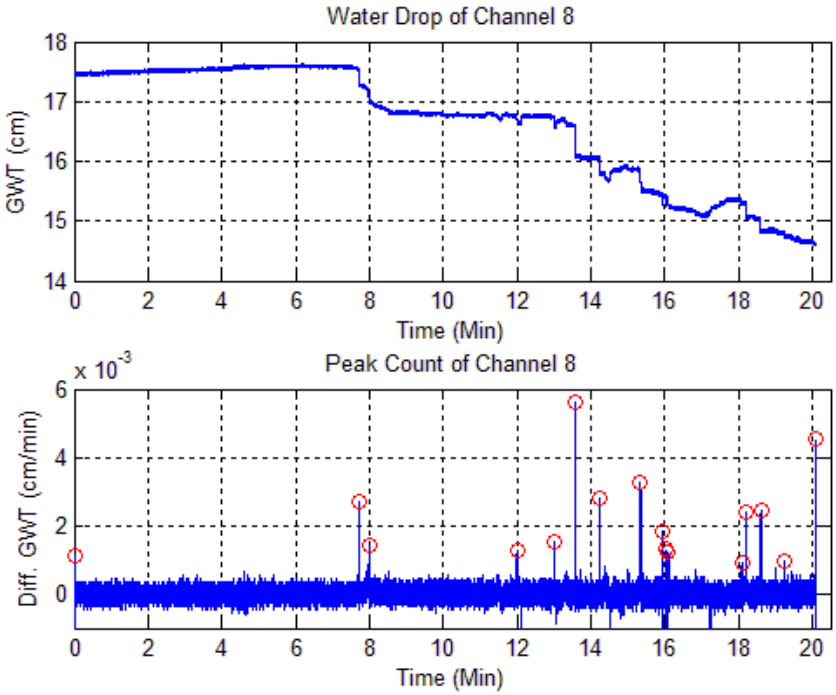

Figure 176: Peak counting of sample 2 with thickness of 200mm, G.W.T = 20mm, and radius (R) = 26.0cm

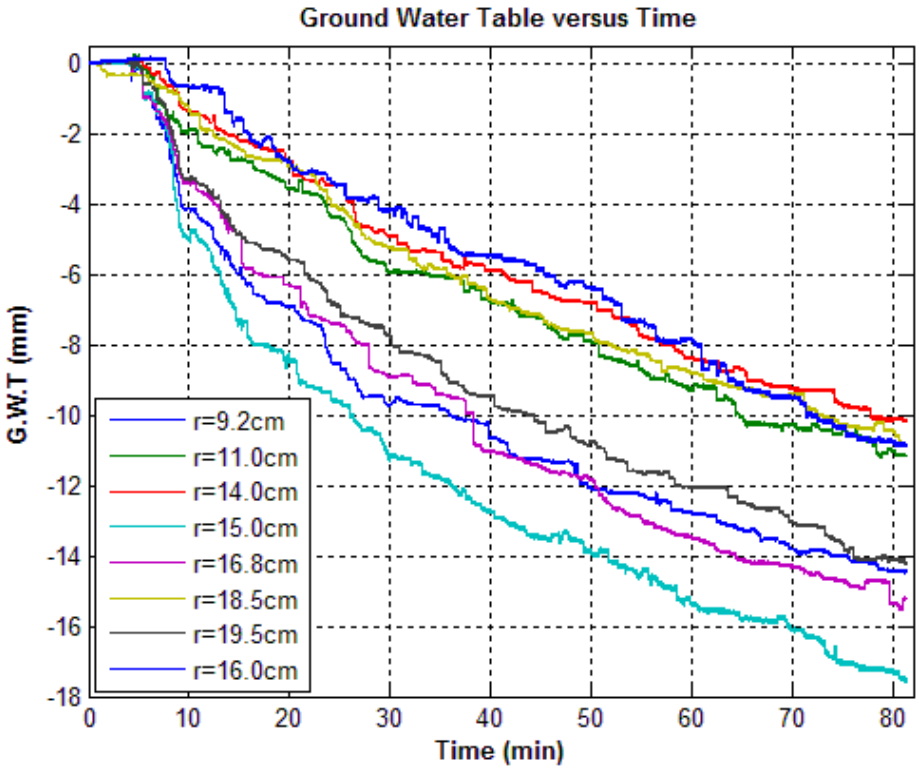

Figure 177: G.W.T over time of sample 2 with soil thickness of 200mm, G.W.T = 20mm

Sample 3 (Soil Thickness = 200mm G.W.T = 20mm)

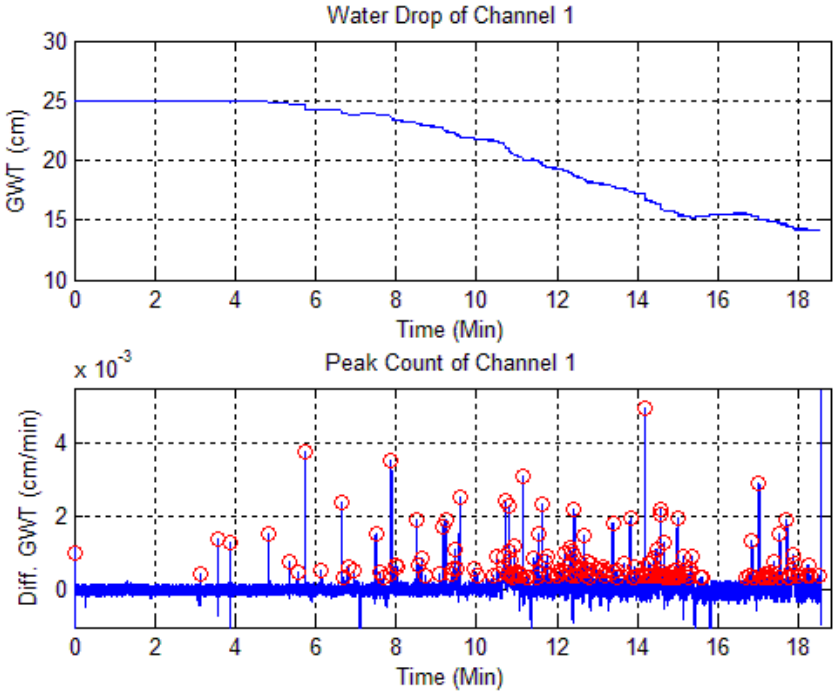

Figure 178: Peak counting of sample 3 with thickness of 200mm, G.W.T = 20mm, and radius (R) = 9.5cm

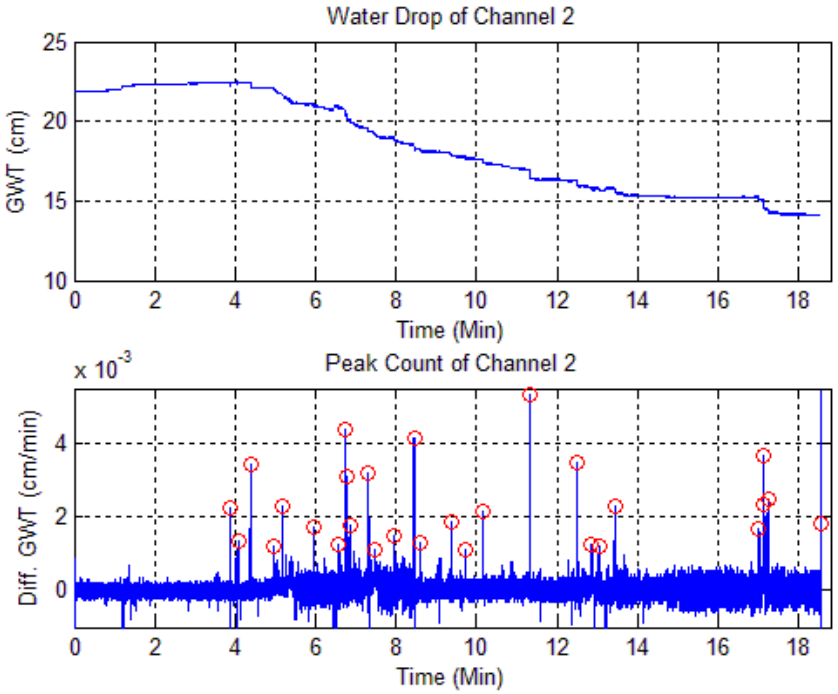

Figure 179: Peak counting of sample 3 with thickness of 200mm, G.W.T = 20mm, and radius (R) = 9.9cm

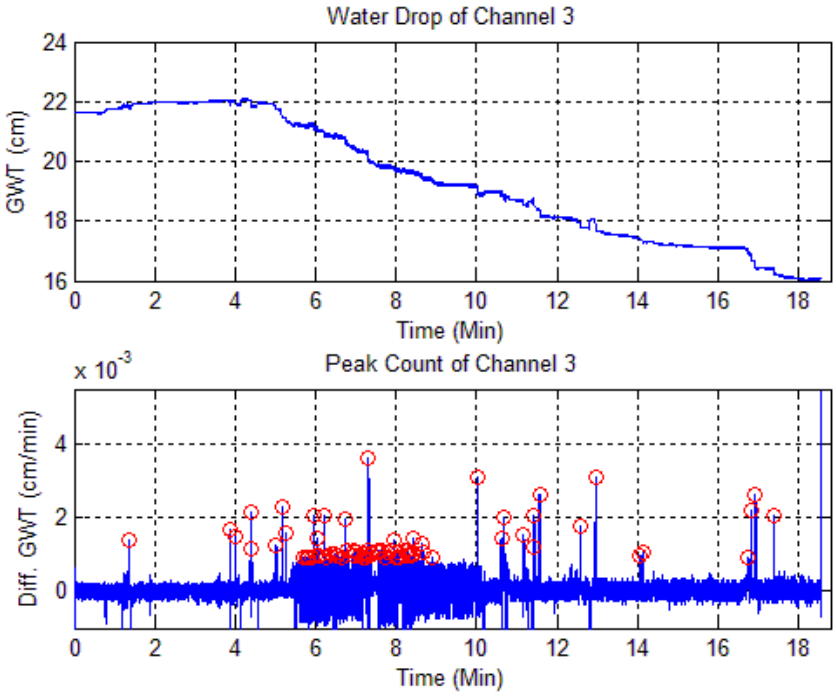

Figure 180: Peak counting of sample 3 with thickness of 200mm, G.W.T = 20mm, and radius (R) = 12.0cm

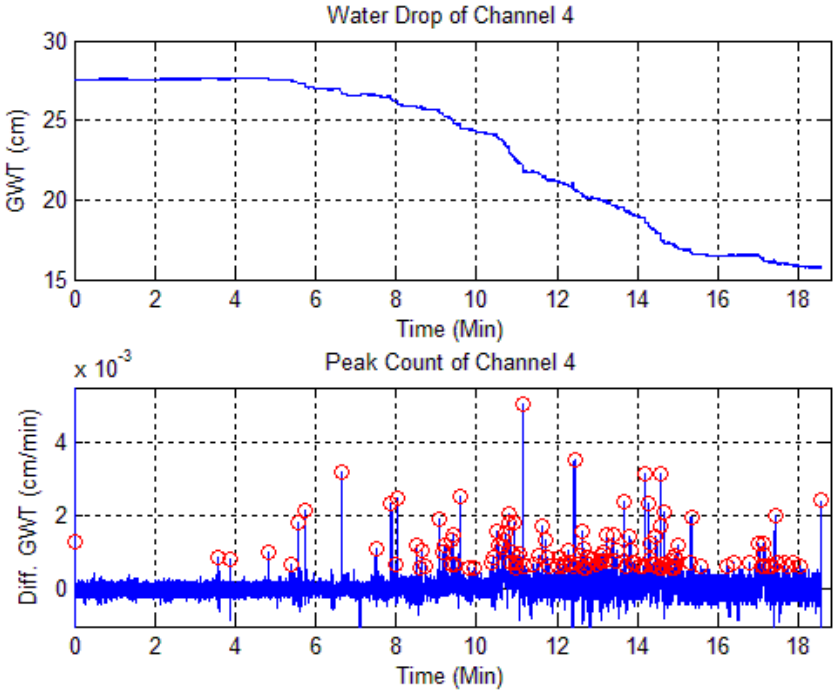

Figure 181: Peak counting of sample 3 with thickness of 200mm, G.W.T = 20mm, and radius (R) = 12.8cm

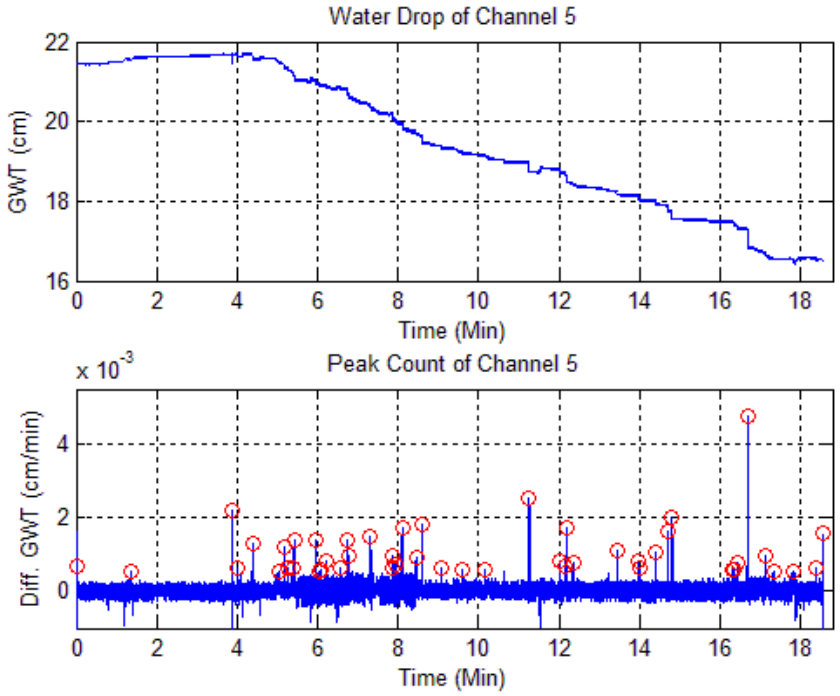

Figure 182: Peak counting of sample 3 with thickness of 200mm, G.W.T = 20mm, and radius (R) = 15.4cm

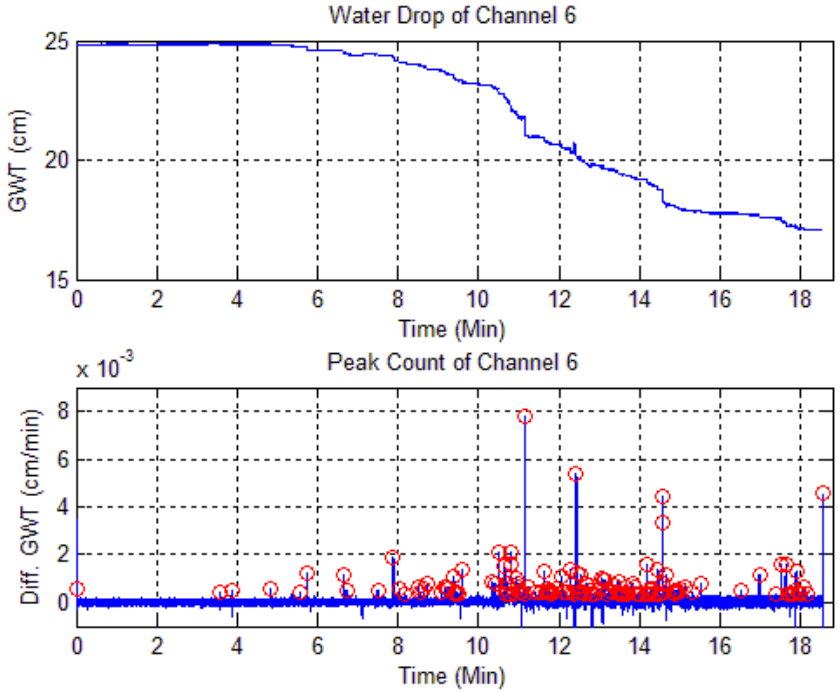

Figure 183: Peak counting of sample 3 with thickness of 200mm, G.W.T = 20mm, and radius (R) = 17.5cm

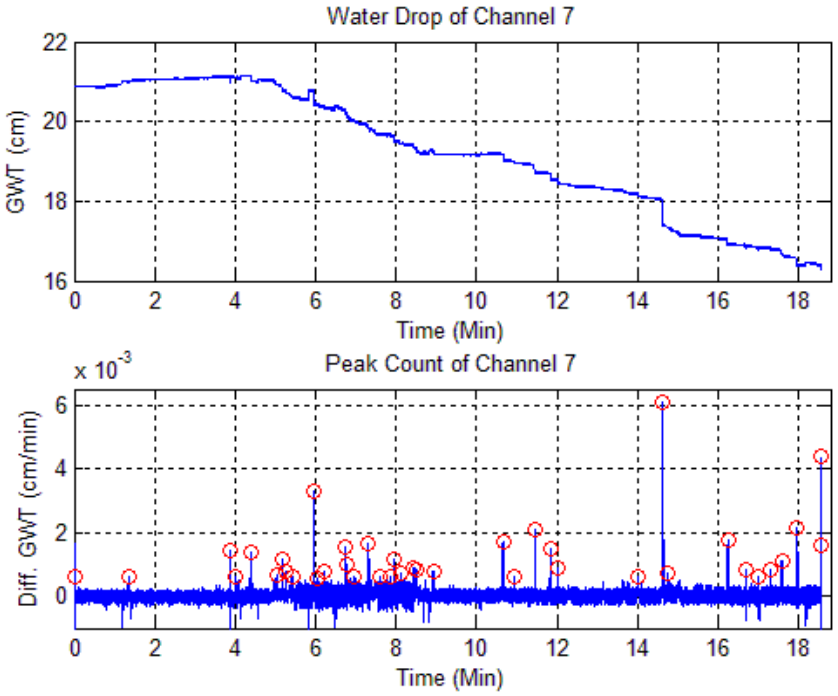

Figure 184: Peak counting of sample 3 with thickness of 200mm, G.W.T = 20mm, and radius (R) = 18.2cm

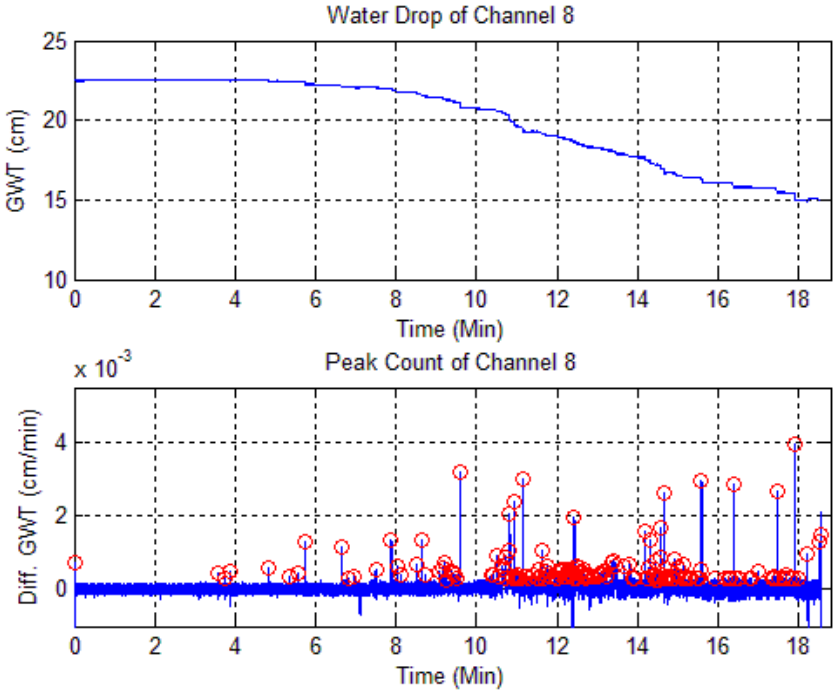

Figure 185: Peak counting of sample 3 with thickness of 200mm, G.W.T = 20mm, and radius (R) = 26.0cm

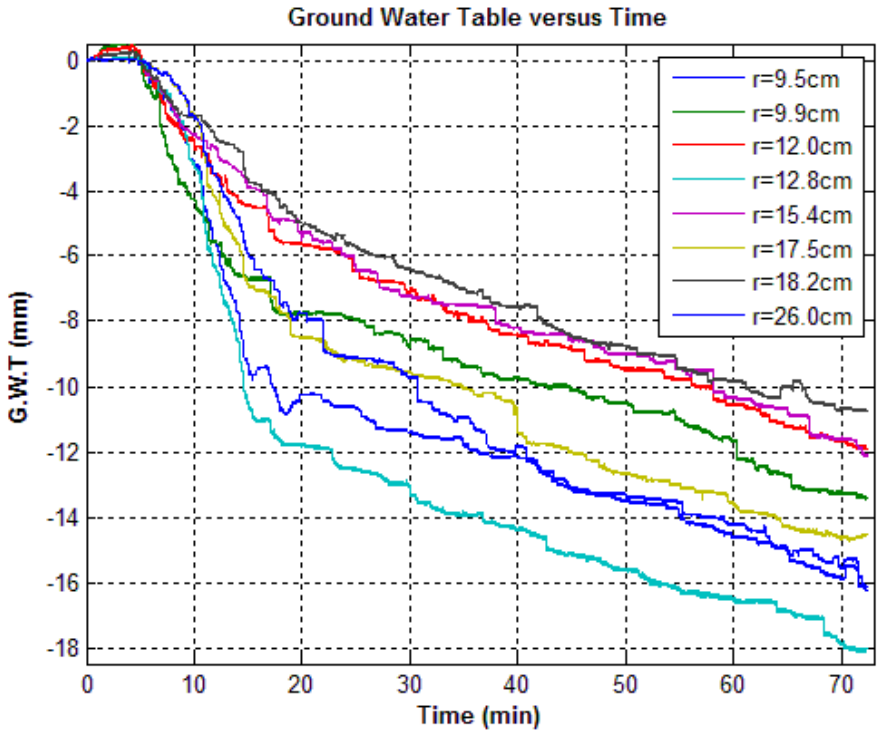

Figure 186: G.W.T over time of sample 3 with soil thickness of 200mm, G.W.T = 20mm

Sample 1 (Soil Thickness = 200mm G.W.T = 30mm)

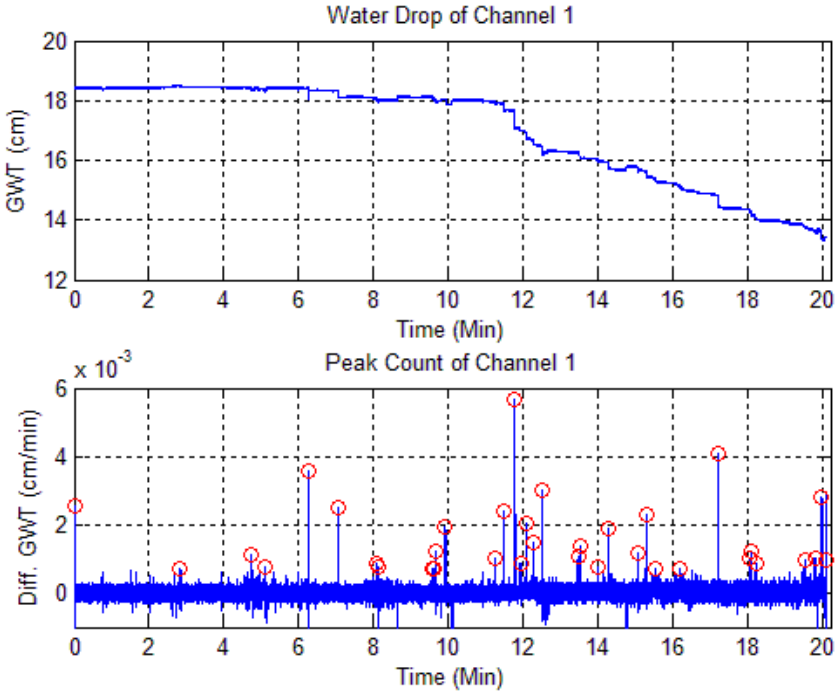

Figure 187: Peak counting of sample 1 with thickness of 200mm, G.W.T = 30mm, and radius (R) = 8.0cm

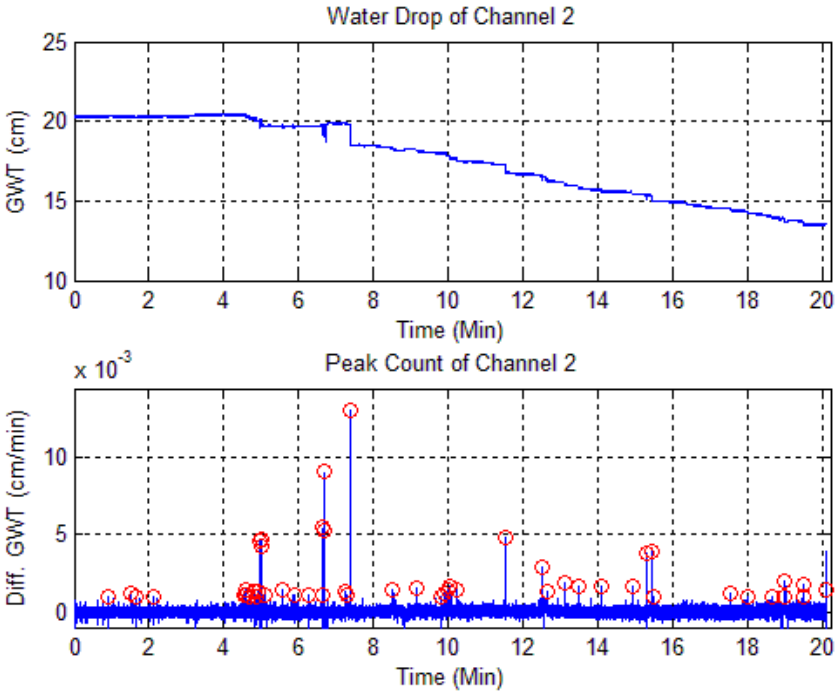

Figure 188: Peak counting of sample 1 with thickness of 200mm, G.W.T = 30mm, and radius (R) = 9.5cm

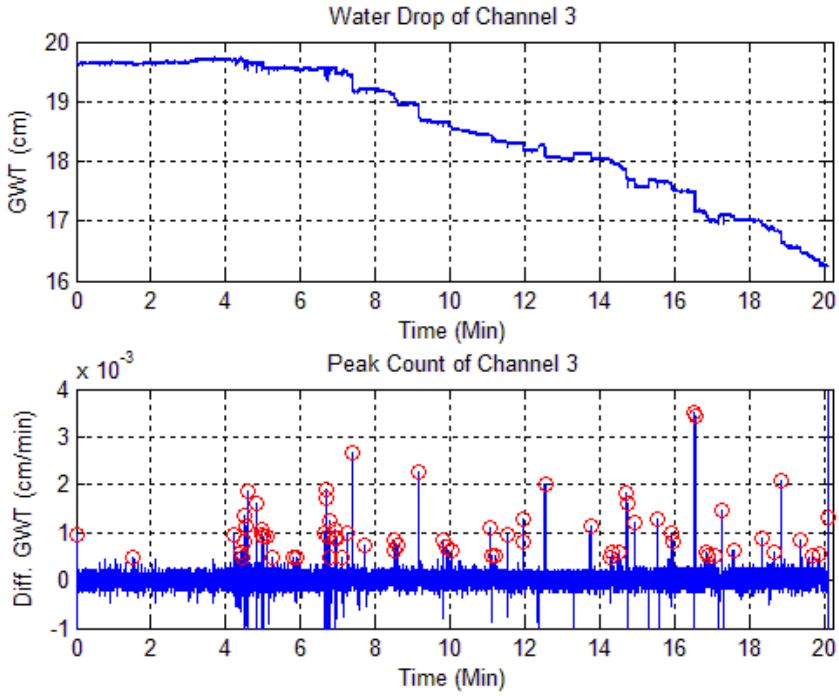

Figure 189: Peak counting of sample 1 with thickness of 200mm, G.W.T = 30mm, and radius (R) = 12.5cm

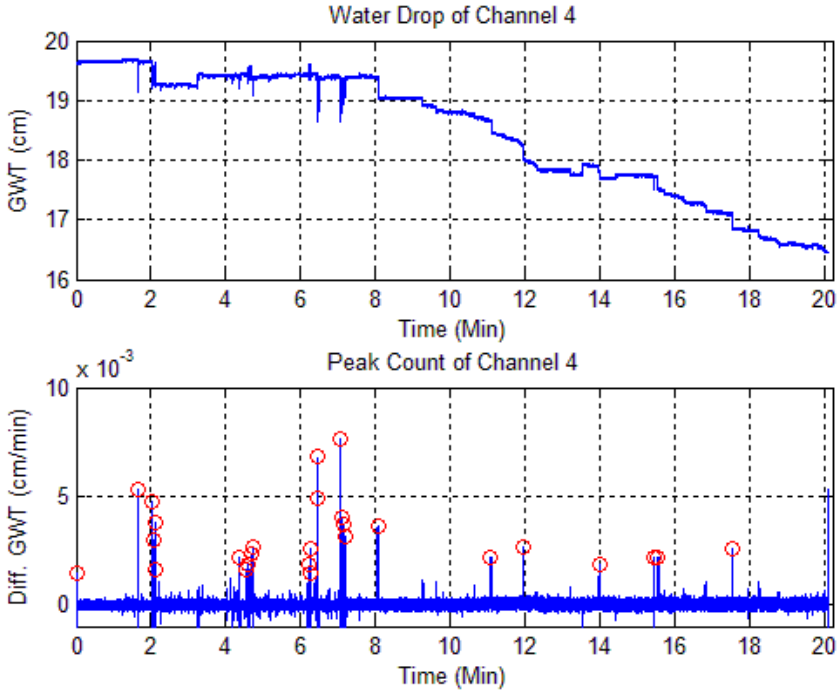

Figure 190: Peak counting of sample 1 with thickness of 200mm, G.W.T = 30mm, and radius (R) = 13.5cm

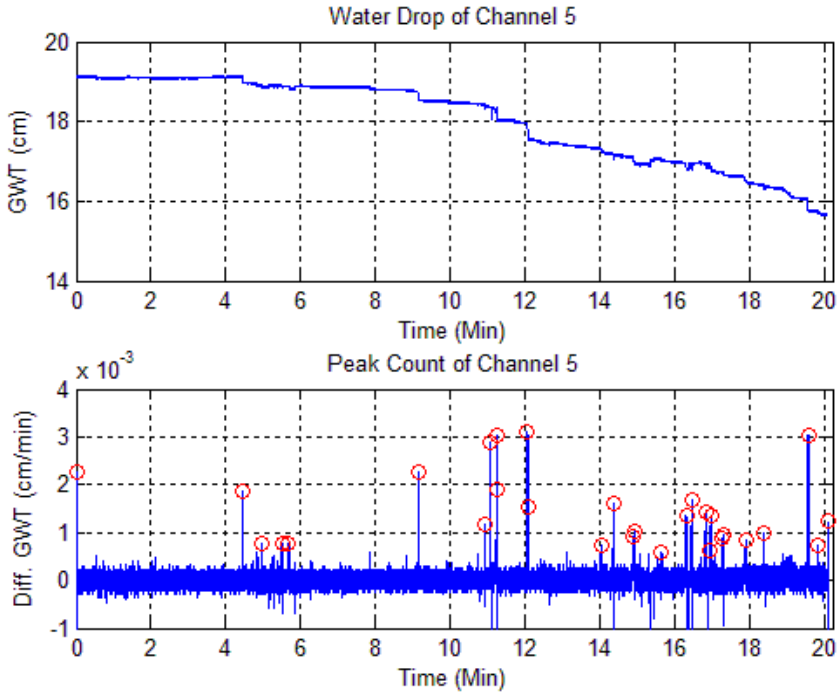

Figure 191: Peak counting of sample 1 with thickness of 200mm, G.W.T = 30mm, and radius (R) = 14.5cm

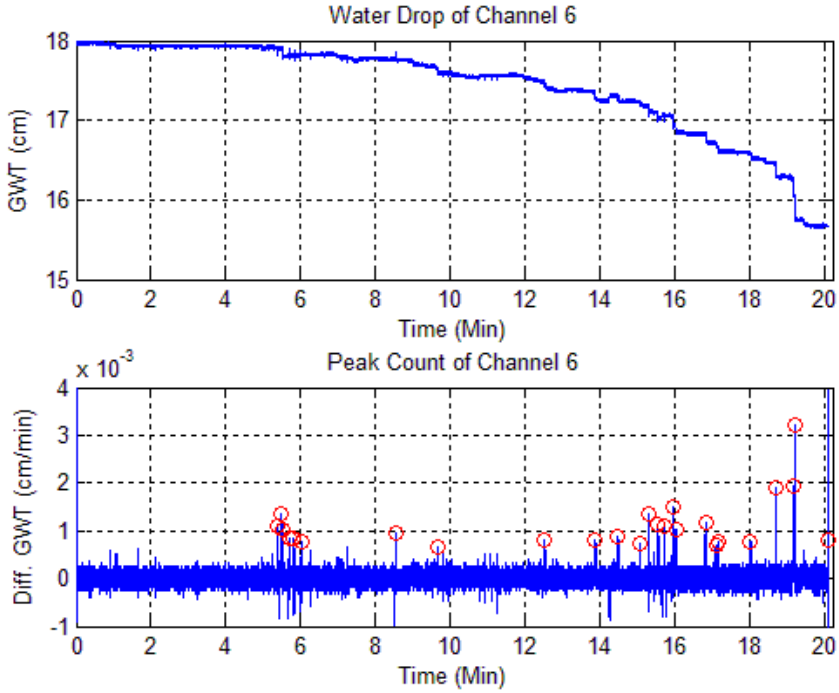

Figure 192: Peak counting of sample 1 with thickness of 200mm, G.W.T = 30mm, and radius (R) = 19.3cm

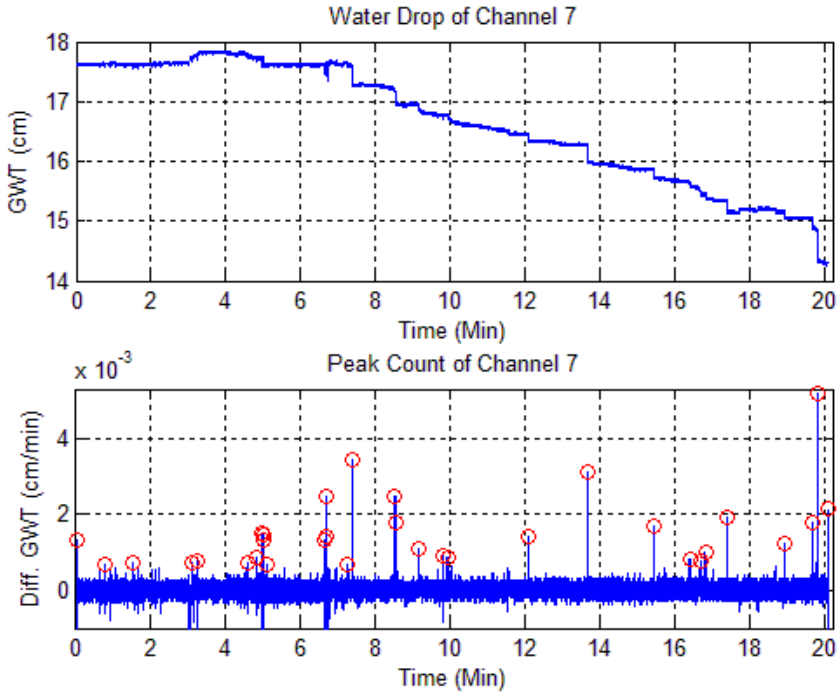

Figure 193: Peak counting of sample 1 with thickness of 200mm, G.W.T = 30mm, and radius (R) = 20cm

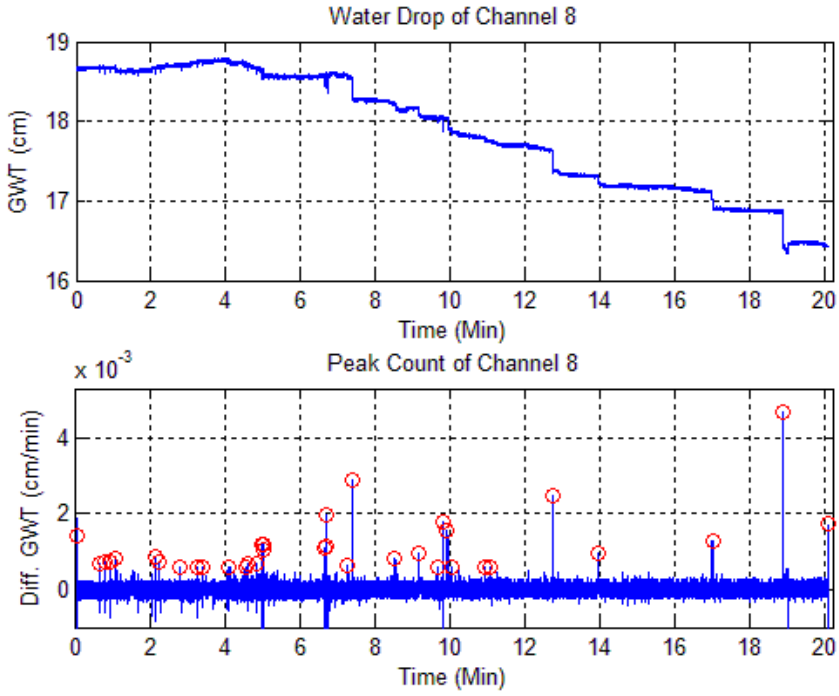

Figure 194: Peak counting of sample 1 with thickness of 200mm, G.W.T = 30mm, and radius (R) = 26cm

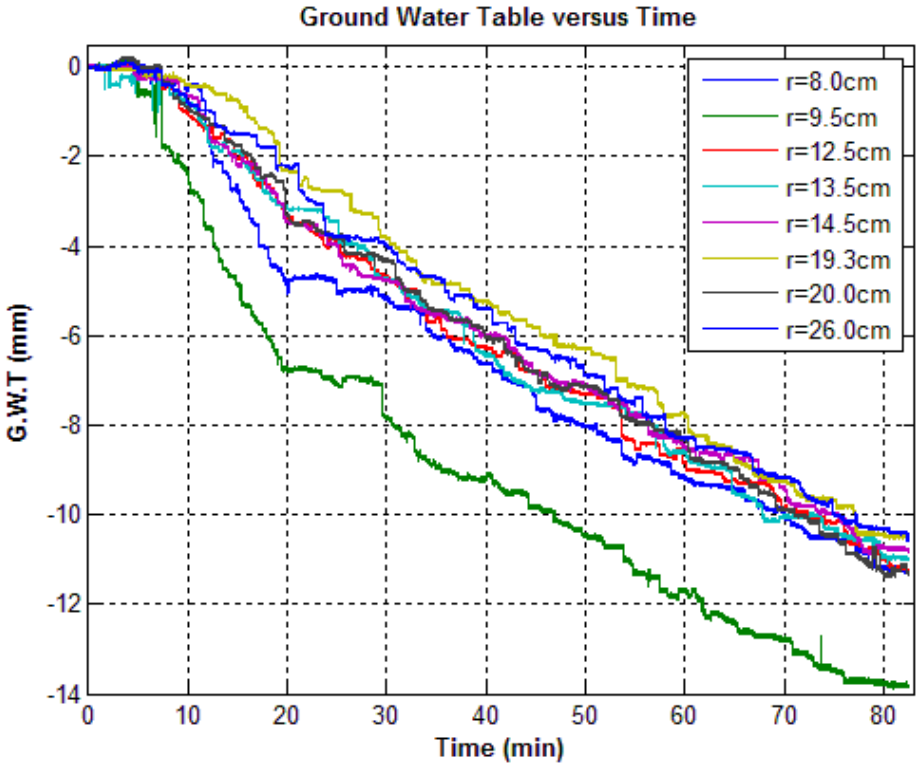

Figure 195: G.W.T over time of sample 1 with soil thickness of 200mm, G.W.T = 30mm

Sample 2 (Soil Thickness = 200mm G.W.T = 30mm)

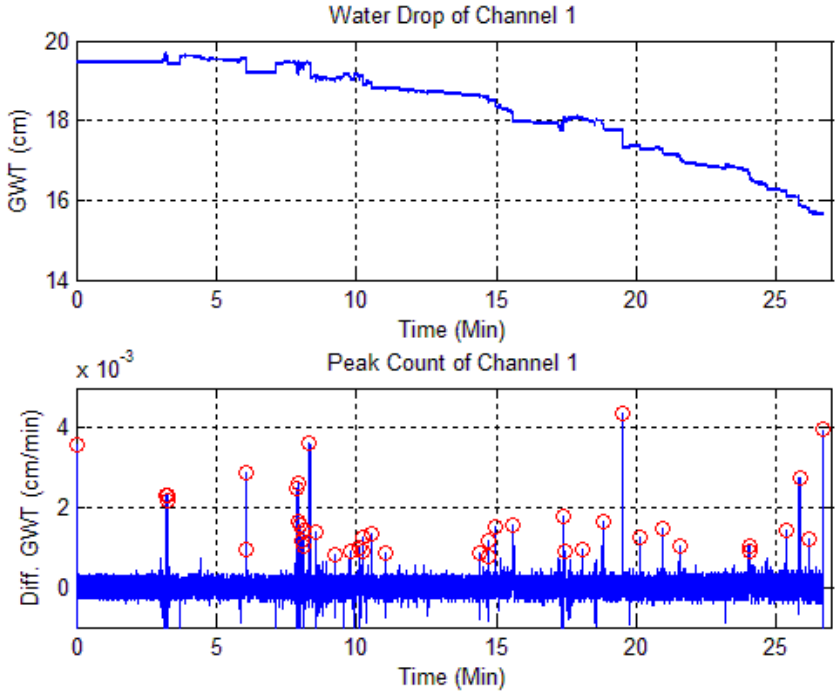

Figure 196: Peak counting of sample 2 with thickness of 200mm, G.W.T = 30mm, and radius (R) = 9.5cm

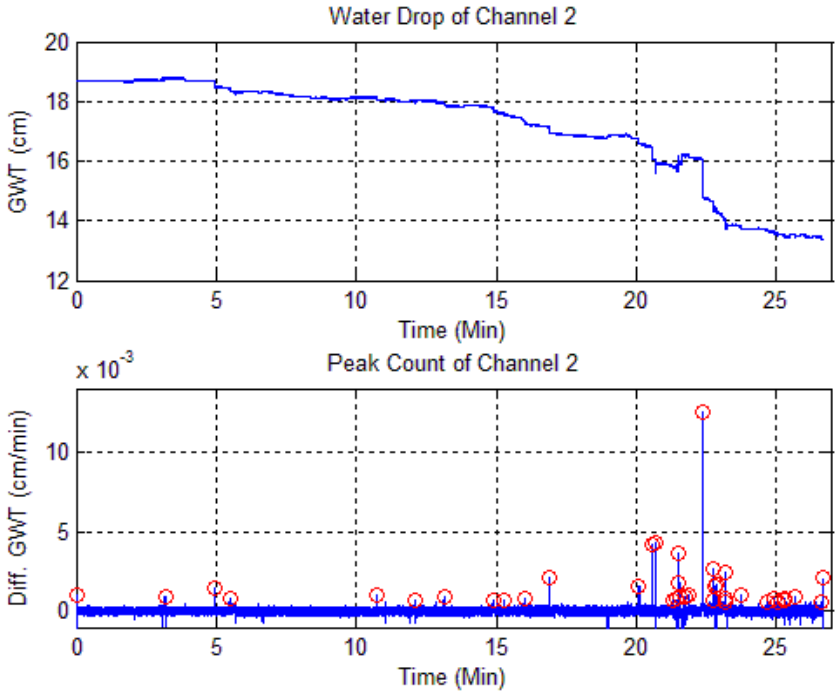

Figure 197: Peak counting of sample 2 with thickness of 200mm, G.W.T = 30mm, and radius (R) = 10.0cm

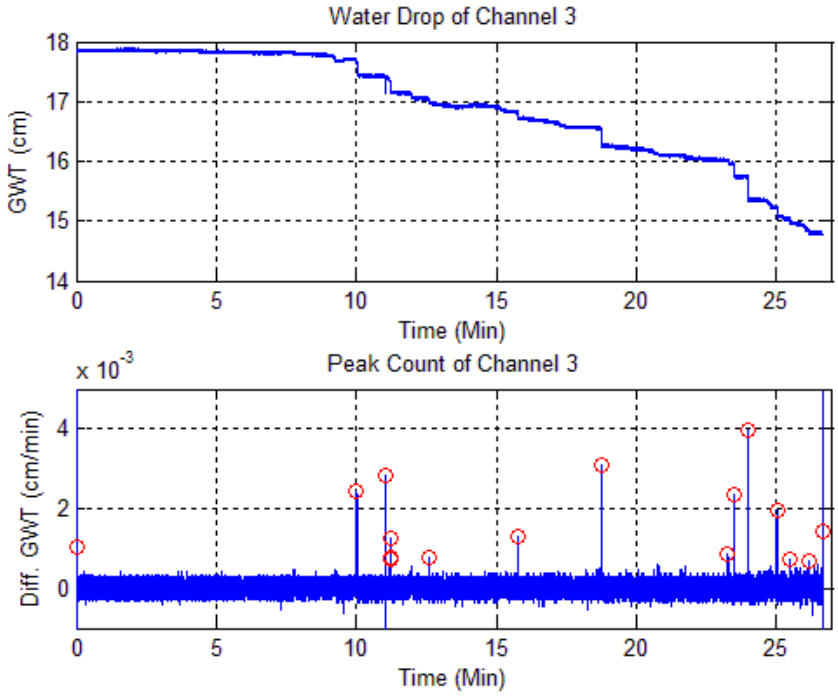

Figure 198: Peak counting of sample 2 with thickness of 200mm, G.W.T = 30mm, and radius (R) = 12.5cm

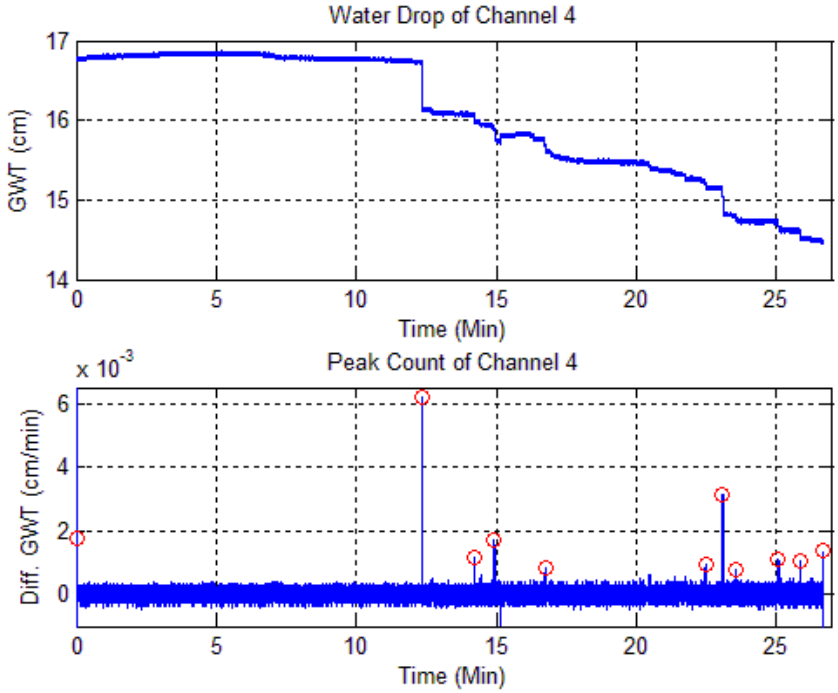

Figure 199: Peak counting of sample 2 with thickness of 200mm, G.W.T = 30mm, and radius (R) = 16.8cm

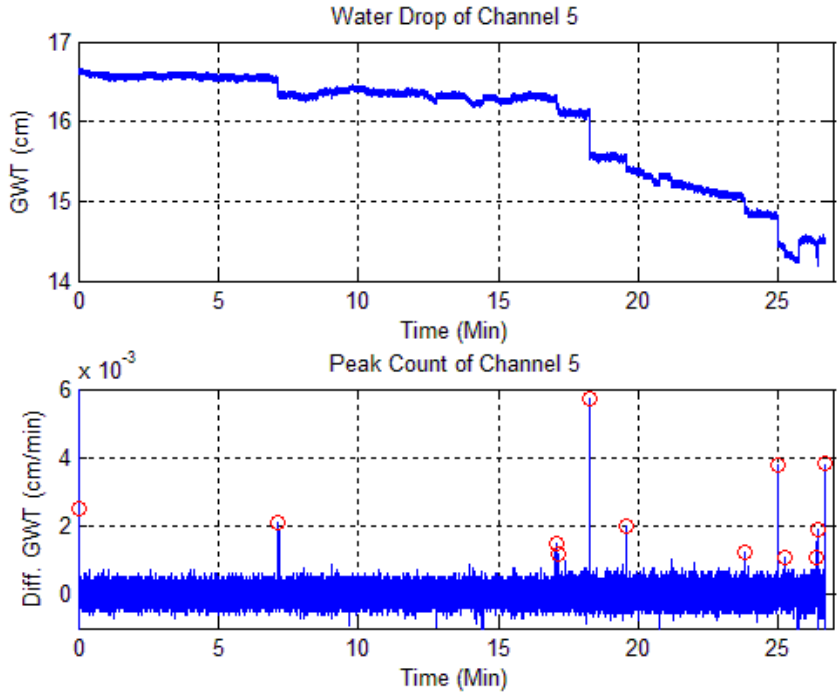

Figure 200: Peak counting of sample 2 with thickness of 200mm, G.W.T = 30mm, and radius (R) = 18.5cm

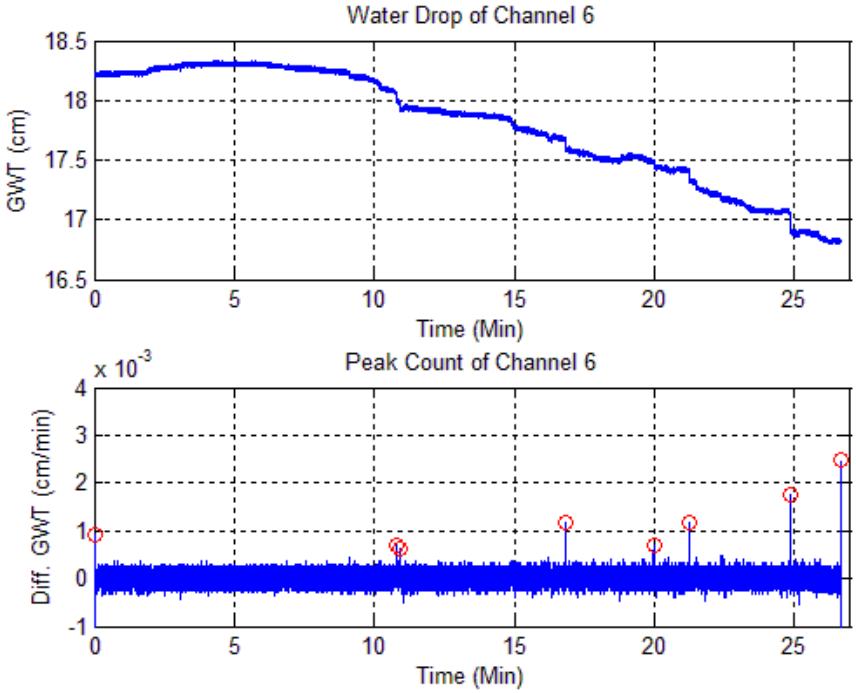

Figure 201: Peak counting of sample 2 with thickness of 200mm, G.W.T = 30mm, and radius (R) = 18.5cm

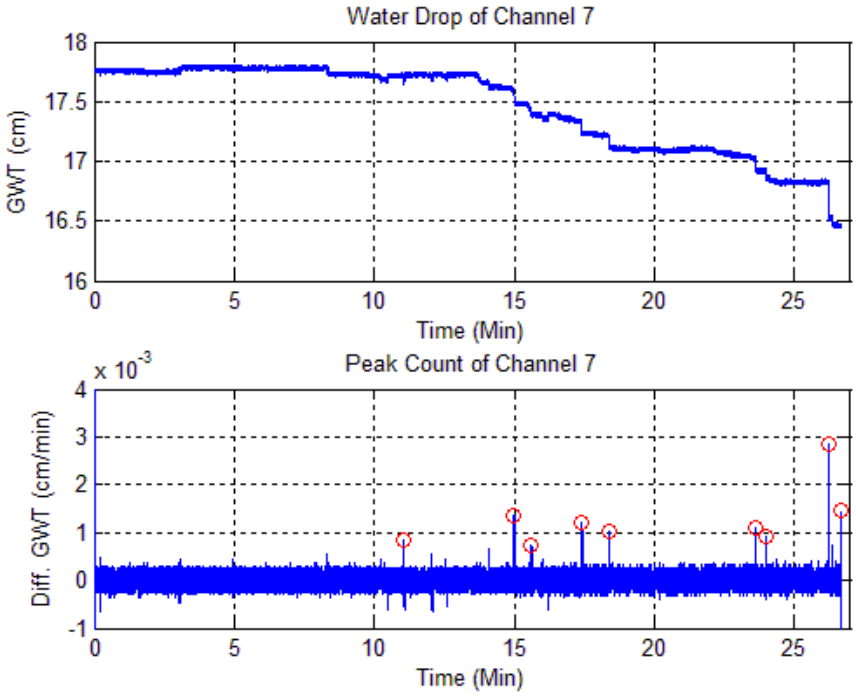

Figure 202: Peak counting of sample 2 with thickness of 200mm, G.W.T = 30mm, and radius (R) = 22.2cm

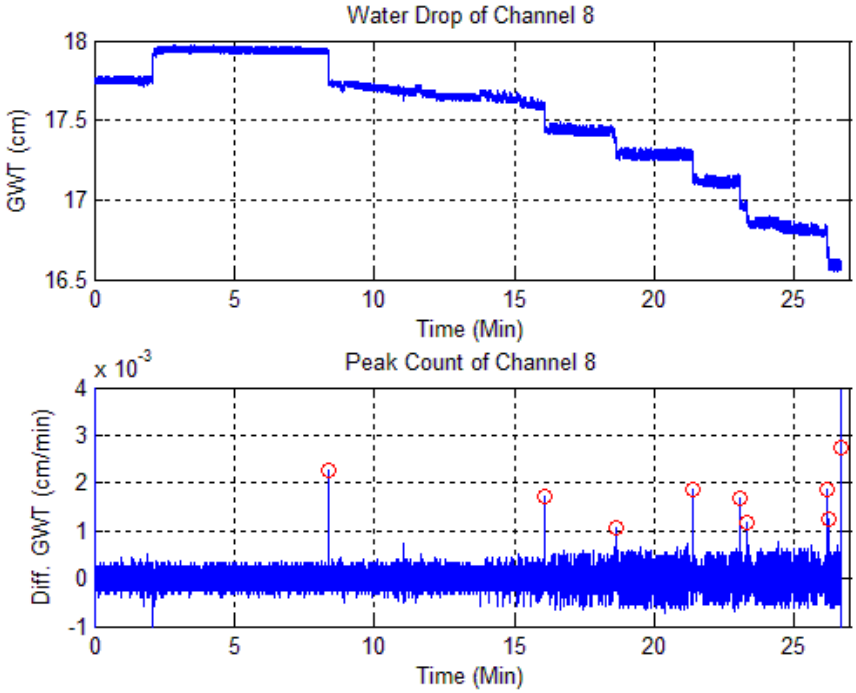

Figure 203: Peak counting of sample 2 with thickness of 200mm, G.W.T = 30mm, and radius (R) = 26.0cm

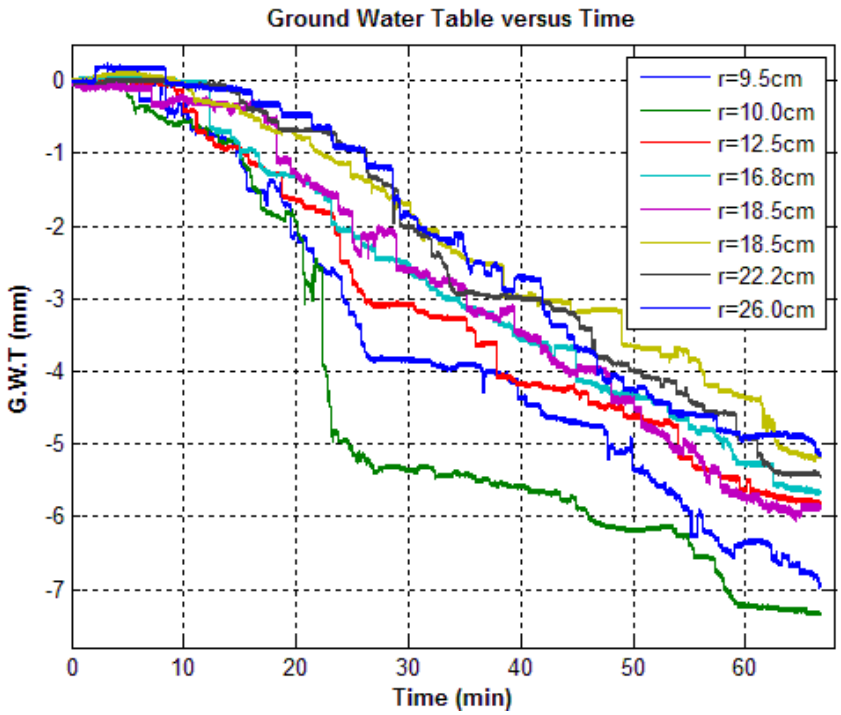

Figure 204: G.W.T over time of sample 2 with soil thickness of 200mm, G.W.T = 30mm

Sample 3 (Soil Thickness = 200mm G.W.T = 30mm)

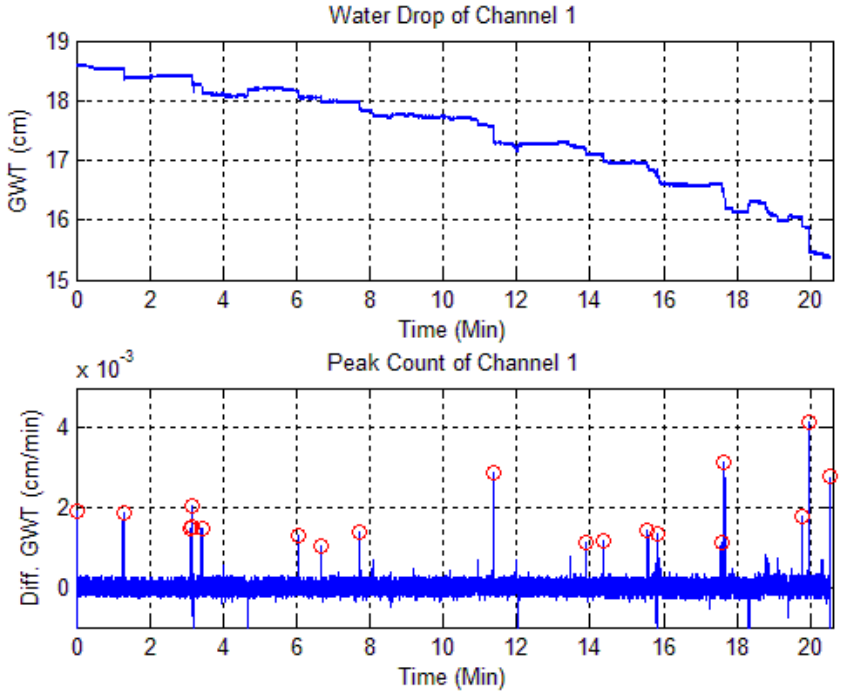

Figure 205: Peak counting of sample 3 with thickness of 200mm, G.W.T = 30mm, and radius (R) = 8.5cm

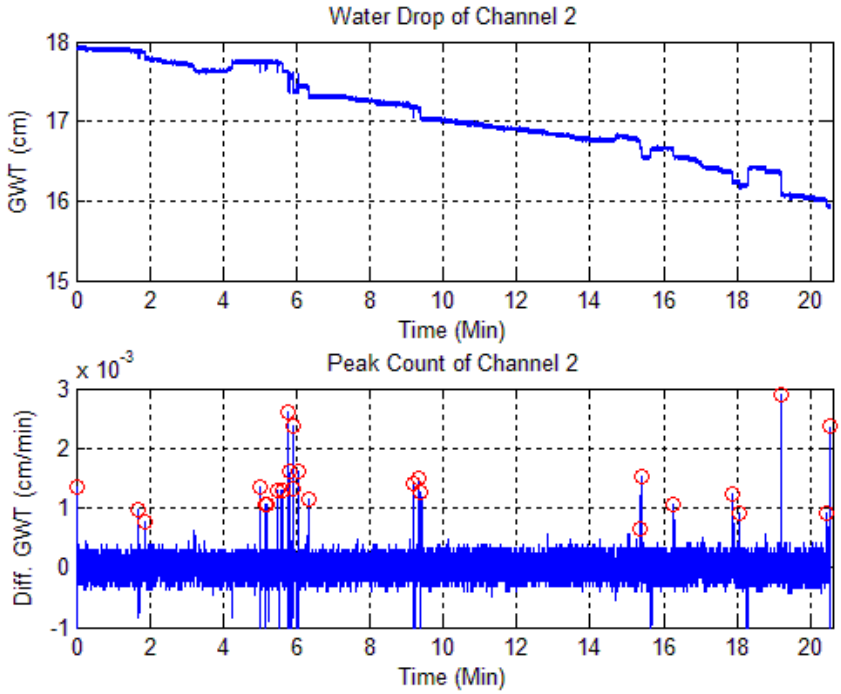

Figure 206: Peak counting of sample 3 with thickness of 200mm, G.W.T = 30mm, and radius (R) = 12.0cm

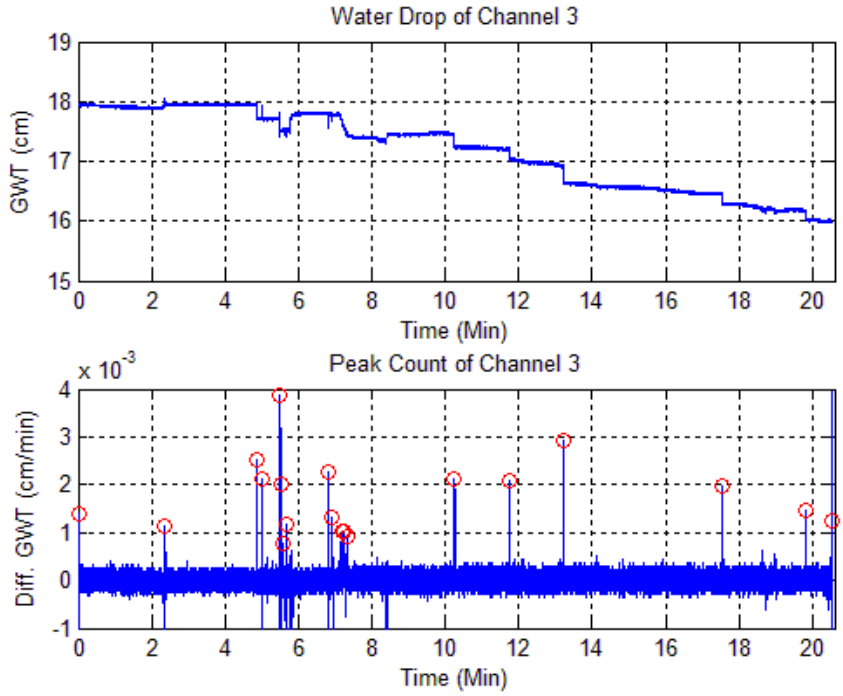

Figure 207: Peak counting of sample 3 with thickness of 200mm, G.W.T = 30mm, and radius (R) = 15.0cm

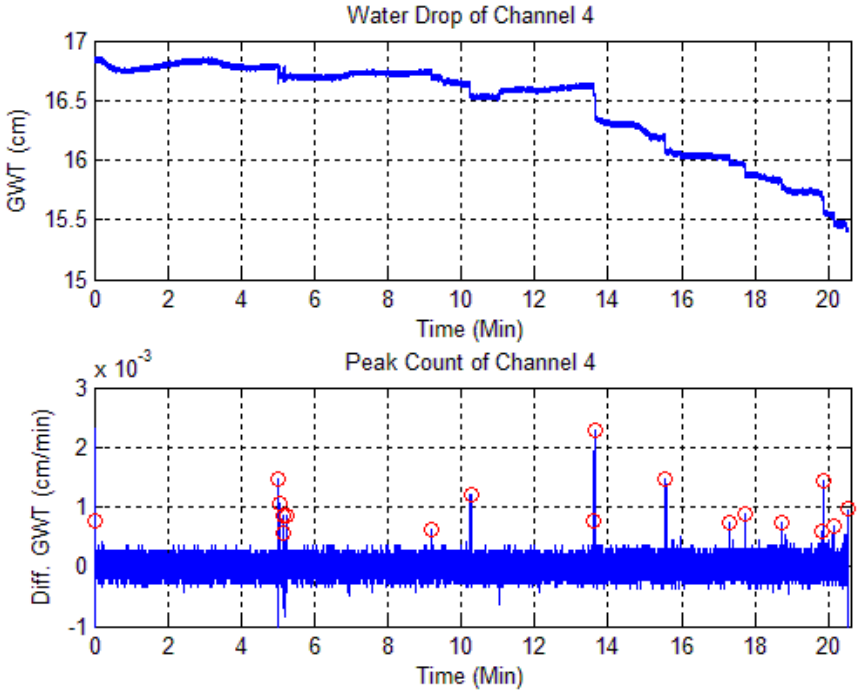

Figure 208: Peak counting of sample 3 with thickness of 200mm, G.W.T = 30mm, and radius (R) = 16.0cm

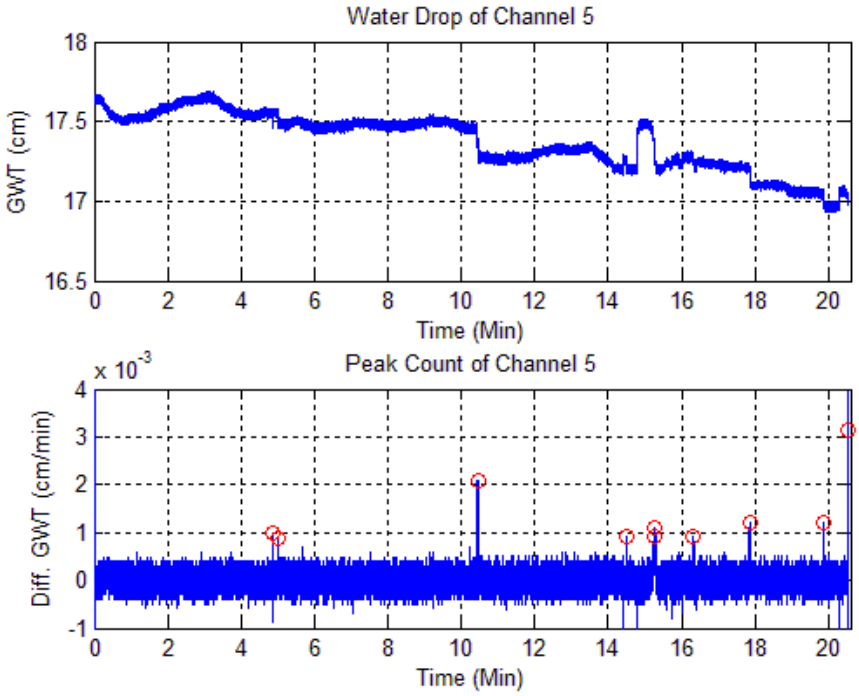

Figure 209: Peak counting of sample 3 with thickness of 200mm, G.W.T = 30mm, and radius (R) = 17.2cm

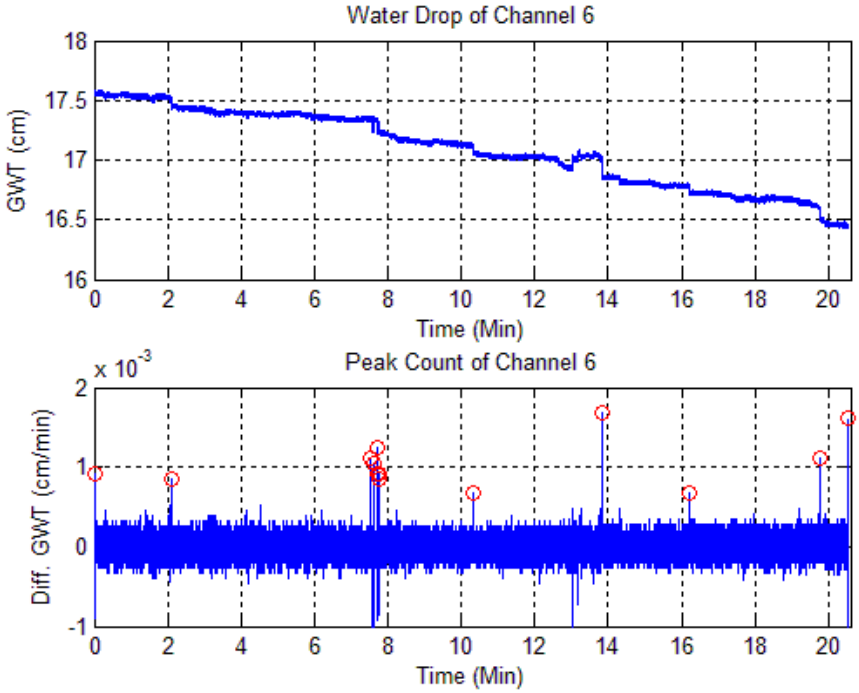

Figure 210: Peak counting of sample 3 with thickness of 200mm, G.W.T = 30mm, and radius (R) = 17.8cm

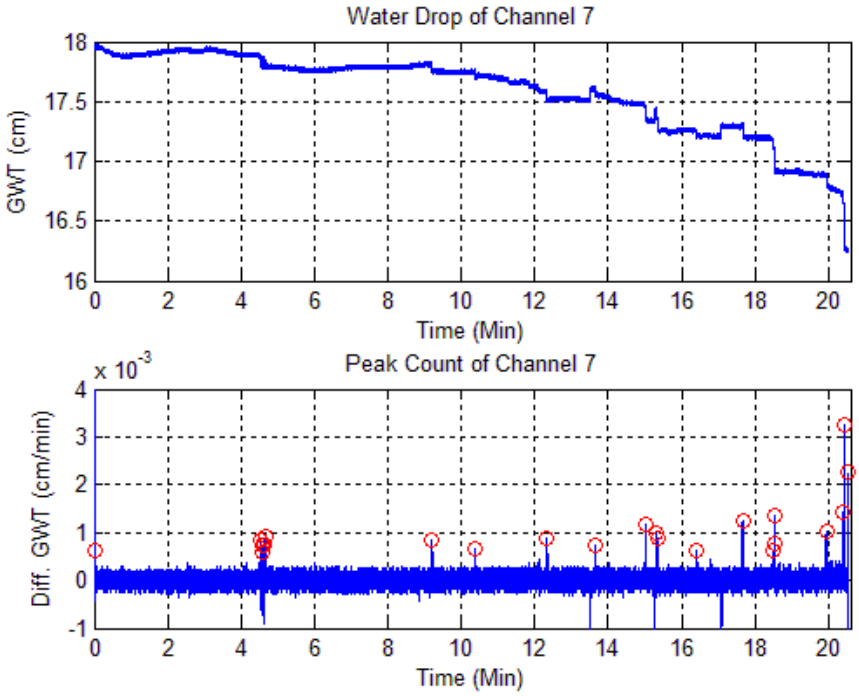

Figure 211: Peak counting of sample 3 with thickness of 200mm, G.W.T = 30mm, and radius (R) = 21.5cm

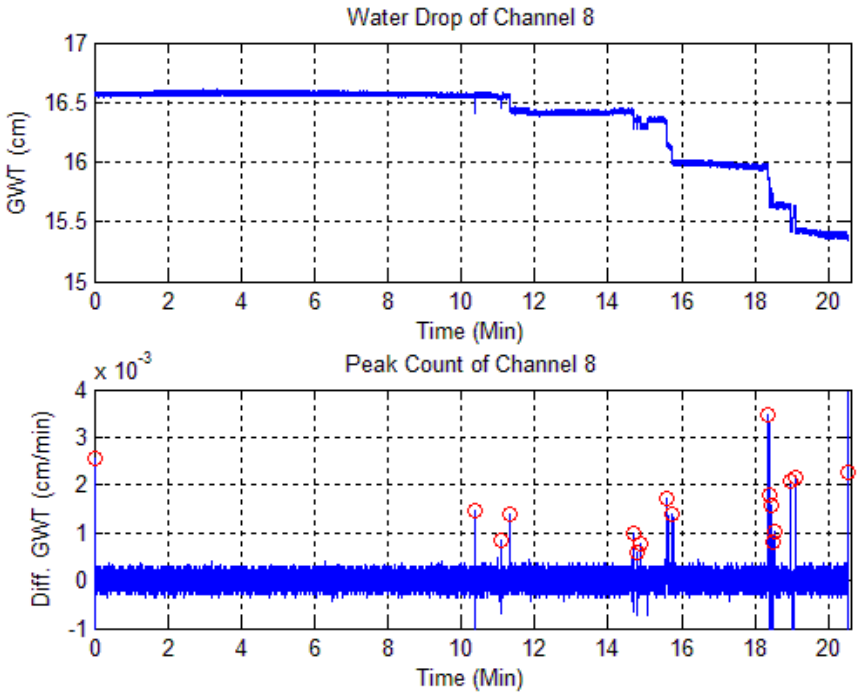

Figure 212: Peak counting of sample 3 with thickness of 200mm, G.W.T = 30mm, and radius (R) = 26.0cm

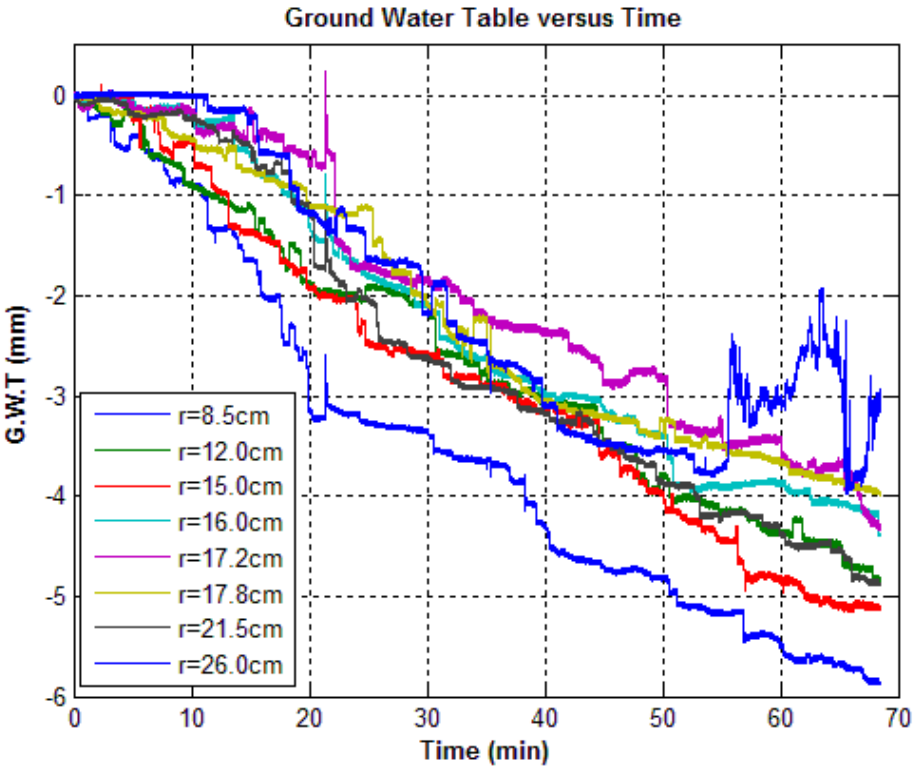

Figure 213: G.W.T over time of sample 3 with soil thickness of 200mm, G.W.T = 30mm

Sample 1 (Soil Thickness = 200mm G.W.T = 40mm)

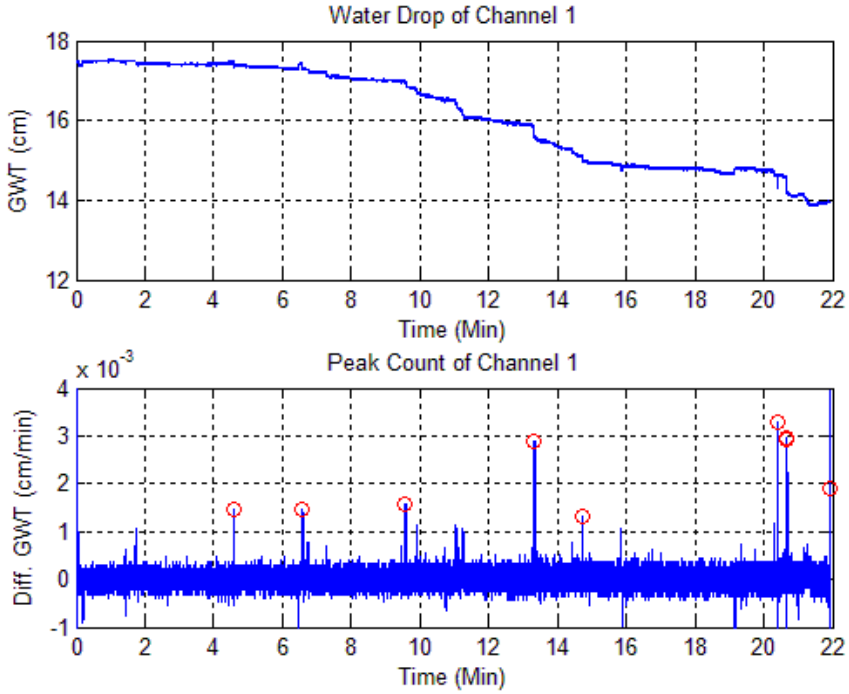

Figure 214: Peak counting of sample 1 with thickness of 200mm, G.W.T = 40mm, and radius (R) = 10.2cm

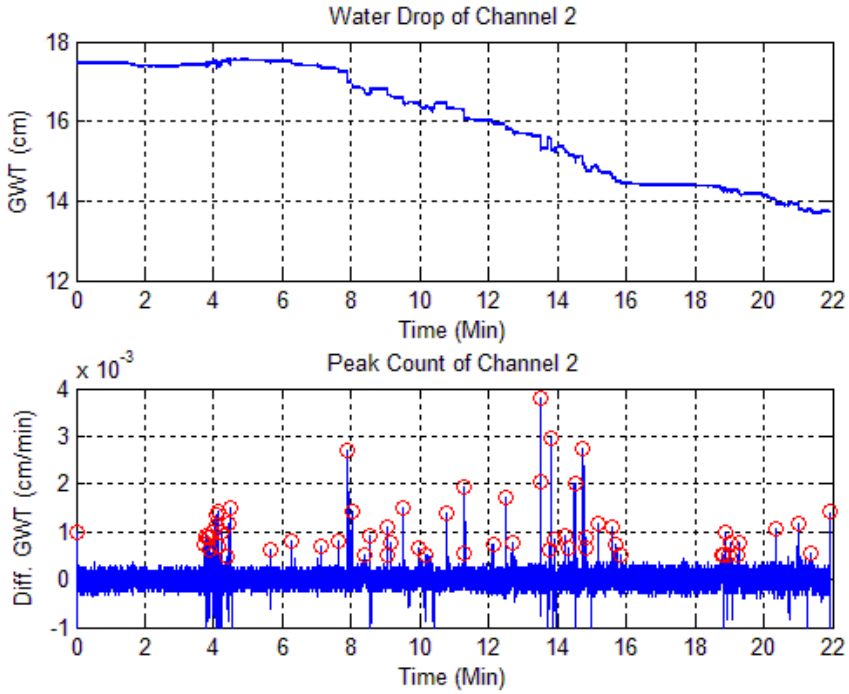

Figure 215: Peak counting of sample 1 with thickness of 200mm, G.W.T = 40mm, and radius (R) = 11.0cm

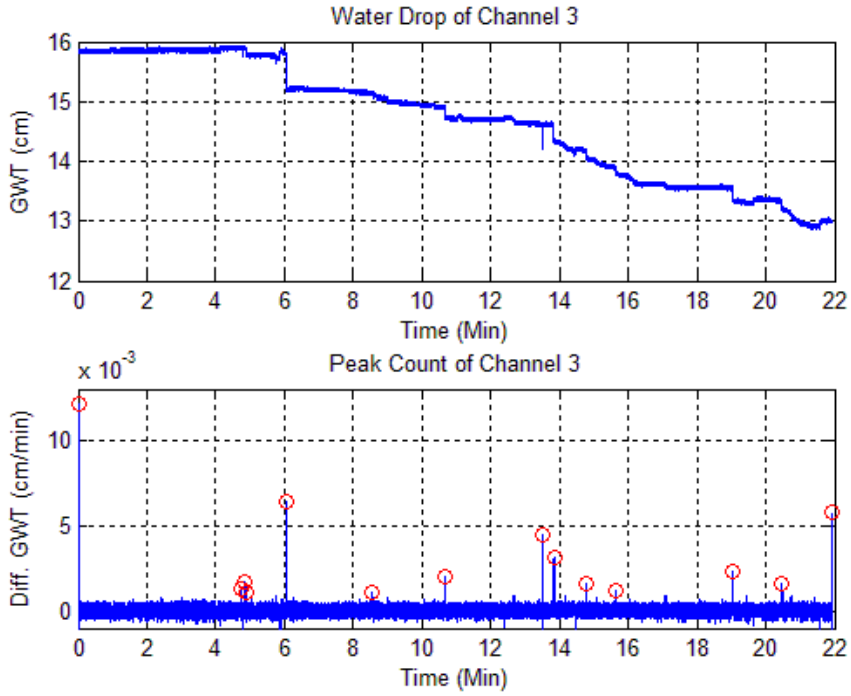

Figure 216: Peak counting of sample 1 with thickness of 200mm, G.W.T = 40mm, and radius (R) = 13.0cm

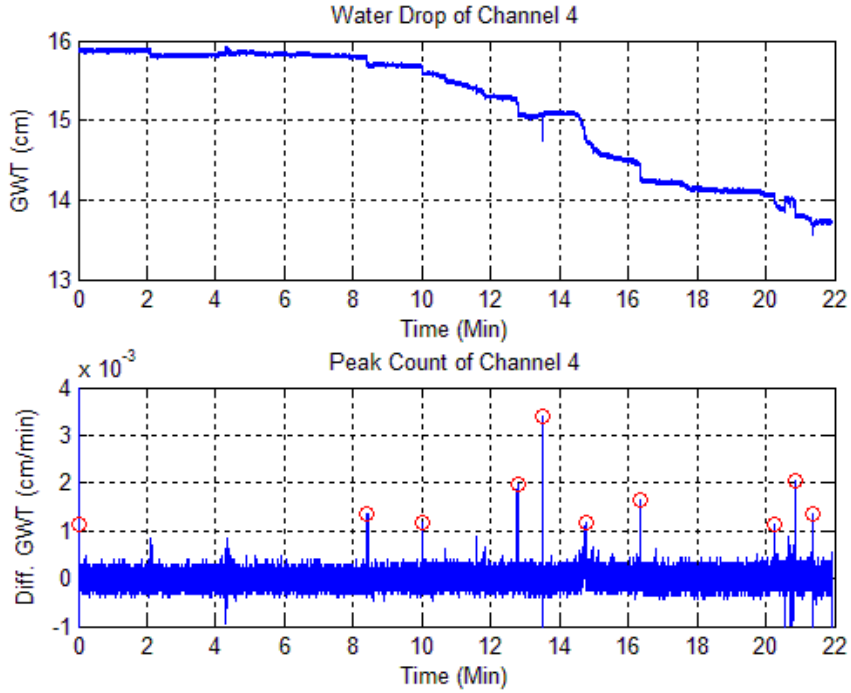

Figure 217: Peak counting of sample 1 with thickness of 200mm, G.W.T = 40mm, and radius (R) = 15.8cm

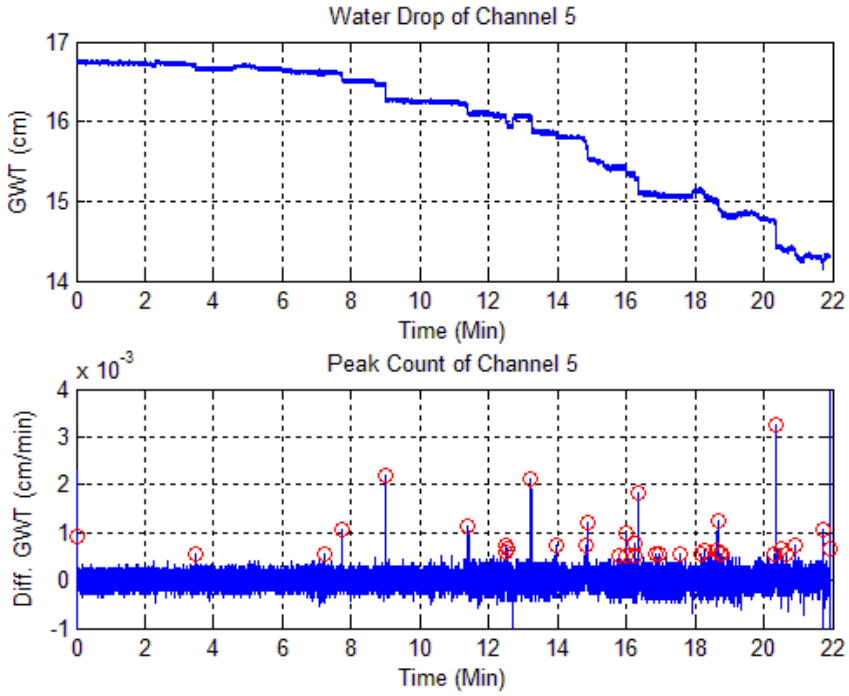

Figure 218: Peak counting of sample 1 with thickness of 200mm, G.W.T = 40mm, and radius (R) = 17.0cm

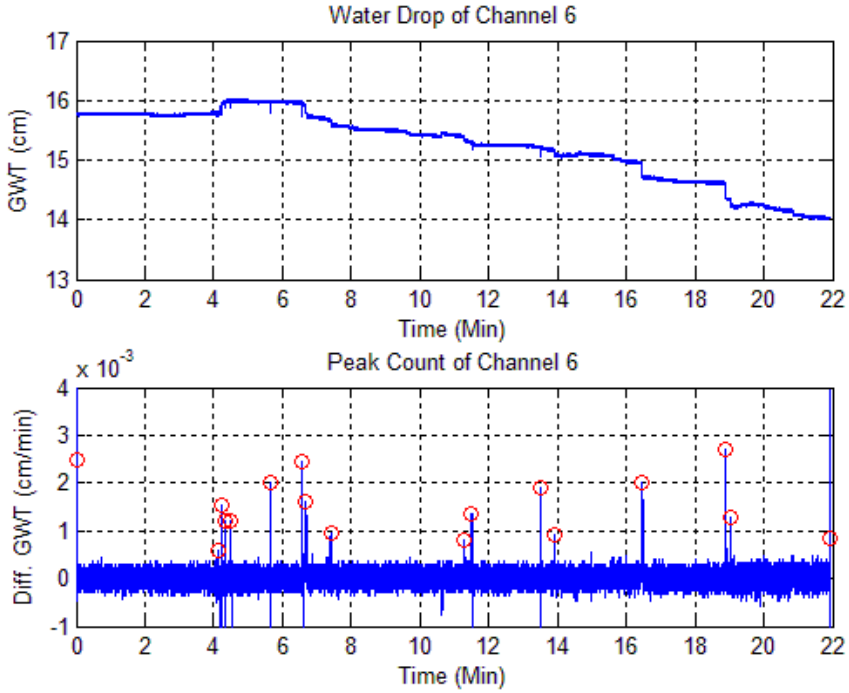

Figure 219: Peak counting of sample 1 with thickness of 200mm, G.W.T = 40mm, and radius (R) = 18.5cm

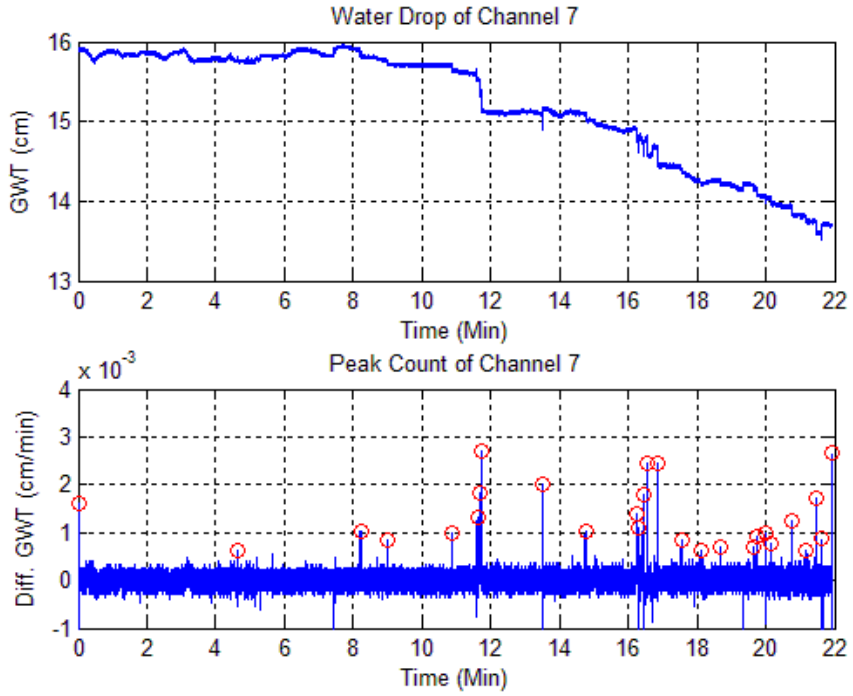

Figure 220: Peak counting of sample 1 with thickness of 200mm, G.W.T = 40mm, and radius (R) = 20.5cm

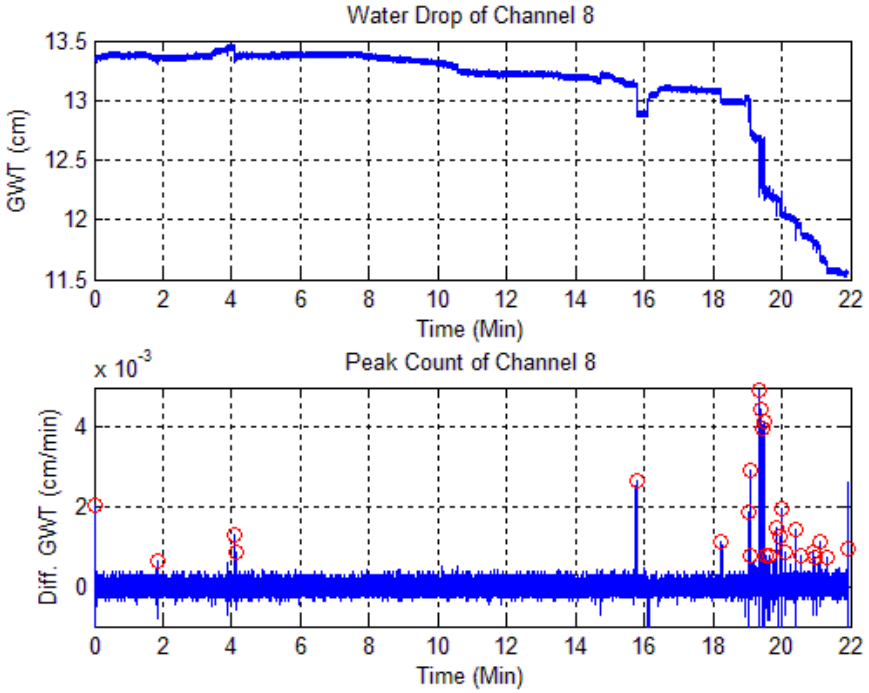

Figure 221: Peak counting of sample 1 with thickness of 200mm, G.W.T = 40mm, and radius (R) = 26cm

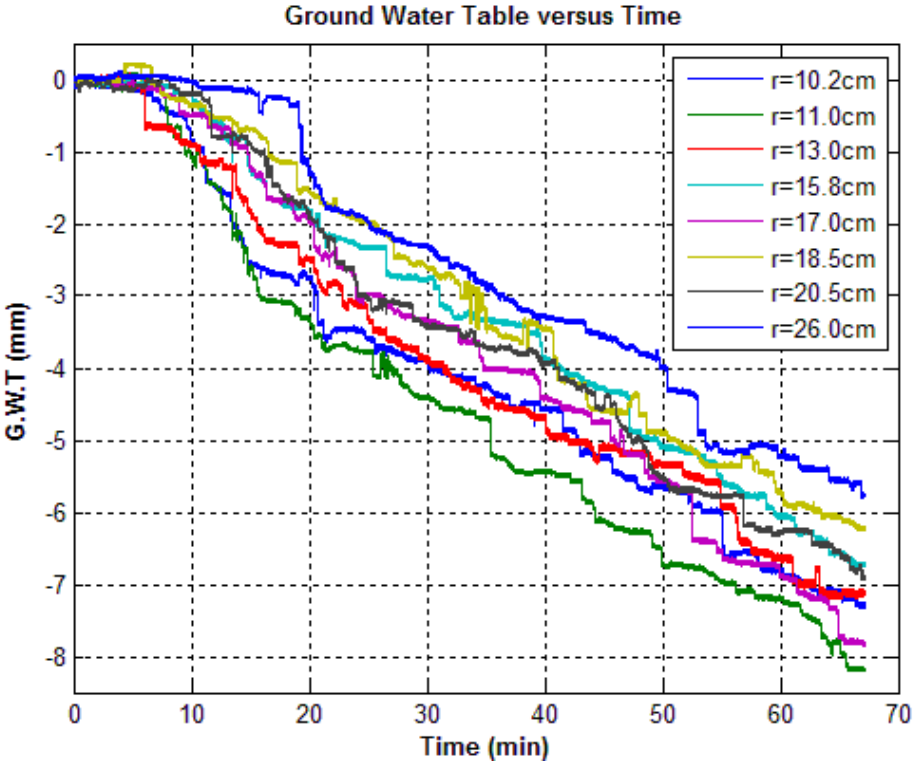

Figure 222: G.W.T over time of sample 1 with soil thickness of 200mm, G.W.T = 40mm

Sample 2 (Soil Thickness = 200mm G.W.T = 40mm)

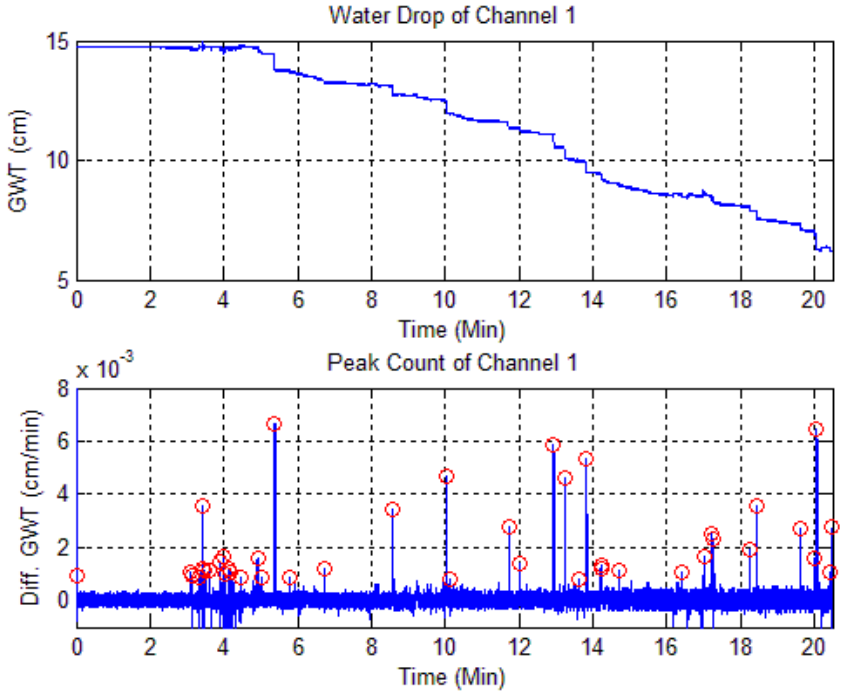

Figure 223: Peak counting of sample 2 with thickness of 200mm, G.W.T = 40mm, and radius (R) = 9.5cm

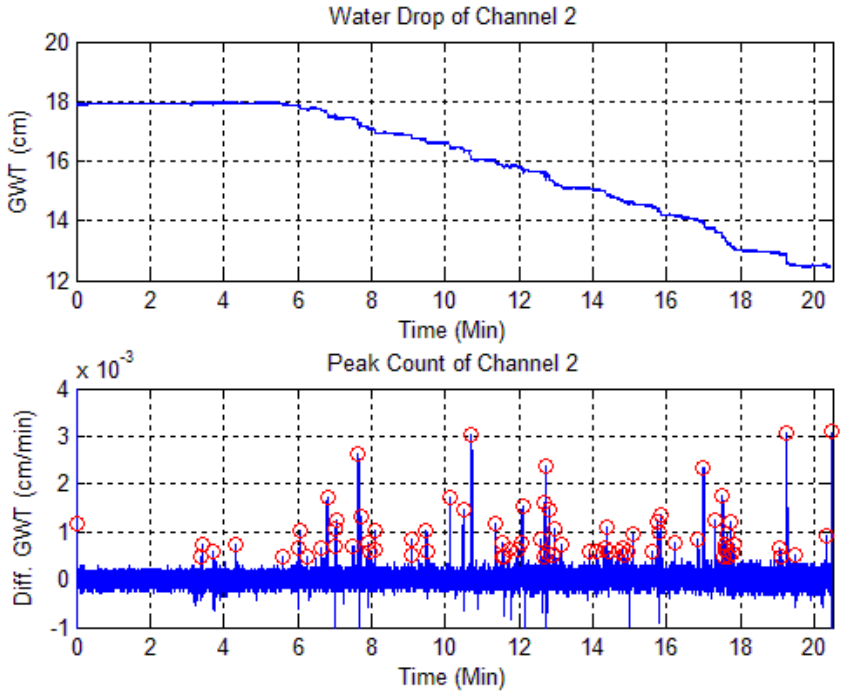

Figure 224: Peak counting of sample 2 with thickness of 200mm, G.W.T = 40mm, and radius (R) = 12.0cm

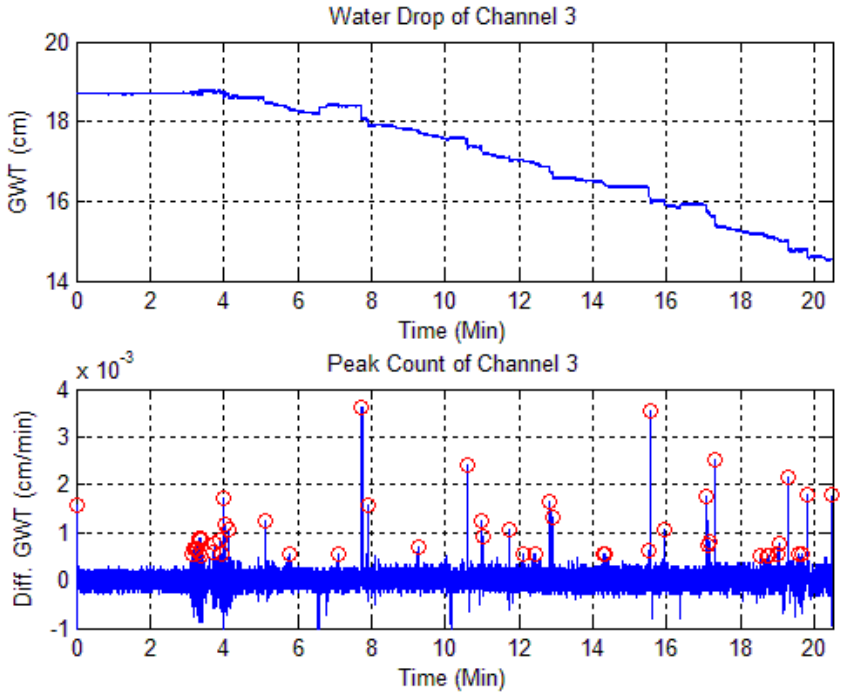

Figure 225: Peak counting of sample 2 with thickness of 200mm, G.W.T = 40mm, and radius (R) = 15.0cm

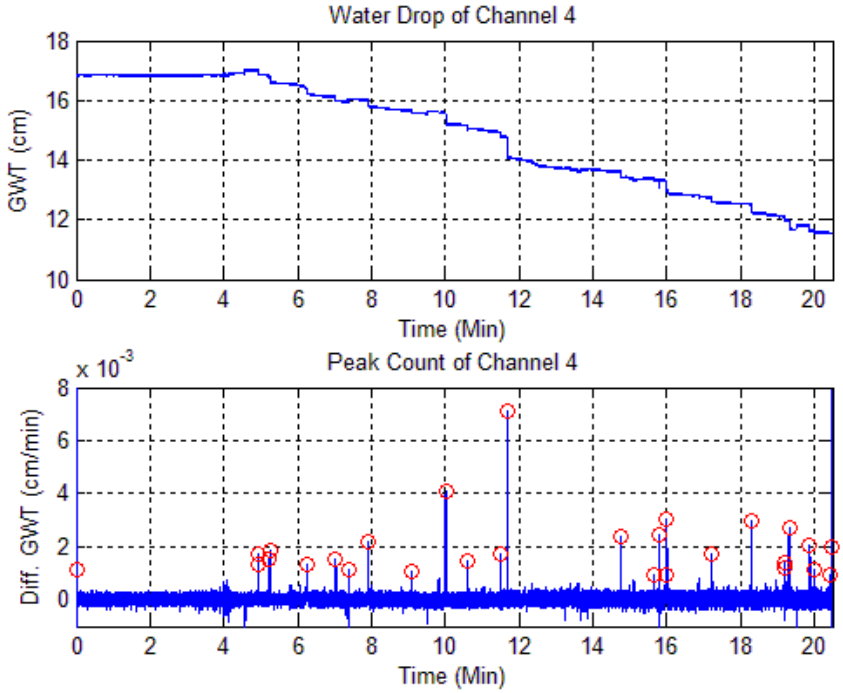

Figure 226: Peak counting of sample 2 with thickness of 200mm, G.W.T = 40mm, and radius (R) = 15.3cm

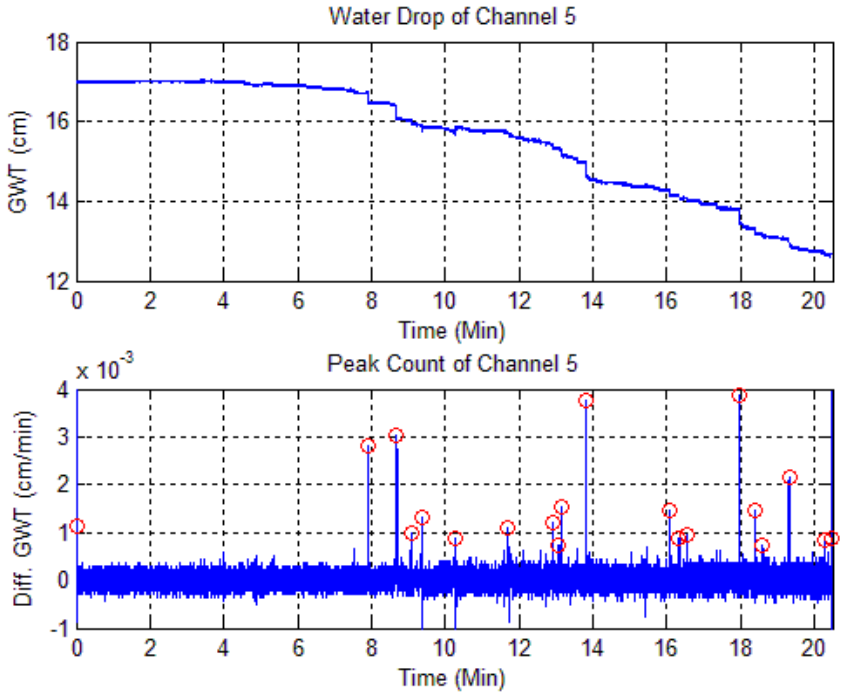

Figure 227: Peak counting of sample 2 with thickness of 200mm, G.W.T = 40mm, and radius (R) = 16.5cm

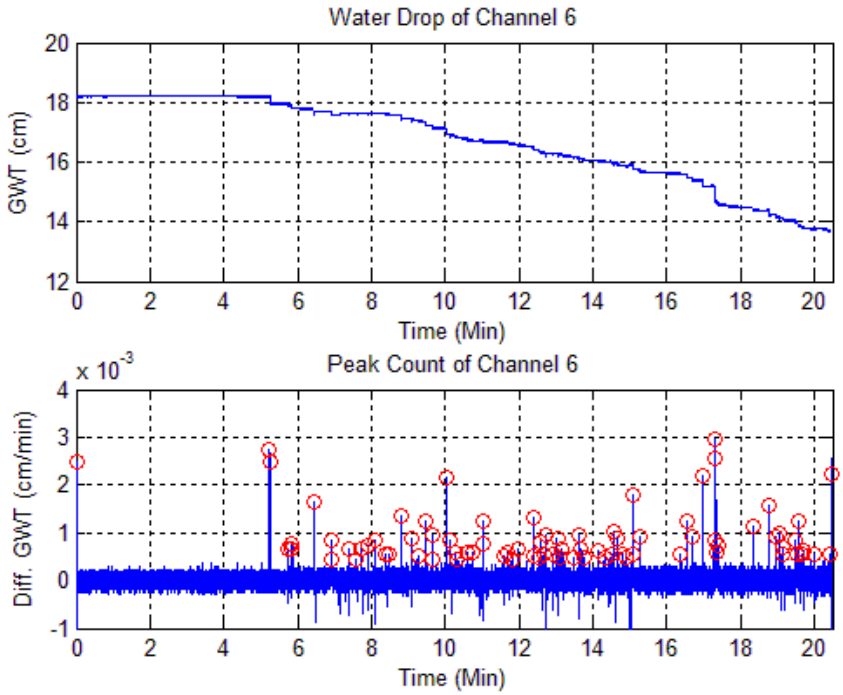

Figure 228: Peak counting of sample 2 with thickness of 200mm, G.W.T = 40mm, and radius (R) = 20.2cm

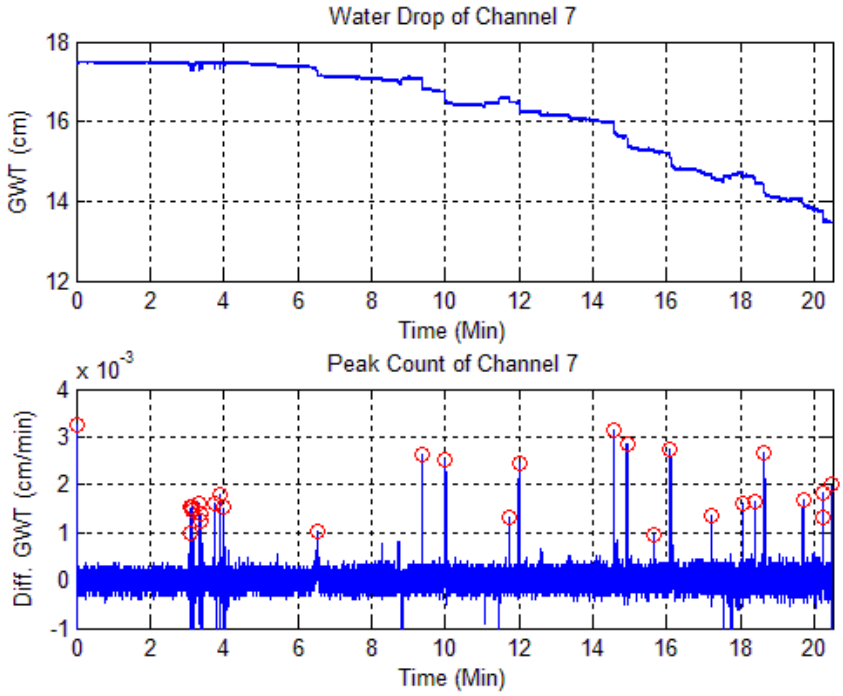

Figure 229: Peak counting of sample 2 with thickness of 200mm, G.W.T = 40mm, and radius (R) = 22.0cm

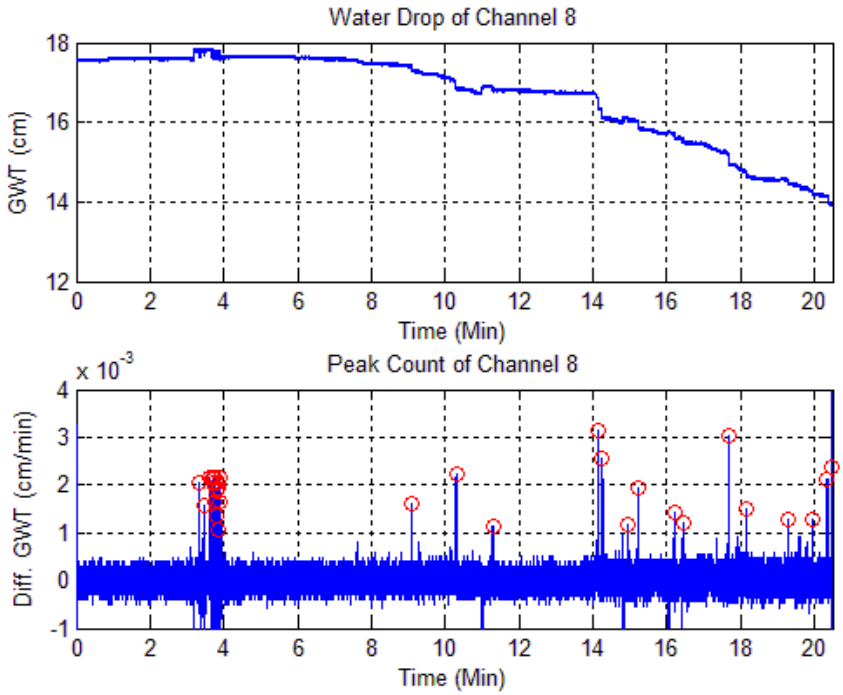

Figure 230: Peak counting of sample 2 with thickness of 200mm, G.W.T = 40mm, and radius (R) = 26.0cm

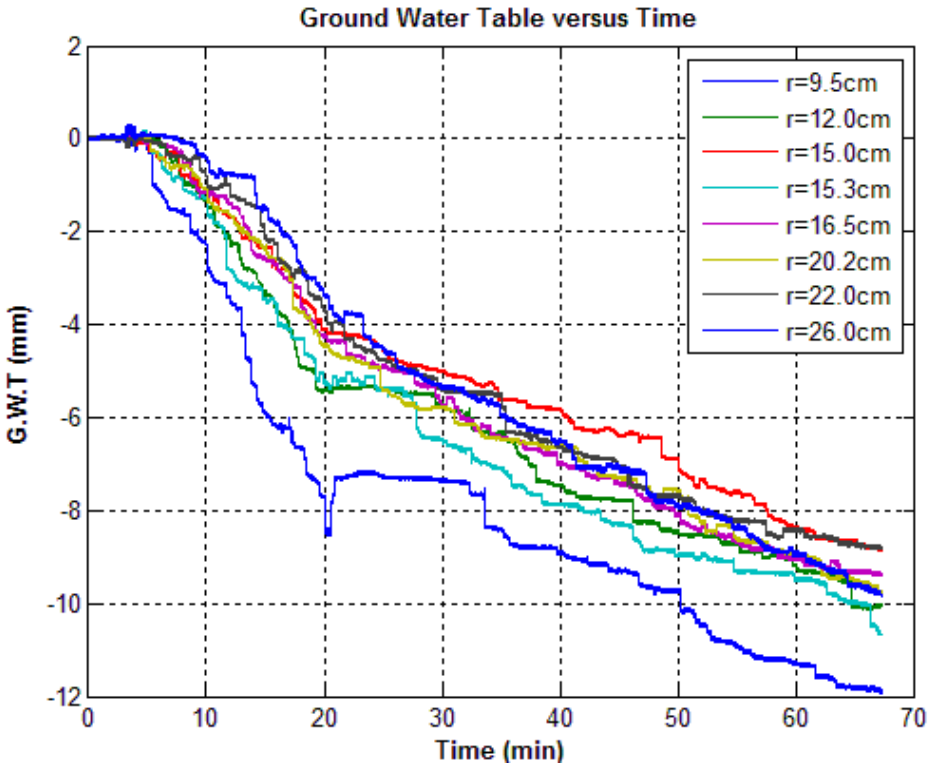

Figure 231: G.W.T over time of sample 2 with soil thickness of 200mm, G.W.T = 40mm

Sample 3 (Soil Thickness = 200mm G.W.T = 40mm)

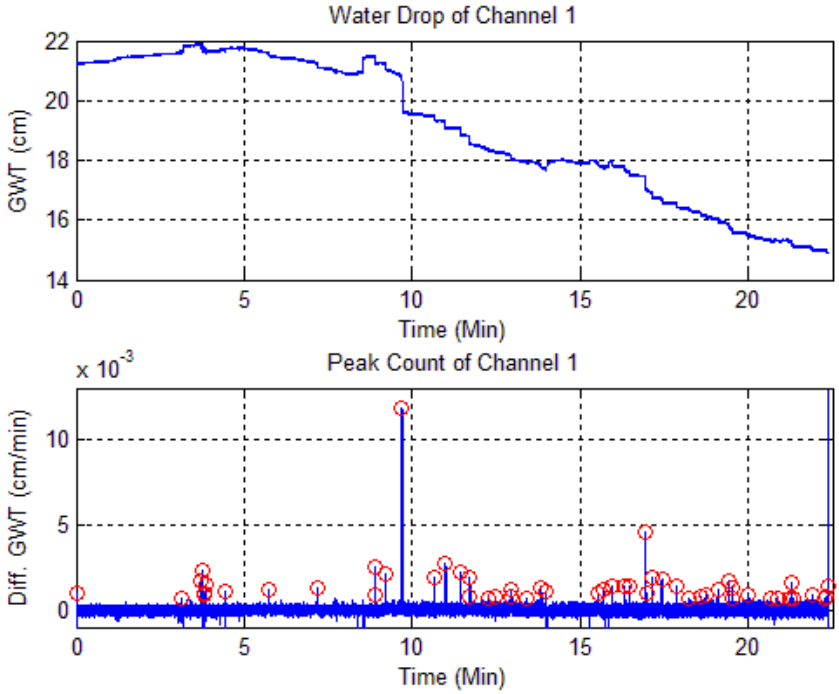

Figure 232: Peak counting of sample 3 with thickness of 200mm, G.W.T = 40mm, and radius (R) = 8.5cm

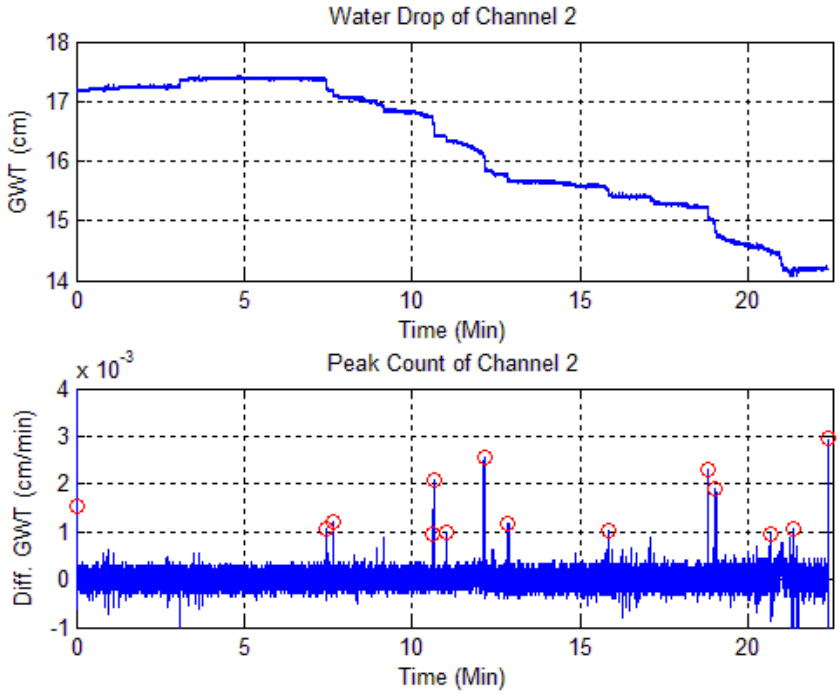

Figure 233: Peak counting of sample 3 with thickness of 200mm, G.W.T = 40mm, and radius (R) = 11.2cm

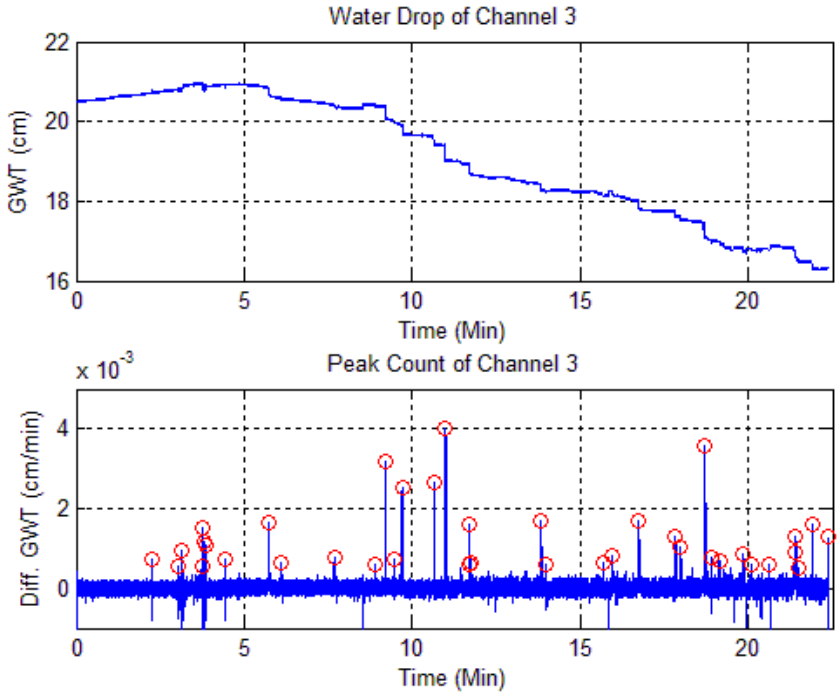

Figure 234: Peak counting of sample 3 with thickness of 200mm, G.W.T = 40mm, and radius (R) = 13.5cm

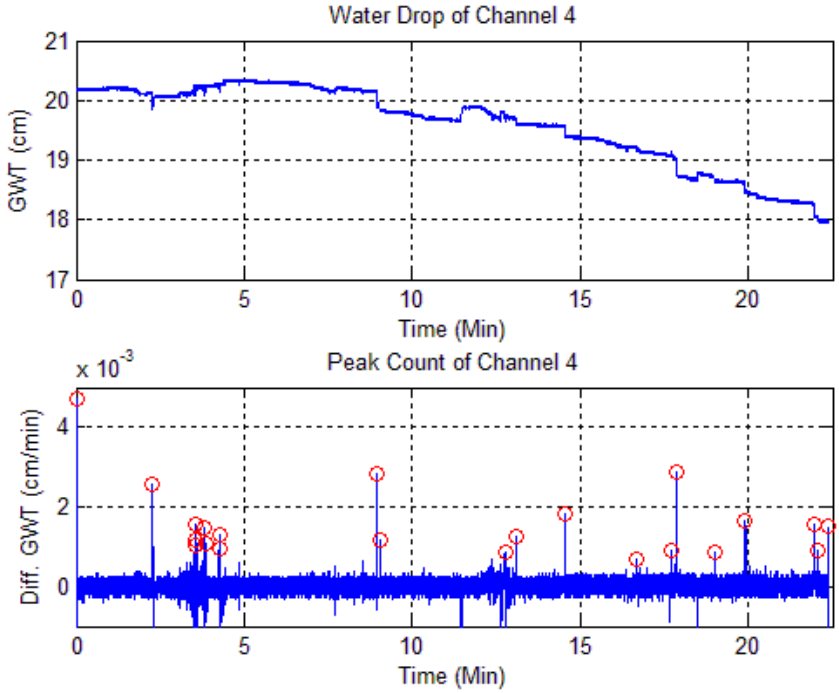

Figure 235: Peak counting of sample 3 with thickness of 200mm, G.W.T = 40mm, and radius (R) = 16.0cm

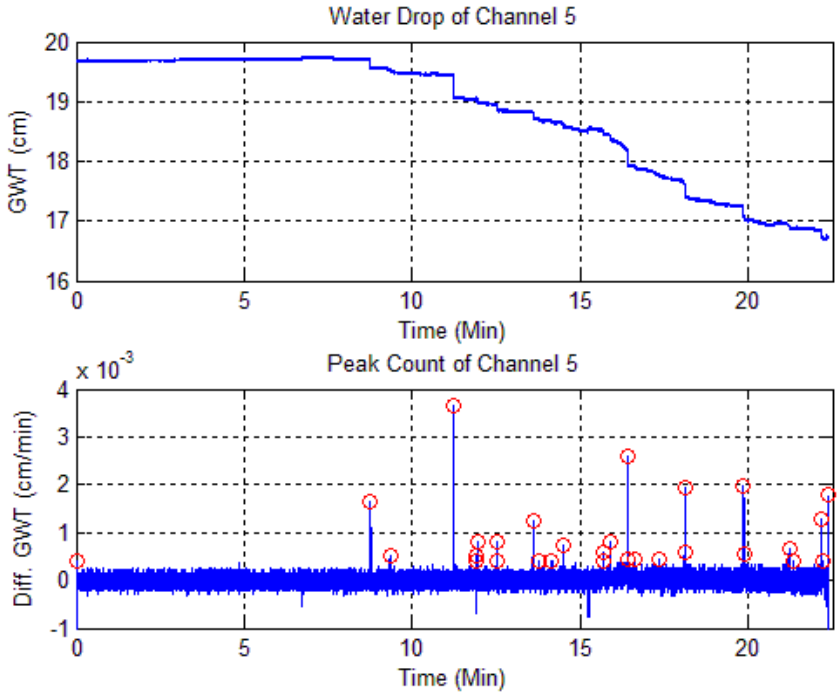

Figure 236: Peak counting of sample 3 with thickness of 200mm, G.W.T = 40mm, and radius (R) = 17.5cm

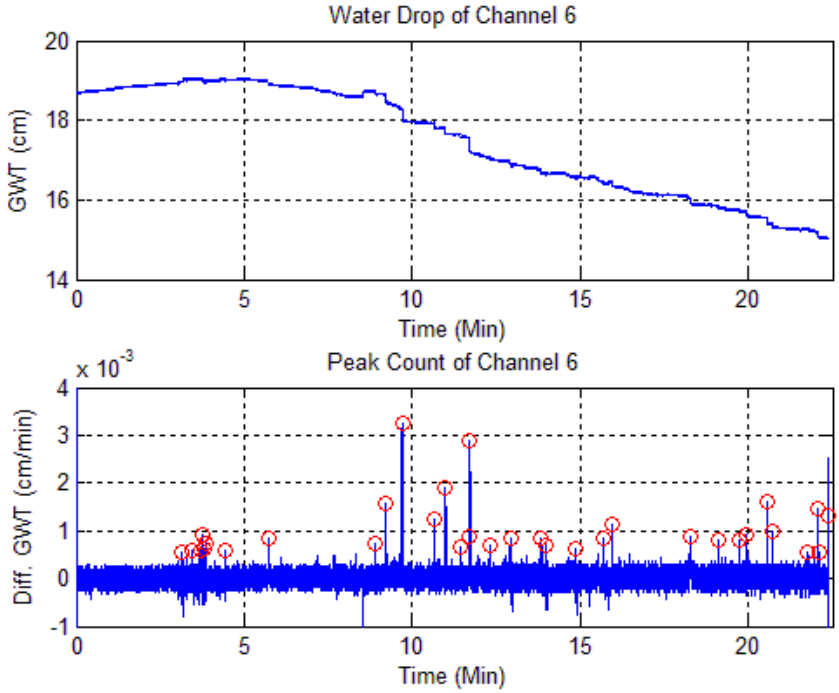

Figure 237: Peak counting of sample 3 with thickness of 200mm, G.W.T = 40mm, and radius (R) = 19.3cm

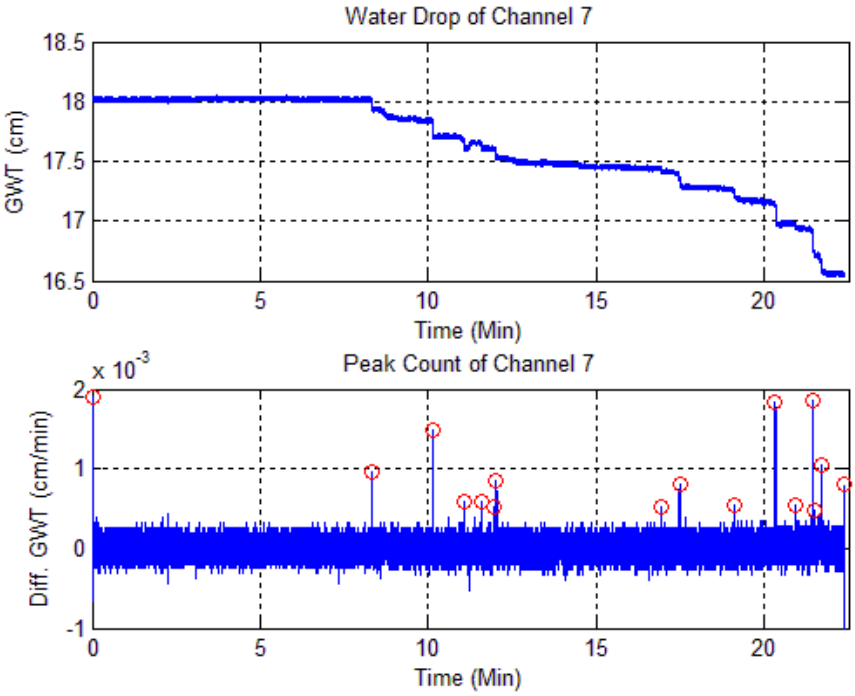

Figure 238: Peak counting of sample 3 with thickness of 200mm, G.W.T = 40mm, and radius (R) = 20.0cm

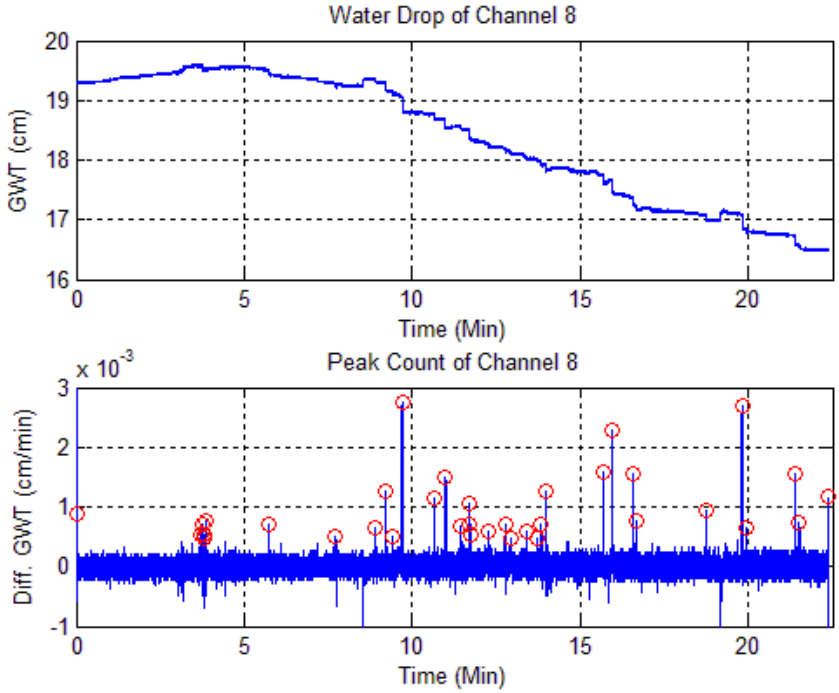

Figure 239: Peak counting of sample 3 with thickness of 200mm, G.W.T = 40mm, and radius (R) = 26.0cm

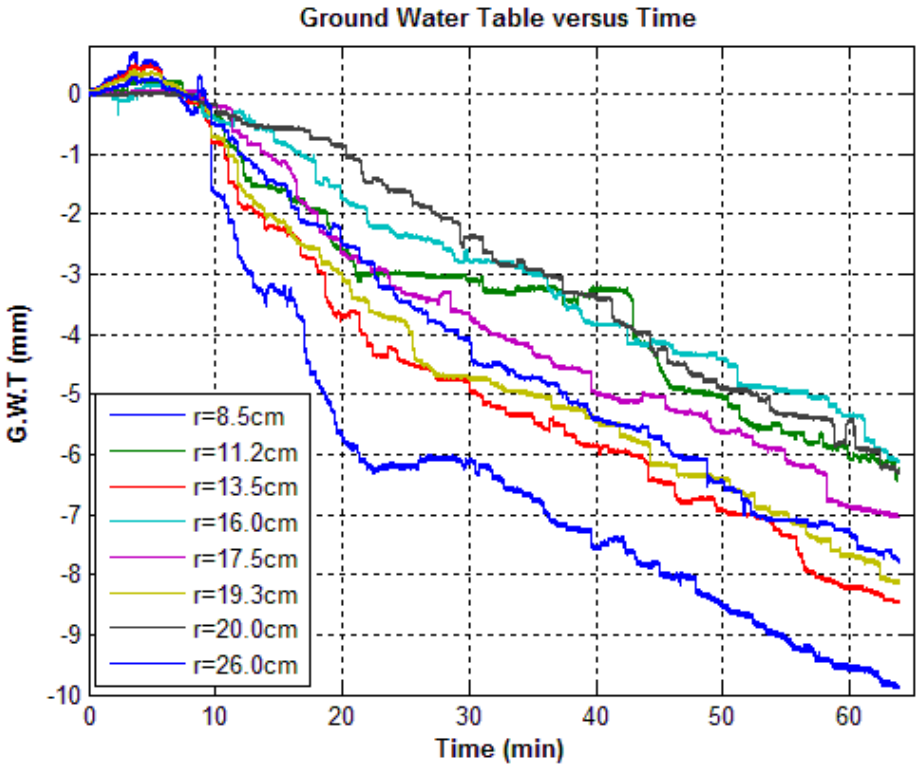

Figure 240: G.W.T over time of sample 3 with soil thickness of 200mm, G.W.T = 40mm

Sample 1 (Soil Thickness = 200mm G.W.T = 60mm)

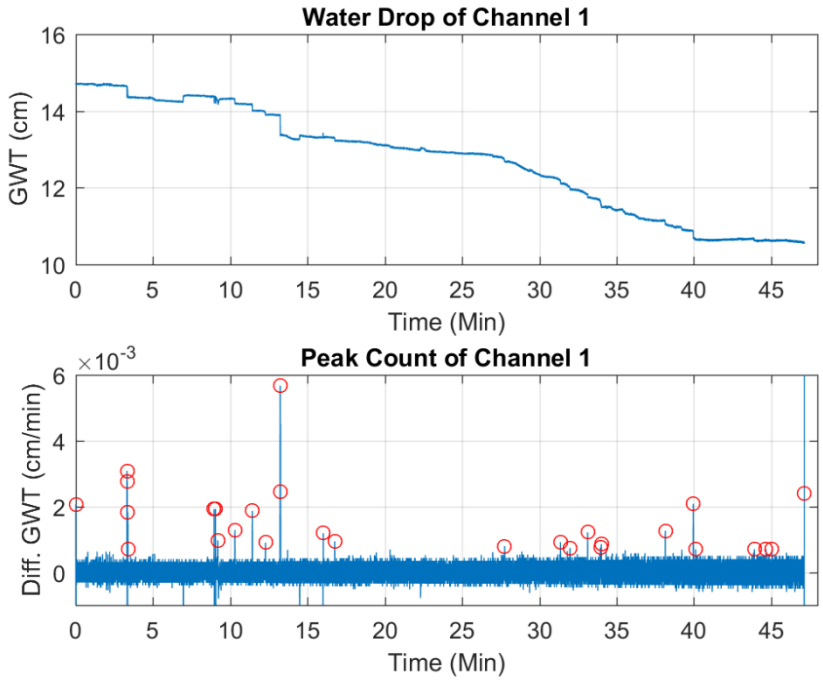

Figure 241: Peak counting of sample 1 with thickness of 200mm, G.W.T = 60mm, and radius (R) = 10 cm

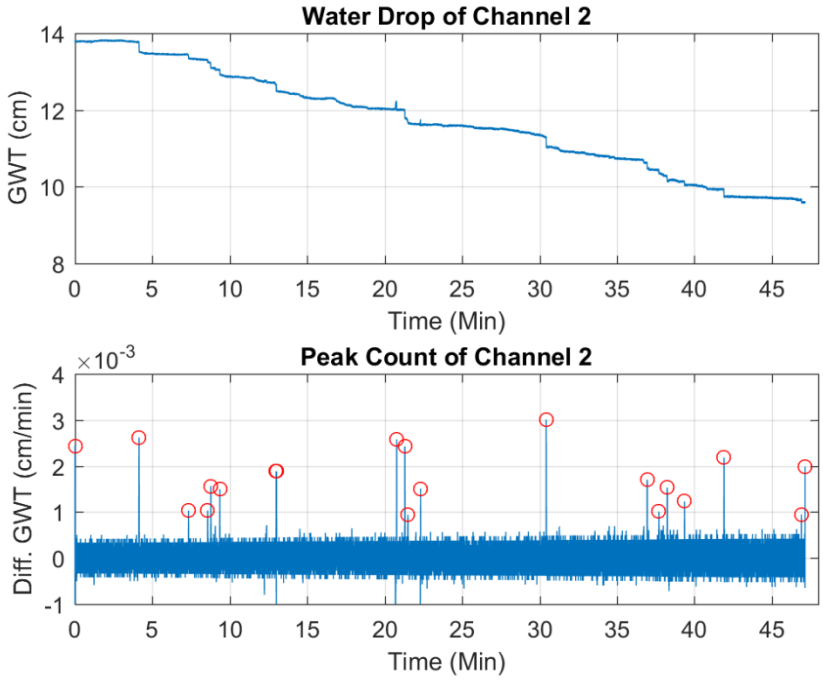

Figure 242: Peak counting of sample 1 with thickness of 200mm, G.W.T = 60mm, and radius (R) = 11 cm

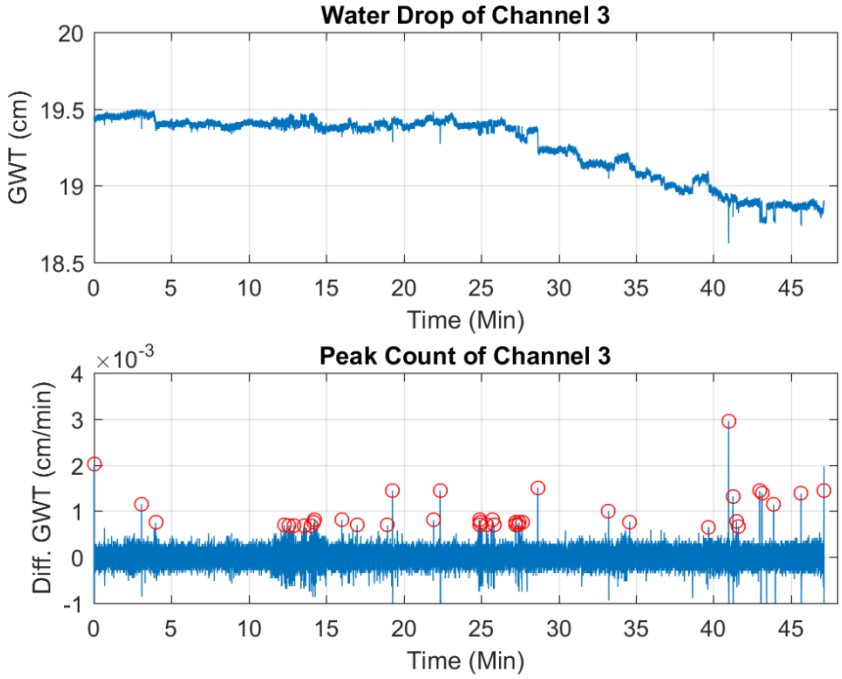

Figure 243: Peak counting of sample 1 with thickness of 200mm, G.W.T = 60mm, and radius (R) = 12 cm

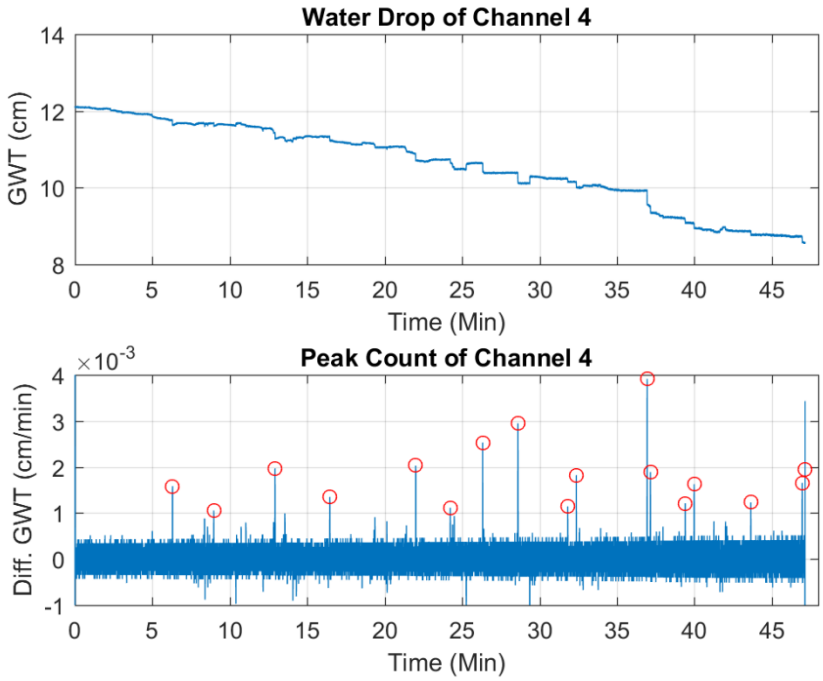

Figure 244: Peak counting of sample 1 with thickness of 200mm, G.W.T = 60mm, and radius (R) = 14.2cm

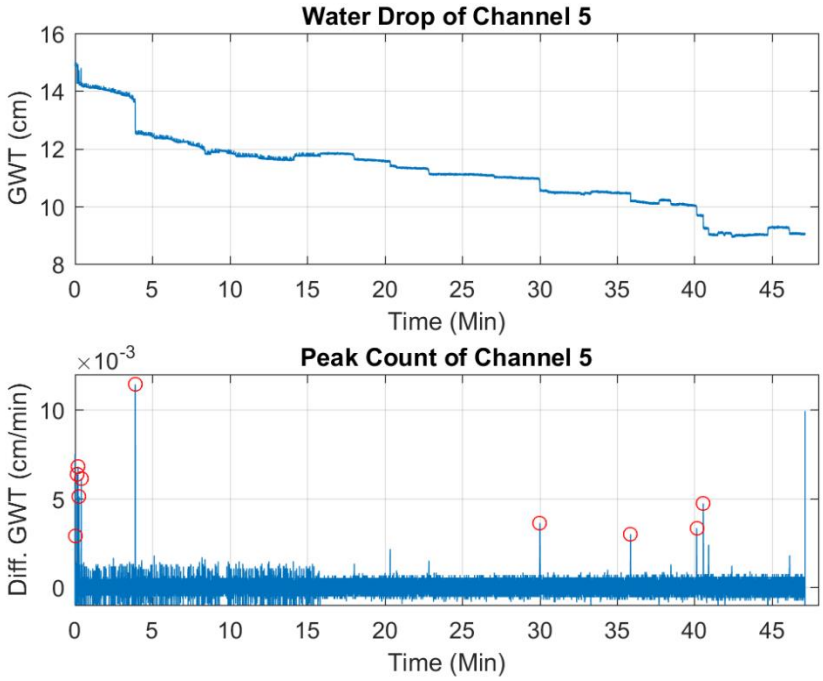

Figure 245: Peak counting of sample 1 with thickness of 200mm, G.W.T = 60mm, and radius (R) = 15.5cm

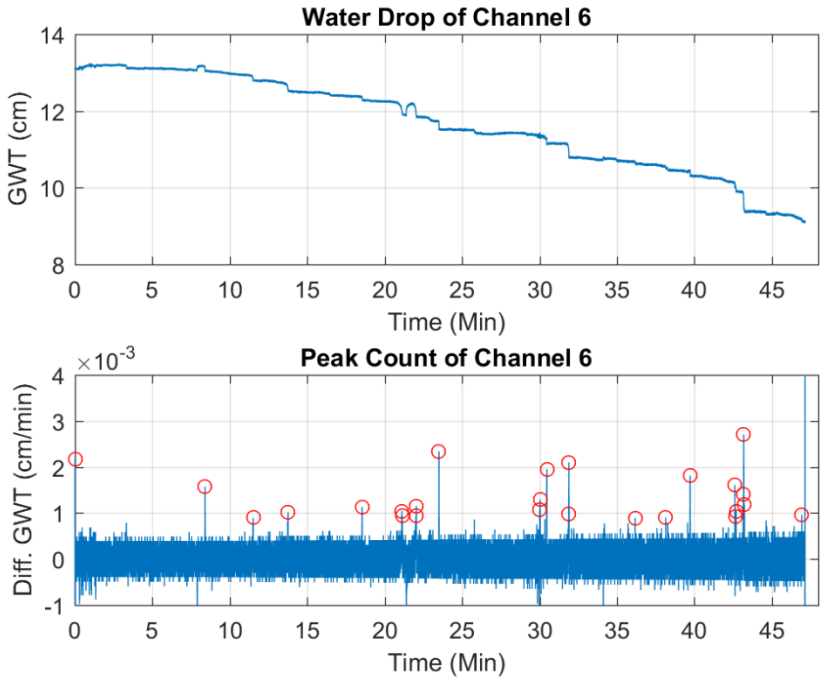

Figure 246: Peak counting of sample 1 with thickness of 200mm, G.W.T = 60mm, and radius (R) = 17.8cm

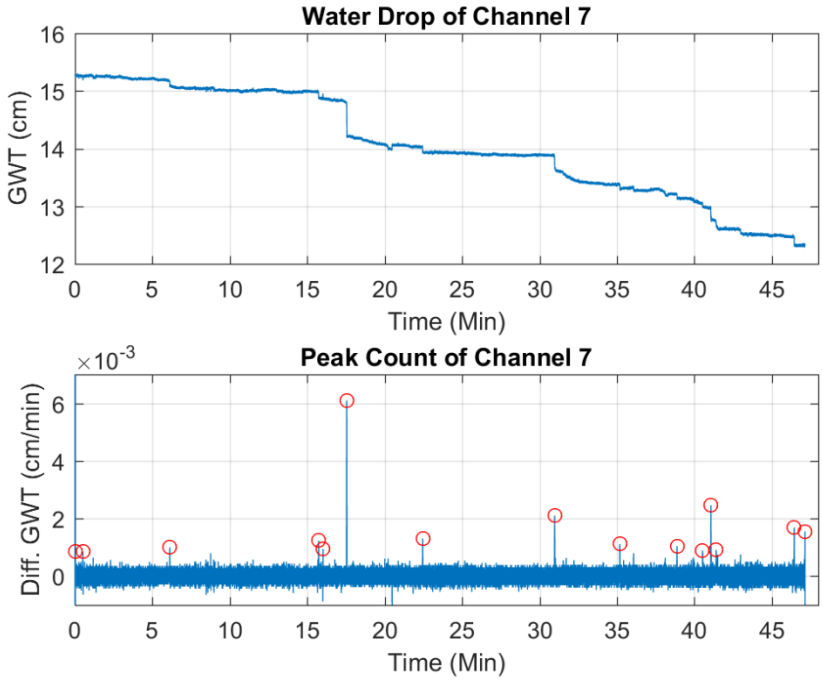

Figure 247: Peak counting of sample 1 with thickness of 200mm, G.W.T = 60mm, and radius (R) = 22.0cm

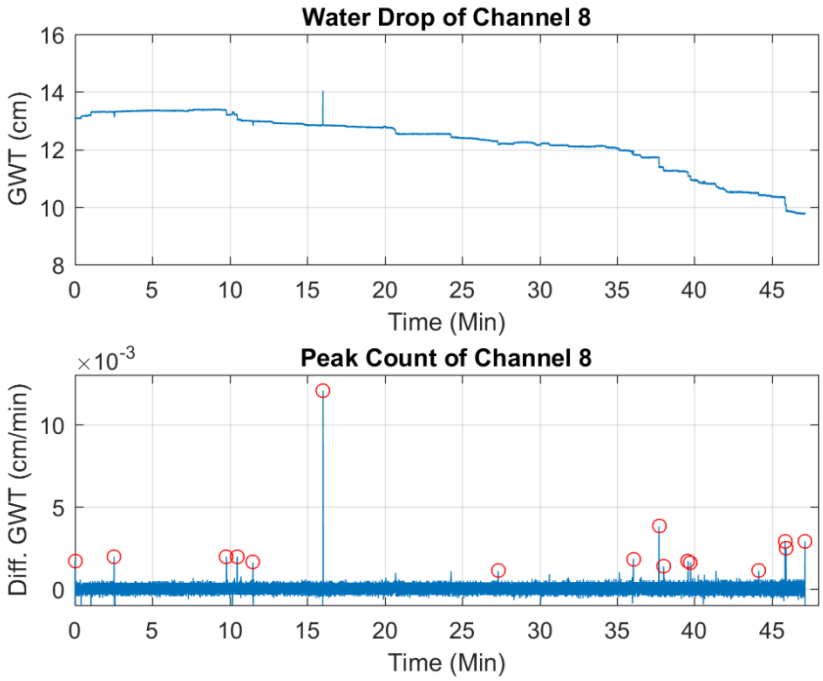

Figure 248: Peak counting of sample 1 with thickness of 200mm, G.W.T = 60mm, and radius (R) = 26 cm

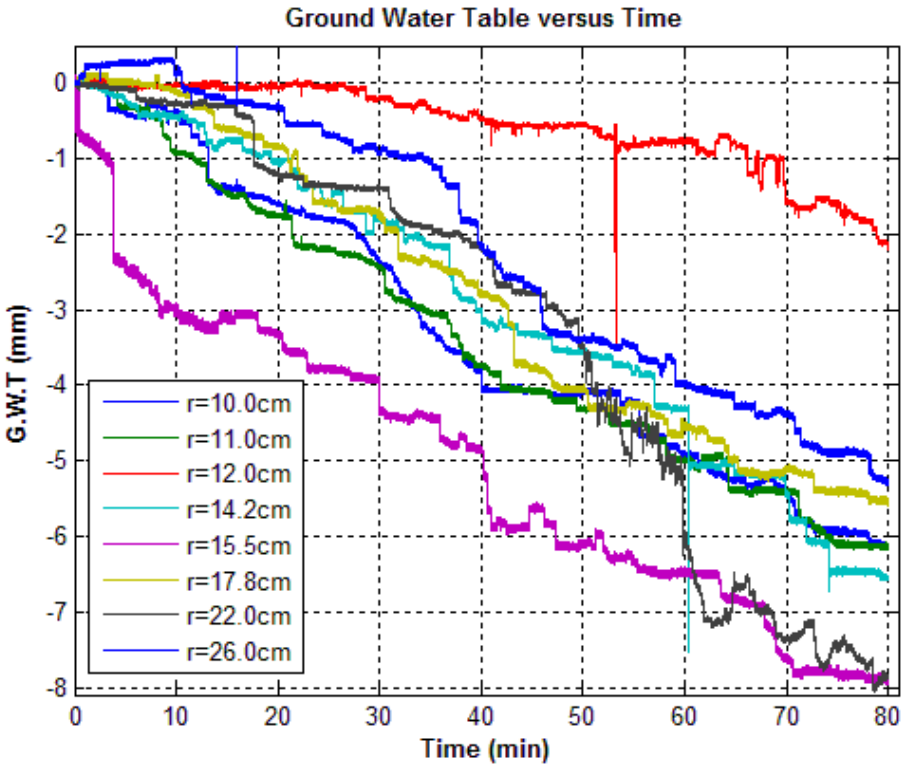

Figure 249: G.W.T over time of sample 1 with soil thickness of 200mm, G.W.T = 60mm

Sample 2 (Soil Thickness = 200mm G.W.T = 60mm)

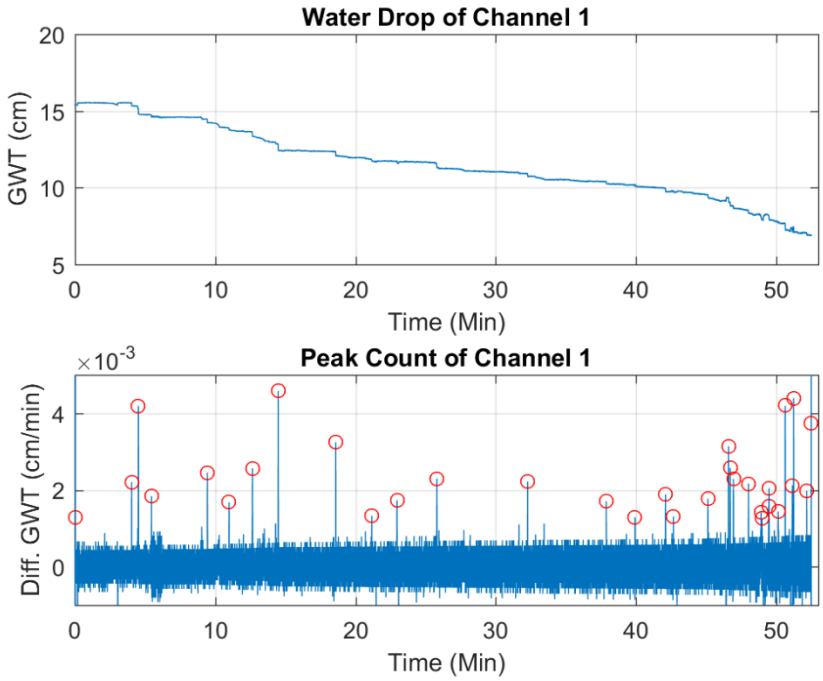

Figure 250: Peak counting of sample 2 with thickness of 200mm, G.W.T = 60mm, and radius (R) = 7.5 cm

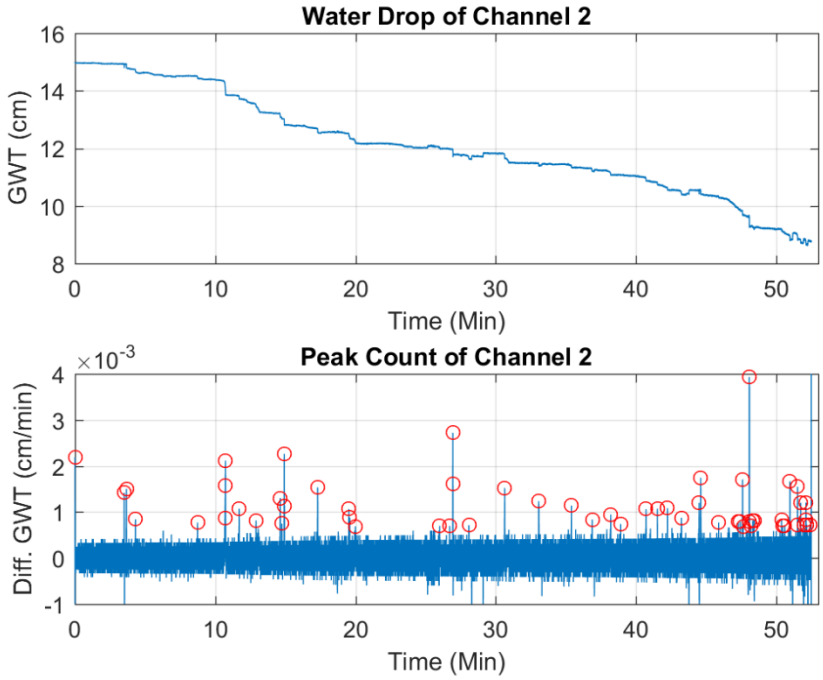

Figure 251: Peak counting of sample 2 with thickness of 200mm, G.W.T = 60mm, and radius (R) =11.5cm

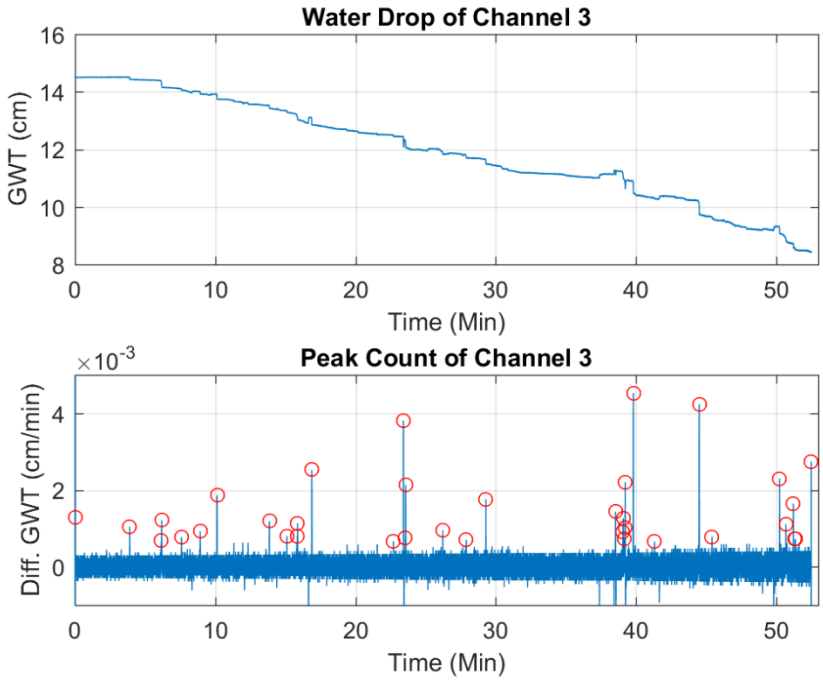

Figure 252: Peak counting of sample 2 with thickness of 200mm, G.W.T = 60mm, and radius (R) = 13.0cm

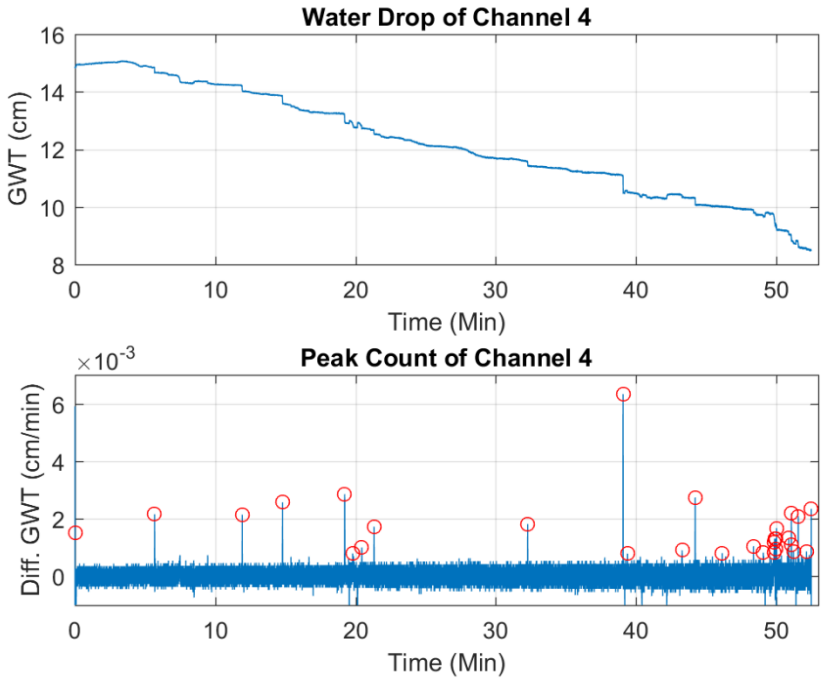

Figure 253: Peak counting of sample 2 with thickness of 200mm, G.W.T = 60mm, and radius (R) = 16.5cm

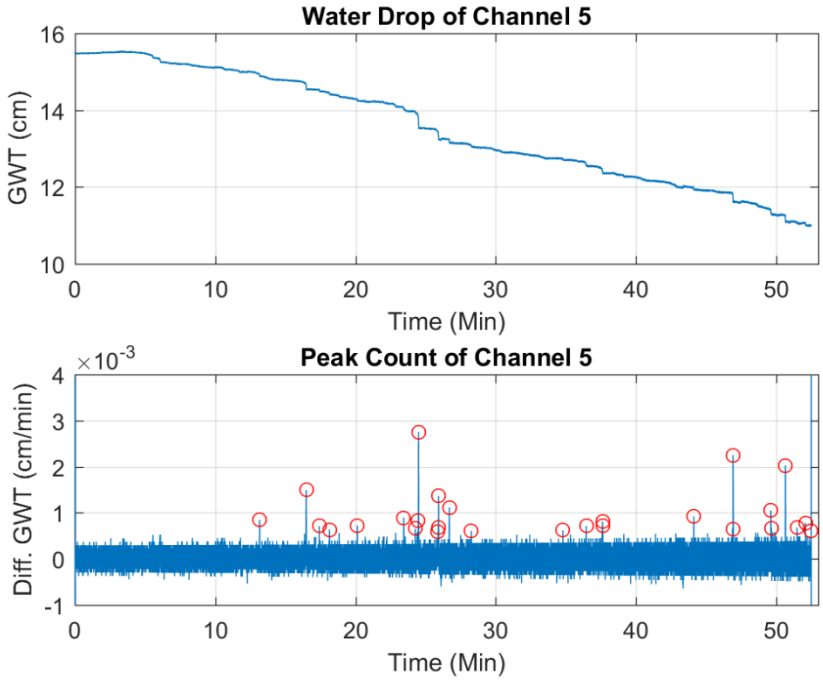

Figure 254: Peak counting of sample 2 with thickness of 200mm, G.W.T = 60mm, and radius (R) = 17.5cm

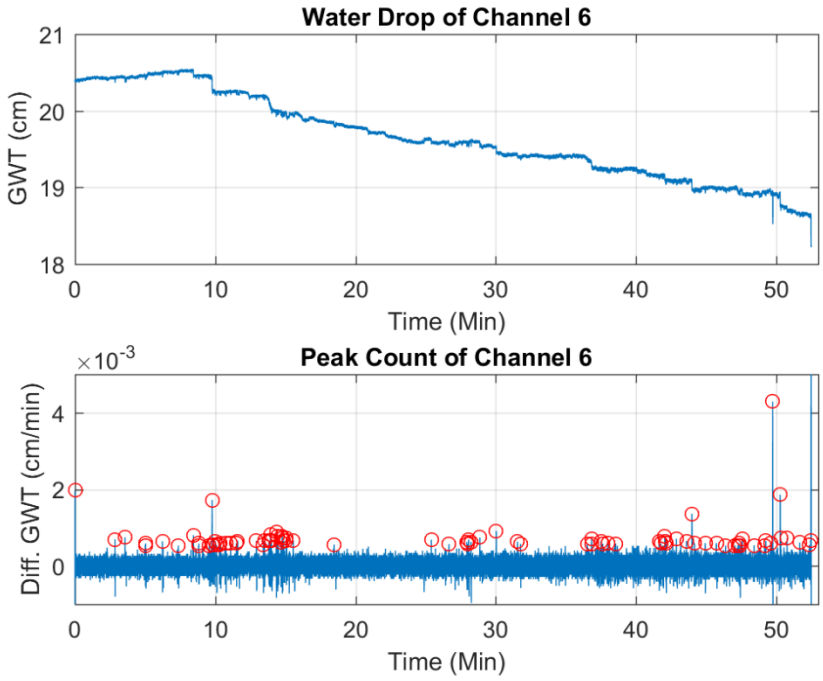

Figure 255: Peak counting of sample 2 with thickness of 200mm, G.W.T = 60mm, and radius (R) = 18.7cm

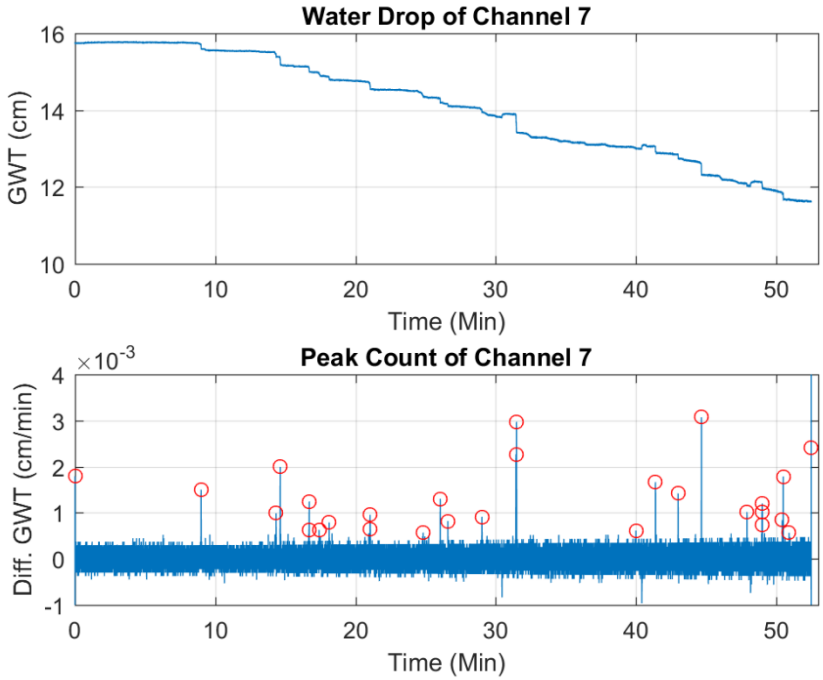

Figure 256: Peak counting of sample 2 with thickness of 200mm, G.W.T = 60mm, and radius (R) = 21.0cm

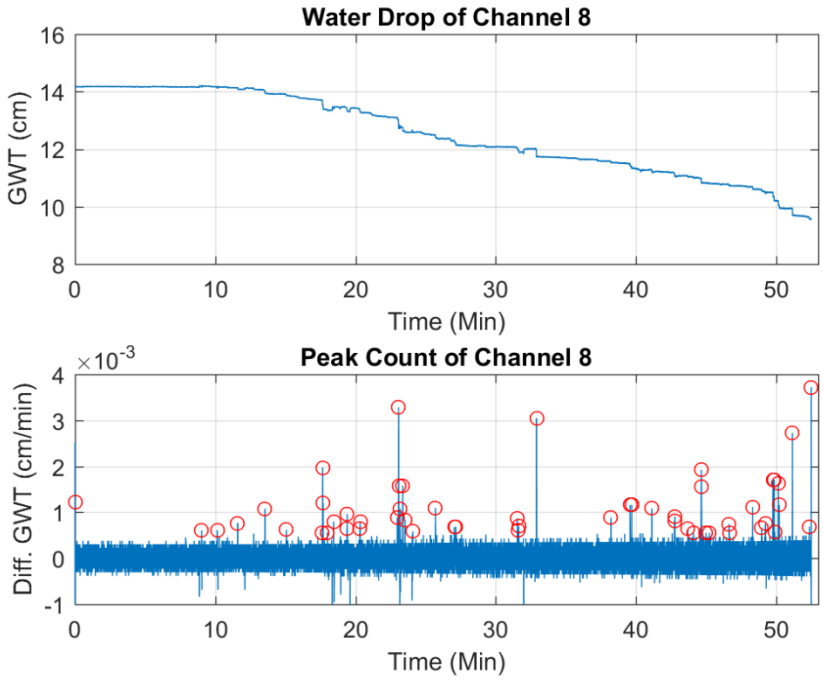

Figure 257: Peak counting of sample 2 with thickness of 200mm, G.W.T = 60mm, and radius (R) = 26.0cm

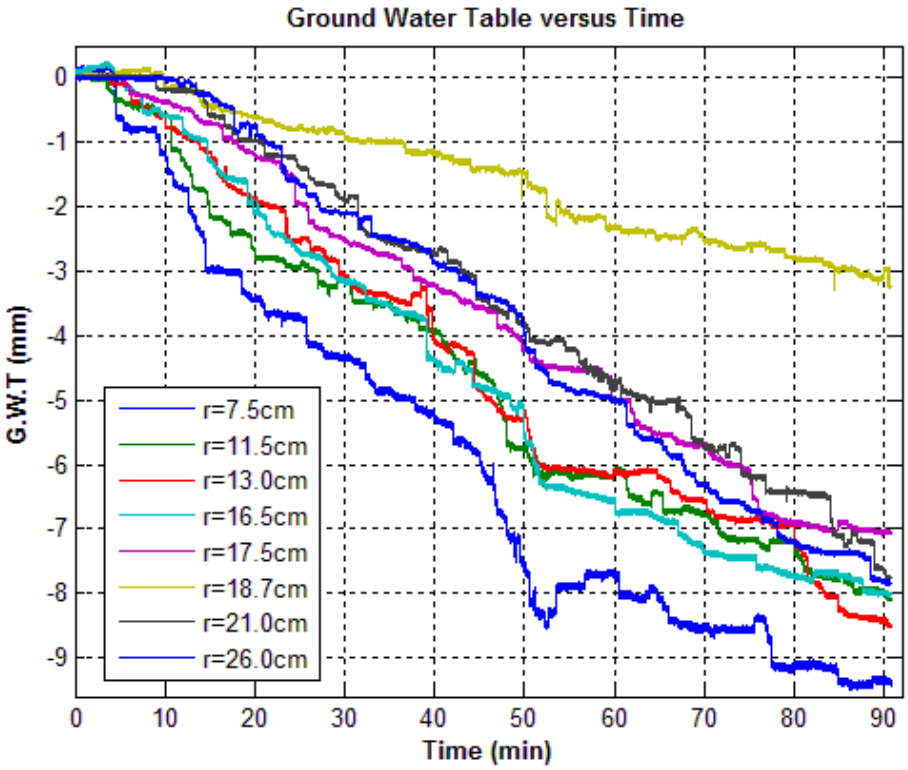

Figure 258: G.W.T over time of sample 2 with soil thickness of 200mm, G.W.T = 60mm

Sample 3 (Soil Thickness = 200mm G.W.T = 60mm)

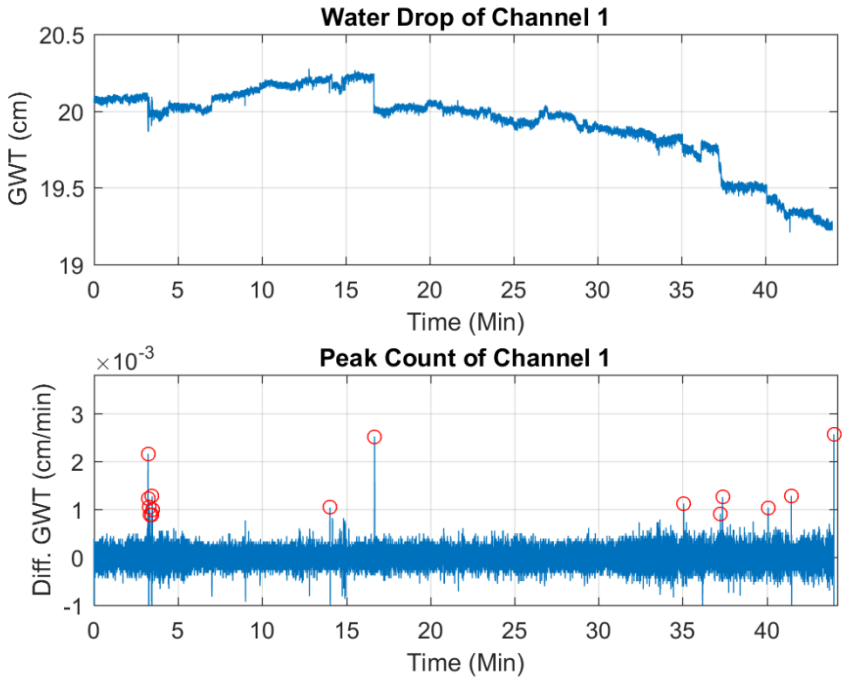

Figure 259: Peak counting of sample 3 with thickness of 200mm, G.W.T = 60mm, and radius (R) = 10.5cm

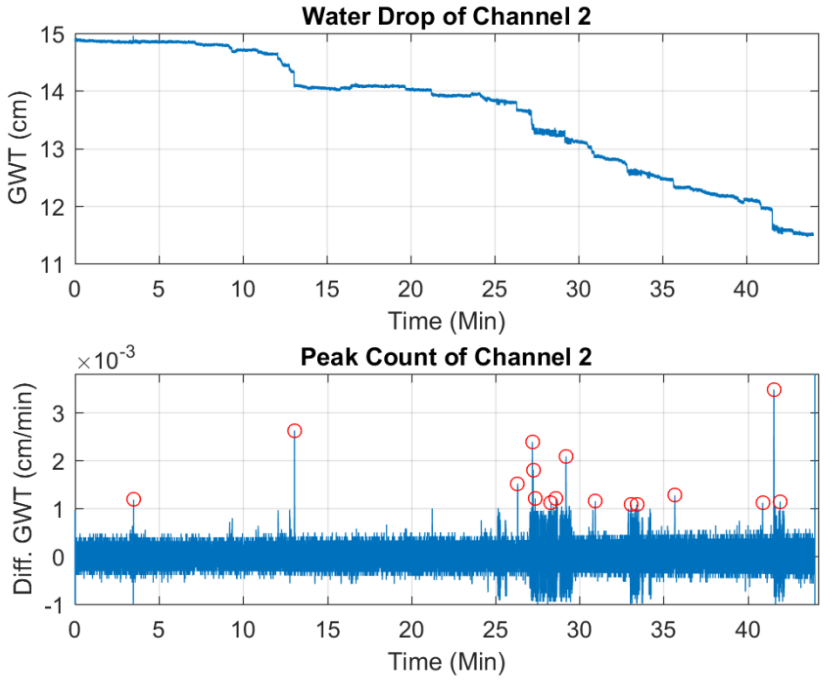

Figure 260: Peak counting of sample 3 with thickness of 200mm, G.W.T = 60mm, and radius (R) = 11.0cm

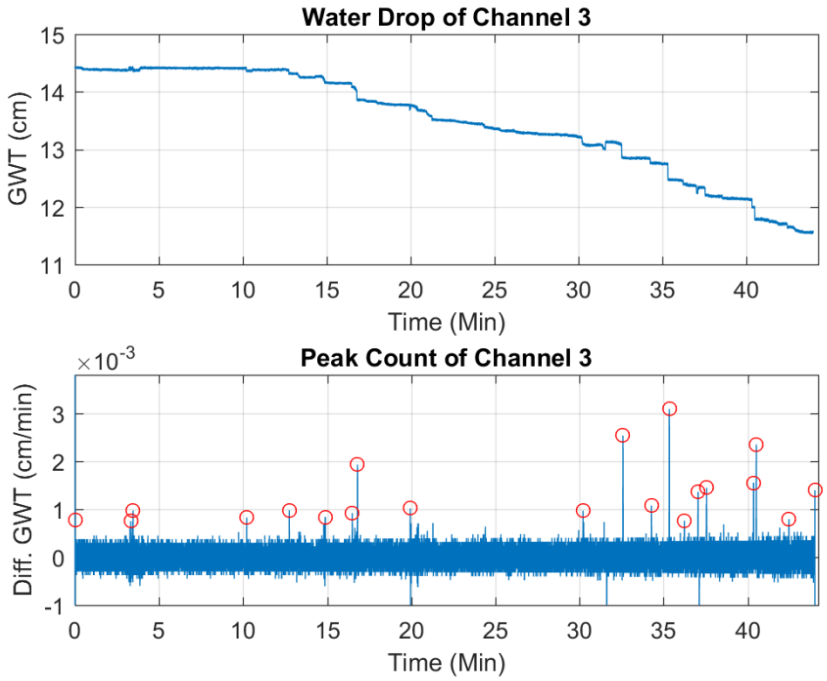

Figure 261: Peak counting of sample 3 with thickness of 200mm, G.W.T = 60mm, and radius (R) = 11.5cm

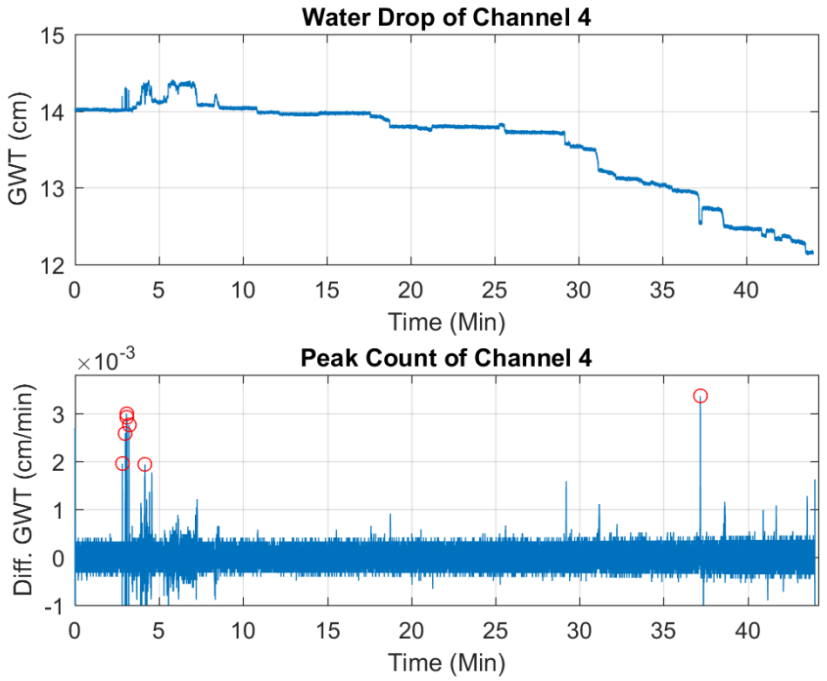

Figure 262: Peak counting of sample 3 with thickness of 200mm, G.W.T = 60mm, and radius (R) = 16.5cm

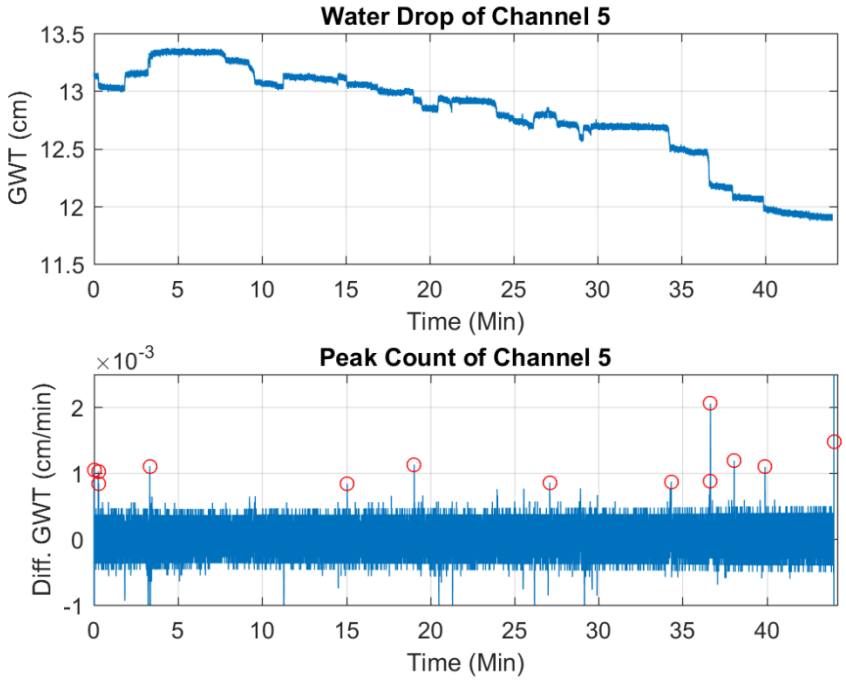

Figure 263: Peak counting of sample 3 with thickness of 200mm, G.W.T = 60mm, and radius (R) = 17.0cm

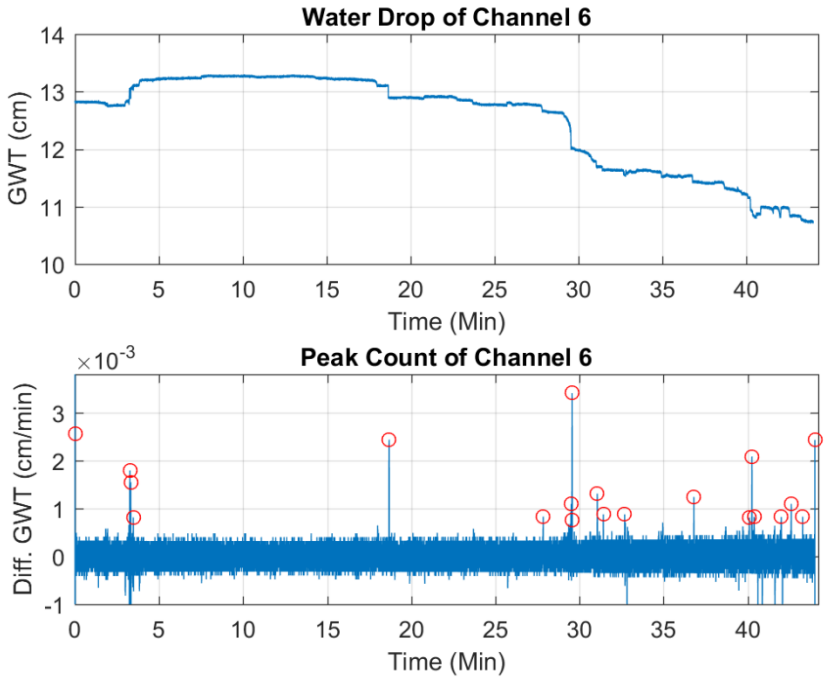

Figure 264: Peak counting of sample 3 with thickness of 200mm, G.W.T = 60mm, and radius (R) = 18.0cm

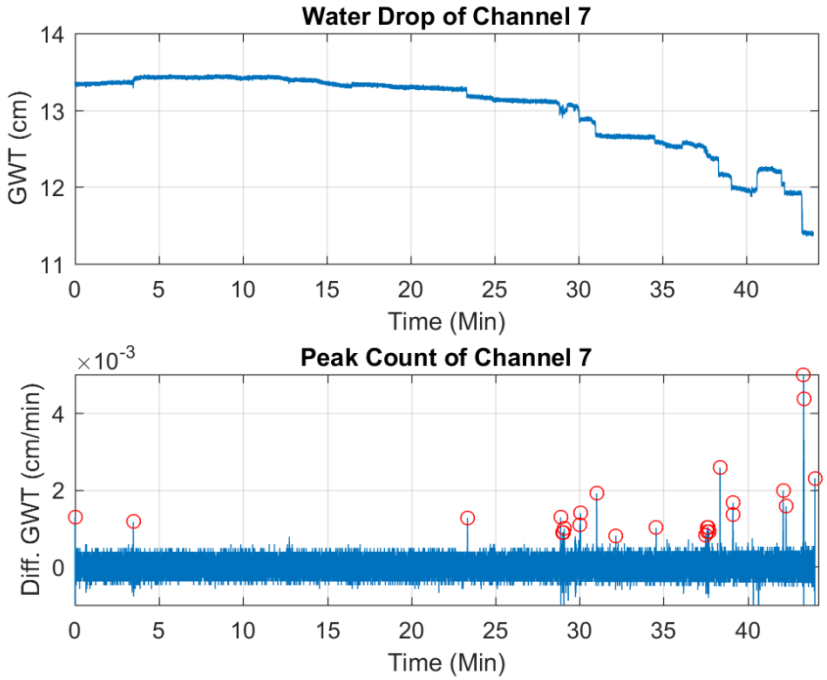

Figure 265: Peak counting of sample 3 with thickness of 200mm, G.W.T = 60mm, and radius (R) = 20.0cm

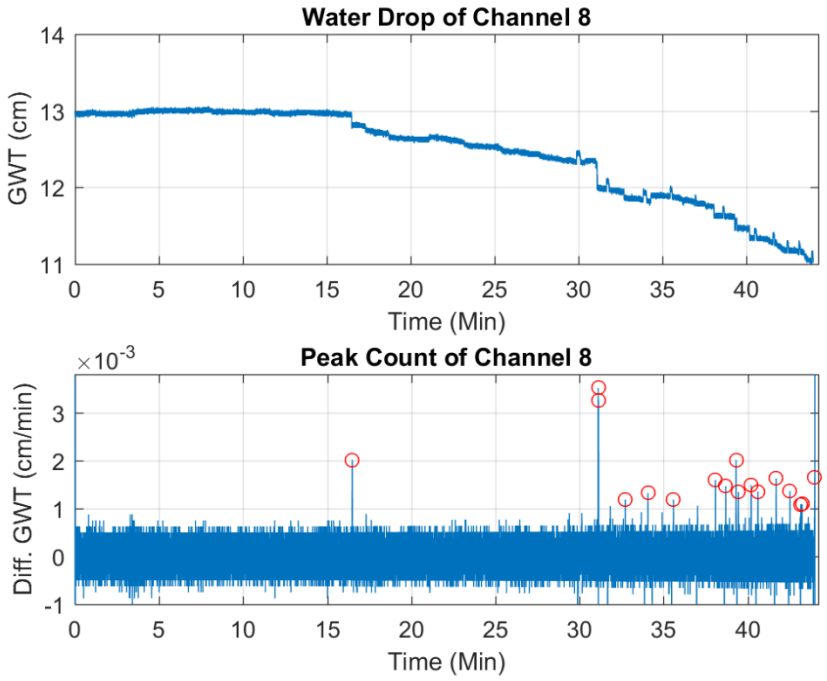

Figure 266: Peak counting of sample 3 with thickness of 200mm, G.W.T = 60mm, and radius (R) = 26.0cm

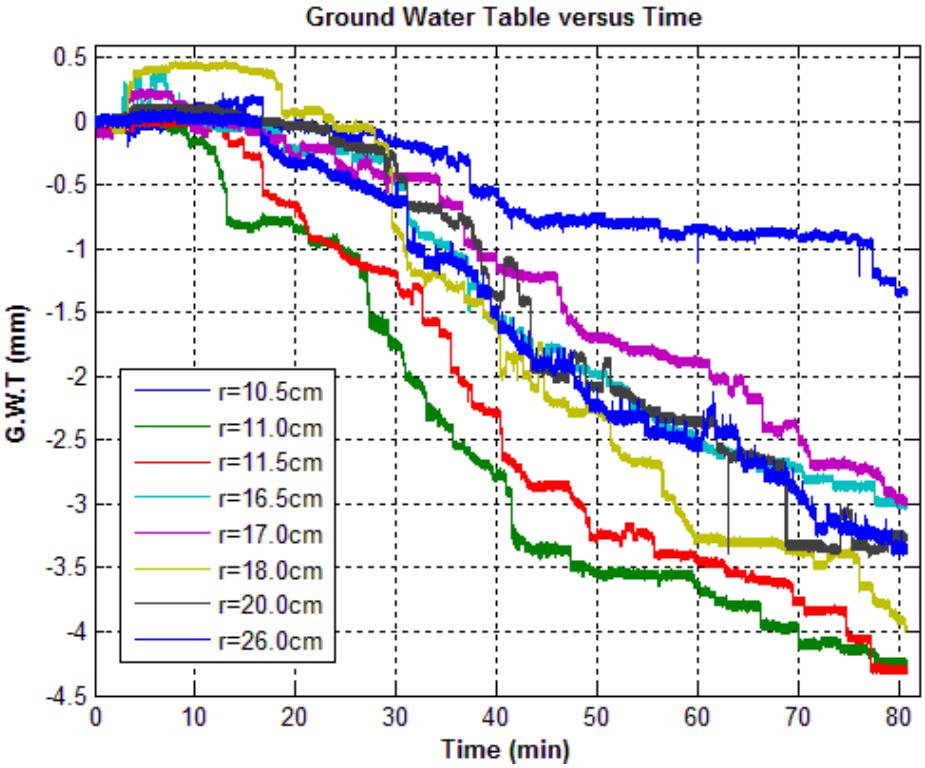

Figure 267: G.W.T over time of sample 3 with soil thickness of 200mm, G.W.T = 60mm

APPENDIX D: RESULTS OF ELECTRIC RESISTIVITY IMAGING

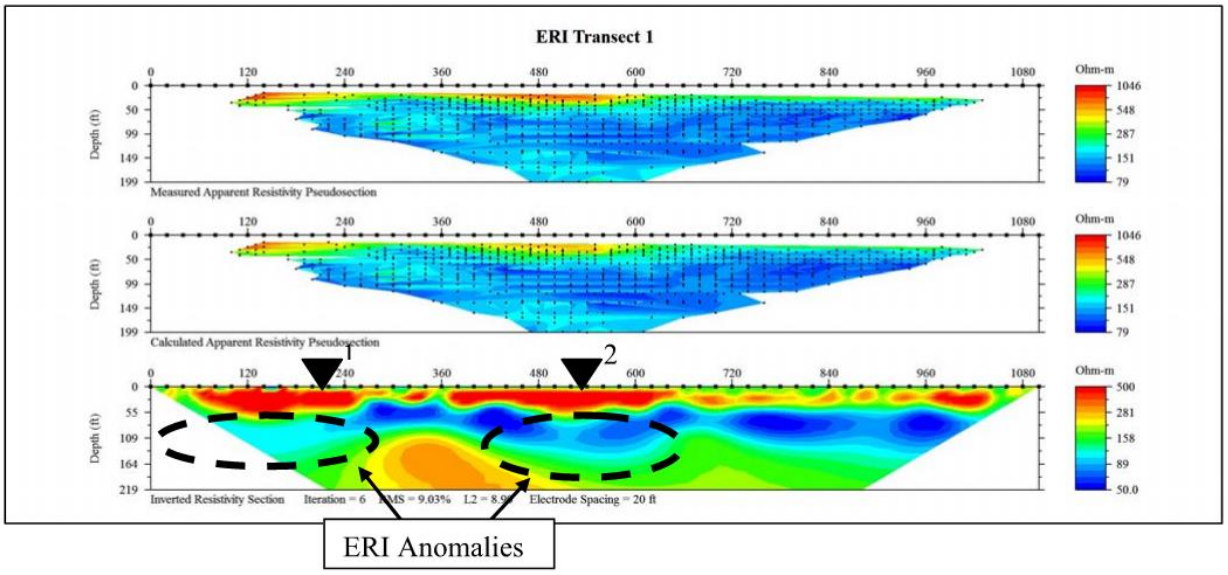

Figure 268: Electric Resistivity Imaging (ERI) Anomaly Transect 1 (Professional Service Industries (PSI), 2014)

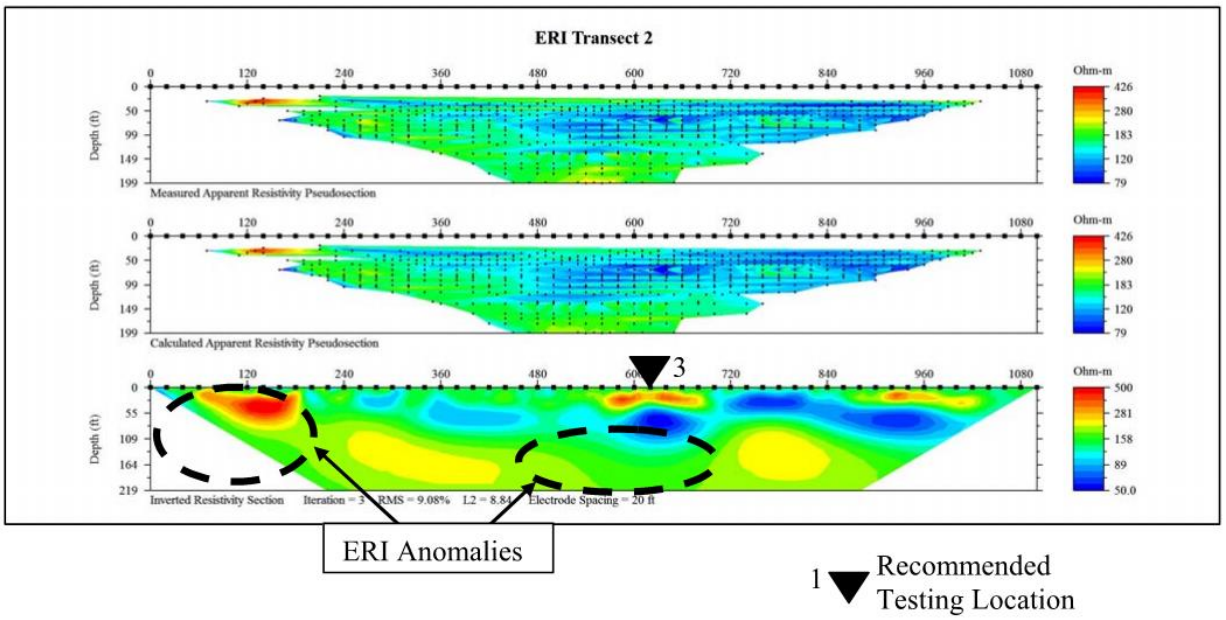

Figure 269: Electric Resistivity Imaging (ERI) Anomaly Transect 2 (Professional Service Industries (PSI), 2014)

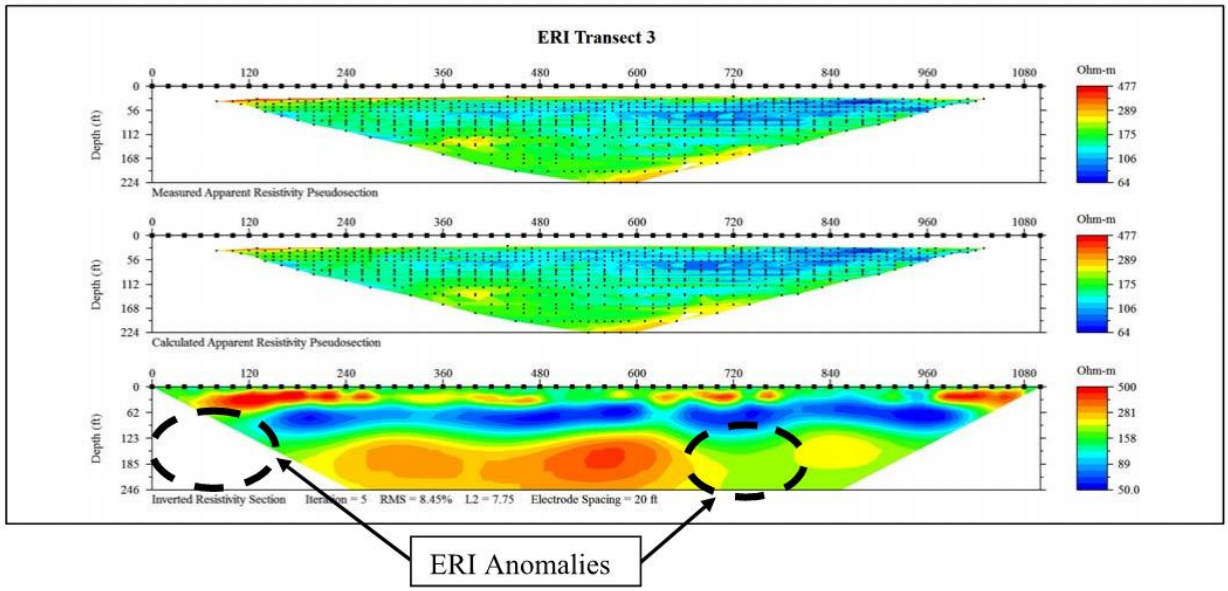

Figure 270: Electric Resistivity Imaging (ERI) Anomaly Transect 3 (Professional Service Industries (PSI), 2014)

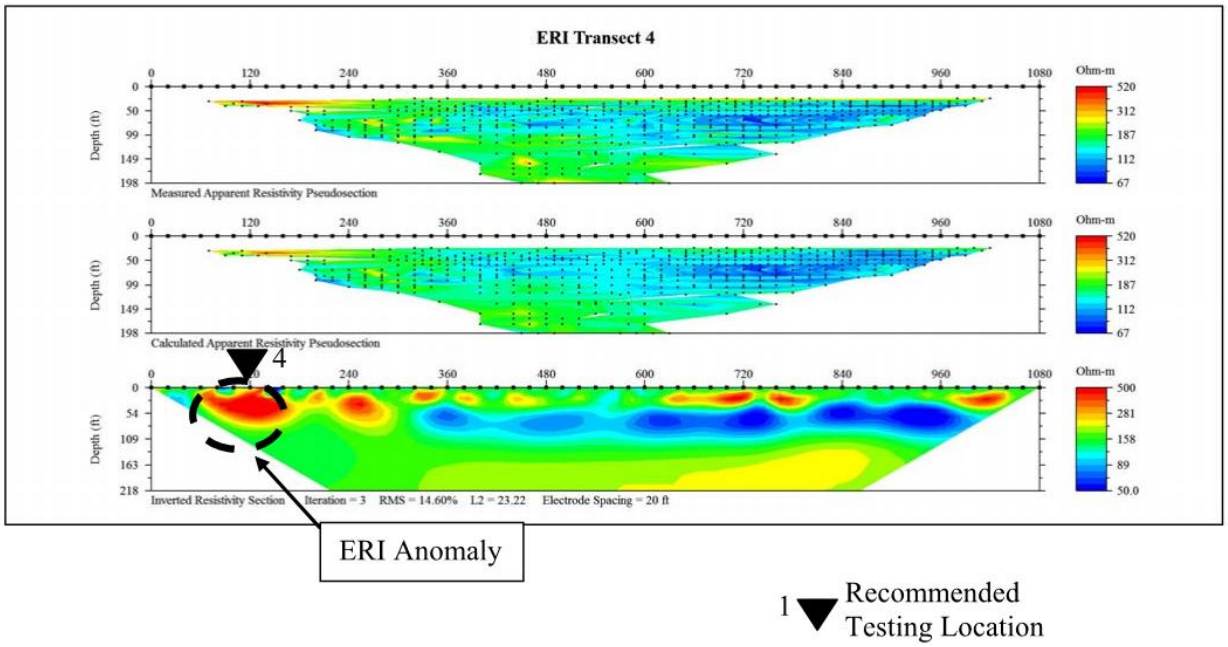

Figure 271: Electric Resistivity Imaging (ERI) Anomaly Transect 4 (Professional Service Industries (PSI), 2014)

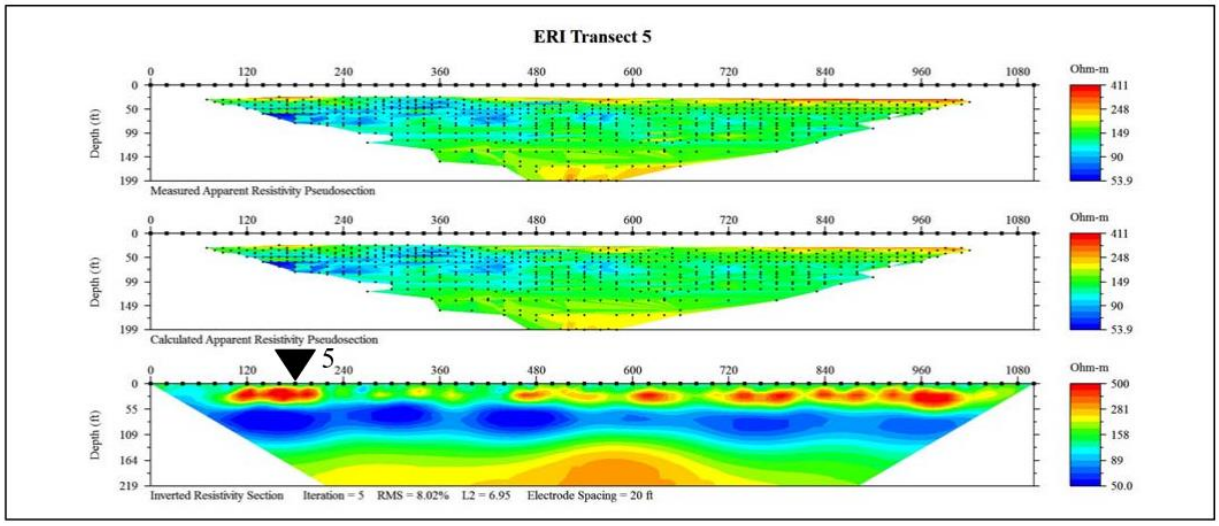

Figure 272: Electric Resistivity Imaging (ERI) Anomaly Transect 5 (Professional Service Industries (PSI), 2014)

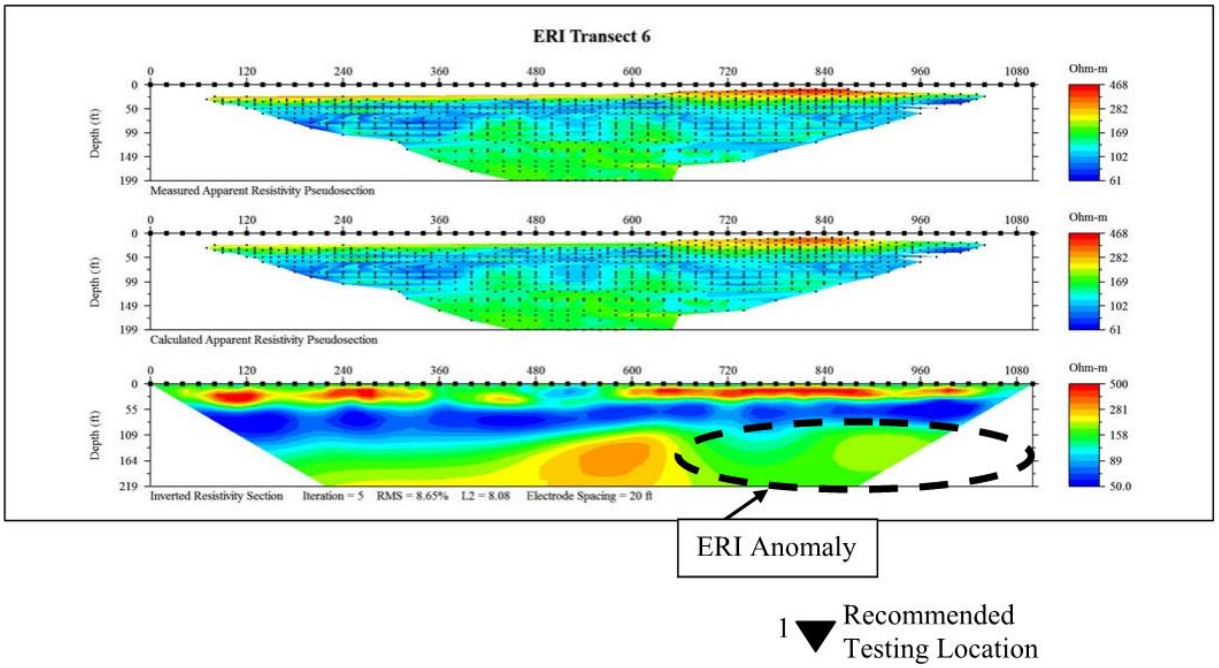

Figure 273: Electric Resistivity Imaging (ERI) Anomaly Transect 6 (Professional Service Industries (PSI), 2014)

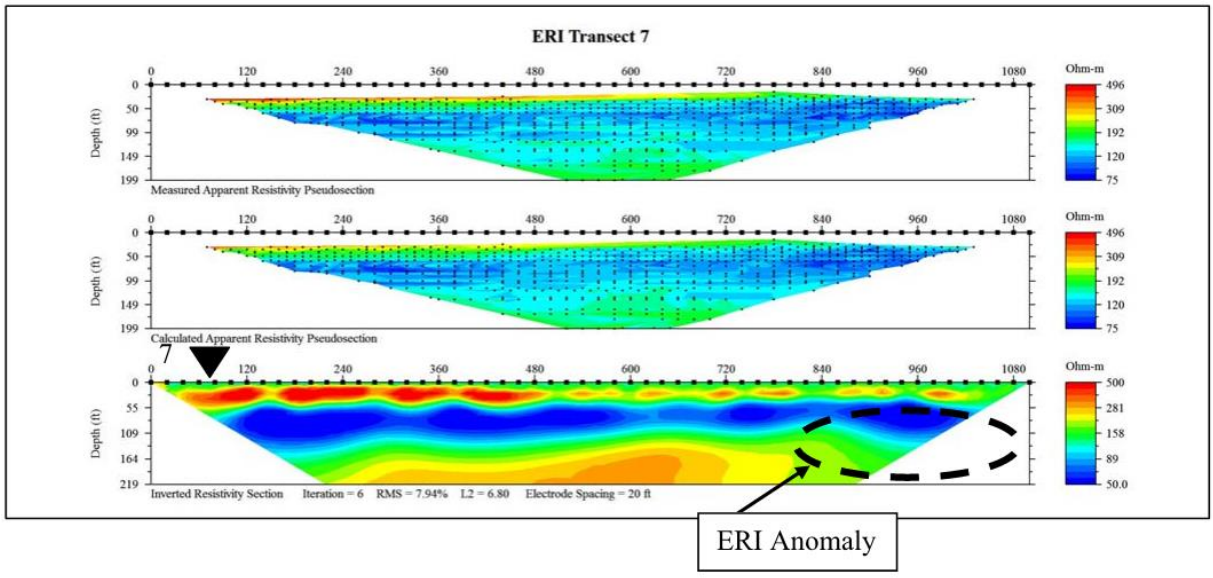

Figure 274: Electric Resistivity Imaging (ERI) Anomaly Transect 7 (Professional Service Industries (PSI), 2014)

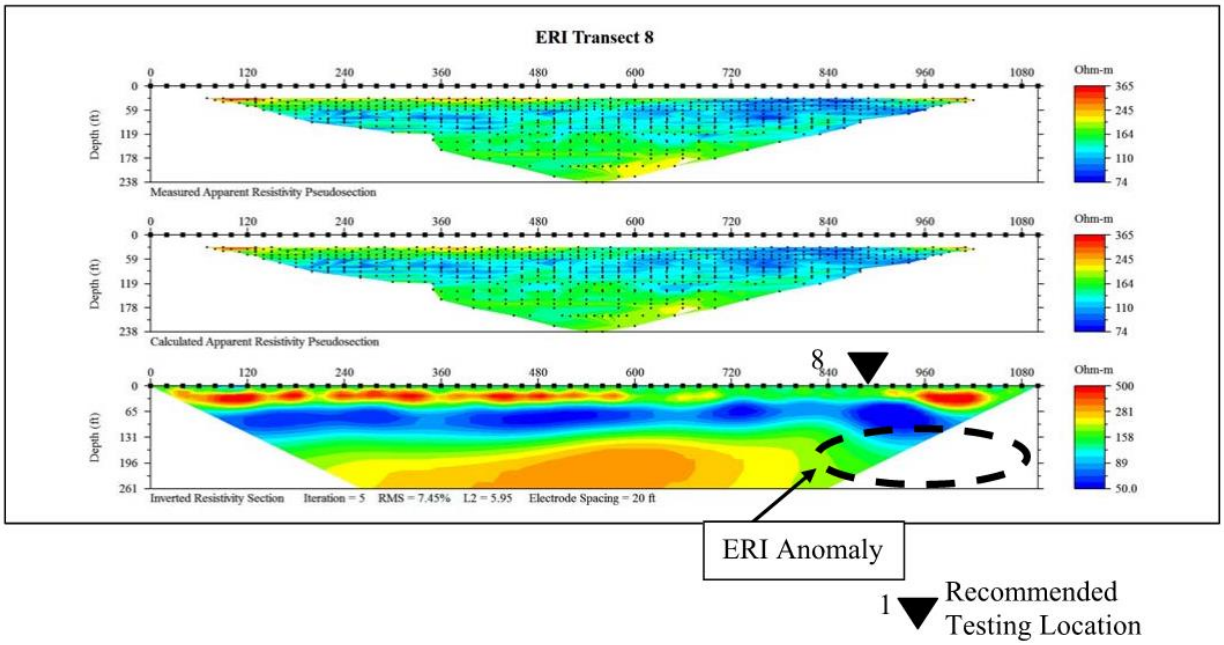

Figure 275: Electric Resistivity Imaging (ERI) Anomaly Transect 8 (Professional Service Industries (PSI), 2014)

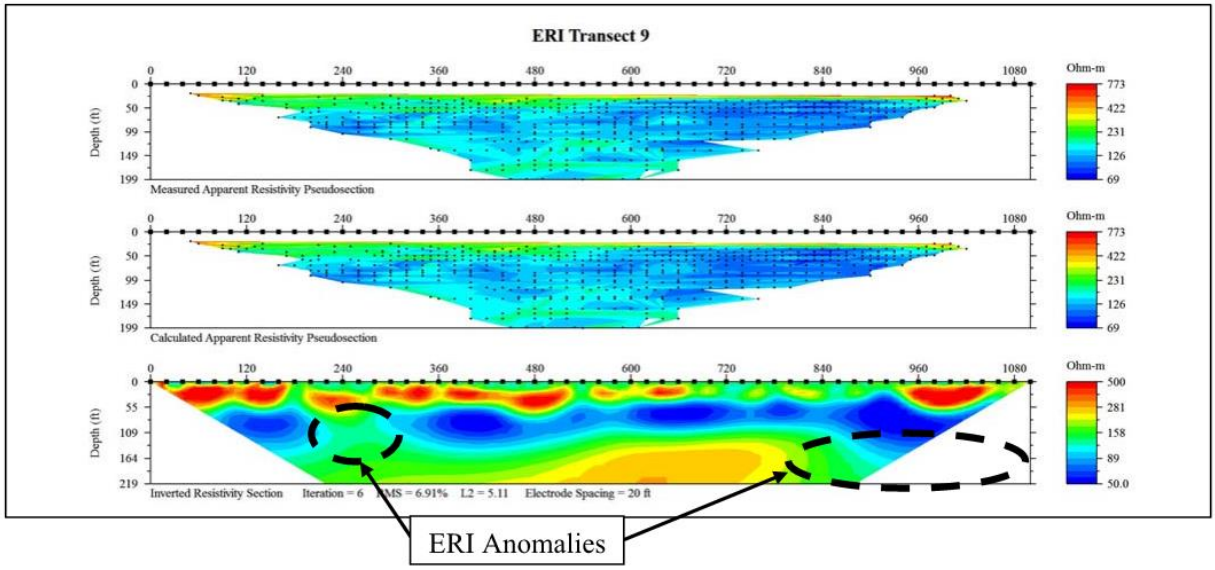

Figure 276: Electric Resistivity Imaging (ERI) Anomaly Transect 9 (Professional Service Industries (PSI), 2014)

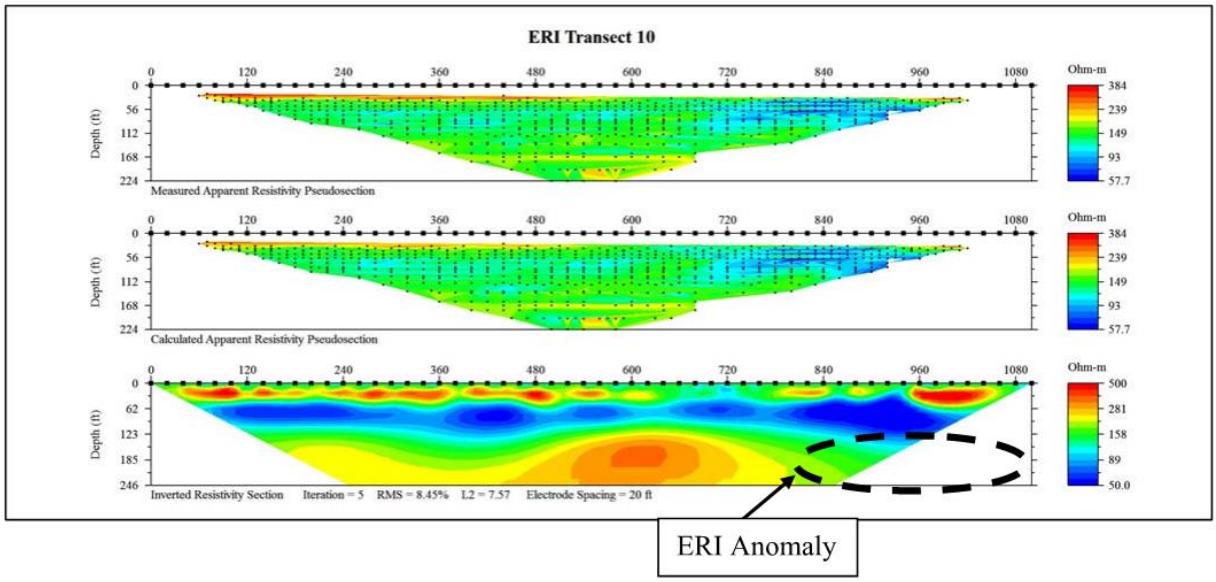

Figure 277: Electric Resistivity Imaging (ERI) Anomaly Transect 10 (Professional Service Industries (PSI), 2014)

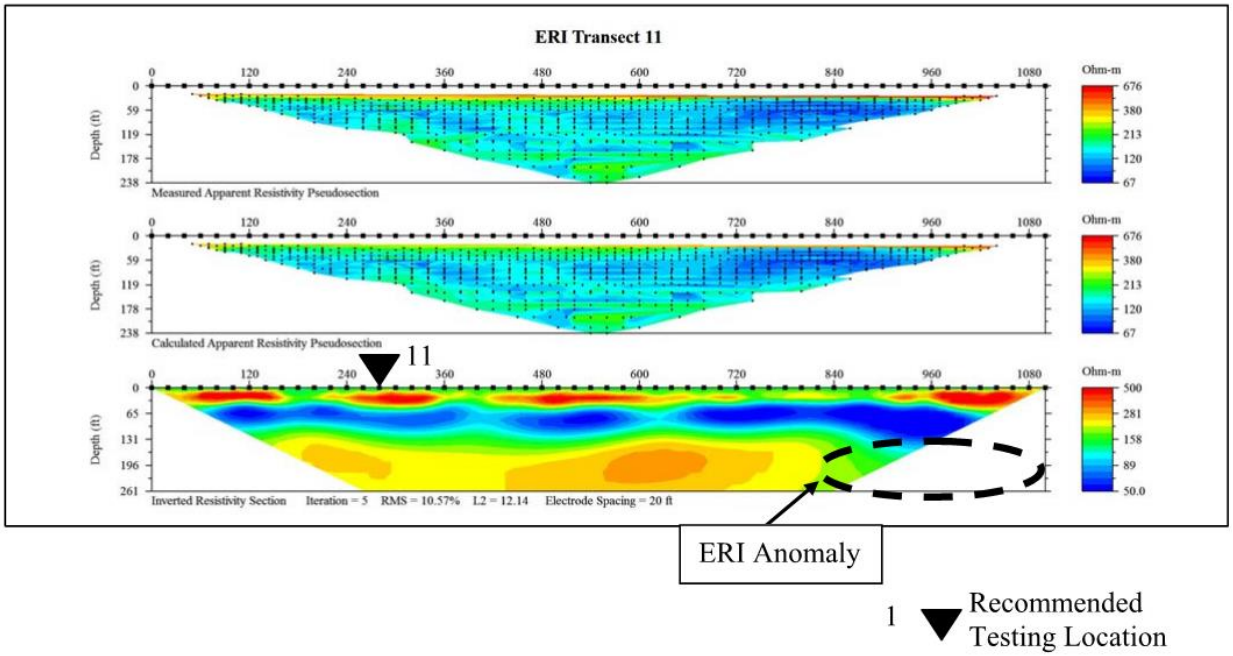

Figure 278: Electric Resistivity Imaging (ERI) Anomaly Transect 11 (Professional Service Industries (PSI), 2014)

REFERENCES

ASTM Standard D3441. (2016). "Standard Test Method for Mechanical Cone Penetration Testing of Soils". West Conshohocken, PA, United State of America: ASTM International.

ASTM Standard D5778. (2012). "Standard Test Method for Electronic Friction Cone and Piezocone Penetration Testing of Soils" . West Conshohocken, PA, United States: ASTM International.

ASTM Standard D6432. (2011). Standard Guide for Using the Surface Ground Penetrating Radar Method for Subsurface Investigation. West Conshohocken, PA, United States: ASTM International. Retrieved 09 26, 2016

Balanis, C. (1989). In *Advanced Engineering Electromagnetics* (p. 981). New York: John Wiley & Sons.

Beck, B. F., & Sinclair, W. C. (1986). *Sinkhole in Florida: An Introduction.* Orlando : The Florida Research Institude at University of Central Florida.

Bloomberg, D., Upchurch, S., Hayden, M., & Williams, R. (1988, 10). Cone-Penetrometer Exploration of Sinkholes: Stratigraphy and Soil Properties. *Environmental Geology, 12*(2), pp. 99-105.

Das, B. M., & Sobhan, K. (2014). Principal of Geotechnical Engineering. In B. M. Das, & K. Sobhan, *Principal of Geotechnical Engineering* (pp. 200-235). Stamford: Cengage Learning.

Environmental Systems Research Institute (ESRI). (2016). *How inverse distance weighted interpolation works*. Retrieved from http://pro.arcgis.com: http://pro.arcgis.com/en/pro-app/help/analysis/geostatistical-analyst/how-inverse-distance-weighted-interpolation-works.htm

FLorida Geological Survey. (2016). Florida Subsidence Incident Reports. Tallahassee, Florida, United States of America. Retrieved from http://www.dep.state.fl.us/geology/geologictopics/sinkhole.htm

Foshee, J., & Bixler , B. (1994). Cover-Subsidance Sinkhole Evaluation of State Road 434, Longwood, Florida. *Journal of Geotechnical Engineering*, 2026-2040.

Geokon. (2016, 9 23). Instruction Manual: Model 4500 Series Vibrating Wire Piezometers. Lebanon, New Hampshire, United States of America.

Jammal amd Associates. (1982). *The Winter Park Sinkhole.* Geotechnical engineering report submitted ti the city of Winter Park, Florida by Jammal amd Associates, Inc.

Lane, E. (1986). *Special Publication No. 29: Karst in Florida.* Tallahassee: Florida Geological Survey .

Lerche, I., & Glaesser, W. (2006). Environmental and Economic Risks from Sinkholes in West-Central Florida. In I. Lerche, & W. Glaesser, *Environmental Risk Assessment* (pp. 67-79). Leizig: Springer.

National Instruments. (2016). *Using Vibrating Wire Sensors with CompactRIO*. Retrieved from http://www.ni.com: http://www.ni.com/white-paper/14671/en/

O'donnell, C. (2016). Mosaic plant sinkhole dumps 215 million gallons of reprocessed water into Floridan Aquifer (w/video). *Tampa Bay Times*.

O'Meara, C. (2016, 9 29). *Water continues to flow into a large sinkhole on the Mosaic Co. property shown in this aerial photo Thursday, Sept. 29, 2016, in Mulberry, Fla.* The Associated Press, Online. Retrieved from http://hosted.ap.org/dynamic/files/photos/0/0fe360ad3ce2424da0da34128781a4b7_1.html?SITE=AP&SECTION=HOME&TEMPLATE=DEFAULT

Professional Service Industries (PSI). (2014). *Sinkhole and Engineering Evaluations Wekiva Parkway and State Road 46 Connector Road Interchange.* Tallahassee: Florida Department of Transportation (FDOT).

Tihansky, A. B. (1999). *Sinkholes West-Central Florida.* Retrieved 09 21, 2016, from U.S. Geological Survey, Tampa, Florida: http://fl.water.usgs.gov/PDF_files/cir1182_tihansky.pdf

U.S Geological Survey. (2016, 10 17). *USGS 284759081232100 Lake Sylvan Park Rain Gage Near Paola, FL*. Retrieved from USGS Current Conditions for the Nation: http://nwis.waterdata.usgs.gov/nwis/uv?cb_00045=on&format=gif&site_no=284759081232100&period=&begin_date=2016-08-17&end_date=2016-10-11

U.S. Geological Survey. (1985). Sinkhole Type. Development, and Distribution in Florida . *Map Series No. 110*. Tallahassee, Florida, United States of America: Florida Department of Natural Resources Bureau of Geology/ Florida Dpartment of Environmental Regulation Bureau of Water Resources Management.

U.S. Geological Survey. (n.d.). *Ground Water Atlas of the United States Alabama, Florida, Georgia, and South Carolina HA 730-G*. Retrieved 9 20, 2016, from United States Geological Survey: http://pubs.usgs.gov/ha/ha730/ch_g/G-Floridan7.html

United States Department of Agriculture (USDA). (n.d.). *Web Soil Survey*. Retrieved 06 19, 2016, from http://websoilsurvey.sc.egov.usda.gov/App/WebSoilSurvey.aspx

Waltham, T., Bell, F., & Culshaw, M. (2005). *Sinkholes and Subsidence Karst and Cavernous in Engineering and Construction* . Chichester, UK: Praxis Publishing Ltd.